JSCSEN 75(9)1167–1313(2010)

Journal of the Serbian Chemical Society

Electronic version

VOLUME 75

No 9

BELGRADE 2010

Available on line at

www.shd.org.rs/JSCS/

The full search of JSCS is available through

DOAJ DIRECTORY OF OPEN ACCESS JOURNALS

www.doaj.org

Journal of the Serbian Chemical Society
JSCS-info@shd.org.rs • www.shd.org.rs/JSCS

J. Serb. Chem. Soc. Vol. 75, No. 9 (2010)

CONTENTS

Published by the Serbian Chemical Society
Karnegijeva 4/III, 11000 Belgrade, Serbia
Printed by the Faculty of Technology and Metallurgy
Karnegijeva 4, P.O. Box 35-03, 11120 Belgrade, Serbia

Journal of the Serbian Chemical Society
JSCS-info@shd.org.rs • www.shd.org.rs/JSCS
J. Serb. Chem. Soc. 75 (9) 1167–1179 (2010)
JSCS–4040
UDC 547.461.5:576.385.5:616–006.04
Original scientific paper

Antiproliferative activity of NCI-DTP glutarimide derivatives. An alignment independent 3D QSAR study

JELENA B. POPOVIĆ-DJORDJEVIĆ[1]*, LJILJANA I. DOŠEN-MIĆOVIĆ[2#], IVAN O. JURANIĆ[2#] and BRANKO J. DRAKULIĆ[3#]

[1]*Faculty of Agriculture, University of Belgrade, Nemanjina 6, 11080 Belgrade,* [2]*Faculty of Chemistry, University of Belgrade, Studentski trg 12–16, 11000 Belgrade and* [3]*ICTM – Department of Chemistry, University of Belgrade, Njegoševa 12, 11000 Belgrade, Serbia*

(Received 2 December 2009, revised 25 January 2010)

Abstract: Alignment-free, three dimensional structure–activity relationships (3D QSAR) of the antiproliferative potency of twenty-two glutarimide-containing compounds, taken from National Cancer Institute Developmental therapeutics Program database, toward eight representative human tumour cell lines are reported. The descriptors used in the QSAR study were derived from GRID molecular interaction fields. The obtained models readily detect structural motifs positively or negatively correlated with the potency of the studied compounds toward each cell line. In this way, the pharmacophoric pattern required for high potency of compounds is reported. This pattern can serve as guidance for the design and syntheses of novel congeners, planned to be tested toward human tumour cell lines.

Keywords: glutarimides; antiproliferative agents; alignment-independent 3D QSAR; GRIND descriptors.

INTRODUCTION

Nitrogen-containing heterocyclic systems having different pharmacological activities are widespread among alkaloids. Five- and six-membered cyclic imide derivatives are a valuable group of bioactive compounds, which act as androgen receptor antagonists, anti-inflammatory agents, anxiolytics, antivirals, antibacterials, and tumour suppressing agents.[1] These compounds rarely occur in natural sources and most of them are made synthetically.

Cancer may affect people at all ages, animals or even plants; it causes about 13 % of all human deaths. Consequently, huge efforts are being made in the search for and exploration of new antitumour agents. In light of the present re-

* Corresponding author. E-mail: jelenadj@agrif.bg.ac.rs
# Serbian Chemical Society member.
doi: 10.2298/JSC091202076P

cession in the world and the reduction of financing in R&D, all pharmaceutical companies retain the development of antitumour agents as top priority projects.

Some naturally occurring glutarimides, such as sesbanimides, cycloheximide, and streptimidone, were investigated as antibiotics during the 60–70s of the last century. Later, it was discovered that they act as very potent cytotoxic agents.[2,3] Recent research in the field of human medicine shows that cycloheximide increases the cytotoxic effect of the recombinant human tumour necrosis factor-α (rHuTNF-α) to nasopharyngeal carcinoma cells (NPC).[4] The structurally related streptimidone derivative, 9-methylstreptimidone (9-MS), exerts significant inhibitory activity to the cancer and inflammatory cells activated nuclear factor-κB (NF-κB).[5]

The non-steroidal aromatase inhibitor aminoglutethimide is used for the treatment of Cushing's syndrome[6] and hormone-sensitive metastatic breast cancer.[7,8] Estrone derivatives with the D-ring replaced with the glutarimide ring have shown potent inhibition of steroid sulphatase, an enzyme which is involved in the pathway of the development of hormone-dependent breast tumours (HDBT).[9] 2-Phenylamino-imidazo[4,5-*h*]isoquinolin-9-ones, inhibitors of kinase p56 (lck) in T-cells, were recently reported as potential therapeutic agents in the treatment of different autoimmune diseases.[10]

The GRIND, alignment independent, interpretable and efficient to compute descriptors derived from GRID molecular interaction fields, was proved relevant in diverse structure–activity relationship studies. The GRIND was used for structure–activity relationships in receptors or enzymes, the classification of large structurally diverse datasets by pharmacophore similarity and virtual screening.[11] Regarding the antiproliferative activity of organic compounds, the structure-based rationalization of the mechanism of action of antitumour drugs on NCI-DTP screening data was reported,[12] together with case studies of potent antiproliferative imidazolium derivatives[13] and histone deacetylase inhibitors.[14]

Continuing our interest in glutarimide derivatives,[15] a structure–activity study is reported herein on the antiproliferative activity of a set of glutarimide-containing compounds (**1**–**22**) toward K562 (leukaemia), A549ATCC (non-small cell lung), malme-3M (melanoma), COLO205 (colon), UO31 (renal), U251 (CNS), IGROV1 (ovarian), and MFC-7 (breast) human tumour cell lines; which are described in the text as models **A**–**H**, respectively. Data were taken from the US National Cancer Institute (NCI) Developmental Therapeutics Program 60 human tumours cell line screen database (NCI60).[16] The results obtained in this study could be a guidance for the design of novel congeners with expected antiproliferative activity. To the best of our knowledge, structure–activity relationships of the antiproliferative potency of glutarimide derivatives cannot be found in the literature.

RESULTS AND DISCUSSION

Aimed at finding the pharmacophoric pattern of glutarimide derivatives responsible for their significant antiproliferative activity, alignment-independent 3D QSAR models for the potency of **1**–**22** toward representative cell lines were obtained. The criteria for the selection of the compounds are given in the Experimental. Within each category, the cell line towards which most of the glutarimide derivatives exert activity were chosen. The structures and classification of the compounds are given in Table I.

Methodology

The program Pentacle[17] uses alignment independent descriptors derived from GRID[18] molecular interaction fields (MIF). A more negative value of GRID MIF for any used probe corresponds to a more favourable interaction between the

TABLE I. Structures of **1**–**22** used in the models

Class No.[a]	Structure	Compound No.
I	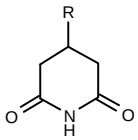 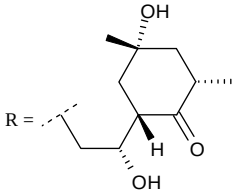	**1**
	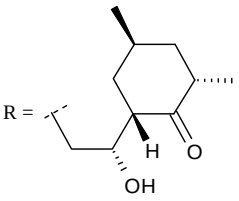	**2**
	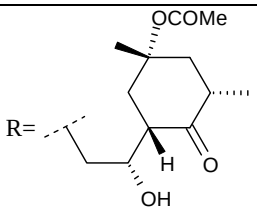	**3**
II	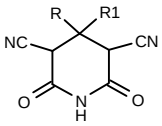 R = Me– R_1 = 2-Cl–Ph–	**4**
	R = Me– R_1 = 4-F–Ph–	**5**
III	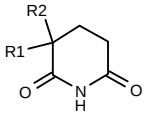 R_1 = *n*-hept– R_2 = 4-NH_2–Ph–	**6**

TABLE I. Continued

Class No.[a]	Structure	Compound No.
IV	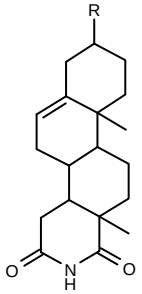 R = –OC(O)Me	**7**
	R = –OH	**8**
V	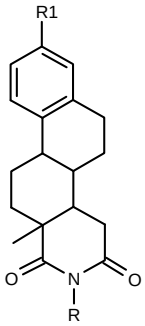 R = $–CH_2CH_2–$Pyr R_1 = –O–Me	**9**
	R = H– R_1 = –O–Me	**10**
	R = Me– R_1 = –O–Me	**11**
	R = *n*-Bu– R_1 = –O–*n*-Bu	**12**
	R = *n*-Bu– R_1 = $–O–CH_2CH_2–$Pyr	**13**
	R= -O-$CH_2CH_2–$Pip R_1= –O–Me	**14**
	R = $–NH_2$ R_1 = –O–Me	**15**
VI	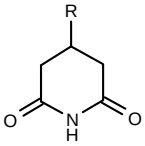 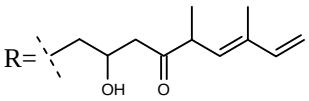	**16**
	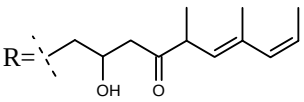	**17**
VII	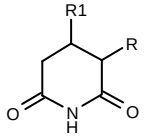 R = –C(O)O–*t*-Bu 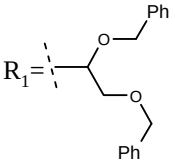	**18**
VIII	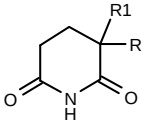 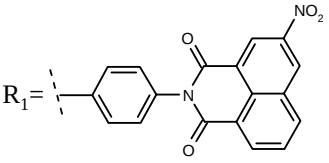	**19**
	R = Et–	

TABLE I. Continued

Class No.[a]	Structure	Compound No.
IX	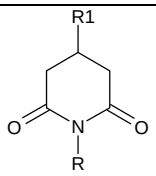 R = Ph– 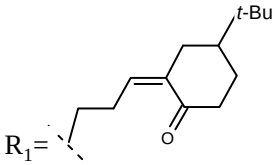 R_1=	**20**
	R= Ph– 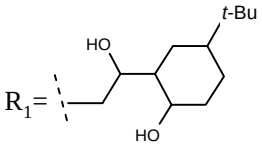 R_1=	**21**
X	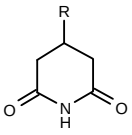 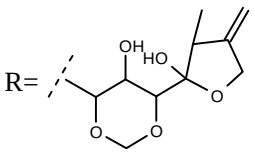	**22**

probe (*e.g.*, hydrogen bond donor, hydrogen bond acceptor, hydrophobic) and a molecule for which the GRID MIF was calculated. By calculating MIFs for different GRID probes around the molecule and extracting the most relevant regions, a fingerprint of a receptor to which a small molecule could fit well can be obtained. These regions show favourable energy of interaction and represent positions where groups of a potential receptor would interact favourably with a ligand. Such an MIF pattern can be described as the virtual receptor site (VRS). Each GRIND descriptor consists of two nodes extracted from MIFs and encodes their energy product and spatial distance. GRIND variables represent geometrical relationships between relevant pharmacophore points around the studied molecules, which are invariable with respect to the position of the molecule in space and their alignment. The derivation of GRIND descriptors includes the following steps: *i*) computing a set of MIF around the studied molecules, *ii*) filtering the MIF, to extract the most relevant regions that define the VRS and *iii*) encoding the VRS into the GRIND variables. GRIND variables can be used for comparison of molecules and their classification within sets of structurally diverse entities and the Pentacle program uses principal component analysis (PCA) for this type of analysis. A dependent variable (*e.g.*, biological activity) can be correlated to GRIND descriptors (as independent variables) obtained on a set of molecules by partial least square analysis (PLS). The most intensive bars in the PLS plots have the highest impact on the model. Bars having positive values on the *y* scale represent variables positively correlated with activity, while those having nega-

tive values on *y* scale are negatively correlated with activity. Within each block (auto or cross-correlograms, which correspond to pairs of nodes of the same or a different probe, respectively) variables are arranged from left to right on the *x* scale of the plot according to ascending distance between their nodes. In addition to the spatial arrangement of molecules and nodes encoded in the GRIND variables, each node of each variable exerts a specific energy of interaction with a target molecule. Therefore, the strength of the interaction between a respective GRID probe in a particular node and the molecules are presented as well as the spatial positions of the VRS regions.

The NCI60 anticancer drug screen[16] was developed in the late 1980s, and was quickly recognized as a rich source of information concerning the mechanisms of growth inhibition and tumour-cell kill. Recently, its role has evolved to that of a service screen supporting the cancer research community.

Structure–activity relationship

The potencies of compounds, given as p(GI_{50}), the negative logarithm of the molar concentration that induces a 50 % reduction of the respective cell growth, are given in Table I-S in the Supplementary material. Eight models were built. All the studied compounds (**1**–**22**) exhibited a similar order of potency towards each cell line, as can be seen from Table I-S, and the intercorrelation matrix of the p(GI_{50}) values for all the studied cell lines (Table XV-S). As all the obtained models were similar in their important parts, a detailed description of the model on the antiproliferative potency of **1**–**22** towards the K562 cell line is given and explained. For the other cell lines, the partial least square coefficient plots, statistical data, and the expression of variables for each compound are given in the supplementary material in tabular format.

The variables of the models positively or negatively correlated with activity readily detected the structural motifs of compounds **1**–**22** that contribute to potency. The smaller molecules were more potent towards all the studied cell lines. Molecules containing both the glutarimide moiety and a HBA, mainly the hydroxyl group, on a spatial distance of ~11 Å expressed higher potency. On the contrary, larger molecules and those with bulky substituents at a distance of ~20 Å from the glutarimide moiety were significantly less potent. The characteristic PLS plot obtained with 4 latent variables (LV) for the K562 model is given in Fig. 1d.

– All the described structural motifs of the compounds important for the antiproliferative potency are anchored to the glutarimide moiety that comprises HBA, HBD, and hydrophobic parts.

– Two hydrophobic moieties, one of which is associated with alkyl part of the glutarimide ring and the other with the distal (8.32–8.64 Å) π systems of the molecules, are negatively correlated with the potency of the compounds – vari-

able DRY–DRY 26 (Fig 1a). Accordingly, this variable is not expressed for the most potent **22**.

– Compounds that comprise two HBD groups at a distance of ~11 Å exert higher potencies. One HBD is always glutarimide, –NH–, while the other is hydroxyl group, positioned at the topological distance of five bonds for **22**, or at the methylene bridge for **1**–**3** (Table I), as given by the variable O–O 111, Fig. 1b.

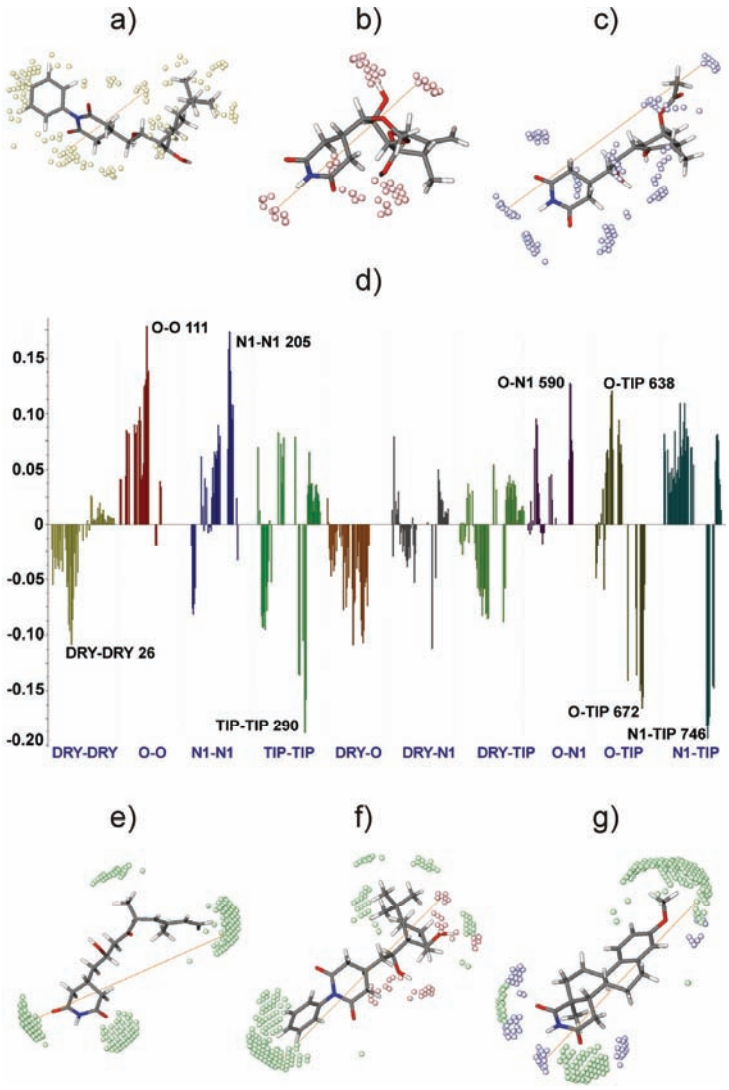

Fig. 1. Examples of variables that have a high impact on the model, associated with compounds: a) variable DRY–DRY 26 for **21**; b) variable O–O 111 for **22**; c) variable N1–N1 205 for **3**; d) 4 LV PLS coefficient plot for the K562 model; e) variable TIP–TIP 290 for **16**; f) variable O–TIP 672 for **21**; g) variable N1–TIP 746 for **10**.

– Two HBA groups at a distance of ~16.8 Å are the next structural motif positively correlated with activity, as given by variable N1–N1 205, Fig. 1c. This variable exists only for compounds of class V and compounds **1** and **3**, which belong to the most potent class I. For compounds of class V, one HBA is always glutarimide >C=O and the other is an alkoxy group, except for compound **13**, which is more potent than the other members of this class. In this point, the model recognized the HBA of the pyrrolidino substituent in place of the alkoxy group of the other compounds within class V. In **1** and **3** (class I), the other HBA is the distal –OH or the carbonyl oxygen of the methyl ester, respectively.

– All structural motifs, as described above, that have a significant impact on the models emphasize that all highly potent molecules bear similar spatially positioned HBD–HBD and HBA–HBA combinations, as exemplified in Figs. 1b and 1c.

– The bulkier compounds exhibited a lower potency ($p(GI_{50}) < 6$), as can be seen from the variable TIP–TIP 290, Fig. 1e. The glutarimide ring distal from bulky substituents, *i.e.*, a terminal methyl or *t*-butyl group; or the glutarimidonaphthyl moiety (classes VI, VIII and IX, respectively), negatively influences the potency. Molecules of the most potent classes (I and X) and some less potent molecules from classes III and IV lack bulky substituents distal from the glutarimide moiety.

– Similar information encoded in variables that have the highest positive impact on the model (O–O 111, N1–N1 205) could be obtained from the additional variables O–N1 590 and O–TIP 638, respectively. Therefore, HBA and HBD of molecules positioned at a spatial distance of ~16.8 Å significantly contribute to the potency. The variable O–N1 590 is expressed for the potent **1** and **3** (class I), as well as for **10** and **15** (class V), see Table VII-S. Implicitly, compounds from class V that have similarly positioned HBA and HBD as in compounds of class I but a rigid backbone exhibit lower potencies. Together with this, structural motifs comprising HBD at ~7.2 Å from the non-polar part of the molecules contribute to the potency.

– Variables O–TIP 672 and N1–TIP 746 offer similar information as the variable TIP–TIP 290. Those variables show that compounds having bulky substituents (TIP) distal from the glutarimide moiety (O or N1) have lower potency.

The structural differences between the most and the least potent compounds can be clearly seen from Pentacle heatmaps (see the experimental for an explanation of matrix representation of correlograms). The heatmaps for the whole set (**1**–**22**) are presented in Fig. 2. The compounds are arranged by decreasing potencies, from top to bottom. A distinct band of O–O correlograms exists for the most potent compounds (yellow framed), which is consistent with the significance of the O–O variables that have a strong positive impact on the model. For the other compounds, the regions of the same correlograms are less populated.

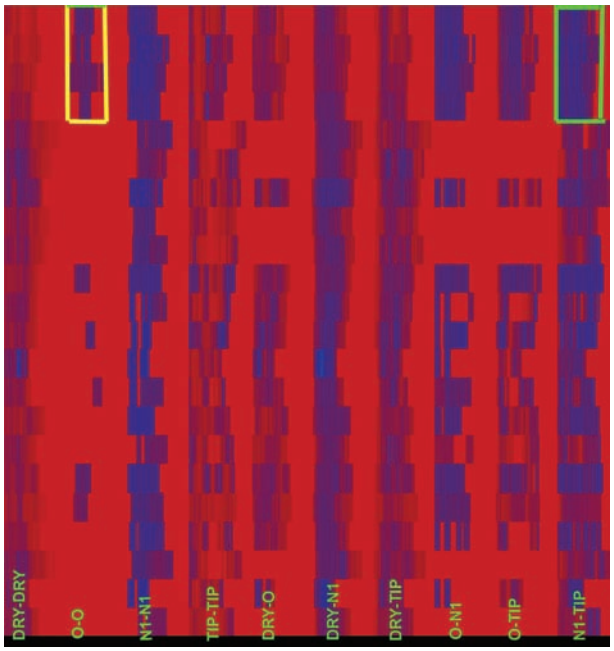

Fig. 2. Matrix-like representation (heatmaps) of the auto- and cross-correlograms of **1**–**22**.

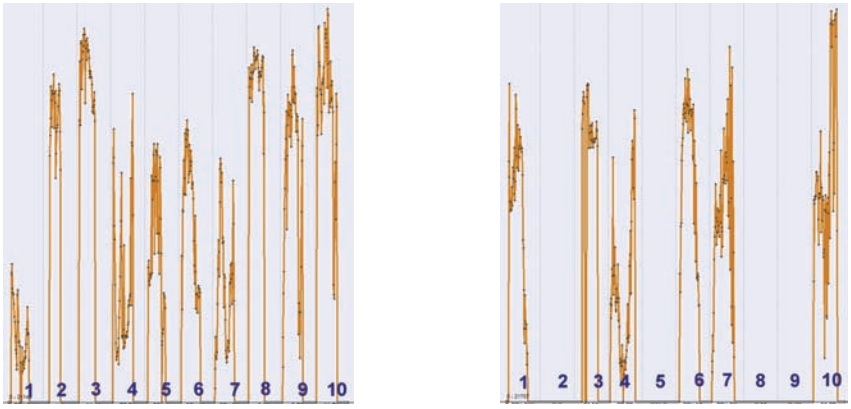

(a) (b)

Fig. 3. Auto- and cross-correlograms of compounds a) **22** and b) **11**, labelled as follows: **1** DRY–DRY, **2** O–O, **3** N1–N1, **4** TIP–TIP, **5** DRY–O, **6** DRY–N1, **7** DRY–TIP, **8** O–N1, **9** O–TIP and **10** N1–TIP.

Together with this, the bands of the TIP–TIP correlograms are broader for the larger, less potent compounds; while the band of the N1–TIP block is narrower for the most potent compounds (framed green), which is consistent with the description of the N1–TIP variables that describe larger node–node distances, and has a high negative impact on potency in all models. As an additional illustration,

all auto- and cross-correlograms for the most (**22**), and one of the least potent (**11**) compounds are given in Figs. 3a and 3b, respectively. Comparing the most important differences in the pattern of the most **22** and less potent **11**, it is evident that the less active compound lacks two HBD (empty O–O block (2)) and the larger strong peaks in the TIP–TIP block (4) are positioned to the right with respect to the same block of **22.** Additionally, there is significantly larger distance between one HBA and the distal part of molecule in the less potent **11** than in **22**, as shown by the strong peaks in the N1–TIP block (10), positioned to the right for **11** compared to **22**.

To summarize the observations mentioned above, two plots are presented in Fig. 4 in which the potency of the compounds (p(GI_{50})) is plotted *vs.* the molecular volume and *vs.* the distance between the glutarimide moiety and the distal HBA or HBD. A clear separation of the most potent compounds was achieved in this way.

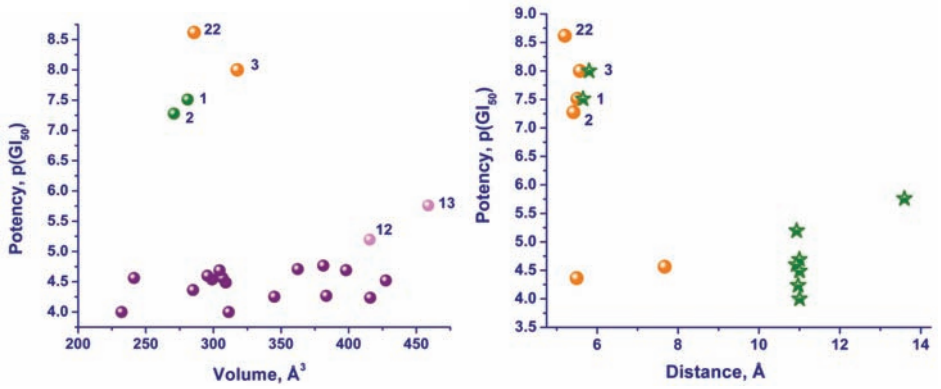

(a) (b)

Fig. 4. a) p(GI_{50}) *vs.* volume of **1**–**22**. The compounds are coloured according to their increasing potencies, in the following order: purple–pink–green–orange. b) p(GI_{50}) *vs.* HBA/HBD distance, given as: HBD–HBD of the compounds associated to the variable O–O 111 (orange spheres) and HBA–HBA of the compounds associated to the variable N1–N1 205 (green stars).

EXPERIMENTAL

The NCI-DTP Database was searched for structures comprising the glutarimide moiety (substructure query as SMILES notation: O=C1CCCC(=O)N1). All compounds that matched the query were saved (**1**–**22**) and their potency expressed as p(GI_{50}) against: leukaemia K562 (**A**); non small cell lung A549ATCC (**B**); colon COLO205 (**C**); CNS U251 (**D**); melanoma malme-3M (**E**); ovarian IGROV1 (**F**); renal UO-31 (**G**) and breast MCF-7 (**H**) tumour cell lines extracted. SMILES Notation of **1**–**22** was converted to 3D by CORINA.[19] Each initial 3D structure was imported in VegaZZ[20] and twenty conformations that represent local minima were obtained by conformational search on the MM level (MMFF94s force field),[21] using the Boltzmann jump algorithm in AMMP.[22] Each conformation of each compound was mini-

mized by the semi-empirical molecular orbital PM6 method,[23] using implicit solvation in water (COSMO) to root mean square gradient of 0.01; by MOPAC2009.[24] The obtained conformation of each compound that had the lowest heat of formation (implied the most stable one) were chosen for model building. All molecules were treated in their neutral form.

For alignment-free 3D QSAR analysis, the molecules were submitted to Pentacle.[17] The molecular interaction fields were computed using the built-in GRID program,[18] with a grid resolution of 0.4 Å. AMANDA algorithms were used for the extraction of hot spots (nodes) from the obtained MIFs (discretization); the distances and relative position of the nodes were described by maximum auto and cross-correlation (MACC2) (encoding). For details, see the original reference.[17] Five principal components/latent variables were used for the initial principal component analysis (PCA) and partial least square (PLS) model. Selection of the variables was realised by one cycle of factorial fractional design (FFD) for the models **A**–**H**. Validation of the models was performed by cross validation using four groups of approximately the same size in which the objects are assigned randomly. The final models were obtained with 3 or 4 latent variables (LV).

A detailed explanation of auto- and cross-correlogram in the ALMOND program can be found in the original reference[25] and the program manual available from the Molecular Discovery web site. Exactly the same correlograms can be found in Pentacle, with the option of a matrix-like presentation of the auto- and cross-correlograms for all compounds, named heatmaps, as depicted in Fig. 2. In the matrix-like representation, every row represents a single compound and every column a single variable. The values of the variables are colour-coded from red (low value) to blue (high value).

Details of the procedure for the determination of GI_{50} values can be found at: http://dtp.nci.nih.gov/branches/btb/ivclsp.html and in the literature.[26]

CONCLUSIONS

It can be concluded that, generally, smaller molecules are more potent towards all studied cell lines. Molecules containing the glutarimide moiety at a distance ~11 Å, or 5 topological bonds, to a HBA (mainly hydroxyl group) express higher potencies. On the contrary, larger molecules and those with bulky substituents at a distance ~20 Å from the glutarimide moiety are significantly less potent. In addition, it was noticed that within a subset having a favourable pharmacophore pattern, as described above, molecules possessing a flexible backbone (classes I and X) are more potent than rigid tetracyclic molecules (class V). These conclusions will be guidance for the selection of compounds previously prepared for *in vitro* antitumour screening; as well as for the design and syntheses of novel compounds that could express significant potency towards dedifferentiated human cells.

SUPPLEMENTARY MATERIAL

Associated with this article; p(GI_{50}) values for **1**–**22** towards cell lines **A**–**H**, PCA models, PLS models, PLS plots, structural motifs associated with important variable for the cell line models **A**–**H**, association of variables with **1**–**22** for cell line models **A**–**H** and the intercorrelation matrix of p(GI_{50}) values for all the reported cell lines are available electronically from http://www.shd.org.rs/JSCS/, or from the corresponding author on request.

Acknowledgements. The corresponding author gratefully acknowledges Professor Milovan D. Ivanović for moral support and great interest in the modelling study. This work was supported by the Ministry of Science and Technological Development of the Republic of Serbia (Project Nos. 142074 and 142010).

ИЗВОД

АНТИПРОЛИФЕРАТИВНА АКТИВНОСТ ГЛУТАРИМИДНИХ ДЕРИВАТА ИЗ БАЗЕ ПОДАТАКА НАЦИОНАЛНОГ ИНСТИТУТА ЗА РАК, САД. 3Д ОДНОС СТРУКТУРЕ И АКТИВНОСТИ НЕЗАВИСАН ОД ПОРАВНАВАЊА МОЛЕКУЛА

ЈЕЛЕНА Б. ПОПОВИЋ-ЂОРЂЕВИЋ[1], ЉИЉАНА И. ДОШЕН-МИЋОВИЋ[2], ИВАН О. ЈУРАНИЋ[2] и БРАНКО Ј. ДРАКУЛИЋ[3]

[1]Пољопривредни факултет , Универзитет у Београду, Немањина 6, 11080 Београд, [2]Хемијски факултет, Универзитет у Београду, Студентски трг 12–16, 11000 Београд и [3]Институт за хемију, технологију и металургију – Центар за хемију, Универзитет у Београду, Његошева 12, 11000 Београд

У тексту је описан однос структуре и антипролиферативне активности 22 глутаримидна деривата према осам репрезентативних линија хуманих тумора. Подаци о структури једињења и њиховој активности су преузети из базе података Националног Института за рак, САД. Дескриптори, независни од поравнавања молекула (GRIND-2), коришћени у проучавању односа структуре и активности су добијени употребом програма GRID. Модели јасно приказују структурне елементе једињења који се позитивно или негативно корелишу са биолошком активношћу. Фармакофорна слика добијена из модела ће бити коришћена за планирање нових аналога који садрже глутаримидни прстен и за које се очекује да ће показати значајну антипролиферативну активност.

(Примљено 2. децембра 2009, ревидирано 25. јануара 2010)

REFERENCES

1. a) M. E. Salvati, A. Balog, W. Shan, D. D. Wei, D. Pickering, R. M. Attar, J. Geng, C. A. Rizzo, M. M. Gottardis, R. Weinmann, S. R. Krystek, J. Sack, Y. An, K. Kish, *Bioorg. Med. Chem. Lett.* **15** (2005) 271; b) A. L. Machado, L. M. Lima, J. X. Araújo Jr., C. A. M. Fraga, V. L. G. Koatz , E. J. Barreiro, *Bioorg. Med. Chem. Lett.* **15**, (2005) 1169; c) J. Kossakowski, M. Jarocka, *Farmaco* **56** (2001) 785; d) J. J. Wang, S. S. Wang, C. F. Lee, M. A. Chung, Y. T. Chern, *Chemotherapy* **43** (1997) 182; e) H. Miyachi, A. Azuma, A. Ogasawara, E. Uchimura, N. Watanabe, Y. Kobayashi, F. Kato, M. Kato, H. Hashimoto, *J. Med. Chem.* **40** (1997) 2858
2. a) F. Matsuda, S. Terashima, *Tetrahedron* **44** (1988) 4721; b) R. G. Powel, C. R. Smith, D. Weisleder G. K. Matsumoto, J. Clardy, J. Kozlovsky, *J. Am. Chem. Soc*. **105** (1983) 3739
3. M. I. Andres, P. Sanz, A. Garfia, G. Repetto, M. Repetto, *In Vitro Mol. Toxicol.* **10** (1997) 319
4. D. K. K. Ha, W. H. Lau, *Cancer Lett.* **41** (1988) 217
5. Y. Ishikawa, M. Tachibana, C. Matsui, R. Obata, K. Umezawa, S. Nishiyama, *Bioorg. Med. Chem. Lett.* **19** (2009) 1726
6. J. Newell-Price, *Cushing's disease*, in *Clinical Endocrine Oncology*, 2nd ed., I. D. Hay, J. A. H. Wass, Eds., Blackwell Publishing, Malden, MA, 2008, p. 253
7. 7. P. E. Lanning, D.C. Jahannessen, *Drugs Today* **27** (1991) 117

8. 8. R. J. Santen, H. Brodie, E. R. Simpson, P. K. Siiteri, A. Brodie, *Endocr. Rev.* **30** (2009) 343
9. D. S. Fischer, L. W. L. Woo, M. F. Mahon, A. Purohit, M. J. Reed, B. V. L. Pottera, *Bioorg. Med. Chem.* **11** (2003) 1685
10. R. J. Snow, M. G. Cardozo, T. M. Morwick, C.A. Busacca, Y. Dong, R. J. Eckner, S. Jacober, S. Jakes, S. Kapadia, S. Lukas, M. Panzenbeck, G. W. Peet, J. D. Peterson, A. S. Prokopowicz, R. Sellati, R. M. Tolbert, M. A. Tschantz, N. Moss, *J. Med. Chem.* **45** (2002) 3394
11. a) M. Pastor, in: *Methods and Principles in Medicinal Chemistry*, *Molecular Interaction Fields: Applications in Drug Discovery and ADME Prediction*, G. Cruciani, Ed., Wiley--VCH, Weinheim, 2006, p. 117; b) A. Duran, I. Zamora, M. Pastor, *J. Chem. Inf. Model*. **49** (2009) 2129
12. G. Cruciani, P. Benedetti, G. Caltabiano, D. F. Condorelli, C. G. Fortuna, G. Musumarra, *Eur. J. Med. Chem.* **39** (2004) 281
13. a) F. P. Ballistreri, V. Barresi, P. Benedetti, G. Caltabiano, C. G. Fortuna, M. L. Longoa, G. Musumarra, *Bioorg. Med. Chem*. **12** (2004) 1689; b) C. G. Fortuna, V. Barresi, G. Berellini, G. Musumarra, *Bioorg. Med. Chem*. **16** (2008) 4150
14. R. Ragno, S. Simeoni, D. Rotili, A. Caroli, G. Botta, G. Brosch, S. Massa, A. Mai, *Eur. J. Med. Chem*. **43** (2008) 621
15. J. B. Popović-Djordjević, M. D. Ivanović, V. D. Kiricojević, *Tetrahedron Lett.* **46** (2005) 2611
16. R. H. Shoemaker, *Nat. Rev. Cancer* **6** (2006) 813
17. Á. Durán, G. C. Martínez, M. Pastor, *J. Chem. Inf. Model.* **48** (2008) 1813; Pentacle 1.0.3, http://cadd.imim.es/grib-cadd/projects/pentacle or http://www.moldiscovery.com (accessed on 29/09/2009)
18. P. J. Goodford, *J. Med. Chem.* **28** (1985) 849; GRID22b, http://www.moldiscovery.com (accessed on 29/09/2009)
19. a) J. Sadowski, J. Gasteiger, *Chem. Rev*. **93** (1993) 2567; b) J. Sadowski, J. Gasteiger, G. Klebe, *J. Chem. Inf. Comput. Sci*. **34** (1994) 1000
20. A. Pedretti, L. Villa, G. Vistoli, *J. Comput.-Aided Mol. Des.* **18** (2004) 167; VegaZZ 2.0.3, http://www.ddl.unimi.it/ (accessed on 29/09/2009)
21. T. A. Halgren, *J. Comput. Chem.* **20** (1999) 720
22. R. W. Harrison, *J. Comput. Chem.* **14** (1993) 1112
23. J. J. P. Stewart, *J. Mol. Model.* **13** (2007) 1173
24. J. J. P. Stewart, *J. Comput.-Aided Mol. Des.* 4 (1990) 1; J. J. P Stewart, *MOPAC2009*, Stewart Computational Chemistry, Colorado Springs, CO, 2009, http://OpenMOPAC.net (accessed on 29/09/2009)
25. M. Pastor, G. Cruciani, I. McLay, S. Pickett, S. Clementi, *J. Med. Chem.* **43** (2000) 3233
26. M. C. Alley, D. A. Scudiero, P. A. Monks, M. L. Hursey, M. J. Czerwinski, D. L. Fine, B. J. Abbott, J. G. Mayo, R. H. Shoemaker, M. R. Boyd, *Cancer Res.* **48** (1988) 589; http://dtp.nci.nih.gov/branches/btb/ivclsp.html (accessed on 29/09/2009).

Journal of the Serbian Chemical Society
JSCS@tmf.bg.ac.rs • www.shd.org.rs/JSCS

J. Serb. Chem. Soc. 75 (9) S1–S21 (2010)
JSCS–4040

Supplementary material

SUPPLEMENTARY MATERIAL TO

Antiproliferative activity of NCI-DTP glutarimide derivatives. An alignment independent 3D QSAR study

JELENA B. POPOVIĆ-DJORDJEVIĆ[1]*, LJILJANA I. DOŠEN-MIĆOVIĆ[2#], IVAN O. JURANIĆ[2#] and BRANKO J. DRAKULIĆ[3#]

[1]*Faculty of Agriculture, University of Belgrade, Nemanjina 6, 11080 Belgrade,* [2]*Faculty of Chemistry, University of Belgrade, Studentski trg 12–16, 11000 Belgrade and* [3]*ICTM – Department of Chemistry, University of Belgrade, Njegoševa 12, 11000 Belgrade, Serbia*

J. Serb. Chem. Soc. 75 (9) (2010) 1167–1179

An alignment-free three dimensional structure-activity relationships (3D QSAR) of the antiproliferative potency of twenty-two glutarimide-containing compounds towards eight representative human tumour cell lines are reported.

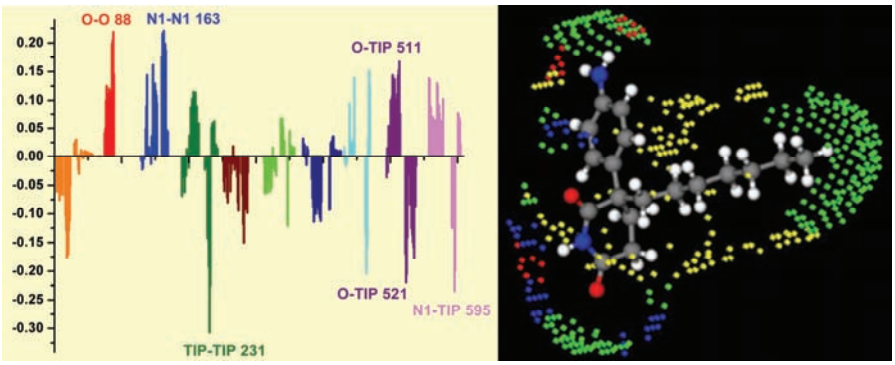

TABLE OF CONTENTS

* Corresponding author. E-mail: jelenadj@agrif.bg.ac.rs
# Serbian Chemical Society member.

TABLE I-S. p(GI_{50}) Values for **1**–**22** towards: K562 (leukaemia), A549 (non-small cell lung), malme-3M (melanoma), COLO205 (colon), UO31 (renal), U251 (CNS), IGROV1 (ovarian), and MFC 7 (breast) human tumour cell lines

Cmpd. No.	Class	NSC No.	Model							
			A	B	C	D	E	F	G	H
			K-562	A549	COLO-205	U251	Malme--3M	IGROV1	UO-31	MFC07
1	I	39147	7.510	7.290	7.419	7.505	7.263	7.534	7.260	7.421
2		185	7.277	7.437	7.453	7.220	7.051	7.274	7.542	/
3		32743	8.000	8.000	8.000	8.000	8.000	8.000	8.000	8.000
4	II	636355	4.562	4.342	4.347	/[a]	4.450	4.193	4.561	/
5		636351	4.000	4.000	4.000	/	4.000	4.000	4.077	/
6	III	622730	4.564	4.500	4.660	/	4.552	4.491	4.688	/
7	IV	645461	4.252	4.000	4.000	4.232	4.000	4.000	4.000	/
8		645462	4.538	4.000	4.434	4.000	4.034	4.014	4.000	/
9	V	655763	4.691	/	4.753	4.358	4.770	4.350	4.747	/
10		653947	4.599	4.000	4.000	4.000	4.000	4.000	4.010	/
11		656924	4.000	4.000	4.000	4.120	4.000	4.000	4.000	4.000
12		671764	5.196	/	4.037	4.000	4.000	4.000	4.000	4.000
13		671765	5.760	5.108	5.717	5.259	5.410	4.803	5.337	5.248
14		655764	4.236	/	4.000	4.000	4.242	4.000	4.080	/
15		655766	4.487	/	4.000	4.000	4.000	4.000	4.137	/
16	VI	66645	4.363	4.290	4.467	4.462	4.795	4.702	4.311	4.561
17		248958	4.688	4.667	4.767	4.506	/	4.721	4.697	4.677
18	VII	677677	4.521	4.517	/	4.689	4.703	4.641	4.567	4.701
19	VIII	679266	4.766	4.256	5.019	5.007	4.696	5.268	5.353	4.525
20	IX	679109	4.709	/	4.682	4.827	4.730	4.705	4.780	4.714
21		677755	4.267	4.171	/	4.253	4.184	4.000	4.117	4.355
22	X	355461	8.618	8.550	8.534	8.561	8.545	8.417	8.691	8.572

[a]Data not available

TABLE II-S. PCA models for K562 and IGROV1. *SSX* – Percentage of the *X* sum of squares; SSX_{acc} – accumulative percentage of the *X* sum of squares; *VarX* – percentage of the *X* variance; $VarX_{aac}$ – accumulative percentage of the *X* variance

Comp.	K562				IGROV1			
	SSX	SSX_{acc}	*VarX*	$VarX_{acc}$	*SSX*	SSX_{acc}	*VarX*	$VarX_{acc}$
1	38.95	38.95	35.82	35.82	41.58	41.58	38.55	38.55
2	13.48	52.43	11.47	47.29	14.85	56.43	13.13	51.68
3	8.14	60.57	6.53	53.82	8.29	64.72	6.95	58.64
4	6.44	67.01	5.22	59.04	6.32	71.04	5.35	63.99
5	5.28	72.29	4.36	63.40	4.15	75.19	3.18	67.17

TABLE III-S. PCA models for A549atcc and COLO205. *SSX* – Percentage of the *X* sum of squares; SSX_{acc} – accumulative percentage of the *X* sum of squares; *VarX* – percentage of the *X* variance; $VarX_{aac}$ – accumulative percentage of the *X* variance

Comp.	A549atcc				COLO205			
	SSX	SSX_{acc}	*VarX*	$VarX_{acc}$	*SSX*	SSX_{acc}	*VarX*	$VarX_{acc}$
1	33.04	33.04	28.46	28.46	43.50	43.50	40.26	40.26
2	18.13	51.17	15.56	44.02	15.65	59.15	13.93	54.20
3	10.36	61.53	8.41	54.42	8.55	67.70	7.26	61.46
4	7.89	69.43	6.55	58.97	6.56	74.26	5.72	67.18
5	5.03	74.46	3.58	62.54	4.24	78.50	3.40	70.58

TABLE IV-S. PCA models for U251 and malme-3M. *SSX* – Percentage of the *X* sum of squares; SSX_{acc} – accumulative percentage of the *X* sum of squares; *VarX* – percentage of the *X* variance; $VarX_{aac}$ – accumulative percentage of the *X* variance

Comp.	U251				malme-3M			
	SSX	SSX_{acc}	*VarX*	$VarX_{acc}$	*SSX*	SSX_{acc}	*VarX*	$VarX_{acc}$
1	48.48	48.48	45.36	45.36	41.93	41.93	38.77	38.77
2	10.59	59.08	8.45	53.81	14.20	56.13	12.32	51.09
3	8.73	67.80	7.36	61.17	8.77	64.90	7.41	58.50
4	5.25	73.05	3.95	65.12	6.39	71.28	5.37	63.87
5	4.59	77.64	3.66	68.78	4.37	75.65	3.40	67.27

TABLE V-S. PCA models for UO31 and MFC-7. *SSX* – Percentage of the *X* sum of squares; SSX_{acc} – accumulative percentage of the *X* sum of squares; *VarX* – percentage of the *X* variance; $VarX_{aac}$ – accumulative percentage of the *X* variance

Comp.	UO31				MFC-7			
	SSX	SSX_{acc}	*VarX*	$VarX_{acc}$	*SSX*	SSX_{acc}	*VarX*	$VarX_{acc}$
1	41.58	41.58	38.55	38.55	54.66	54.66	50.05	50.05
2	14.85	56.43	13.13	51.68	12.96	67.62	10.25	60.30
3	8.29	64.72	6.95	58.64	7.14	74.77	4.83	65.13
4	6.32	71.04	5.35	63.99	6.17	80.94	4.72	69.85
5	4.15	75.19	3.18	67.17	4.56	85.50	3.34	73.19

TABLE VI-S. PLS models. *SSX* – Percentage of the *X* sum of squares; SSX_{acc} – accumulative percentage of the *X* sum of squares; *SDEP* – standard deviation of error of the predictions; R^2 – coefficient of determination; R^2_{acc} – accumulative coefficient of determination; Q^2_{acc} – accumulative squared predictive correlation coefficient

Comp.	*SSX*	SSX_{acc}	*SDEC*	*SDEP*	R^2	R^2_{acc}	Q^2_{acc}
				K562 for **1**–**22**			
1	37.13	37.13	0.97	1.19	0.47	0.47	0.21
2	13.46	50.59	0.46	0.86	0.41	0.88	0.59
3	7.84	58.43	0.34	0.84	0.05	0.93	0.60
4	6.83	65.26	0.23	0.87	0.04	0.97	0.58

TABLE VI-S. Continued

Comp.	*SSX*	SSX_{acc}	*SDEC*	*SDEP*	R^2	R^2_{acc}	Q^2_{acc}
			IGROV1 for **1**–**22**				
1	40.22	40.22	0.99	1.20	0.50	0.50	0.26
2	9.26	49.48	0.58	1.04	0.33	0.83	0.44
3	5.80	55.28	0.34	1.05	0.11	0.94	0.43
4	11.50	66.78	0.24	1.09	0.03	0.97	0.40
			A549atcc for **1**–**22**				
1	26.22	26.22	0.84	1.10	0.70	0.70	0.49
2	17.88	44.10	0.42	0.83	0.22	0.93	0.71
3	13.57	57.66	0.33	0.80	0.03	0.95	0.73
4	7.01	64.68	0.21	0.83	0.03	0.98	0.71
			COLO205 for **1**–**22**				
1	41.69	41.69	1.02	1.25	0.50	0.50	0.25
2	10.05	51.74	0.57	1.06	0.35	0.85	0.46
3	6.10	57.84	0.37	1.06	0.09	0.94	0.46
4	11.53	69.37	0.26	1.10	0.03	0.97	0.42
			U251 for **1**–**22**				
1	50.04	50.04	1.00	1.22	0.53	0.53	0.30
2	12.58	62.62	0.48	0.83	0.36	0.89	0.68
3	3.91	66.54	0.26	0.82	0.08	0.97	0.69
4	6.36	72.90	0.18	0.81	0.02	0.98	0.70
			malme-3M for **1**–**22**				
1	44.02	44.02	0.92	1.09	0.55	0.55	0.38
2	16.48	60.50	0.54	0.78	0.29	0.85	0.69
3	6.74	67.24	0.39	0.82	0.07	0.92	0.65
4	5.07	72.31	0.26	0.85	0.05	0.96	0.62
			UO31 for **1**–**22**				
1	45.69	45.69	1.03	1.22	0.47	0.47	0.26
2	12.35	58.04	0.62	0.92	0.34	0.81	0.57
3	7.45	65.49	0.45	0.93	0.09	0.90	0.56
4	4.85	70.34	0.31	0.97	0.06	0.95	0.52
			MFC-7 for **1-22**				
1	52.12	52.12	1.06	1.34	0.54	0.54	0.25
2	14.50	66.62	0.57	1.10	0.33	0.86	0.49
3	5.32	71.94	0.23	1.15	0.11	0.98	0.45
4	4.27	76.21	0.09	1.14	0.02	1.00	0.46

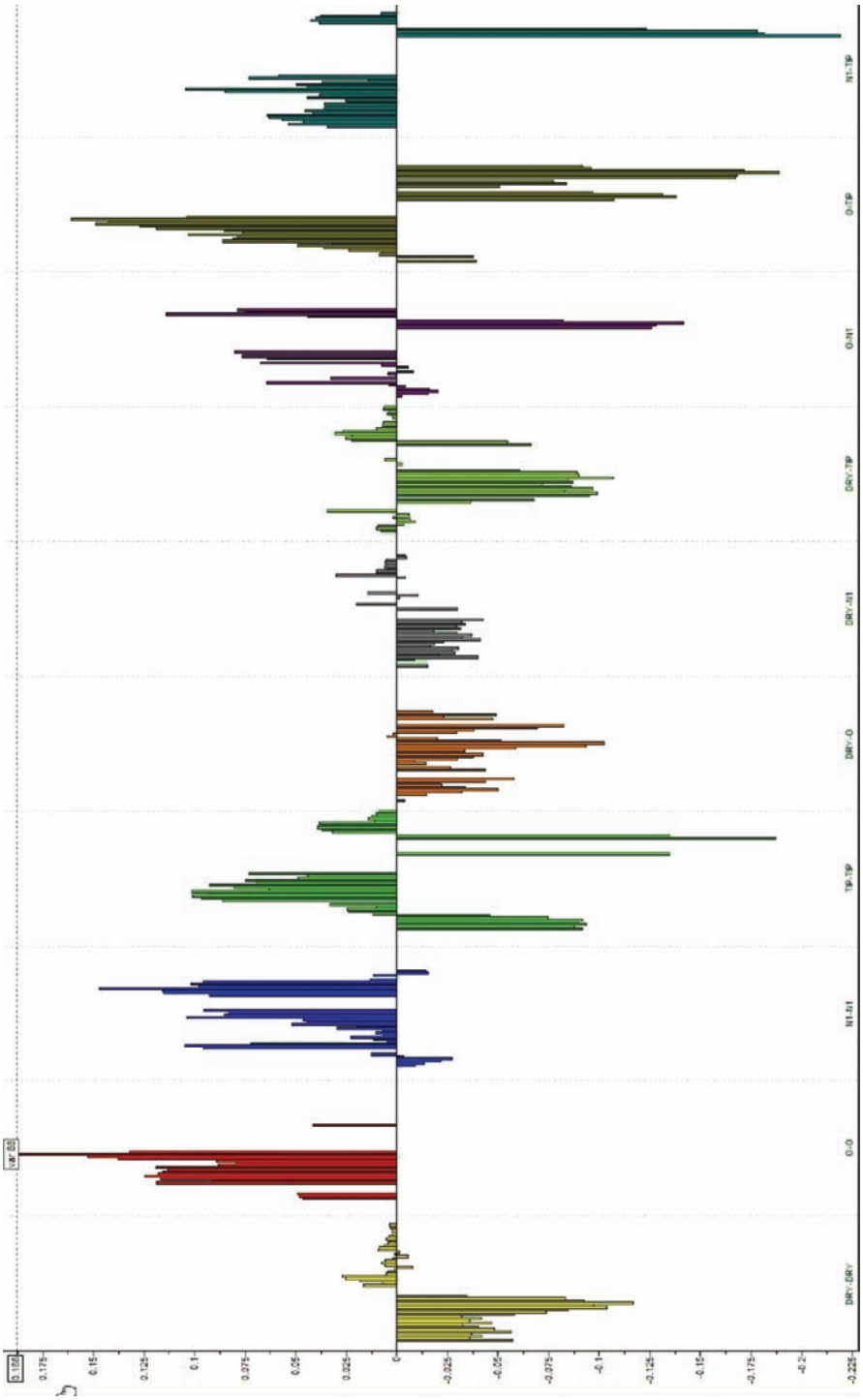

Fig. 1-S. 4LV PLS plot for IGROV1.

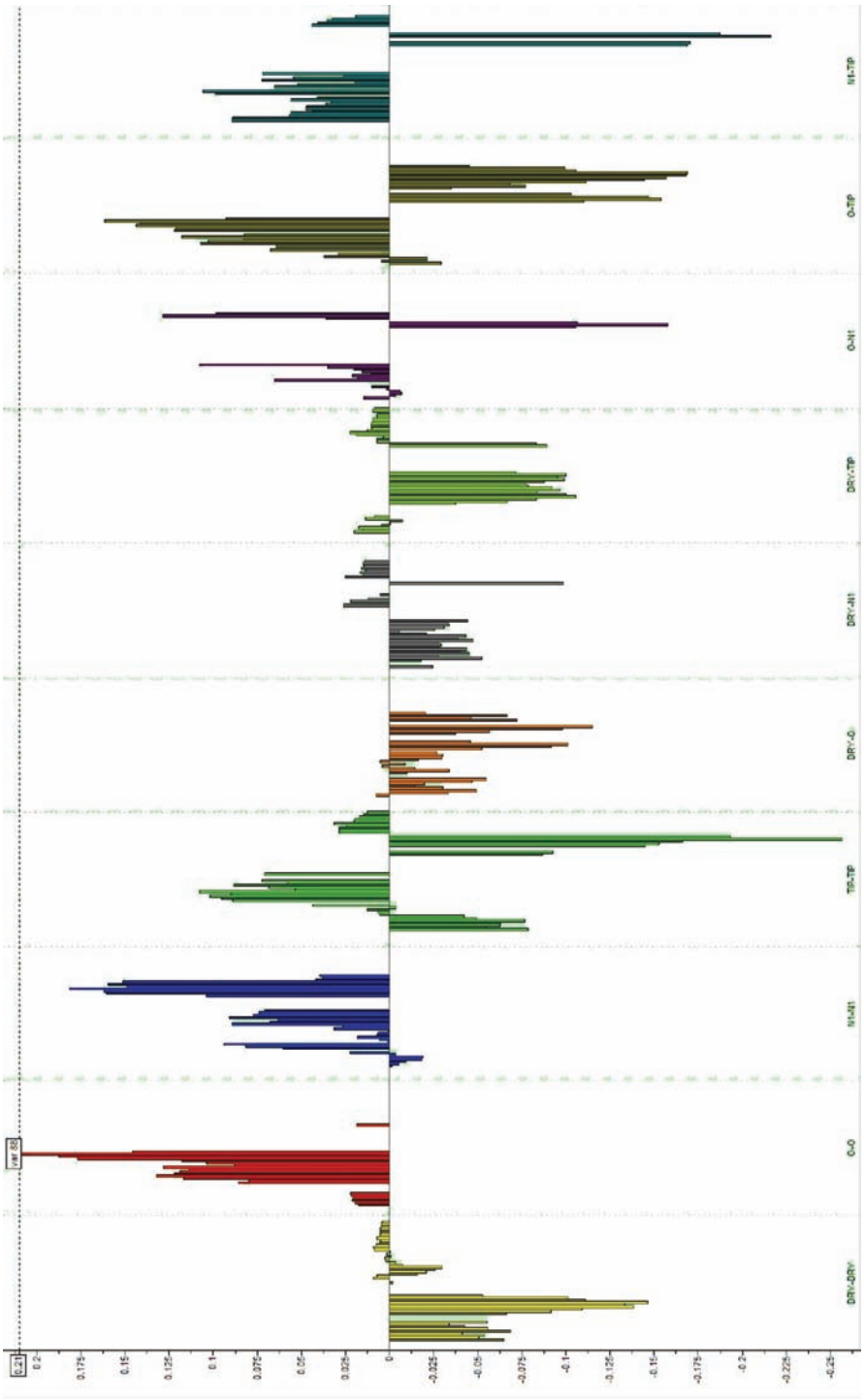

Fig. 2-S. 4LV PLS plot for A549.

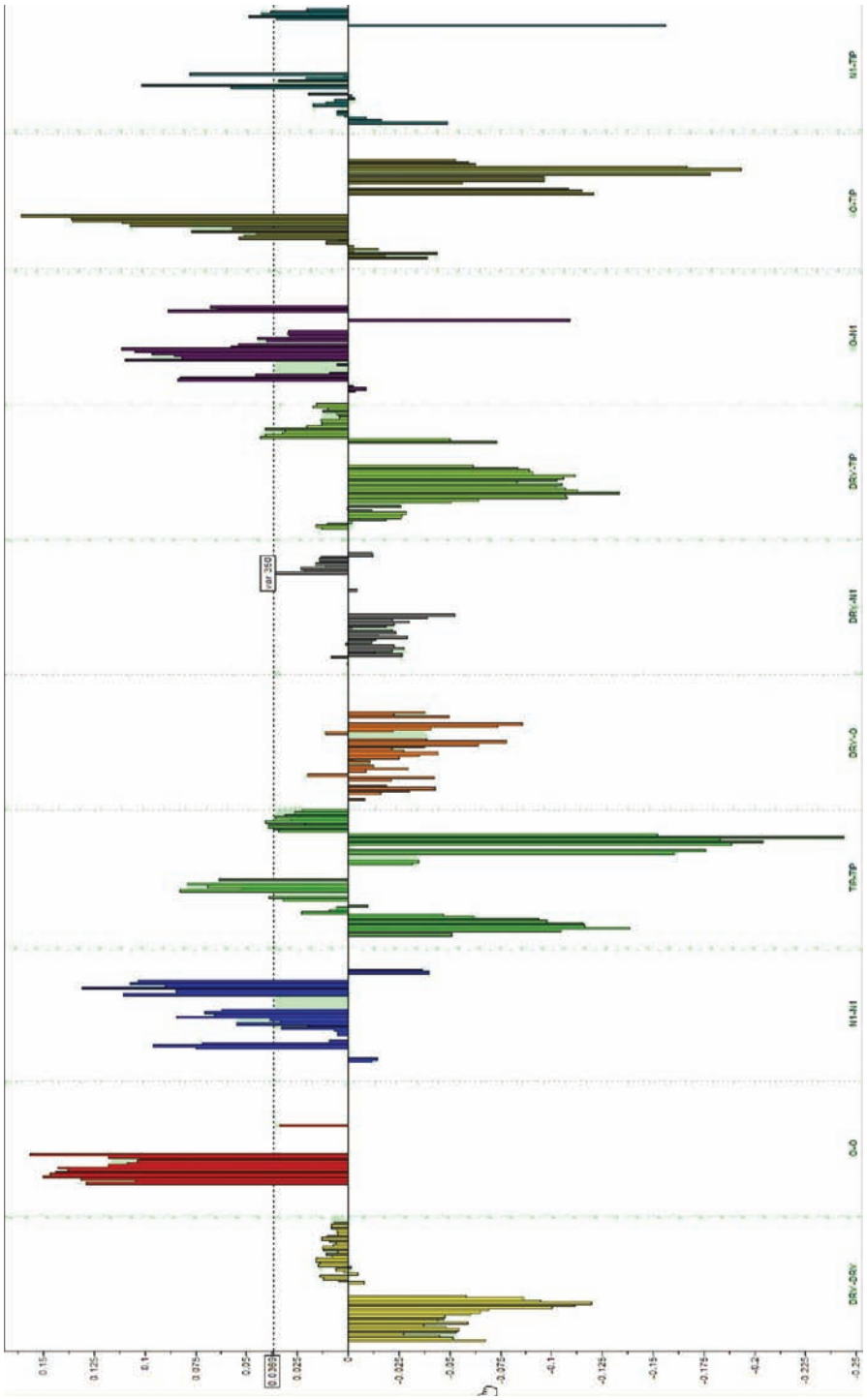

Fig. 3-S. 4LV PLS plot for COLO205.

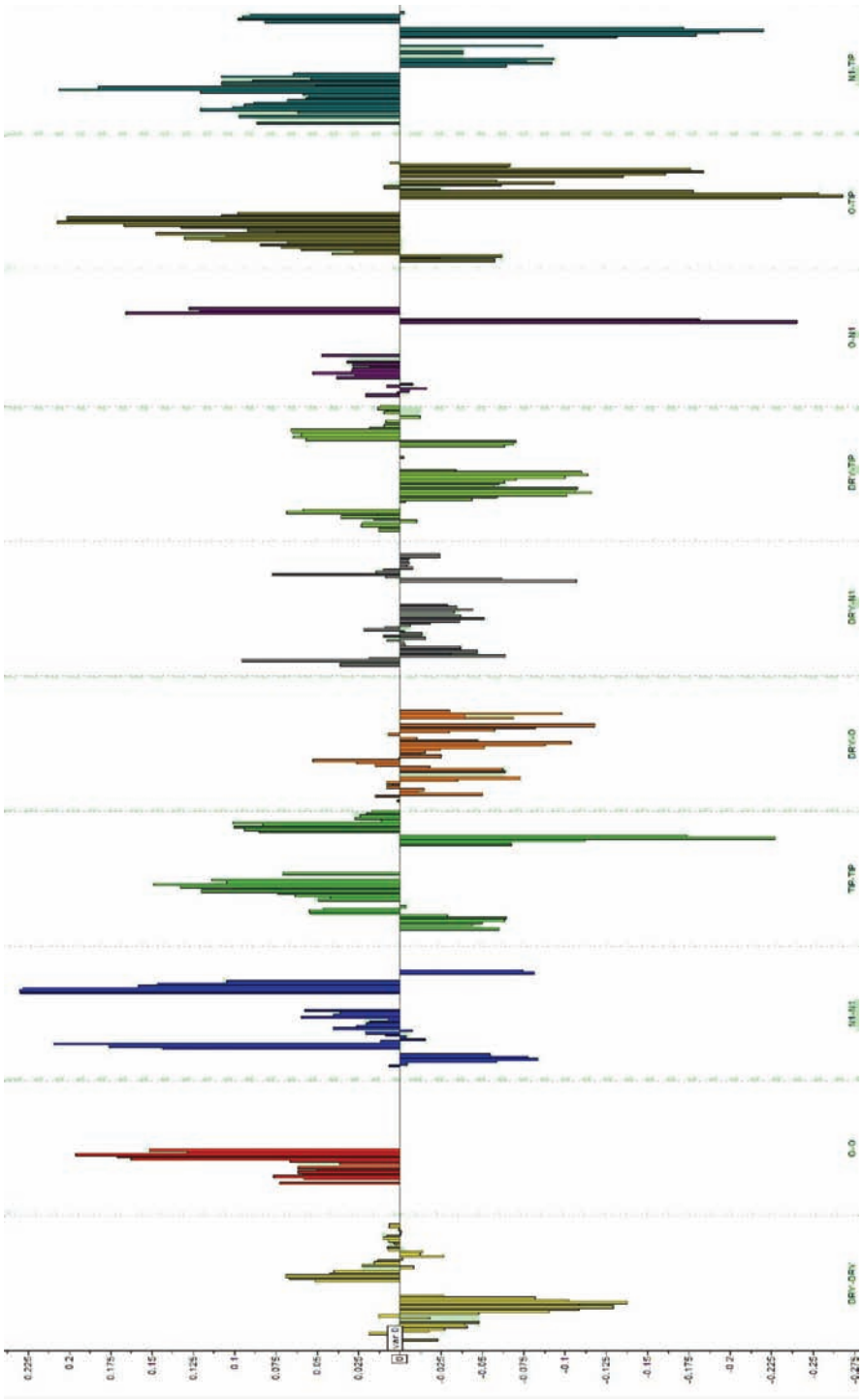

Fig. 4-S. 4LV PLS plot for U251.

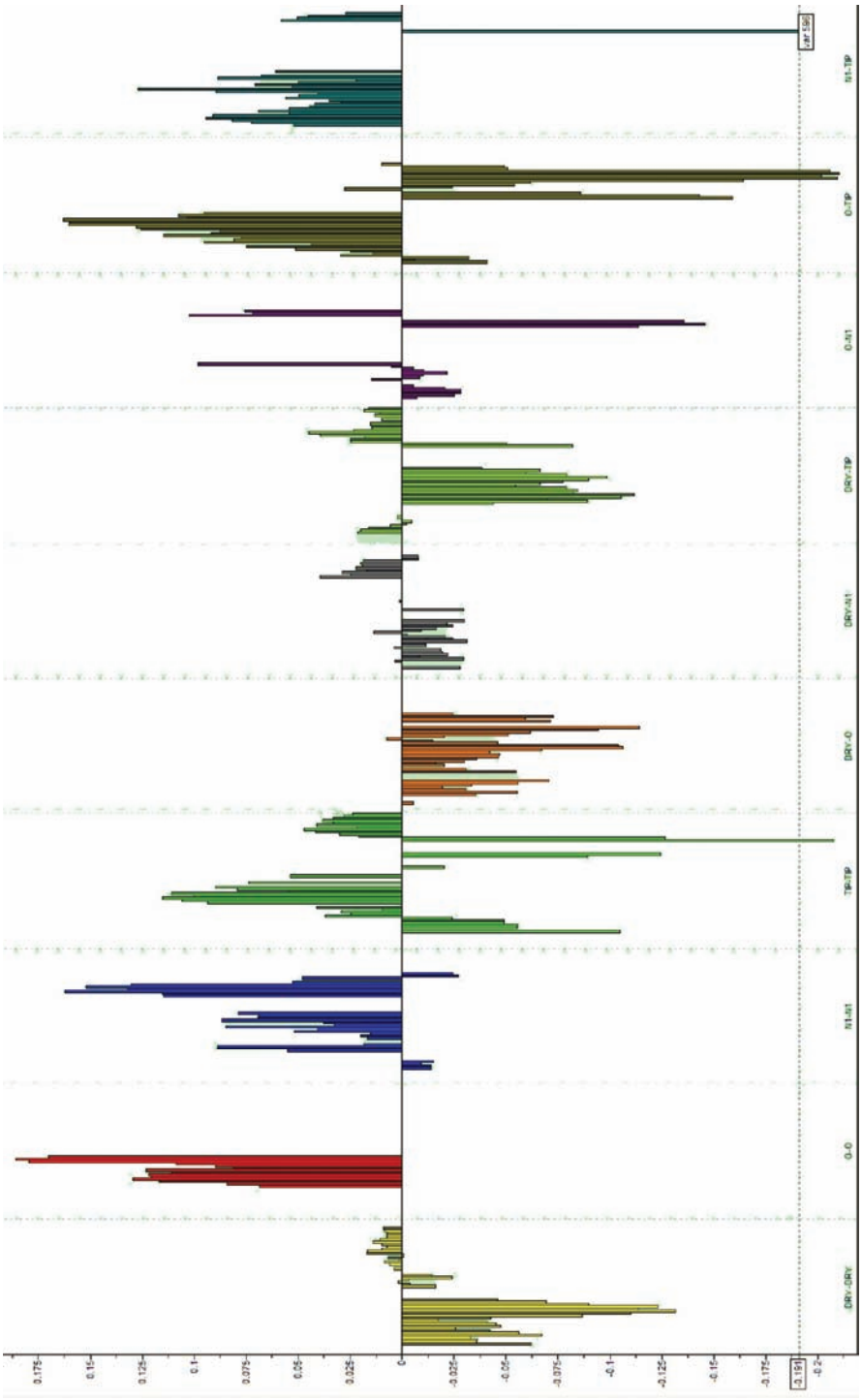

Fig. 5-S. 4LV PLS plot for malme-3M.

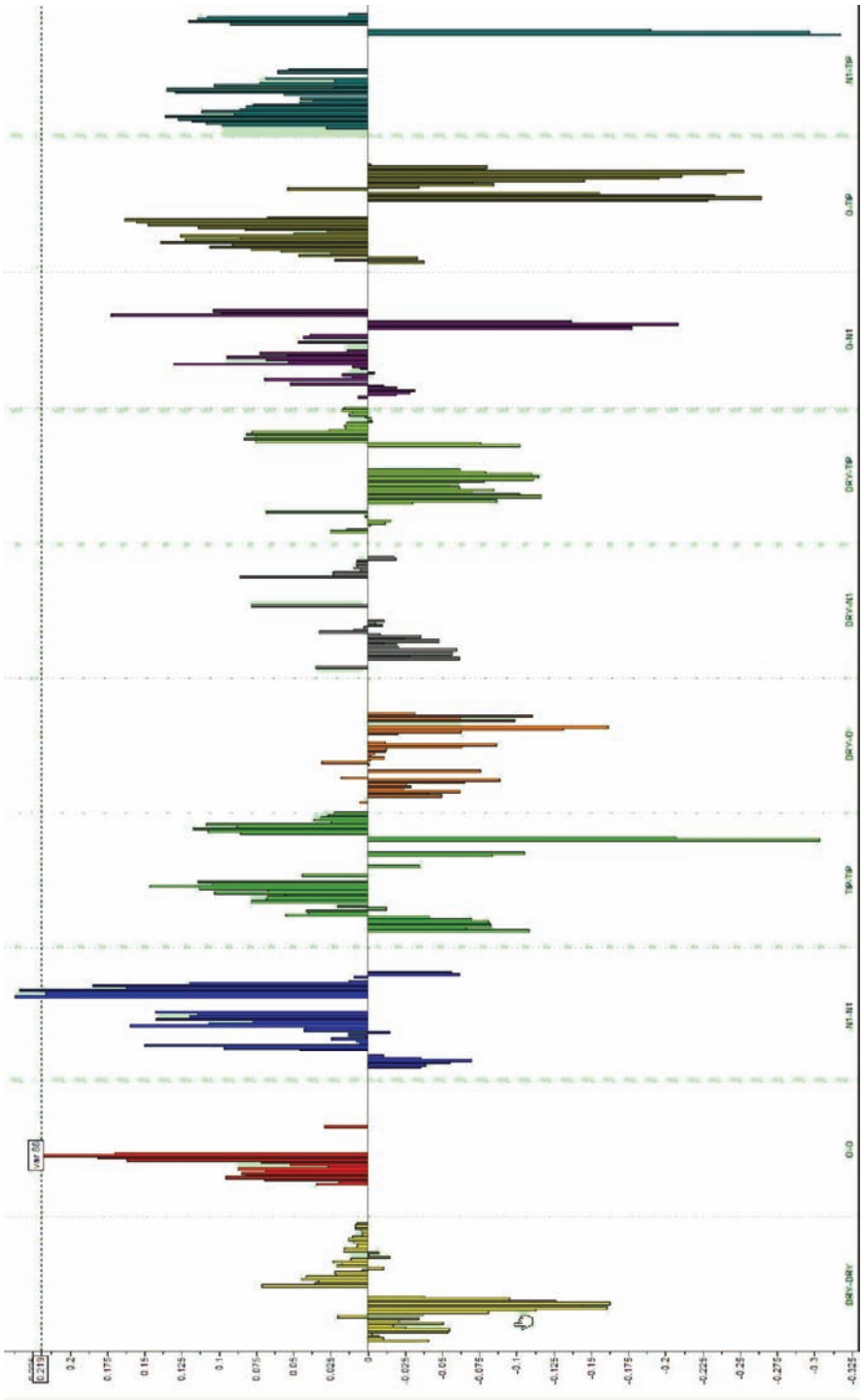

Fig. 6-S. 4LV PLS plot for UO31.

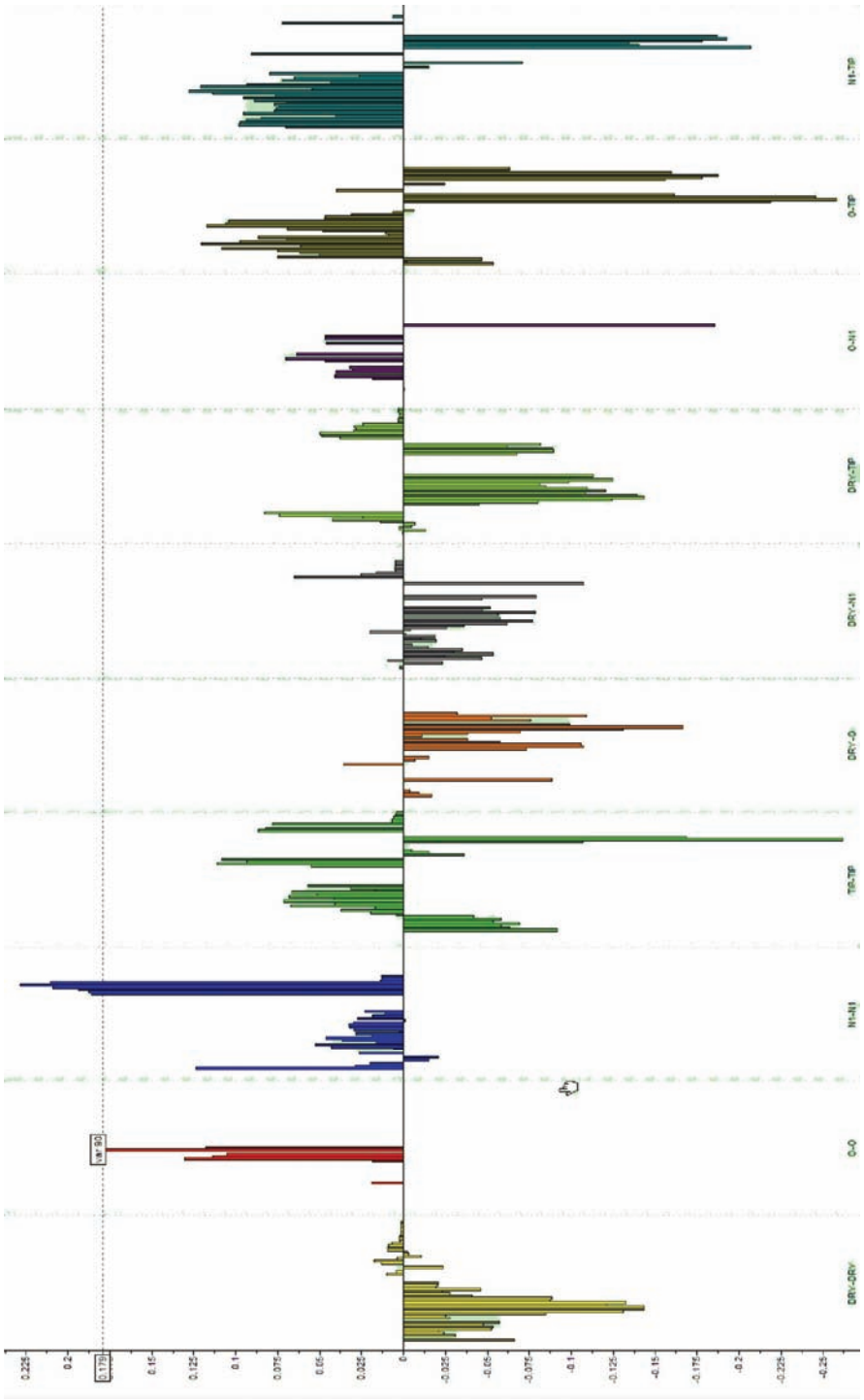

Fig. 7-S. 4LV PLS plot for MFC-7.

TABLE VII-S. Leukaemia K-562

Probe block	Variable No.	Impact	Distance Å	Regions
DRY–DRY	26	–	8.32–8.64	$–CH_2–$ of glutarimide ring and: alkyl part of cyclohexanone ring (I), phenyl (II, III, V), double bond of ring B dodecahydrophenanthrene system (IV), conjugated double bonds (VI), oxybenzyl group (VII), glutarimide naphthyl moiety (VIII), substituted cyclohexanone or cyclohexanol ring (IX).
O–O	111	+	10.88–11.20	Glutarimide (NH) hydrogen and: hydroxyl group on $–(CH_2)_2–$ bridge (I), hydroxyl group (VI), –OH group on 1,3-dioxane ring (X), amino group (III)
N1–N1	205	+	16.32–16.64	Glutarimide >C=O and: ester group (I), oxygen of alkoxy substituents or tertiary-N (**13**) (V)
TIP–TIP	290	–	18.80–19.20	Length of molecule: substituent on glutarimide ring and alkoxy group on benzene ring (V) *N*-Phenyl and *t*-butyl group on cyclohexanone or cyclohexanol ring (IX) Glutarimide ring and terminal methyl group (VI) Glutarimide ring and glutarimide naphthyl moiety (VIII)
O–N1	590	+	16.64–16.96	Glutarimide (NH) hydrogen (**10**) or *N*-amino group (**15**) and methoxy group (V) Glutarimide (NH) hydrogen and ester group (**3**) or *t*-hydroxyl group and glutarimide (NH) hydrogen (**1**) (I)
O–TIP	638	+	7.04–7.36	*t*-Hydroxyl group and glutarimide ring (X) Hydroxyl group of $–(CH_2)_2–$ bridge and glutarimide ring (I), *N*-phenyl group (IX) Glutarimide (NH) hydrogen and: cyano groups (II), aminophenyl group (III), *t*-butyl group (VII), ethyl group (VIII) Amino glutarimide group and carbonyls of glutarimide group (V) Hydroxyl group and glutarimide ring (VI)
O–TIP	672	–	17.92–18.24	Glutarimide (NH) hydrogen and methyl ester group (I), nitro group (VIII), methylene oxybenzyl group (VII), ester group (IV), terminal double bond (VI) *p*-Hydroxyl group and *N*-phenyl group (IX) *N*-Amino group and methoxy group (V)

TABLE VII-S. Continued

Probe block	Variable No.	Impact	Distance Å	Regions
N1–TIP	746	–	16.96–17.28	Glutarimide >C=O and: ester group (I, IV), *n*-heptyl group (III), terminal double bond or terminal methyl group (VI), methylene oxybenzyl group (VII), naphthyl moiety (VIII), *t*-butyl group (**20**) Glutarimide >C=O or *N*-glutarimide substituents and alkoxy substituent (V) Hydroxyl group and *N*-phenyl (**21**) (IX)

TABLE VIII-S. Non-small cell lung cancer A549

Probe block	Variable No.	Impact	Distance Å	Regions
O–O	88	+	10.80–11.20	Glutarimide (NH) hydrogen and: hydroxyl group on 1,3-dioxane ring (X), hydroxyl group of $-(CH_2)_2-$ bridge (I, VI), amino group (III)
N1–N1	163	+	16.40–16.80	Glutarimide >C=O and: ester group (**3**) or *t*-hydroxyl group (**1**) (I), alkoxy substituent (**10**, **11**) or *t*-N (**13**) (V)
TIP–TIP	231	–	19.20–19.60	Length of molecule: substituent on glutarimide ring and alkoxy groups (V) *N*-phenyl and *t*-butyl group (IX) Glutarimide ring and terminal methyl group (**17**) or terminal double bond (**16**) (VI) Glutarimide ring and aminonaphthyl moiety (VIII)
O–TIP	511	+	9.20–9.60	*t*-Hydroxyl group and glutarimide ring (X) Hydroxyl group of $-(CH_2)_2-$ bridge and glutarimide ring (I), *N*-phenyl group (IX) Glutarimide (NH) hydrogen and: cyano groups (**5**) or Cl-phenyl (**4**) (II), *t*-butyl group (VII), ethyl group (VIII) Aminophenyl group and *n*-heptyl group (III) Hydroxyl group and glutarimide ring (VI)
O–TIP	521	–	13.20–13.60	Hydroxyl group and ester group (**3**), glutarimide (NH) hydrogen and *o*-methyl group (**2**), *t*-hydroxyl group and glutarimide ring (**1**) (I) Aminophenyl group and glutarimide ring (III) Hydroxyl group and: glutarimide ring (**8**) or glutarimide (NH) hydrogen and ring D (**7**) (IV) Hydroxyl group and terminal double bond (**16**) or terminal methyl group (**17**) (VI), *N*-phenyl group (IX)

TABLE VIII-S. Continued

Probe block	Variable No.	Impact	Distance Å	Regions
O–TIP	521	–	13.20–13.60	Glutarimide (NH) hydrogen and benzyl ring (VII), naphthyl moiety (VIII) glutarimide (NH) hydrogen and furan ring (X)
N1–TIP	595	–	18.40–18.80	Glutarimide >C=O and: ester group (I, IV), terminal double bond or terminal methyl group (VI), amino naphthyl moiety (VIII) Hydroxyl group and *N*-phenyl group (IX) *t*-Nitrogen and *N*-butyl group (**13**) or amino and methoxy group (**11**) (V)

TABLE IX-S. Melanoma malme-3M

Probe block	Variable No.	Impact	Distance Å	Regions
O–O	87	+	10.40–10.80	Glutarimide (NH) hydrogen and: hydroxyl group of $–(CH_2)_2–$ bridge (I), amino group (III), hydroxyl group (VI), *t*-hydroxyl group (X)
N1–N1	163	+	16.40–16.80	Oxygen of glutarimide group and: (C=O) of ester group (**3**) or *t*-hydroxyl group (**1**) (I) Oxygen of glutarimide group and methoxy group (**10**, **11**, **12**) (V) *N*-Amino group and methoxy group (**15**) (V) *tert-N* of glutarimide ring substituents and methoxy group (**9**, **14**) or glutarimide oxygen (**13**) (V)
TIP–TIP	231	–	19.20–19.60	*N*-Substituent on glutarimide ring and substituents on benzene ring (V) Glutarimide ring and terminal double bond (VI) Glutarimide ring and amino naphthyl moiety (VIII) *N*-Phenyl and *t*-butyl group (IX)
O–TIP	510	+	8.80–9.20	Hydroxyl group of $–(CH_2)_2–$ bridge and glutarimide ring (I, X) Glutarimide (NH) hydrogen and aminophenyl group (III), cyano groups (II), *t*-butyl group (VII), ethyl group (VIII) Hydroxyl group and glutarimide ring (VI) Hydroxyl group of $–(CH_2)_2–$ bridge and *t*-butyl group (IX)
O–TIP	533	–	18.00–18.40	Glutarimide (NH) hydrogen and: ester group (I, IV), terminal double bond (VI), benzyl group (VII), aminophenyl group (VIII) Amino group hydrogen and methoxy group (V) Hydroxyl group and *N*-phenyl group (IX)

TABLE X-S. Colon COLO205

Probe block	Variable No.	Impact	Distance Å	Regions
DRY–DRY	21	–	8.40–8.80	$–CH_2–$ of $–(CH_2)_2–$ bridge and *p*-methyl group (**3**) or $–(CH_2)–$ groups of the glutarimide ring and cycloalkyl groups (**1**, **2,** respectively) (I) Aromatic moiety and: cyano groups (II), *n*-heptyl group (III) Glutarimide ring and double bond of ring C (IV) $–(CH_2)–$ Groups of glutarimide ring and aromatic moiety (V), conjugated double bonds (VI), cycloalkyl groups (IX), glutarimide naphthyl moiety (VIII)
O–O	88	+	10.80–11.20	Glutarimide (NH) hydrogen and: hydroxyl group on $–(CH_2)_2–$ bridge (I), amino group (III), hydroxyl group (VI), 1,3-dioxane ring (X)
N1–N1	163	+	16.40–16.80	Glutarimide >C=O and: ester group (**3**) or *t*-hydroxyl group (**1**) (I), alkoxy group (**10**, **11**, **12**, **15**), pyrrolidine nitrogen (**13**) (V) Alkoxy group and pyrrolidine nitrogen (**14**) or piperidine nitrogen (**9**) (V)
TIP–TIP	231	–	19.20–19.60	*N*-Glutarimide ring substituents and alkoxy group (V) Glutarimide ring and terminal methyl group or terminal double bond (VI) Glutarimide ring and glutarimide naphthyl moiety (VIII) *N*-Phenyl group and *t*-butyl group (IX)
O–TIP	532	–	17.60–18.00	*t*-Hydroxyl group and glutarimide ring (X) Hydroxyl group of $–(CH_2)_2–$ bridge and glutarimide ring (I), *N*-phenyl group (IX) Glutarimide (NH) hydrogen and: *t*-butyl group (I), ester group (IV), alkoxy group (**10**) (V), terminal methyl group or terminal double bond (VI), amino group (VIII)
N1–TIP	596	–	18.80–19.20	*N*-Amino group and alkoxy group (V) Glutarimide >C=O and ester group (I, IV), butoxy group (**12**) (V), terminal methyl group or terminal double bond (VI), amino naphthyl moiety (VIII) Pyrrolidine nitrogen and *N*-alkyl group (**13**) (V), Piperidine nitrogen and alkoxy group (**14**) (V) Methoxy oxygen and pyrrolidine ring (**9**) (V)

TABLE XI-S. Renal UO31

Probe block	Variable No.	Impact	Distance Å	Regions
O–O	88	+	10.80–11.20	Glutarimide (NH) hydrogen and: hydroxyl group on $–(CH_2)_2–$ bridge (I), amino group (III), hydroxyl group (VI), 1,3-dioxane ring (X)
N1–N1	160	+	15.20–15.60	Glutarimide >C=O and: ester group (**3**) or hydroxyl group (**1**) (I), ester group (IV), *t*-hydroxyl group (IX), >C=O of glutarimide naphthyl moiety (VIII)
				Alkoxy group and: glutarimide >C=O (**10**, **11**, **12**, **13**, **15**) or piperidine N (**14**) or pyrrolidine N (**9**) (V)
TIP–TIP	231	–	19.20–19.60	Length of molecule: substituent on glutarimide ring and substituent on benzene ring (V)
				Glutarimide ring and terminal methyl group (VI), aminonaphthyl moiety (VIII)
				N-Phenyl and *t*-butyl group (IX)
O–N1	464	–	14.60-15.20	*t*-Hydroxyl group and glutarimide oxygen (I, IX)
				N-Amino hydrogen and methoxy group (**15**) or glutarimide (NH) hydrogen and methoxy group (**10**) (V)
				Glutarimide (NH) hydrogen and ester group (**7**) or hydroxyl group and glutarimide (NH) oxygen (**8**) (IV), keto group (VI)
O–TIP	521	–	13.20–13.60	Hydroxyl group of $–(CH_2)_2–$ bridge and ester group (**3**), *t*-hydroxyl group and glutarimide ring (**1**), glutarimide (NH) hydrogen and *o*-Me group (**2**) (I)
				Amino group and glutarimide ring (III)
				Glutarimide (NH) hydrogen and: ring C (**7**) or hydroxyl group and glutarimide ring (**8**) (IV), benzyl group (VII), naphthyl moiety (VIII), substituted pyrrolidine ring (X)
				N-Amino group and benzene ring (V)
				Hydroxyl group and: terminal double bond or terminal Me group (VI)
				Hydroxyl group of $–(CH_2)_2–$ bridge and aromatic ring (IX)
N1–TIP	595	–	18.40–18.80	Glutarimide (NH) hydrogen and ester group (I)
				t-Hydroxyl and *N*-phenyl group (IX)
				Glutarimide >C=O and: nitro group (VIII), terminal methyl group or double bond (VI), alkoxy group (**11**, **12**) (V)
				Pyrrolidine N and *n*-butyl (**13**) (V) or methoxy group (**9**)

TABLE XII-S. CNS U251

Probe block	Variable No.	Impact	Distance Å	Regions
O–O	88	+	10.80–11.20	Glutarimide (NH) hydrogen and: hydroxyl group on $–(CH_2)_2–$ bridge (I), hydroxyl group (VI), 1,3-dioxane ring (X)
N1–N1	163	+	15.60–16.00	Glutarimide >C=O and: ester group (**3**) or *t*-hydroxyl group (**1**) (I), pyrrolidine N (**13**) (V)
				Alkoxy group and: glutarimide >C=O (**10**, **11**, **12**, **15**) or piperidine N (**14**) or pyrrolidine N (**9**) (V)
TIP–TIP	231	–	19.20–19.60	Length of molecule: *N*-substituent and alkoxy substituent (V)
				Glutarimide >C=O and: *t*-Me or double bond (VI), nitro group (VIII)
				N-Phenyl and *t*-butyl group (IX)
O–N1	464	–	14.80–15.20	*t*-Hydroxyl group and glutarimide oxygen (I)
				Glutarimide (NH) hydrogen and ester group (**7**) or hydroxyl group and glutarimide >C=O (**8**) (IV)
				N-Amino hydrogen and methoxy group (**15**) or glutarimide (NH) hydrogen and methoxy (**10**) (V)
				Glutarimide (NH) hydrogen and keto group (VI)
				Hydroxyl group and glutarimide oxygen (IX)
O–TIP	509	+	8.40–8.80	*t*-Hydroxyl group and glutarimide ring (X), hydroxyl group on $–(CH_2)_2–$ bridge and glutarimide ring (I, VI)
				Glutarimide (NH) hydrogen and *t*-butyl group (VII), ethyl group (VIII)
				Hydroxyl group of $–(CH_2)_2–$ bridge and aromatic ring (IX)
O–TIP	521	–	13.20–13.60	Glutarimide (NH) hydrogen and substituted pyrrolidine ring (X)
				t-OH and glutarimide ring (**1**), or glutarimide (NH) hydrogen and *o*-Me (**2**), or hydroxyl and ester group (**3**) (I)
				Glutarimide (NH) hydrogen and ring C (**7**) or hydroxyl and glutarimide ring (**8**) (IV)
				N-Amino group and aromatic ring (V)
				Hydroxyl group and terminal methyl group or terminal double bond (VI)
				Glutarimide (NH) hydrogen and benzyl ring (VII), naphthyl moiety (VIII)
				Hydroxyl group on $–(CH_2)_2–$ bridge and aromatic ring (IX)

TABLE XIII-S. Ovarian IGROV1

Probe block	Variable No.	Impact	Distance Å	Regions
O–O	88	+	10.80–11.20	Glutarimide (NH) hydrogen and: hydroxyl group on 1,3-dioxane ring (X), hydroxyl group of $–(CH_2)_2–$ bridge (I), hydroxyl group (VI), amino group hydrogens (III)
N1–N1	163	+	16.40–16.80	Glutarimide >C=O and: ester (C=O) group (**3**) or *t*-hydroxyl group (**1**) (I), or *t*-nitrogen (**13**) (V)
				Alkoxy group and: glutarimide >C=O (**10**, **11**, **12**, **15**), piperidine N (**14**), pyrrolidine N (**9**) or glutarimide >C=O and pyrrolidine N (**13**) (V)
TIP–TIP	231	–	19.20–19.60	Length of molecule: substituent on glutarimide ring and alkoxy group (V)
				Glutarimide ring and terminal methyl group (**17**) or terminal double bond (**16**) (VI)
				Glutarimide ring and aminonaphthyl moiety (VIII)
				N-Phenyl and *t*-butyl group (IX)
O–TIP	511	+	9.20–9.60	Hydroxyl group of $–(CH_2)_2–$ bridge and glutarimide ring (I), *N*-phenyl group (IX)
				Glutarimide (NH) hydrogen and: cyano groups (**5**) or Cl-phenyl (**4**) (II), *t*-butyl ester group (VII), ethyl group (VIII)
				Aminophenyl group and *n*-heptyl group (III)
				Hydroxyl group and glutarimide ring (VI)
				t-Hydroxyl group and glutarimide ring (X)
O–TIP	532	–	17.60–18.00	Glutarimide (NH) hydrogen and methyl ester group (I, IV), terminal methyl group or terminal double bond (VI), methylene oxy-benzyl group (VII), nitro group (VIII)
				N-Amino and alkoxy group (V)
				t-Hydroxyl group and *N*-phenyl group (IX)
N1–TIP	594	–	18.00–18.40	Glutarimide >C=O and: ester group (I, IV), terminal double bond or terminal methyl group (VI), aminonaphthyl moiety (VIII), oxybenzyl group (VII)
				Hydroxyl group and *N*-phenyl group (IX)
				Glutarimide >C=O and alkoxy group (**10**, **11**, **12**, **15**) or *t*-nitrogen and: alkoxy (**9**, **14**), *N*-alkyl group (**13**) (V)

TABLE XIV-S. Breast MFC7

Probe block	Variable No.	Impact	Distance Å	Regions
O–O	90	+	11.60–12.00	Glutarimide (NH) hydrogen AND: *t*-hydroxyl group (I), 1,3-dioxane ring (X)
N1–N1	165	+	17.20–17.60	Glutarimide >C=O and: ester (C=O) (I), pyrrolidine N (V)
TIP–TIP	231	–	19.20–19.60	*N*-Alkyl and alkoxy group (V)
				Length of molecule: glutarimide ring and: double bond or terminal methyl group (VI), aminonaphthyl moiety (VIII)
				N-Phenyl and *t*-butyl group (VII)
O–TIP	521	–	13.20–13.60	Hydroxyl group on $–(CH_2)_2–$ bridge and methyl ester (**3**) or glutarimide >C=O and *t*-OH group (**1**) (I)
				Hydroxyl group and terminal methyl group or double bond (VI)
				Glutarimide (NH) hydrogen and oxybenzyl ring (VII), naphthyl moiety (VIII)
				Hydroxyl group on $–(CH_2)_2–$ bridge and aromatic ring (IX)
N1–TIP	590	–	16.40–16.80	*t*-OH or ester carbonyl and glutarimide ring (**1**, **3,** respectively) (I)
				Glutarimide oxygen and: alkoxy group (**11**, **12**) (V), terminal methyl group or double bond (VI), benzyl ring (VII), aminonaphthyl moiety (VIII), *t*-butyl group (**20**) (IX)
				t-OH and aromatic ring (**21**) (IX)
				Alkoxy and *N*-alkyl group (**13**) (V)

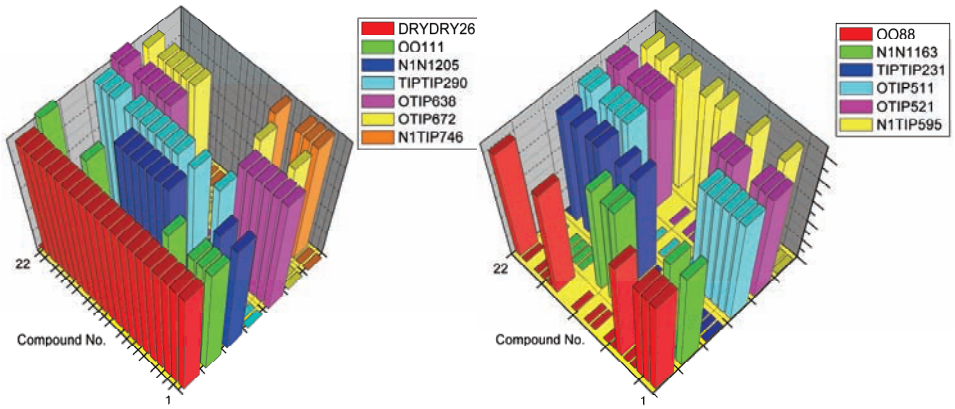

K562 A549

Fig. 8-S. Association of variables with **1**–**22** for the model on the studied cell lines.

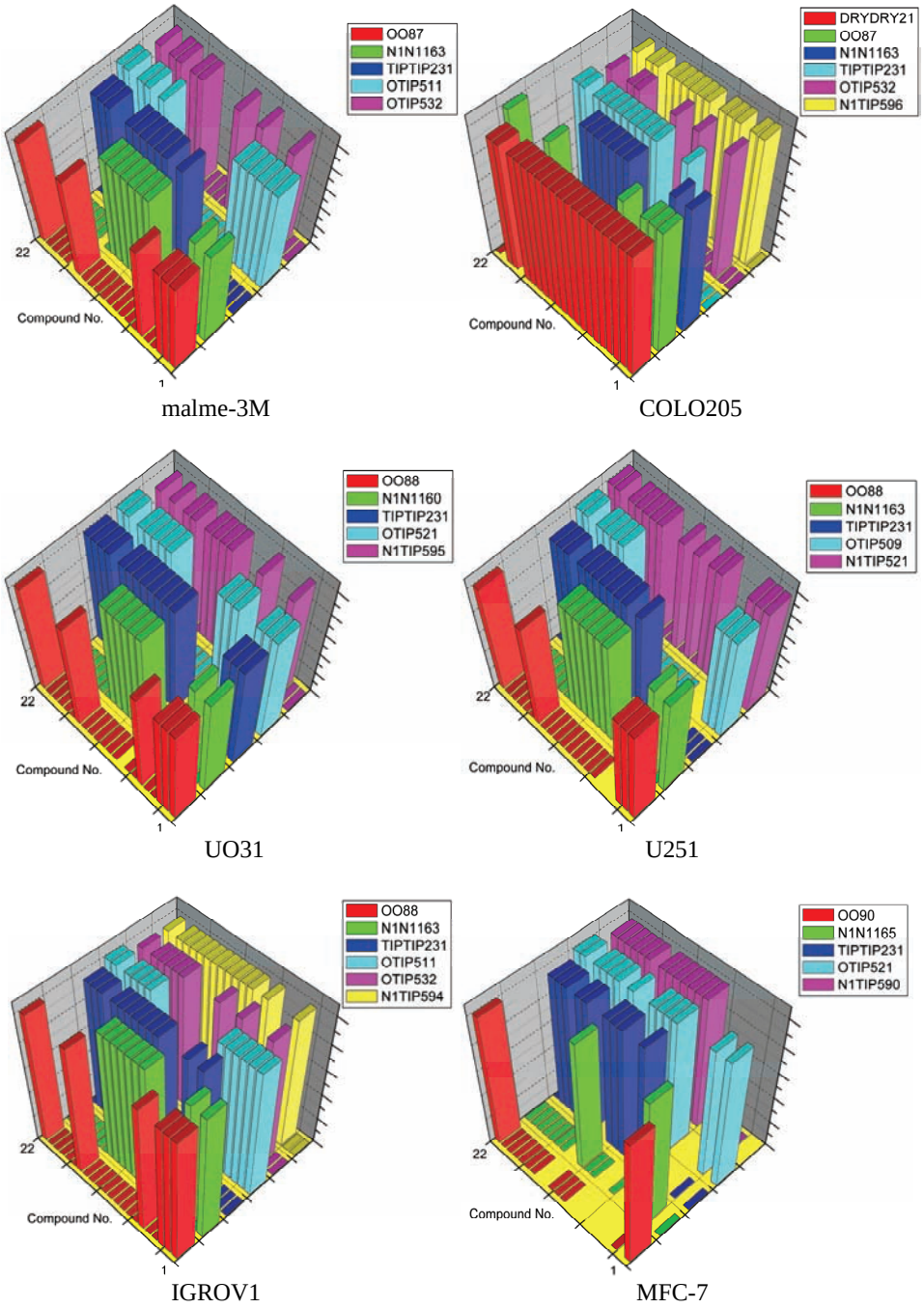

Fig. 8-S. Association of variables with **1**–**22** for the model on the studied cell lines (continued).

TABLE XV-S. Intercorrelation matrix of p(GI_{50}) values for **1**–**22**

	Leukaemia K-562	Non-small cell lung cancer A549	Colon cancer COLO-205	CNS Cancer U251	Melanoma Malme-3M	Ovarian cancer IGROV1	Renal cancer UO-31	Breast cancer MFC-7
Leukaemia K-562	1							
Non-small cell lung cancer A549	0.988	1						
Colon cancer COLO205	0.976	0.989	1					
CNS cancer U251	0.972	0.991	0.991	1				
Melanoma malme-3M	0.971	0.992	0.992	0.992	1			
Ovarian cancer IGROV1	0.962	0.982	0.985	0.993	0.986	1		
Renal cancer UO-31	0.969	0.985	0.992	0.992	0.988	0.989	1	
Breast cancer MFC-7	0.971	0.998	0.992	0.994	0.997	0.983	0.985	1

Journal of the Serbian Chemical Society
JSCS@tmf.bg.ac.rs • www.shd.org.rs/JSCS

J. Serb. Chem. Soc. 75 (9) 1181–1189 (2010)
JSCS–4041

UDC 547.292+547.586.2+547.53.024:
54–732+537.5
Original scientific paper

Acetic acid-promoted condensation of *o*-phenylenediamine with aldehydes into 2-aryl-1-(arylmethyl)-1*H*-benzimidazoles under microwave irradiation

DAVOOD AZARIFAR[1]*, MOJGAN PIRHAYATI[1], BEHROOZ MALEKI[2], MEHRANGIZ SANGINABADI[1] and RAZIEH NEJAT YAMI[1]

[1]*Faculty of Chemistry, Bu-Ali Sina University, Hamadan-65178 and* [2]*Department of Chemistry, Sabzevar Tarbiat Moallem University, Sabzevar-397, Iran*

(Received 1 September 2009, revised 30 April 2010)

Abstract: An efficient and simple procedure was developed for the green synthesis of various 2-aryl-1-(arylmethyl)-1*H*-benzimidazoles in high yields by acetic acid-promoted condensation of *o*-phenylenediamine with aldehydes in air under microwave irradiation and transition metal catalyst-free conditions.

Keywords: 2-aryl-1-(arylmethyl)-1*H*-benzimidazoles; *o*-phenylenediamine; aldehydes; microwave irradiation, acetic acid.

INTRODUCTION

The benzimidazole nucleus is of significant importance in medicinal chemistry and many benzimidazole-containing compounds exhibit important biological activities, *i.e.*, as selective neuropeptide YY1 receptor antagonists,[1–4] 5-lipoxygenase inhibitors for use as novel anti-allergic agents,[5] factor Xa (FXa) inhibitors,[6] poly (ADP-ribose) polymerase (PARP) inhibitors,[7] and as human cytomegalovirus (HCMV) inhibitors.[8] In addition, several substituted benzimidazole derivatives have been recently reported to have commercial applications in veterinarian medicine, *i.e.*, as anthelmintic agents, and in diverse human therapeutic areas, such as treatment of ulcers and as antihistaminic.[9] In the light of the affinity they display towards a variety of enzymes and protein receptors, medicinal chemists would certainly classify them as "privileged sub-structures" for drug design.[10] Therefore, the clinical significance of this class of compounds stimulated interest in the synthesis of novel ring systems agents, with retention of the core imidazole moiety.

Traditionally, the synthesis of benzimidazoles involves the condensation of *o*-phenylenediamine with aldehydes,[11–13] and carboxylic acids or their deriva-

* Corresponding author. E-mail: azarifar@basu.ac.ir
doi: 10.2298/JSC090901096A

tives (nitriles, amidates, orthoesters) under harsh dehydrating conditions.[14–20] Benzimidazoles have also been prepared on a solid-phase to provide a combinatorial approach.[21,22] The most popular strategies for their synthesis utilize *o*-nitroanilines as intermediates or resort to direct *N*-alkylation of an unsubstituted benzimidazole.[23] A number of synthetic methods that involve intermediate *o*-nitroanilines have evolved to include the synthesis of benzimidazoles on solid supports.[24–29] Another reported approach to these compounds is the reaction of *o*-phenylenediamine with aldehydes in the presence of catalysts under various reaction conditions.[30–41] Recently, a one-pot, solvent-free synthesis of biologically active benzimidazole derivatives using a simple grinding method,[42] and another under heterogeneous catalysis of amberlite IR-120[43] have been reported.

RESULTS AND DISCUSSION

In continuation of previously reported research on the use of acetic acid in various transformations,[44–46] herein, a very simple and selective synthesis of 2-aryl-1-(arylmethyl)-1*H*-benzimidazoles **2a**–**m** by acetic acid-promoted condensation of *o*-phenylenediamine with aldehydes **1a**–**m** both under microwave irradiation and conventional thermal heating in air is reported (Scheme 1, Table I).

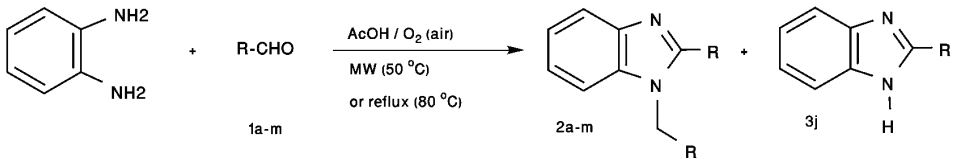

Scheme 1. The synthesis of the title compounds.

The structural elucidations of the products were based on their spectral (IR, ^{1}H- and ^{13}C-NMR and mass) data as given below.

*1-Benzyl-2-phenyl-1*H*-benzimidazole (**2a**)*. IR (KBr, cm^{-1}): 3031 (C–H stretching of aromatic ring), 2926 (C–H stretching of aliphatic), 1594 (C=N stretching of imidazole ring), 1549, 1502, 1549, 1448 (C=C stretching of aromatic ring), 1371 (C–N stretching of imidazole ring). ^{1}H-NMR (90 MHz, $CDCl_3$, δ / ppm): 5.34 (2H, *s*, –CH_2–), 7.02–7.28 (15H, *m*, Ar–H). ^{13}C-NMR (22.5 MHz, $CDCl_3$, δ / ppm): 47.80, 110.32, 119.41, 122.23, 125.72, 127.31, 128.46, 128.78, 128.80, 129.42, 135.51, 135.84, 142.62, 149.82 (C=N), 153.70. MS (*m*/*z*): 284 (M^+).

*1-(4-Methylbenzyl)-2-(4-methylphenyl)-1*H*-benzimidazole (**2b**)*. IR (KBr, cm^{-1}): 3024 (C–H stretching of aromatic ring), 2930 (C–H stretching of aliphatic), 1623 (C=N stretching of imidazole ring), 1520, 1488 (C=C stretching of aromatic ring), 1284 (C–N stretching of imidazole ring). ^{1}H-NMR (90 MHz, $CDCl_3$, δ / / ppm): 2.45 (3H, *s*, CH_3), 2.51 (3H, *s*, CH_3), 5.53 (2H, *s*, –CH_2–), 7.10–7.95

(12H, *m*, Ar–H). ^{13}C-NMR (22.5 MHz, $CDCl_3$, δ / ppm): 21.0, 21.3, 48.2, 110.3, 119.7, 122.5, 122.7, 125.7, 127.0, 128.9, 129.3, 129.5, 133.2, 136.1, 137.4, 139.8, 143.1, 154.2 (C=N). MS (*m*/*z*): 312 (M^+).

TABLE I. Acetic acid-promoted synthesis of 2-aryl-1-(arylmethyl)-1*H*-benzimidazoles

Product[a]	R	Time[b], min	Yield[b,c], %	M.p., °C	
				Found	Reported
2a	C_6H_5	25 (4)	92 (97)	132–134	132[32]
2b	4-MeC_6H_4	60 (6)	64 (82)	126–128	126[32]
2c	4-$MeOC_6H_4$	30 (5)	90 (96)	130–131	131[32]
2d	2-$MeOC_6H_4$	40 (5)	80 (95)	154–155	151[32]
2e	4-HOC_6H_4	30 (7)	60 (85)	250–253	254–256[41]
2f	2-HOC_6H_4	35 (8)	58 (78)	205–208	207–208[41]
2g	4-ClC_6H_4	30 (6)	82 (85)	138–140	137[32]
2h	2-ClC_6H_4	50 (8)	70 (80)	158–159	155[32]
2i	4-$Me_2NC_6H_4$	35 (5)	92 (98)	254–256	252[32]
2j	2-Furyl	50 (5)	70 (75)[d]	96–98	96[32]
2k	4-CNC_6H_4	20 (4)	92 (95)	190–191	187–188[41]
2l	4-$NO_2C_6H_4$	35 (6)	68 (86)	119–120	118[32]
2m	2-$NO_2C_6H_4$	35 (8)	52 (75)	169–170	168–170[33]

[a]The products were characterized by their physical properties and spectral analysis and compared with authentic samples; [b]the reaction times and yields obtained using microwave irradiation are shown in the parenthesis; [c]yield isolated; [d]the product **3j** was isolated in 20 (thermal) and 25 % (microwave irradiation) yields. M.p. 122–124 °C (lit.:[33] 120 °C)

*1-(4-Methoxybenzyl)-2-(4-methoxyphenyl)-1*H*-benzimidazole (**2c**)*. IR (KBr, cm^{-1}): 3030 (C–H stretching of aromatic ring), 2932 (C–H stretching of aliphatic), 1609 (C=N stretching of imidazole ring), 1538, 1460 (C=C stretching of aromatic ring), 1244 (C–N stretching of imidazole ring). ^{1}H-NMR (90 Mz, $CDCl_3$, δ / ppm): 3.79 (3H, *s*, OCH_3), 3.89 (3H, *s*, OCH_3), 5.34 (2H, *s*, $–CH_2–$), 6.92––7.78 (12H, *m*, Ar–H). ^{13}C-NMR (22.5 MHz, $CDCl_3$, δ / ppm): 47.8, 55.2, 55.3, 110.3, 114.2, 114.4, 119.6, 122.5, 122.7, 127.2, 128.4, 130.6, 136.1, 143.2, 154.0 (C=N), 159.1, 160.9. MS (*m*/*z*): 344 (M^+).

*1-(2-Methoxybenzyl)-2-(2-methoxyphenyl)-1*H*-benzimidazole (**2d**)*. IR (KBr, cm^{-1}): 3063 (C–H stretching of aromatic ring), 2961 (C–H stretching of aliphatic), 1600 (C=N stretching of imidazole ring), 1583, 1454 (C=C stretching of aromatic ring), 1258 (C–N stretching of imidazole ring); ^{1}H-NMR (90 MHz, $CDCl_3$, δ / ppm): 3.46 (3H, *s*, OCH_3), 3.64 (3H, *s*, OCH_3), 5.21 (2H, *s*, $–CH_2–$), 6.64––7.81 (12H, *m*, Ar–H). ^{13}C-NMR (22.5 MHz, $CDCl_3$, δ / ppm): 43.2, 55.0, 55.1, 109.8, 110.5, 110.6, 119.7, 120.2, 120.6, 121.8, 122.3, 124.3, 127.4, 128.2, 131.3, 132.1, 135.3, 143.1, 152.4 (C=N), 156.3, 157.3. MS (*m*/*z*): 344 (M^+).

*4-{[2-(4-Hydroxyphenyl)-1*H*-benzimidazol-1-yl]methyl}phenol (**2e**)*. IR (KBr, cm^{-1}): 3348 (O–H stretching of phenyl ring), 3002 (C–H stretching of aromatic ring), 2925 (C–H stretching of aliphatic), 1597 (C=N stretching of imidazole

ring), 1515, 1412 (C=C stretching of aromatic ring), 1266 (C–N stretching of imidazole ring). ^{1}H-NMR (90 MHz, DMSO-d_6, δ / ppm): 5.32 (2H, *s*, –CH_2–), 6.78–7.80 (12H, *m*, Ar–H), 9.33 (1H, *brs*, OH), 9.89 (1H, *brs*, OH). MS (*m*/*z*): 316 (M^+).

*2-{[2-(2-Hydroxyphenyl)-1*H*-benzimidazol-1-yl]methyl}phenol* (***2f***). IR (KBr, cm^{-1}): 3384 (O–H stretching of phenyl ring), 3010 (C–H stretching of aromatic ring), 2910 (C–H stretching of aliphatic), 1600 (C=N stretching of imidazole ring), 1460, 1425 (C=C stretching of aromatic ring), 1298 (C–N stretching of imidazole ring). ^{1}H-NMR (90 MHz, DMSO-d_6, δ / ppm): 5.58 (2H, *s*, –CH_2–), 6.18–7.34 (12H, *m*, Ar–H), 9.48 (1H, *brs*, OH), 10.04 (1H, *brs*, OH). MS (*m*/*z*): 316 (M^+).

*1-(4-Chlorobenzyl)-2-(4-chlorophenyl)-1*H*-benzimidazole* (***2g***). IR (KBr, cm^{-1}): 3050 (C–H stretching of aromatic ring), 2920 (C–H stretching of aliphatic), 1546 (C=N stretching of imidazole ring), 1522, 1441 (C=C stretching of aromatic ring), 1346 (C–N stretching of imidazole ring). ^{1}H-NMR (90 MHz, $CDCl_3$, δ / ppm): 5.49 (2H, *s*, –CH_2–), 7.14–8.19 (12H, *m*, Ar–H). ^{13}C-NMR (22.5 MHz, $CDCl_3$, δ / ppm): 47.6, 110.3, 120.1, 123.2, 123.4, 127.2, 128.4, 129.1, 129.2, 130.3, 133.7, 134.6, 135.7, 136.2, 142.9, 152.8 (C=N); MS (*m*/*z*): 353 (M^+).

*1-(2-Chlorobenzyl)-2-(2-chlorophenyl)-1*H*-benzimidazole* (***2h***). IR (KBr, cm^{-1}): 3059 (C–H stretching of aromatic ring), 2924 (C–H stretching of aliphatic), 1612 (C=N stretching of imidazole ring), 1512, 1418 (C=C stretching of aromatic ring), 1396 (C–N stretching of imidazole ring). ^{1}H-NMR (90 MHz, $CDCl_3$, δ / ppm): 5.33 (2H, *s*, –CH_2–), 6.57–7.85 (12H, *m*, Ar–H). ^{13}C-NMR (22.5 MHz, $CDCl_3$, δ / ppm): 45.6, 110.4, 120.3, 122.4, 123.3, 126.7, 127.0, 127.6, 128.8, 129.4, 129.3, 129.7, 131.2, 132.1, 132.3, 133.2, 134.1, 134.6, 142.8, 151.3 (C=N). MS (*m*/*z*): 353 (M^+).

*1-[4-(Dimethylamino)benzyl]-2-[4-(dimethylamino)phenyl]-1*H*-benzimidazole* (***2i***). IR (KBr, cm^{-1}): 3029 (C–H stretching of aromatic ring), 2912 (C–H stretching of aliphatic), 1590 (C=N stretching of imidazole ring), 1520, 1412 (C=C stretching of aromatic ring), 1348 (C–N stretching of imidazole ring). ^{1}H--NMR (90 MHz, $CDCl_3$, δ / ppm): 2.84 (6H, *s*, NMe_2), 2.92 (6H, *s*, NMe_2), 5.42 (2H, *s*, –CH_2–), 6.68–7.03 (12H, *m*, Ar–H). ^{13}C-NMR (22.5 MHz, $CDCl_3$, δ / / ppm): 40.1, 40.4, 48.0, 110.4, 111.6, 112.6, 117.0, 119.1, 122.2, 124.2, 126.7, 130.3, 136.2, 143.0, 149.8, 151.1 (C=N), 155.2. MS (*m*/*z*): 370 (M^+).

*2-(2-Furyl)-1-(2-furylmethyl)-1*H*-benzimidazole* (***2j***). IR (KBr, cm^{-1}): 3020 (C–H stretching of aromatic ring), 2925 (C–H stretching of aliphatic), 1577 (C=N stretching of imidazole ring), 1512, 1470 (C=C stretching of aromatic ring), 1328 (C–N stretching of imidazole ring), 1248 (C–O stretching of furyl ring). ^{1}H-NMR (90 MHz, $CDCl_3$, δ / ppm): 5.60 (2H, *s*, –CH_2–), 6.21–7.60 (10H, *m*, Ar–H). ^{13}C-NMR (22.5 MHz, DMSO-d_6, δ / ppm): 41.6, 108.2, 109.8,

110.0, 110.4, 112.0, 112.8, 119.7, 122.8, 123.2, 135.3, 142.5, 142.9, 143.7, 145.3, 149.5 (C=N). MS (*m*/*z*): 264 (M^+).

*4-{[2-(4-Cyanophenyl)-1*H*-benzimidazol-1-yl]methyl}benzonitrile (**2k**)*. IR (KBr, cm^{-1}): 3061 (C–H stretching of aromatic ring), 2912 (C–H stretching of aliphatic), 2227 (C–N stretching of phenyl ring) 1608 (C=N stretching of imidazole ring), 1504, 1478, 1457 (C=C stretching of aromatic ring), 1386 (C–N stretching of imidazole ring). ^{1}H-NMR (90 MHz, $CDCl_3$, δ / ppm): 5.49 (2H, *s*, $–CH_2–$), 7.21–7.72 (12H, *m*, Ar–H); ^{13}C-NMR (22.5 MHz, $CDCl_3$, δ / ppm): 48.0, 110.2, 111.1, 112.3, 113.7, 117.9, 120.6, 123.5, 124.2, 126.6, 129.6, 132.5, 133.0, 134.1, 135.9, 141.1, 143.1, 151.7 (C=N). MS (*m*/*z*): 334 (M^+).

*1-(4-Nitrobenzyl)-2-(4-nitrophenyl)-1*H*-benzimidazole (**2l**)*. IR (KBr, cm^{-1}): 3075 (C–H stretching of aromatic ring), 2926 (C–H stretching of aliphatic), 1614 (C=N stretching of imidazole ring), 1526, 1350 ($–NO_2$ stretching of aromatic ring), 1507, 1445 (C=C stretching of aromatic ring), 1390 (C–N stretching of imidazole ring). ^{1}H-NMR (90 MHz, $CDCl_3$, δ / ppm): 5.50 (2H, *s*, $–CH_2–$), 7.22––8.37 (12H, *m*, Ar–H). ^{13}C-NMR (22.5 MHz, $CDCl_3$, δ / ppm): 47.8, 110.2, 120.5, 123.6, 124.0, 124.5, 124.7, 126.6, 130.1, 135.6, 135.8, 142.5, 143.0, 147.5, 148.5, 151.2 (C=N); MS (*m*/*z*): 374 (M^+).

*1-(2-Nitrobenzyl)-2-(2-nitrophenyl)-1*H*-benzimidazole (**2m**)*. IR (KBr, cm^{-1}): 3085 (C–H stretching of aromatic ring), 2964 (C–H stretching of aliphatic), 1611 (C=N stretching of imidazole ring), 1529, 1347 ($–NO_2$ stretching of aromatic ring), 1576, 1459, 1433 (C=C stretching of aromatic ring), 1314 (C–N stretching of imidazole ring). ^{1}H-NMR (90 MHz, $CDCl_3$, δ / ppm): 5.56 (2H, *s*, $–CH_2–$), 6.59–7.64 (12H, *m*, Ar–H). ^{13}C-NMR (22.5 MHz, $CDCl_3$, δ / ppm): 45.6, 110.2, 120.3, 123.0, 123.6, 124.8, 125.0, 125.5, 128.2, 128.7, 131.4, 131.8, 133.2, 134.1, 134.6, 143.0, 146.5, 148.7, 149.6 (C=N); MS (*m*/*z*): 374 (M^+).

The ^{1}H- and ^{13}C-NMR spectra of the obtained products are in full consonance with benzimidazole structures and their melting points are in agreement with those reported,[13] (Table I). It was observed that the reactions performed under microwave irradiation were brought to completion in 4–12 min at the 60 % power level. When these reactions were performed under reflux condition at 80 °C for the same time, lower yields of products were obtained, as given in Table I.

A possible mechanism proposed for these reactions is depicted in Scheme 2. This mechanism probably involves an initial acetic acid-promoted condensation of *o*-phenylenediamine with aldehydes **1a**–**m** to yield a di-imine intermediate **A** followed by cyclization to the 2-aryl-1-(arylmethyl)-1*H*-benzimidazoles **2a**–**m** through the intermediate **B** (path a). In order to confirm the involvement of the diarylidene-*o*-phenylenediamine (**A**) as an intermediate, dibenzylidene-*o*-phenylenediamine was prepared separately by the reaction of *o*-phenylenediamine with two equimolar amounts of benzaldehyde in AcOH at 100 °C after 20 min. Microwave irradiation of purely separated dibenzylidene-*o*-phenylenediamine as a

test compound in acetic acid under the same conditions as used for the reactions resulted merely in the formation of 1-benzyl-2-phenyl-1*H*-benzimidazole (**2a**). This can be indicative that the reaction probably occurs *via* path a, with the formation of **A**, followed by 1,3-hydride transfer, according to previous suggestions.[32,36,41,47] However, the formation of 2-(2-furyl)benzimidazole **3j** in minor yield in the case of furylaldehyde (Table I) can be explained possibly through path b involving the formation of dihydrobenzimidazole **C** intermediate followed by dehydrative oxidation in air to yield 2-arylbenzimidazole **3**, as suggested by Xiangming[48] and Zelenin *et al.*[49] A direct oxidative condensation of aldoses with diamines using molecular iodine in AcOH has already been reported for an improved synthesis of aldo-benzimidazoles and aldo-naphthimidazoles, which supports the observations in this work.[50] It is important to emphasize that, when these reactions were conducted under nitrogen atmosphere, no formation of compound **3** was detected and compounds **2a**–**m** were isolated as the sole products in slightly improved yields. This ratifies the role of air in partial oxidation of the intermediate **C** to provide 1*H*-benzimidazole **3j**.

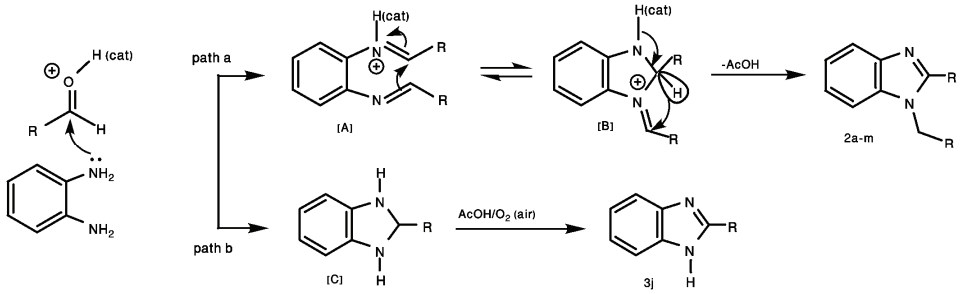

Scheme 2. The suggested mechanism for the formation of the title compounds.

EXPERIMENTAL

Solvents, reagents, and chemical materials were obtained from Aldrich and Merck and purified prior to use. Melting points were determined in open capillary tubes in a Stuart SMP3 apparatus and are uncorrected. Nuclear magnetic resonance spectra were recorded on a JEOL FX 90Q using tetramethylsilane (TMS) as the internal standard. Infrared spectra were recorded on a Perkin Elmer GX FT IR spectrometer (KBr pellets). The microwave-assisted reactions were conducted in a Milstone CombiChem microwave synthesizer. In all irradiation experiments, rotation of rotor, irradiation time, temperature and power were monitored with the "Easy Wave" software package. Benzimidazoles were characterized based on their melting points and IR, ^{1}H- and ^{13}C-NMR spectral data, which were compared with reported data.[32,33,41]

*General procedure for the synthesis of 2-aryl-1-(arylmethyl)-1*H*-benzimidazoles (**2a**–**m**) under microwave irradiation and thermal conditions*

A mixture of *o*-phenylenediamine (0.11 g, 1.0 mmol) and aldehyde **1** (2.0 mmol) dissolved in glacial acetic acid (10 ml) was capped and irradiated in a Milstone CombiChem microwave synthesizer for the appropriate time at 50 °C (Table I). The progress of the reac-

tion was monitored by intermittent rapid cooling of the mixture to r.t. every one minute and analyzing by TLC (*n*-hexane/ethyl acetate, 2:8). After complete conversion of the substrate as indicated by TLC analysis, the solvent was evaporated under reduced pressure to leave the products **2a**–**m** (and **3j**), which were recrystallized from EtOH (96 %) (Table I). Similarly, in a separate set of experiments, these reactions were all repeated in acetic acid under reflux condition at 80 °C (Table I). Their melting points and yields are summarized in Table I.

CONCLUSIONS

In conclusion, the present work offers a simple procedure promoted by inexpensive and non-toxic glacial acetic acid as an efficient methodology for the synthesis of 2-aryl-1-(arylmethyl)-1*H*-benzimidazoles *via* condensation of aromatic aldehydes with *o*-phenylenediamine both under microwave irradiation and conventional thermal heating. A mild, manipulatable procedure, eco-friendly and green aspects avoiding hazardous solvents, shorter reaction times and high yields of the products are the advantages of this method.

Acknowledgment. We wish to thank the research council of Bu-Ali Sina University, Hamadan, Iran, for financial support to carry out this research.

И З В О Д

КОНДЕНЗАЦИЈА *o*-ФЕНИЛЕНДИАМИНА И АЛДЕХИДА ДО 2-АРИЛ-1-(АРИЛМЕТИЛ)--1*H*-БЕНЗИМИДАЗОЛА У ПРИСУСТВУ СИРЋЕТНЕ КИСЕЛИНЕ ПОД УСЛОВИМА МИКРОТАЛАСНОГ ЗРАЧЕЊА

DAVOOD AZARIFAR[1], MOJGAN PIRHAYATI[1], BEHROOZ MALEKI[2], MEHRANGIZ SANGINABADI[1] и RAZIEH NEJAT YAMI[1]

[1]*Faculty of Chemistry, Bu-Ali Sina University, Hamadan-65178 и* [2]*Department of Chemistry, Sabzevar Tarbiat Moallem University, Sabzevar-397, Iran*

Развијен је једноставан, ефикасан и еколошки прихватљив поступак за синтезу различитих 2-арил-1-(арилметил)-1*H*-бензимидазола, кондензацијом *o*-фенилендиамина и алдехида у присуству сирћетне киселине под условима микроталасног озрачивања без инертне атмосфере и присуства прелазних метала као катализатора.

(Примљено 1. септембра 2009, ревидирано 30. априла 2010)

REFERENCES

1. H. Zarrinmayeh, A. M. Nunes, P. L. Ornstein, D. A. Zimmerman, S. L. Gackenheimer, R. F. Bruns, P. A. Hipskind, T. C. Britton, B. E. Cantrell, D. R. Gehlert, *J. Med. Chem.* **41** (1998) 2709
2. G. L. Gravatt, B. C. Baguley, W. R. Wilson, W. A. Denny, *J. Med. Chem.* **37** (1994) 4338
3. B. Jayashankara, K. M. L. Rai, *ARKIVOC* **11** (2008) 75
4. K. C. Ravindra, H. M. Vagdevi, V. P. Vaidya, *ARKIVOC* **11** (2008) 1
5. H. Nakano, T. Inoue, N. Kawasaki, H. Miyataka, H. Matsumoto, T. Taguchi, N. Inagaki, H. Nagai, T. Satoh, *Bioorg. Med. Chem.* **8** (2000) 373
6. Z. S. Zhao, D. O. Arnaiz, B. Griedel, S. Sakata, J. L. Dallas, M. Whitlow, L. Trinh, J. Post, A. Liang, M. M. Morrissey, K. J. Shaw, *Bioorg. Med. Chem. Lett.* **10** (2000) 963

7. A. W. White, R. Almassy, A. H. Calvert, N. J. Curtin, R. J. Griffin, Z. Hostomsky, K. Maegley, D. R. Newell, S. Srinivasan, B. T. Golding, *J. Med. Chem.* **43** (2000) 4084
8. Z. Zhu, B. Lippa, J. C. Drach, L. B. Townsend, *J. Med. Chem*. **43** (2000) 2430
9. A. A. Spasov, I. N. Yozhitsa, L. I. Bugaeva, V. A. Anisimova, *Pharm. Chem. J.* **33** (1999) 232
10. B. E. Evans, K. E. Rittle, M. G. Bock, R. M. Dipardo, R. M. Freidinger, W. L Whitter, G. F. Lundell, D. F. Veber, P. S. Anderson, R. S. Chang, R. S. L. Chang, V. J. Lotti, D. J. Gerino, T. B. Chen, P. J. Kling, K. A. Kunkel, J. P. Springer, J. Hirshfield, *J. Med. Chem.* **42** (1988) 2235
11. S. M. Landge, B. Török, *Catal. Lett*. **122** (2008) 338
12. R. S. Keri, K. M. Hosamani, H. R. Seetharama Reddy, R. V. Shingalapur, *Catal. Lett*. **131** (2009) 552
13. C. Yu, P. Guo, C. Jin, W. Su, *J. Chem. Res*. **5** (2009) 333
14. M. M. Heravi, B. Baghernegad, H. A. Oskooei, R. Malakooti, *J. Chin. Chem. Soc*. **55** (2008) 1129
15. S. M. Radwan, K. A. M. El-Dean, E. A. Bakhite, *J. Chin. Chem. Soc*. **52** (2005) 303
16. Y. C. Chi, C. M. Sun, *Synlett* (2000) 591
17. L. M. Dudd, E. Venardou, E. Garcia-Verdugo, P. Licence, A. J. Blake, C. Wilson, M. Poliakoff, *Green Chem*. **5** (2003) 187
18. Z. H. Zhang, L. Yin, Y. M. Wang, *Catal. Commun*. **8** (2007) 1126
19. M. L. Richards, S. C. Lio, A. Sinha, H. Banie, R. J. Thomas, M. Major, M. Tanji, J. C. Sircar, *Eur. J. Med. Chem*. **41** (2006) 950
20. R. Wang, X. X. Lub, X. Q. Yu, L. Shi, Y. Sun, *J. Mol. Catal. A: Chem*. **266** (2007) 198
21. Z. Wu, P. Rea, G. Wickam, *Tetrahedron Lett*. **41** (2000) 9871
22. A. Mazurov, *Bioorg. Med. Chem. Lett.* **10** (2000) 67
23. B. H. Kim, R. Han, J. S. Kim, Y. M. Jun, W. Baik, B. M. Lee, *Heterocycles* **63** (2004) 41
24. D. Tumelty, K. Cao, C. P. Holmes, *Org. Lett.* **3** (2001) 83
25. D. Tumelty, M. K. Schwarz, M. C. Needels, *Tetrahedron Lett.* **38** (1998) 7467
26. J. P. Mayer, G. S. Lewis, C. Mc Gee, D. Bankaitis-Davis, *Tetrahedron Lett.* **39** (1998) 6655
27. W. Huang, R. M. Scarborogh, *Tetrahedron Lett.* **40** (1999) 2665
28. J. M. Smith, V. Krchnak, *Tetrahedron Lett.* **40** (1999) 7633
29. J. P. Kilburn, J. Lau, R. C. F. Jones, *Tetrahedron Lett*. **41** (2000) 5419
30. R. J. Perry, B. D. Wilson, *J. Org. Chem.* **58** (1993) 7016
31. D. Anastasiou, E. M. Campi, H. Chaouk, W. R. Jackson, *Tetrahedron* **48** (1992) 7467
32. S. Perumal, S. Mariappan, S. Selvaraj, *ARKIVOC* **8** (2004) 46
33. M. Chakrabarty, S. Karmakar, A. Mukherji, S. Arima, Y. Harigay, *Heterocycles* **68** (2006) 967
34. P. Salehi, M. Dabiri, M. A. Zolfigol, S. Otokesh, M. Baghbanzadeh, *Tetrahedron Lett.* **47** (2006) 2557
35. H. Ma, Y. Wang, J. Li, J. Wang, *Heterocycles* **71** (2007) 135
36. M. Chakrabarty, R. Mukherjee, S. Karmakar, Y. Harigaya, *Monatsh. Chem.* **138** (2007) 1279
37. P. P. Sun, Z. Hu, *J. Heterocycl. Chem.* **43** (2006) 773
38. M. Chakrabarty, A. Mukherji, R. Mukherjee, S. Arimab, Y. Harigayab, *Tetrahedron Lett.* **48** (2007) 5239
39. R. Varala, A. Nasreen, R. Enugala, S. R. Adapa, *Tetrahedron Lett.* **48** (2007) 69
40. N. D. Kokare, J. N. Sangshetti, D. B. Shinde, *Synthesis* (2007) 2829

41. V. Ravi, E. Ramu, K. Vijay, S. Rao, *Chem. Pharm. Bull.* **55** (2007) 1254
42. H. Thakuria, G. Das, *ARKIVOC* **15** (2008) 321
43. S. D. Sharma, D. Kowar, *Synth. Commun*. **39** (2009) 980
44. D. Azarifar, M. Shaebanzadeh, *Molecules* **8** (2002) 885
45. D. Azarifar, B. Maleki, M. Sahraei, *J. Heterocycl. Chem.* **45** (2008) 563
46. D. Azarifar, B. Maleki, M. Setayeshnazar, *Phosphor, Sulfur Silicon Relat. Elem.***184** (2009) 2097
47. R. G. Jacob, L. G. Dutra, C. S. Radatz, S. R. Mendes, G. Perin, E. J. Lenardão, *Tetrahedron Lett*. **50** (2009) 1495
48. X. Han, H. Ma, Y. Wang, *ARKIVOC* **8** (2007) 150
49. K. N. Zelenin, I. V. Ukraintsev, V. V. Alekseev, *Chem. Heterocycl. Compd*. **34** (1998) 329
50. C. Lin, P. T. Lai, S. K. Liao, W. T. Hung, W. B. Yang, J. M. Fang, *J. Org. Chem.* **73** (2008) 3848.

Journal of the Serbian Chemical Society
JSCS-info@shd.org.rs • www.shd.org.rs/JSCS
J. Serb. Chem. Soc. *75* (9) 1191–1201 (2010)
JSCS–4042
UDC 542.9+547.571.+547.551:
577.113:577.112.387:547.576
Original scientific paper

Interaction between tryptophan-vanillin Schiff base and herring sperm DNA

YAN ZHANG[1], XINGMING WANG[1]* and LISHENG DING[2]

[1]*Department of Chemistry, School of Materials Science and Engineering, Southwest University of Science and Technology, Mianyang 621010, P. R. China and* [2]*Chengdu Institute of Biology, Chinese Academy of Sciences, Chengdu 610041, P. R. China*

(Received 28 January, revised 31 March 2010)

Abstract: The interaction of the Schiff base (K[HL]) with herring sperm DNA was studied by UV–Vis absorption, fluorescence and viscosity methods in a physiological pH environment (pH 7.40), where the Schiff base was derived from vanillin and L-tryptophan. A binding ratio of *n*K[HL]:*n*DNA = 5:1 and an apparent molar absorption coefficient of ε(K[HL]–DNA) = 4.98×10^5 L mol^{-1} cm^{-1} were confirmed by the mole ratio method. The binding constants of $K_B^{\ominus}$(301 K) =1.94×10^5 L mol^{-1} and $K_B^{\ominus}$(310 K) = 1.09×10^5 L·mol^{-1} were obtained by the double reciprocal method. Thermodynamic parameters suggest that the interaction between K[HL] and DNA is driven mainly by enthalpy. Combined with Scatchard methods and viscosity methods, the results indicate the presence of intercalation and groove binding between K[HL] and DNA.

Keywords: vanillin; L-tryptophan; Schiff base; herring sperm DNA; interaction.

INTRODUCTION

The numerous hitherto performed biological experiments suggest that DNA is the primary intracellular target of an anticancer complex because the interaction between this molecule and DNA can cause DNA damage in cancer cells, blocking the division of cancer cells and resulting in cell death.[1,2] Generally, there are three modes for reversible binding of molecules with double-helix DNA in a non-covalent way: *i*) electrostatic interaction – electrostatic attractions with the anionic sugar-phosphate backbone of DNA, *ii*) groove binding–interactions with the DNA groove and *iii*) intercalation between the base pairs. Depending on the structural features of both the molecules and DNA, many molecules show more than a single interaction mode with DNA.[3]

* Corresponding author. E-mail: xmwang_xkd@yahoo.com.cn
doi: 10.2298/JSC100128107Z

A Schiff base is obtained by the condensation reaction between an aldehyde and an amine. They have recently received considerable attention due to their good performance in coordination chemistry, unique anti-bacterial, anti-cancer, and other physical activities.[4–6] In particular, Schiff base complexes obtained from amino acids are finding applications in the understanding of many biochemical reactions *in vivo*. An amino acid is a kind of important biological ligand, which contains several N and O atoms. Cancerous cells have a much greater demand for amino acids than normal cells. Hence, amino acid Schiff base may deliver an anti-cancer base to cancerous cells, thereby increasing the selectivity of anti-cancer cells.[7]

L-Tryptophan (Trp) is an essential amino acid which is required for the biosynthesis of proteins. It is important in nitrogen balance and the maintenance of muscle mass and body weight in humans.[8]

In this study, a Schiff base containing an azomethine group was prepared by the condensation of vanillin with L-tryptophan, and then the interaction of the Schiff base with DNA was investigated systematically by spectroscopy and viscosity approaches. A series of thermodynamic parameters and binding constants were also obtained. The results are helpful to understand the interaction modes between the amino acid Schiff base and DNA.

EXPERIMENTAL

Apparatus

Carbon, hydrogen and nitrogen were obtained using a Vario El Cube instrument. The IR spectra (400–4000 cm^{-1}) were recorded as KBr pellets on a Spectrum One FTIR spectrophotometer. The absorption spectra were measured on an UV-210 spectrophotometer. The fluorescence spectra were recorded with a FL-4500 spectrofluorometer. The pH was measured using a pHS-2C digital pH-meter with a combined glass-calomel electrode.

Materials

Herring sperm DNA (hsDNA) was purchased from Sigma Biological Co. and used as received. The purity of the DNA was checked by monitoring the ratio of the absorbance at 260 and 280 nm. The ratio was 1.89, indicating that the DNA was free from protein.[9] The DNA was dissolved in doubly distilled deionized water with 50 mM NaCl and dialyzed for 48 h against a buffer solution at 4 °C. The concentration of the hsDNA stock solution was determined according to the absorbance at 260 nm using an extinction coefficients of 6600 L mol^{-1} cm^{-1}.

A tris-HCl buffer (pH 7.40) was used to control the pH of the reaction system. All of the samples were dissolved in the Tris-HCl buffer. L-Tryptophan was purchased from the Chengdu-China Kelong Chemical Plant (A.R.). Vanillin was purchased from the Xian-China Chemical Plant (A.R.). Acridine orange (AO) was purchased from the Shanghai-China Medicine Chemical Plant (A.R.). Other reagents were of at least analytical grade and were used without further purification.

Preparation of K[HL]

The Schiff base (K[HL]) derived from vanillin and L-tryptophan was prepared using a method similar to one given in the literature.[10] To a solution of vanillin (0.18 g, 1.2 mmol) in MeOH (10 cm^3), L-tryptophan (0.20 g, 1.0 mmol) in MeOH (15 cm^3) containing KOH (0.056 g, 1.0 mmol) was added. The obtained solution was then magnetically stirred for 5 h at 50–60 °C on a water bath. The volume of the obtained brownish red solution was reduced *in vacuo* using a rotary evaporator and then washed with absolute ethanol. After standing for several days, black crystals formed. Anhydrous diethyl ether was added to wash the black crystals and they were then dried in *vacuo* for 2 h.

Absorption spectral measurements

A solution (3 mL) containing an appropriate concentration of K[HL] in 1.0 cm quartz cells was titrated by successive additions of a certain concentration of DNA stock solution. The titration was performed manually using a micro-injector. Each addition was 10 μL to avoid a change in the volume. Appropriate blanks corresponding to the buffer were used as the reference. The absorption spectra were measured 5 min after each addition.

Fluorescence spectral measurements

A solution (3 mL) containing an appropriate concentration of K[HL]–DNA in 1.0 cm quartz cells was titrated using a stock solution of AO and a solution (3.0 mL) containing an appropriate concentration of AO–DNA in 1.0 cm quartz cells was titrated using a stock solution of K[HL]. The titrations were performed manually using a micro-injector. Each addition was 10 μL to avoid a change in the volume. The widths of both the excitation slit and the emission slit were set at 5.0 nm; and the excitation wavelength was set at 411.7 nm. The fluorescence emission spectra were measured 5 min after each addition.

Viscosity measurements

The viscosity experiments were realized using a viscometer which was immersed in a water-bath thermostated at room temperature. Different amounts of K[HL] were then added into the viscometer to give different values of c(K[HL]) while keeping the DNA concentration constant. The flow times of the samples were repeatedly measured with an accuracy of ±0.2 s using a digital stopwatch. Each point value was the average of at least three time measurements. The data are presented as $(\eta/\eta_0)^{1/3}$ *versus* c(K[HL]), where η and η_0 are the viscosity of DNA in the presence and absence of the Schiff base, respectively.

RESULTS AND DISCUSSION

The IR spectrum of the black crystals of the synthesized Schiff base displayed clearly a strong band at 1627 cm^{-1} that can be assigned to the ν(C=N) azomethine stretching vibration. The symmetric carboxyl stretching $\nu_{sym}(COO^-)$ and the asymmetric carboxyl stretching $\nu_{asym}(COO^-)$ were at 1390 and 1593 cm^{-1}, respectively. The IR spectrum also showed a broad band at 3398 cm^{-1}, which can be attributed to the stretching vibration of the –OH group.[11] This indicates that a water molecule was present in the Schiff base.

Anal. Calcd. for $C_{19}H_{17}N_2O_4K{\cdot}2H_2O$: C, 55.34; H, 4.13; N, 6.80 %. Found: C, 55.91; H, 4.58; N, 6.61 %.

From the above results, the structure of K[HL] can be deduced (Scheme 1).

Absorption spectral studies

The binding of small molecules to DNA is classically characterized through absorption titrations.[12] Generally, a red shift (or blue shift) and hypochromic (or hyperchromic) effect are observed in the absorption spectra of small molecules if they intercalate with DNA.

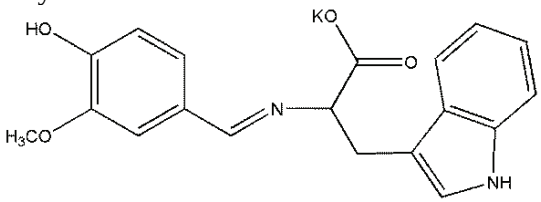

Scheme 1. Structure of the Schiff base (K[HL]).

UV–Vis absorption spectra were obtained by titration of a K[HL] solution with increasing concentrations of DNA (Fig. 1). In the absence of DNA, the UV––Vis spectrum of K[HL] is characterized by three transitions: two higher energy absorptions bands at 213 and 280 nm; and a lower energy absorption band at 340 nm. With increasing concentration of DNA, the intensity of both the 213 and 280 nm absorbance peaks gradually increased, but the intensity of the 340 nm peak decreased. Isochromatic points were obtained at 317 and 375 nm.

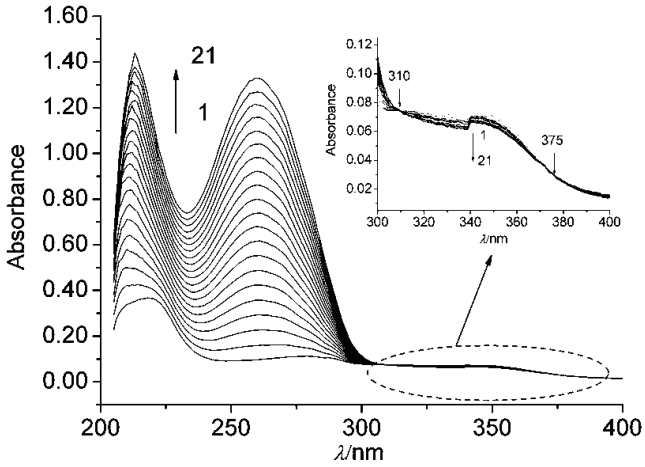

Fig. 1. Absorption spectra of K[HL] in different concentration of DNA (pH 7.40); for curve 1–21, c(K[HL]) = 1.00×10^{-5} mol L^{-1}, c(DNA) = 0.00, 0.02, 0.04, 0.06, 0.08, 0.10, 0.12, 0.14, 0.16, 0.18, 0.20, 0.22, 0.24, 0.26, 0.28, 0.30, 0.32, 0.34, 0.36, 0.38 and 0.40×10^{-5} mol L^{-1}, respectively.

A hypochromic effect and isosbestic points are evidence of DNA-intercalation.[13,14] The absorption spectra of K[HL] in the presence of DNA showed hypochromicity and isochromatic points, indicating the presence of intercalation between K[HL] and DNA.

In order to determine the stoichiometry for the formation of the K[HL]–DNA complex, the mole ratio method[15] was applied to the peak 213 nm. The mole ratio plots of DNA with K[HL] are shown in Fig. 2. The binding ratio of the complex was obtained: $n_{K[HL]}$:n_{DNA} = 5:1. According to the Lambert–Beer law: $A = \varepsilon bc$, where A is the absorbance of K[HL]–DNA, ε is the apparent molar absorption coefficient of K[HL]–DNA and c is the concentration of K[HL]–DNA. The apparent molar absorption coefficient of K[HL]–DNA was $\varepsilon = 4.98\times10^5$ L mol^{-1} cm^{-1}.

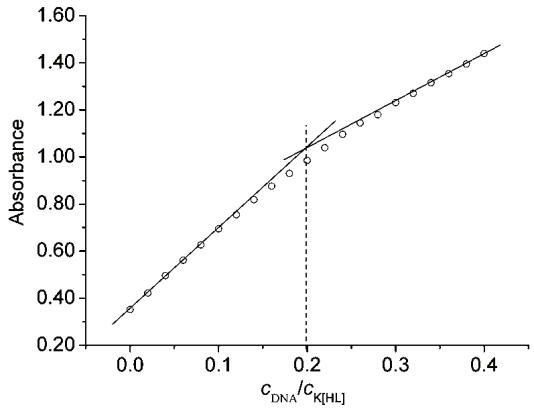

Fig. 2. Mole ratio plots of K[HL]–DNA in tris-HCl buffer (pH 7.40); c(K[HL]) = = 1.00×10^{-5} mol L^{-1}; c(DNA) = = 6.00×10^{-5} mol L^{-1}, λ = 213 nm.

Double reciprocal method

In order to determine the interaction between K[HL] and DNA, the binding constant was determined. The absorption relationship between the complex and DNA was expressed by the double reciprocal equation:[16–18]

$$1/(A_0 - A) = 1/A_0 + 1/(KA_0c_{DNA}) \quad (1)$$

where A_0 and A are the absorbances of K[HL] in the absence and in the presence of DNA, respectively. K is the binding constant between K[HL] and DNA and c_{DNA} is the concentration of DNA.

The double reciprocal plots of $1/(A_0 - A)$ *versus* $1/c_{DNA}$ were linear at 28 °C and 37 °C and the binding constants were calculated from the ratio of the intercept on the vertical (Fig. 3): $K_B^{\ominus}$(301 K) = 1.94×10^5 L mol^{-1}, $K_B^{\ominus}$(310 K) = = 1.09×10^5 L mol^{-1}. The above observed values are smaller than those of classical intercalators (ethidium–DNA,[19] 7×10^7 L mol^{-1}; proflavin–DNA,[20] 4.1×10^5 L mol^{-1}).

To obtain a detailed view of the interaction, the approach of parsing the free energy into component terms is a powerful and insightful method. The enthalpy change (ΔH) is considered as 0 for a small change of temperature.[21] The standard molar reaction enthalpy ($\Delta_r H_m^{\ominus}$), $K^{\ominus}$ and T are estimated from the following relationship:

$$\ln K_2^{\ominus}/K_1^{\ominus} = -\Delta_r H_m^{\ominus} (1/T_2 - 1/T_1)/R \quad (2)$$

where $K_1^{\ominus}$ and $K_2^{\ominus}$ are the standard binding constant of K[HL] and DNA at 28 and 37 °C, respectively, T_1 is 301.15 K, T_2 is 310.15 K. $\Delta_r H_m^{\ominus}$ is the standard molar reaction enthalpy. Then $\Delta_r H_m^{\ominus}$ is –49.7 kJ mol^{-1}. This result shows that the binding of K[HL] to DNA is exothermic.

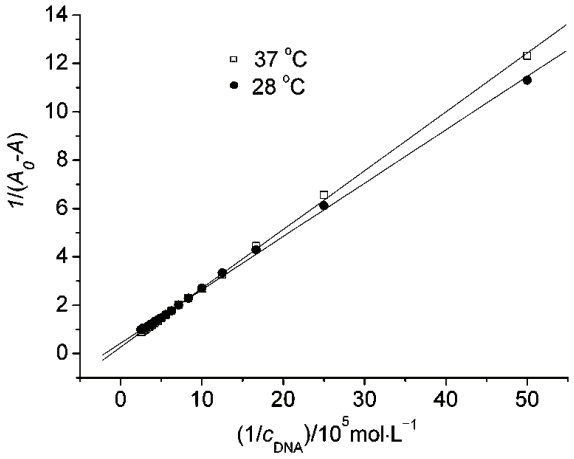

Fig. 3. Double reciprocal plots of K[HL]–DNA in tris-HCl buffer (pH 7.40) at 28 and 37 °C; c(K[HL]) = 1.00×10^{-5} mol L^{-1}.

The standard molar reaction Gibbs free energy ($\Delta_r G_m^{\ominus}$) and the standard molar reaction entropy ($\Delta_r S_m^{\ominus}$) are estimated from the following relationships:

$$\Delta_r G_m^{\ominus} = \Delta_r H_m^{\ominus} - T\Delta_r S_m^{\ominus} \quad (3)$$

$$\Delta_r G_m^{\ominus} = -RT \ln K^{\ominus} \quad (4)$$

where T is 301.15 K; $K^{\ominus}$ is the standard binding constant of K[HL] and DNA at 28 °C. $\Delta_r G_m^{\ominus}$ is –30.5 kJ mol^{-1} and $\Delta_r S_m^{\ominus}$ is –63.8 J mol^{-1} K^{-1}. The negative Gibbs free energy value indicates that the reaction between K[HL] and DNA is possible. The negative entropy value indicates that the degree of freedom of K[HL] is decreased after the binding, and that the DNA conformational freedom is also reduced upon K[HL]–DNA binding. It is obvious that the process of interaction of K[HL] and DNA is energetically highly favorable at room temperature and the binding reaction is driven mainly by enthalpy.[22]

Fluorescence measurements using Acridine Orange as a probe

Fluorescence is very useful method to investigate the interaction between small molecules and DNA. The fluorescence of DNA is weak, hence the utilization of fluorescence probes enables the study of interaction between small molecules and DNA. Acridine orange (AO) is a kind of cationic dye. Due to its planar aromatic chromophore, it can insert between two adjacent base pairs in a DNA helix.

The emission spectra of K[HL] bound to DNA in the absence and the presence of AO are given in Fig. 4. There was a significant increase in the fluorescence intensity and a red shift in the emission wavelength from 527 to 533 nm as a result of AO insertion between the base pairs of DNA.

If K[HL] has the same binding mode with DNA as AO, there will be competition between AO and the complex with DNA. Hence, the fluorescence spectrum will be changed.[23] The emission spectra of AO bound to DNA in the absence and the presence of K[HL] are given in Fig. 5. It could be seen that the fluorescence intensity of DNA–AO was efficiently quenched. This phenomenon suggested that K[HL] substituted for AO in the DNA–AO system, which led to a large decrease in the emission intensity of the DNA–AO system.

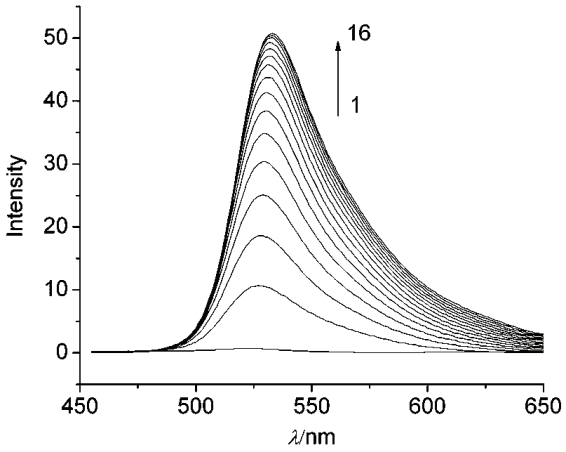

Fig. 4. Emission spectra of K[HL]–DNA in different concentrations of AO (pH 7.40; λ_{ex} = 411.7 nm); from curve 1–16, c_{DNA} = 2.00×10^{-5} mol L^{-1}, c_{AO} = 0.00, 0.02, 0.04, 0.06, 0.08, 0.10, 0.12, 0.14, 0.16, 0.18, 0.20, 0.22, 0.24, 0.26, 0.28, and 0.30×10^{-4} mol L^{-1}, respectively.

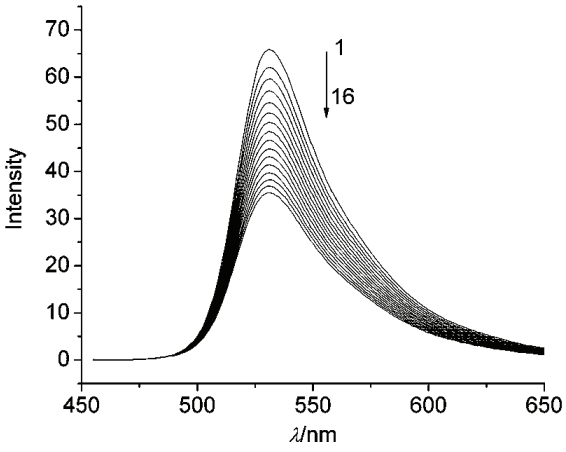

Fig. 5. Emission spectra of DNA–AO in different concentrations of K[HL] (pH 7.40; λ_{ex} = 411.7 nm); from curve 1–16, c_{DNA-AO} = = 2.00×10^{-5} mol·L^{-1}, $c_{K[HL]}$ = 0.00, 0.01, 0.02, 0.03, 0.04, 0.05, 0.06, 0.07, 0.08, 0.09, 0.10, 0.11, 0.12, 0.13, 0.14 and 0.15×10^{-3} mol L^{-1}, respectively.

From the changes in the emission spectra of Figs. 4 and 5, it can be seen that the competition between AO and K[HL] for DNA was remarkable. As the inter-

action between AO and DNA is intercalation, then the presence of intercalation between K[HL] and DNA is basically confirmed.[24]

Scatchard method

The binding mode between small molecules with DNA can be determined using the Scatchard procedure.[25] The Scatchard Equation expresses the binding of DNA–AO in the presence of K[HL].

$$r_{AO}/c_{AO} = K(n - r_{AO}) \quad (5)$$

where r_{AO} is moles of AO bound per mole of DNA, c_{AO} is the molar concentration of free AO, n is binding site multiplicity per class of binding sites and K is the association binding constant of AO with DNA. Generally, if K[HL] interacts with DNA by the intercalation mode, the value of n remains constant and that of K changes in the Scatchard plot. If K[HL] interacts with DNA by a non-intercalation binding mode involving groove binding or electrostatic interaction, the value of K remains constant and that of n changes in the Scatchard plot. If K[HL] interacts with DNA by a mix binding mode containing non-intercalation and intercalation modes, the values of both n and K change in the Scatchard plot.[26]

Different concentrations of K[HL] ($R_t = c_{K[HL]}/c_{DNA}$ = 0.00, 0.15, 0.30 and 0.45) were used. In order to investigate the effects of electrostatic binding on the interaction between K[HL] and DNA, two groups of experiments with and without the addition of NaCl as a contrast were performed. The influence of NaCl, which is not an anionic quencher of DNA, on K[HL]–AO–DNA comes only from ionic strength.[27] From the Scatchard plots, the values of K and n were obtained. The results are shown in Table I.

TABLE I. Data from the Scatchard Equation for the interaction between K[HL] and DNA

Curve	R_t	NaCl, mass%	Scatchard	K / L mol^{-1}	n
a	0.00	5.00	3.86×10^5–$1.81\times10^7 r_{AO}$	1.81×10^7	0.0212
		0	5.12×10^5–$3.42\times10^7 r_{AO}$	3.42×10^7	0.0145
b	0.15	5.00	5.47×10^5–$2.67\times10^7 r_{AO}$	2.67×10^7	0.0215
		0	3.91×10^5–$2.64\times10^7 r_{AO}$	2.64×10^7	0.0148
c	0.30	5.00	7.55×10^5–$2.60\times10^7 r_{AO}$	2.60×10^7	0.0290
		0	4.30×10^5–$2.43\times10^7 r_{AO}$	2.43×10^7	0.0176
d	0.45	5.00	5.48×10^5–$1.75\times10^7 r_{AO}$	1.75×10^7	0.0303
		0	3.97×10^5–$2.23\times10^7 r_{AO}$	2.23×10^7	0.0178

As can be seen from Table I, the values of both n and K changed with the different concentrations of K[HL]. The variation of the parameters n and K suggested a mixed interaction between K[HL] and DNA. Generally, if n is reduced in the presence of NaCl, electrostatic interaction are indicated,[28] but if n is increased, the existence of groove interactions in the K[HL]–DNA system is indicated. Thus, the results suggest the presence of intercalation and groove binding of K[HL] to DNA.

Viscosity method

In the absence of crystallographic structural data, hydrodynamic measurements, being sensitive to length change, are regarded as the most critical tests for a binding model in solution.[29] To further clarify the interaction between K[HL] and DNA, viscosity measurements were performed.

A classical intercalation mode is known to cause a significant increase in the viscosity of a DNA solution, as the presence of an intercalator forces the effected base-pairs away from each other, thereby causing unwinding the double helix and the lengthening by a given amount of DNA. In contrast, a partial intercalation mode could bend (or kink) the DNA helix and reduce its effective length and, concomitantly, its viscosity. Non-intercalation binding causes no obvious increase in DNA viscosity.[29,30]

The values of the relative specific viscosity $(\eta/\eta_0)^{1/3}$ (where η_0 and η are the specific viscosity contributions of DNA in the absence and in the presence of the K[HL], respectively) were plotted against $c_{K[HL]}$ (Fig. 6). In this study, the relative viscosity of the DNA increased slightly with increasing amounts of the K[HL], but the increase was not as pronounced as those observed for the classical intercalator ethidium bromide.[31] This might be due to the lengthening of the DNA double helix resulting from partial intercalation. This conclusion is in agreement with the other above-mentioned studies.

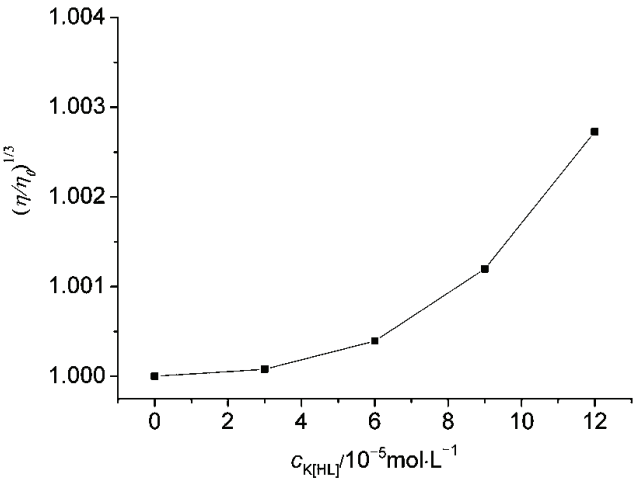

Fig. 6. Effect of increasing amounts of K[HL] on the relative viscosities of DNA at 25 °C; c_{DNA} = = 1.00×10^{-4} mol L^{-1}.

CONCLUSIONS

The Schiff base (K[HL]) derived from vanillin and L-tryptophan was synthesized. The interaction of the Schiff base with hsDNA was studied by UV–Vis absorption, fluorescence and viscosity methods. The obtained results suggest the presence of intercalation and groove binding between K[HL] and DNA. The

internal molecular structure of L-tryptophan, which contains an aromatic indole ring plane, enables K[HL] to insert into the DNA molecule. The information obtained from this work could be helpful to the understanding of the mechanism of the interaction of small molecules with nucleic acids, and should be useful in the development of potential probes of DNA structure and conformation.

Acknowledgments. This work was supported by National Natural Science Foundation of China (No. 30572254) and the Postgraduate Innovation Foundation of the Southwest University of Science and Technology. We are grateful for the instrumental support of the Analytical and Testing Center of the Southwest University of Science and Technology.

И З В О Д

ИНТЕРАКЦИЈА ИЗМЕЂУ ТРИПТОФАН–ВАНИЛИН ШИФОВЕ БАЗЕ И ДНК ИЗ СПЕРМЕ ХАРИНГЕ

YAN ZHANG[1], XINGMING WANG[1] и LISHENG DING[2]

[1]*Department of Chemistry, School of Materials Science and Engineering, Southwest University of Science and Technology, Mianyang 621010 и* [2]*Chengdu Institute of Biology, Chinese Academy of Sciences, Chengdu 610041, P. R. China*

Интеракција Шифове базе (K[HL]) са ДНК из сперме харинге је проучавана одређивањем UV–Vis апсорпције, флуоресценције и вискозитета у физиолошким условима pH (pH 7,40). Шифова база је синтетисана од ванилина и L-триптофана. Молекули су реаговали у односу $n_{K[HL]}$:n_{DNA} = 5:1. Измерени молски апсорпциони коефицијент, $\varepsilon_{K[HL]\text{-}DNA}$ = 4,98×10^5 L mol^{-1} cm^{-1}, је потврђен методом молских односа. Константе везивања, $K_B^{\ominus}$(301 K) = 1,94×10^5 L mol^{-1} и $K_B^{\ominus}$(310 K) =1,09×10^5 L mol^{-1}, су добијене двоструком реципрочном методом. Термодинамичка мерења указују да је интеракција између K[HL] и ДНК зависна од енталпије. У комбинацији са Скачардовом методом и методом мерења вискозитета, резултати указују на везивање интеркалацијом и преко бразде између K[HL] за DNA.

(Примљено 28. јануара, ревидирано 31. марта 2010)

REFERENCES

1. V. G. Vaidyanathan, T. Weyhermuller, B. U. Nair, J. Subramanian, *J. Inorg. Biochem.* **99** (2005) 2248
2. Y. M. Song, Q. Wu, P. J. Yang, N. N. Luan, L. F. Wang, Y. M. Liu, *J. Inorg. Biochem.* **100** (2006) 1685
3. L. Strekowski, B. Wilson, *Mutat. Res.* **623** (2007) 3
4. H. Schiff, *Ann. Chem. Pharm. Suppl.* **3** (1864) 343
5. R. L. Dutta, B. R. Das, *J. Sci. Ind. Res.* **47** (1988) 547
6. P. G. Cozzi, *Chem. Soc. Rev.* **33** (2004) 410
7. X. L. Xi, Z. C. Li, *Amino Acids Biotic Res.* **20** (1998) 40
8. X. Q. Zhang, Y. He, M. Ding, *J. Chromatogr., B* **877** (2009) 1678
9. W. Y. Zhong, J. S. Yu, W. L. Huang, K. Y. Ni, Y. Q. Liang, *Biopolymers* **62** (2001) 315
10. M. Sivasankaran Nair, R. Selwin Joseyphus, *Spectrochim. Acta A* **70** (2008) 749
11. K. Nakamoto, *Infrared and Raman Spectra of Inorganic and Coordination Compounds*, 3rd ed., Wiley, New York, 1986
12. A. M. Pyle, R. J. Rehmann, R. Meshoyrer, C. V. Kumar, N. J. Turro, J. K. Barton, *J. Am. Chem. Soc.* **111** (1989) 3051

13. Mudasir, K. Wijaya, E. T. Wahyuni, H. Inoue, N. Yoshioka, *Spectrochim. Acta A* **66** (2007) 163
14. Y. Zhang, X. M. Wang, D. Fei, N. Zhao, T. T. Zhao, H. F. Zhu, L. S. Ding, *Chin. Optics Lett.* **8** (2010) 236
15. J. H. Yoe, A. L. Joens, *Ind. Eng. Chem. (Anal. Ed.)* **16** (1944) 111
16. G. Z. Chen, X. Z. Huang, J. G. Xu, Z. Z. Zheng, Z. B. Wang, *Analytical Method of Fluorescence*, Science Publisher, Beijing, 1990 (in Chinese)
17. A. A. Ouameur, R. Marty, H. A. Tajmir-Riahi, *Biopolymers* **77** (2005) 129
18. H. M. Berman, P. R. Young, *Annu. Rev. Biophys. Bioeng.* **10** (1981) 87
19. M. J. Waring, *J. Mol. Biol.* **13** (1965) 269
20. Y. Baba, C. L. Beathy, A. Kagemato, C. Gebelien, *Biological Activity of Polymers, ACS Symposium Series, 186*, American Chemical Society, Washington, DC, 1962, Chapter 14, pp. 177–189
21. Y. T. Sun, S. Y. Bi, D. Q. Song, C. Y. Qiao, D. Mu, H. Q. Zhang, *Sens. Actuators, B* **22** (2008) 799
22. Y. J. Liu, C. H. Zeng, *Transition Met. Chem.* **34** (2009) 455
23. N. Shahabadi, S. Kashanian, M. Purfoulad, *Spectrochim. Acta A* **72** (2009) 7571
24. B. W. Jing, M. H. Zhang, T. Shen, *Spectrochim. Acta A* **60** (2004) 2635
25. W. R. Ware, *J. Phys. Chem.* **66** (1962) 455
26. G. Scatchard, *Ann. N. Y. Acad. Sci.* **51** (1949) 660
27. L .Jin, P. Yang, Q. S. Li, *Chem. J. Chin. Uni.* **17** (1996) 1345
28. S. Tabassum, S. Parveen, F. Arjmand, *Acta Biomater.* **1** (2005) 677
29. S. Satyanarayana, J. C. Dabrowiak, J. B. Chaires, *Biochemistry* **31** (1992) 9319
30. S. Satyanarayana, J. C. Dabrowiak, J. B. Chaires, *Biochemistry* **32** (1993) 2573
31. V. G. Vaidyanathan, B. U. Nair, *J. Inorg. Biochem.* **94** (2003) 121.

Journal of the Serbian Chemical Society
JSCS-info@shd.org.rs • www.shd.org.rs/JSCS
J. Serb. Chem. Soc. 75 (9) 1203–1208 (2010)
JSCS–4043
UDC 547.233'447+541.64+
678.684:615.281–188
Short communication

SHORT COMMUNICATION

Molecular weight dependent antistaphylococcal activities of oligomers/polymers synthesized from 3-aminopyridine

CAHIT AKGUL* and MEHMET YILDIRIM

Department of Chemistry, Faculty of Sciences and Arts, Canakkale Onsekiz Mart University, Terzioglu Campus, Canakkale, Turkey

(Received 1 February, revised 23 March 2010)

Abstract: The main aim of this study was to investigate the relationship between molecular weight and the antistaphylococcal activity of oligomers/polymers synthesized from 3-aminopyridine. Different oligomers/polymers were synthesized from 3-aminopyridine by changing the oxidative polycondensation reaction conditions. They were characterized by size exclusion chromatography and their antibacterial activities were compared by employing standardized susceptibility assays. The obtained experimental results demonstrated that 3-aminopyridine had no antistaphylococcal activity. However, as a result of polymerization, strong antistaphylococcal activity was obtained. Oligomers/polymers synthesized from 3-aminopyridine had varying degrees of antistaphylococcal activity and the maximum activity was obtained from relatively very short oligomers. It was therefore concluded that polymerization of 3-aminopyridine is required for antistaphylococcal activity and strength of this activity depends on the molecular weights of the synthesized molecules.

Keywords: antibacterial; 3-aminopyridine; oligomer; *Staphylococcus aureus*.

INTRODUCTION

Staphylococcus aureus is one of the bacterial strains that can cause serious infections. Whilst several antibiotics, including penicillin, methicillin and vancomycin, have been successfully employed to eradicate *S. aureus* infections, bacterial resistance against common antibiotics has increased dramatically over the past few decades.[1] Thus, the need for the discovery and development of novel antibacterial agents is of paramount importance. The basic mechanisms of antibacterial action include inhibition of cell wall synthesis, inhibition of protein synthesis, alteration of the cell membrane, inhibition of nucleic acid synthesis and antimetabolite activity.[2] Bacterial cell wall and membrane structures are the

* Corresponding author. E-mail: cahitakgul@yahoo.com
doi: 10.2298/JSC100201104A

main targets of several commercial antibiotics.[3] However, intracellular bacterial components also carry the potential to be promising targets for antimicrobial compounds.[4] The search for novel antibacterial agents and new targets for antimicrobial agents will undoubtedly continue to be among the priorities of researchers in the future.

Synthetic polymeric materials have been widely utilized for multiple purposes, including the exploitation of their *in vivo* and *in vitro* antimicrobial activities.[5,6] Since many properties of polymers are dependent on their molecular weight, it is reasonable to think that their antibacterial activities can also be molecular weight dependent.[7] In a previous study, it was shown that oligo-3-aminopyridine has strong antibacterial activity against gram positive bacterial species.[8] This observation led to the notion that the bioactivity might be molecular weight dependent. Thus, in this study, novel oligomers/polymers were prepared from 3--aminopyridine by changing oxidative polycondensation reaction conditions and their molecular weights determined using chromatographic techniques. Then, the antibacterial activities of these monomers/oligomers/polymers were comparatively analyzed to determine whether the bioactivity was molecular weight dependent.

EXPERIMENTAL

Materials

Blank, gentamicin and vancomycin discs were obtained from Oxoid Ltd. (Basingstoke, UK) Mueller–Hinton broth, Mueller–Hinton agar (MHA), 3-aminopyridine, KOH and CH_3COOH were supplied by Merck KGaA (Darmstadt, Germany) and were used as received. The dimethylformamide (DMF–HPLC grade) used for the size exclusion chromatography was from Merck. A 30 % aqueous solution of sodium hypochlorite (NaOCl) was supplied by Paksoy Chemical Co. (Turkey).

Bacterial strains

Gram-positive *S. aureus* (ATCC 25923) from the Refik Saydam National Public Health Agency, Ankara, Turkey, was used as a representative strain.

Synthesis of oligomers/polymers from 3-aminopyridine

3-Aminopyridine (AP) was converted into its oligomer/polymer derivatives (OAP) through oxidative polycondensation (OP) reactions in an aqueous alkaline or acid medium using NaOCl (30 %) as the oxidant, as described in the literature (Scheme 1).[9] The polymerizations were performed in 250 mL three-necked round-bottom flasks which were fitted with a condenser, thermometer and magnetic stirrer. Alkaline and acid media were realized using aqueous solutions of KOH and CH_3COOH, respectively. The polymerizations performed in acid medium were terminated *via* neutralization by the addition of 1 M aqueous KOH solution and the oligomers/polymers were precipitated. In addition, OAP-1, which was synthesized in alkaline medium, was precipitated in the reaction medium without neutralization. The oligomer/polymer syntheses were performed under different reaction conditions to obtain compounds of various molecular weights (Table I).

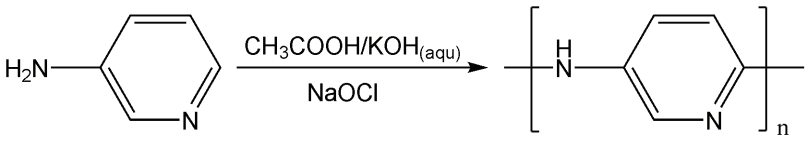

Scheme 1. Oxidative polycondensation reaction of 3-aminopyridine.

TABLE I. Experimental conditions of the oxidative polymerization reactions and the results of the size exclusion chromatography (SEC) of the oligomers and polymers synthesized from 3-aminopyridine (monomer and oxidant concentrations used in the experiments: $[AP]_0$ = = 0.266 mol L^{-1} and $[NaOCl]_0$ = 0.120 mol L^{-1})

Compound	*t* / °C	Time, h	Media	M_n	M_w	*PDI*	Yield, %
OAP-1	25	1	alkaline[a]	700	1950	2.79	69
OAP-2	25	1	acid[b]	1450	2500	1.72	65
OAP-3	90	1	acid	37000	59350	1.60	54
OAP-4	25	5	acid	16400	18500	1.13	59

[a]($[KOH]_0$ = 0.0625 mol L^{-1}; [b]$[CH_3COOH]_0$ = 1.131 mol L^{-1}

Molecular weight determination of the oligomers/polymers

The number average molecular weight (M_n), weight average molecular weight (M_w) and polydispersity index (*PDI*) were determined by the size exclusion chromatography (SEC) technique (Shimadzu) at 25 °C. For the SEC investigations, an SGX (100 Å and 7 nm diameter loading material) 3.3 mm i.d.×300 mm column was used; eluent: DMF (0.4 mL min^{-1}), polystyrene standards were used for calibration. A refractive index detector (RID) was used to analyze the products.

Antibacterial susceptibility testing using disc diffusion assay

The oligomers/polymers synthesized from 3-aminopyridine were dissolved in DMSO to obtain a concentration of 100 μg per 20 μL and 100 μg per disc were used in the disc diffusion assay.[10] Briefly, the microorganisms were grown on MHA plates and then 3 mL of MHB was inoculated with 3 well separated colonies for each strain. After incubation at 37 °C, the concentrations of suspensions were adjusted to 10^8 cells mL^{-1}. Each bacterial suspension was spread over the surface of the MHA using sterile cotton swabs. 100 μg per 20 μL of the chemicals were pipetted onto filter paper disks (6 mm in diameter). The discs were then placed onto the inoculated agar surface. After keeping at room temperature for ≈30 min, the plates were incubated at 37 °C for 20 h. Discs containing gentamicin (10 μg) and vancomycin (30 μg) were included as the positive controls and DMSO-only (20 μL) the negative control. The results are expressed as the diameter of inhibition zones and the presented values are the average of three separate experiments.

*Determination of the minimum inhibitory concentration (*MIC*)*

The broth macrodilution assay was performed, as recommended by NCCLS, to determine the minimum inhibitory concentration (*MIC*).[11] Bacterial strains were cultured overnight at 37 °C and suspended in MHB to obtain a final inoculum density of 10^6 cells mL^{-1} and 0.5 mL of this suspension was added to 0.5 mL of susceptibility test broth containing serial 2-fold dilutions of the chemicals. Two tubes were also included to check the sterility of the media. All the tubes were incubated at 37 °C for 20 h. The *MIC* was considered as the lowest concentration at which the chemical prevented visible bacterial growth.

RESULTS AND DISCUSSION

It was demonstrated in this study that the average molecular weights of the synthesized oligomers depended on the employed reaction conditions. These observations were similar to those of previous studies reporting that many factors, such as temperature, reaction time, initial concentration of monomer, acidic or basic medium and the oxidant type, can affect the yields of oxidative polymerization reactions.[12] The polymerization conditions and the size exclusion chromatography (SEC) results calculated from the chromatograms are given in Table I, from which it can be seen that oligomers with different molecular weights were obtained in the four different sets of employed reaction conditions. These values clearly show that when the alkaline medium was used, the average molecular weight of the OAP was relatively low (see Table I, OAP-1). However, when the acid medium was used under the same conditions, such as monomer and oxidant concentrations, temperature, and the reaction time, the average molecular weight was clearly higher. When the temperature was increased from 25 to 90 °C, with the other conditions being constant, the number average molecular weight (M_n) and weight average molecular weight (M_w) values increased from 1450 and 2500 to 37000 and 59350 g mol^{-1}, respectively (see Table I, OAP-2 and OAP-3). However, when the temperature and other conditions were constant but the reaction time was increased from one to five hours, the M_n and M_w values increased from 1450 and 2500 to 16400 and 18500 g mol^{-1}, respectively (see Table I, OAP-2 and OAP-4). All other reaction conditions are summarized in Table I.

The antibacterial activities of the synthesized oligomers/polymers were assessed using the standard disc diffusion assay and broth macrodilution assay. The results of these assays are summarized in Table II. Neither 3-aminopyridine (AP) monomer itself nor its relatively longer oligomers or polymers showed any antibacterial activity against *S. aureus*. In a previous study, a smaller oligomer of 3--aminopyridine (OAP) was synthesized, characterized and the M_n, M_w and polydispersity index (*PDI*) values were found to be 250 and 800 g mol^{-1} and 3.20, respectively.[9] When 50 μg of this OAP was used, the inhibition zone was 17 mm in the disc diffusion assay and the *MIC* was found to be 25 μg mL^{-1} in broth macrodilution assay.[8] These values for this oligomer were included in Table II just for comparison. No inhibition of bacterial growth was observed in cultures containing 3-AP, OAP-2, OAP-3, OAP-4 at concentrations of up to 1 mg mL^{-1} (Table II). When all these molecular weight values of the previous and the current study and the corresponding antibacterial activities of the oligomers/polymers are considered, it can easily be seen that the maximum antibacterial activity was obtained with relatively very short oligomers synthesized from 3-aminopyridine. It can imply that short oligomers of 3-aminopyridine can easily diffuse into bacterial cells and show their antibacterial activities inside the cell. On the contrary, since relatively longer oligomers and polymers of 3-aminopyridine

cannot cross the cell wall and/or cell membrane structures of bacterial cells, they cannot inhibit bacterial growth under similar growth conditions. The requirement of polymerization of 3-aminopyridine for this antistaphylococcal activity could entail that its oligomers can mimic some intracellular components. However, the exact inhibitory mechanism remains to be elucidated and requires much more detailed investigations.

TABLE II. Antibacterial activities of oligomers/polymers synthesized from 3-aminopyridine

Compound	Diameter of inhibition zone[a], mm	*MIC* / μg mL^{-1}
3-AP	NI	–[b]
OAP	17	25
OAP-1	13	100
OAP-2	NI	–
OAP-3	NI	–
OAP-4	NI	–
Gentamicin (10 μg)	19	
Vancomycin (30 μg)	17	
DMSO (20 μL)	NI	

[a]Includes the diameter of the disc (6 mm) and 100 μg disc was used for each compound. Values are average of three separate experiments. NI: No zone of inhibition was observed; [b]no inhibition of bacterial growth with concentrations up to 1 mg mL^{-1}

CONCLUSIONS

From all these experimental results, it can be concluded that polymerization is required for 3-aminopyridine to possess antistaphylococcal activity. The antibacterial activity of the oligomers/polymers synthesized from 3-aminopyridine are molecular weight dependent and the maximum antibacterial activity was supplied by relatively, very short oligomers. In addition, the molecular structures and properties of short oligomers can be thought essential for antibacterial activity to be exhibited, since 3-aminopyridine monomer itself has no inhibitory effect on bacterial growth.

Acknowledgements. The authors thank Dilek Bahceci for technical assistance in the SEC analyses. Funding: COMU Scientific Research Projects Commission (Project No.: 2008/75)

И З В О Д

ЗАВИСНОСТ АНТИСТАФИЛОКОКНЕ АКТИВНОСТИ ОЛИГОМЕРА И ПОЛИМЕРА СИНТЕТИСАНИХ ОД 3-АМИНОПИРИДИНА ОД ЊИХОВЕ МОЛЕКУЛСКЕ ТЕЖИНЕ

CAHIT AKGUL и MEHMET YILDIRIM

Department of Chemistry, Faculty of Sciences and Arts, Canakkale Onsekiz Mart University, Terzioglu Campus, Canakkale, Turkey

Циљ ове студије је био да испита везу између молекулске тежине и антистафилококне активности олигомера и полимера синтетисаних од 3-аминопиридина. Различити олигомери и полимери су синтетисани од 3-аминопиридина променом услова реакције оксидативне поликондензације. Окарактерисани су гел хроматографијом, а антибактеријске активности су

упоређиване стандардним тестовима. Експериментални резултати су показали да 3-аминопиридин нема антистафилококну активност. Са друге стране, полимеризацијом се стиче јака активност. Олигомери и полимери су имали различиту активност и најјачу су испољили релативно кратки олигомери. Закључено је да је полимеризација 3-аминопиридина неопходна за постизање антистафилококне активности и да та активност зависи од молекулске тежине синтетисаних молекула.

(Примљено 1. фебруара, ревидирано 23. марта 2010)

REFERENCES

1. M. Michel, L. Gutmann, *Lancet* **349** (1997) 1901
2. D. Greenwood, R. J. Whitley, In *Antibiotic and Chemotherapy*, 8th ed., R. G. Finch, D. Greenwood, S. R. Norrby, R, Whitley, Eds., Churchill Livingstone, Edinburgh, 2003, p. 1000
3. O. Aguilera, H. Ostolaza, L. M. Quiros, J. F. Fierro, *FEBS Lett.* **462** (1999) 273
4. M. Cudic, L. Otvos, *Curr. Drug Targets* **3** (2002) 101
5. G. N. Tew, D. Liu, B. Chen, R. J. Doerksen, J. Kaplan, P. J. Carroll, M. L. Klein, W. F. De Grado, *Proc. Natl. Acad. Sci. USA* **99** (2002) 5110
6. G. L. Woo, M. W. Mittelman, J. P. Santerre, *Biomaterials* **21** (2000) 1235
7. H. K. No, N. C. Y. Park, S. H. Lee, S. P. Meyers, *Int. J. Food Microbiol*. **74** (2002) 65
8. C. Akgul, I. Kaya, *Indian J. Biochem. Biophys.* **41** (2004) 120
9. I. Kaya, R. Gulel, *Int. J. Polym. Anal. Charact.* **10** (2005) 109
10. *Performance standards for antimicrobial disk susceptibility tests*, M2-A6, NCCLS – National Committee for Clinical Laboratory Standards Villanova, PA, 1997
11. *Methods for Dilution Antimicrobial Susceptibility Tests for Bacteria that Grow Aerobically*, M7-A5, NCCLS - National Committee for Clinical Laboratory Standards Villanova, PA, 2000
12. I. Kaya, M. Yildirim, *Eur. Polym. J.* **43** (2007) 127.

Journal of the Serbian Chemical Society
JSCS-info@shd.org.rs • www.shd.org.rs/JSCS
J. Serb. Chem. Soc. *75* (9) 1209–1218 (2010)
JSCS–4044
UDC 546.472–38:548.7:54–77+543
Original scientific paper

Synthesis and crystal structure of 1,2,3,4-tetrahydro-9--aminoacridine tetrachlorozincate(II) monohydrate

DJENANA U. MIODRAGOVIĆ[1#], DRAGOLJUB JOVANOVIĆ[2], GORAN A. BOGDANOVIĆ[3], DRAGANA MITIĆ[1#] and KATARINA ANDJELKOVIĆ[1*#]

[1]Faculty of Chemistry, University of Belgrade, P.O. Box 158, 11001 Belgrade, [2] Department of Nutrition and Botany, Faculty of Veterinary Medicine, University of Belgrade, Bulevar oslobodjenja 18, Belgrade and [3]Institute Vinča, Laboratory of Theoretical Physics and Condensed Matter Physics, P.O. Box 522, 11001 Belgrade, Serbia

(Received 2 March, revised 26 April 2010)

Abstract: In the reaction of $ZnCl_2$ with tacrine hydrochloride in water novel tetracoordinated $(C_{13}H_{15}N_2)_2[ZnCl_4]\cdot H_2O$ complex was obtained and characterized by elemental analysis, molar conductivity and X-ray analysis. The complex crystallizes in the space group $P\bar{1}$ of the triclinic crystal system. The structure contains two crystallographically different molecules of protonated tacrine present as counter cations, the $[ZnCl_4]^{2-}$ complex anion and one water solvent molecule. The counter cations slightly differ in the puckering of the cyclohexene ring. The molecules of protonated tacrine are involved in different intermolecular hydrogen bonds. In the crystal, the hydrogen bonding generates a 3D assembly. In the crystal, π···π stacking interactions between the rings of protonated tacrine were evidenced. The $[ZnCl_4]^{2-}$ complex anion has a distorted tetrahedral geometry. Three out of the four Cl atoms are involved in intermolecular hydrogen bonding. The intermolecular H-bond interactions involving the Cl atoms affect the Zn–Cl bond lengths.

Keywords: Zinc; tacrine; X-ray analysis.

INTRODUCTION

Alzheimer's disease (AD) is a late-onset and the most common form of dementia affecting one in ten people over the age of 65 and one out of every two people over the age of 80. Symptoms include memory loss, anxiety, aggression, delusion, disorientation and loss of intellectual facilities, including cognition and eventually loss of physiological functions due to the advancing dementia.[1] Both genetic and environmental factors are implicated in its development.[2]

* Corresponding author. E-mail: kka@chem.bg.ac.rs
# Serbian Chemical Society member.
doi: 10.2298/JSC100302059M

The major hypothesis as to the cause of AD relates to the deposition in the brain of a peptide termed β-amyloid (Aβ).[1] β-Amyloid fragments can polymerize to form what are referred to as "plaques".[3]

It is well known that the brain contains large amounts of metals (Cu(II), Zn(II) and Fe(III)).[4] High levels of zinc, copper and iron are constitutively found in the neocortical regions which are most prone to AD pathology.[2] Although Zn(II), Cu(II) and Fe(III) play important roles in cortical physiology, only Cu(II) and Zn(II) are released during neurotransmission.[4,5] These metal ions interact with the amyloid precursor protein (APP) and Aβ.[6–8] Recently, research of copper/zinc chelators as inhibitors of Aβ accumulation was initiated.[9,10]

It is well known that many neurotransmitter systems are implicated in the etiology of AD; a cholinergic deficit having been clearly established. In addition, there is a decrease of choline acetyltransferase activity.[2] In the last two decades, various cholinergic drugs, primarily inhibitors of the enzyme acetylcholinesterase, such as tacrine, donepezil, rivastigmin and galantamin, are used in the medical treatment of AD patients.[11,12] Tacrine is a drug that is used to treat the symptoms of mild to moderate Alzheimer's disease. The drug retards the breakdown of acetylcholine; hence, it can build up and have a greater effect. It can improve thinking ability in some patients with AD. Bearing in mind that tacrine (Scheme 1) is widely used in the treatment of AD and that zinc is related to AD, it was considered interesting to investigate the possibilities of coordination of tacrine with Zn(II).

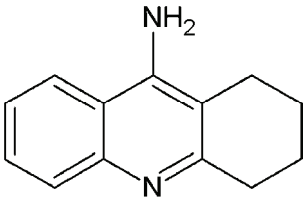

Scheme 1. Structure of tacrine.

EXPERIMENTAL

*Synthesis of $(C_{13}H_{15}N_2)_2[ZnCl_4]\cdot H_2O$ (**1**)*

A solution of 0.068 g (0.50 mmol) $ZnCl_2$ in 5 cm^3 of water was added to a suspension of 0.234 g (1.0 mmol) tacrine hydrochloride ($C_{13}H_{14}N_2\cdot HCl$) in 15 cm^3 acetonitrile–water (9:1). The mixture was refluxed for 2.5 h (60 °C). The resulting solution was cooled to room temperature and after 16 h, a white microcrystalline product was obtained.

*Synthesis of $C_{13}H_{14}N_2\cdot 2H_2O$ (**2**)*

An analogous reaction was performed using $Na_2[Zn(OH)_4]$ and tacrine hydrochloride whereby tacrine dihydrate was obtained. Yield: 40%.

Physical measurements

Elemental analyses were performed using an Elemental Vario EL III microanalyser. The molar conductivity of an aqueous solution of the complex (1.0×10^{-3} mol dm^{-3}) was measured at room temperature on a Jenway-4009 digital conductivity meter.

X-Ray analysis

The single crystal X-ray data for compound **1** were collected on an Enraf-Nonius CAD-4 diffractometer[13] using Mo $K\alpha$ radiation (λ = 0.71073 Å) and $\omega/2\theta$ scans in the 1.74 to 26.00° θ range. The cell constants and an orientation matrix for data collection, obtained from 24 centered reflections in the θ range 12.01 to 15.81° corresponded to a triclinic cell. The data were corrected for Lorentz and polarization effects.[14] The crystal structure was solved by direct methods[15] and difference Fourier methods, and refined on F^2 by the full-matrix least--square method.[16] All six hydrogen atoms bonded to nitrogen atoms (N1a, N1b, N2a and N2b) as well as the two H atoms from the water molecule were taken from the ΔF map and refined isotropically. This treatment of H atoms resulted in unrealistically short X–H distances for some of the X–H (X = O,N) bonds. Due to this, all H atoms were included in the refinement at their geometrically calculated positions and treated with a riding model. Anisotropic displacement parameters were refined for all non-hydrogen atoms. PLATON,[17,18], WinGX,[19] PARST,[20] ORTEPIII[21] and Mercury[22] software were used for the preparation of the crystallographic materials for publication.

RESULTS AND DISCUSSION

Compound **1** was obtained in the reaction of aqueous solutions of $ZnCl_2$ and tacrine hydrochloride in the molar ratio 1:2 (yield: 142 mg (45 %)).

*Elemental analysis of compound **1***. C, 49.77, H, 5.50, N, 8.98 % corresponds to $C_{26}H_{32}Cl_4N_4OZn$ (*FW* = 623.77); Calcd.: C, 50.04; H, 5.18; N 8.98 %. The result of the molar conductivity of compound **1** (λ_M = 252 Ω^{-1} cm^2 mol^{-1} (H_2O, 1.0×10^{-3} mol dm^{-3}) is in agreement with a 2:1 electrolyte type.

Compound **2** was obtained by the same procedure as employed for **1** but starting from $Na_2[Zn(OH)_4]$. Elemental analysis of **2** showed it to be tacrine which had crystallized as the dihydrate. Anal. Calcd. for $C_{13}H_{18}N_2O_2$: (*FW* = 234.3): C, 66.64; H, 6.02; N 11.96 %. Found: C, 66.28, H, 5.50, N, 12.05 %.

*Crystal data of **1***. $C_{26}H_{32}Cl_4N_4OZn$; crystal system, triclinic; space group, P–1; unit cell dimensions: a = 9.972(3) Å, b = 11.843(3) Å, c = 12.626(3) Å, α = = 76.61(2)°, β = 72.32(3)°, γ = 87.10(3)°, V = 1381.7(6) Å^3; Z = 2; ρ_c = 1.499 mg m^{-3}; μ = 1.303 mm^{-1}; reflections collected, 5750; independent reflections, 5421 (R_{int} = 0.0218); final R indices ($I > 2\sigma(I)$), *R1* = 0.0647, *wR2* = 0.1629 (for 325 refined parameters); goodness-of-fit, 0.978.

The results of the single crystal X-ray analysis of **1** revealed that in the reaction of $ZnCl_2$ with tacrine, the more stable tetrachlorozincate(II) complex was obtained in which protonated tacrine ($C_{13}H_{15}N_2^+$) serves as a counter cation (Fig. 1). This is the first structure of a typical complex compound with protonated tacrine as a counter ion. Only two crystal structures: ($C_{13}H_{15}N_2Cl\cdot H_2O$, CSD refcode GICMEK01, and $C_{13}H_{15}N_2[B(Ph)_4]\cdot CH_3CN$, CSD refcode

GOLFIW), containing protonated tacrine ($C_{13}H_{15}N_2^+$) were found in the Cambridge Structural Database (CSD).[23] Both of them are structures of salts of protonated tacrine. In the crystal structures of $C_{13}H_{15}N_2Cl{\cdot}H_2O$ (GICMEK01)[24] and $C_{13}H_{15}N_2[B(Ph)_4]{\cdot}CH_3CN$ (GOLFIW),[25] two and four C-atoms in the cyclohexenyl ring, respectively, are disordered. In the crystal structure of compound **1**, positional disorder was not observed. The crystal structure of **1** contains two different molecules of protonated tacrine ($C_{13}H_{15}N_2^+$), present as counter cations, and $[ZnCl_4]^{2-}$, as a complex anion, *i.e.*, two crystallographically independent molecules of protonated tacrine ($C_{13}H_{15}N_2^+$) and a $[ZnCl_4]^{2-}$ complex anion are in an asymmetric unit. There is also one molecule of crystal water in the asymmetric unit.

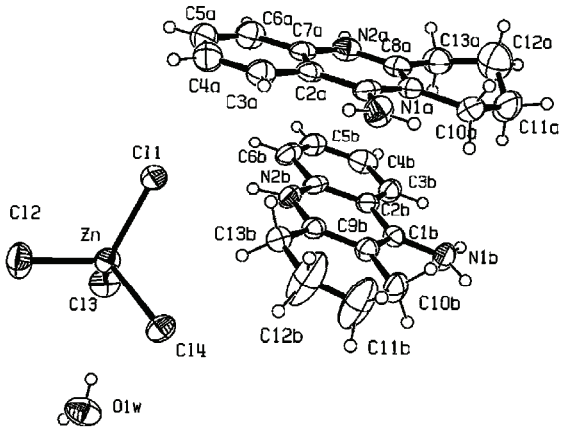

Fig. 1. The molecular geometry and atom labeling scheme of $(C_{13}H_{15}N_2)_2[ZnCl_4]{\cdot}H_2O$ (**1**). Selected bond distances (Å): Zn–Cl(1) = 2.282(2), Zn–Cl(2) = 2.232(2), Zn–Cl(3) = 2.293(2), Zn–Cl(4) = 2.273(2) and angles (°): Cl(2)–Zn–Cl(4) = 109.13(7), Cl(2)–Zn–Cl(1) = = 114.97(7), Cl(4)–Zn–Cl(1) = 109.57(7), Cl(2)–Zn–Cl(3) = 111.49(7), Cl(4)–Zn–Cl(3) = 105.54(7), Cl(1)–Zn–Cl(3) = 105.70(7).

The cation molecules (labeled as A and B) are comparable in terms of conformational and geometrical parameters (bond lengths and angles) except in the position of the C(12) atom (from the $C(12)H_2$ group) that is out of plane in the case of the protonated tacrine A. The displacement from the mean plane of the C(8)–C(9)–C(10)–C(11)–(C13) fragment in the case of C(12a) is 0.58(1) Å (in the case of the protonated tacrine B, such a displacement is not significant, 0.02(1) Å for the C(12b) atom). Two molecules of protonated tacrine (A and B) form different H-bonds (Table I, Fig. 2). The most obvious difference is in the case of the pyridinium nitrogen [N(2)], which in molecule A forms a hydrogen bond with a water oxygen atom, while in molecule B it forms a weak H-bond with a chloride from $[ZnCl_4]^{2-}$. In addition, the amino group of cation A acts as a

single hydrogen bond donor, while that of cation B acts as a double hydrogen bond donor (*vide infra*). The solvent water molecule [O(1w)] serves as a double donor (to Cl(3) and Cl(3) at $-x+2,-y+2,-z$) and a single acceptor which is common for a water molecule. The chloride atoms (Cl(3) and Cl(3) at $-x+2,-y+2,-z$) help in completing the water rings around the centre of inversion at 0 0 0. The system of H-bond interactions spreads in three-dimensions. In the crystal packing, π-stacking interactions between the rings of protonated tacrine molecules occur. For example, the mean planes of the pyridinium rings are approximately parallel and they are at a distance of about 3.5 Å from each other. The cation molecules are stacked in the ···A–A–B–B–A–A–··· order (Fig. 2).

TABLE I. The geometry of hydrogen bonding and selected intermolecular interactions (Å and °, respectively) for compound **1**. Symmetry codes: *i*) x,y,z; *ii*) $x-1,y,z$; *iii*) $-x+1,-y+1,-z$; *iv*) $-x+2,-y+2,-z$; *v*) $-x+1,-y+1,-z+1$; *vi*) $x,y-1,z$

D–H···A	D–H	D···A	H···A	D–H–A
N(2b)–H(2n2)···Cl(1)^{i}	0.86	3.318(5)	2.49	162
N(1b)–H(1b)···Cl(1)^{ii}	0.86	3.483(5)	2.70	153
N(1b)–H(2b)···Cl(3)^{iii}	0.86	3.433(6)	2.66	149
O(1w)–H(1w)···Cl(3)^{i}	0.85	3.279(5)	2.45	163
O(1w)–H(2w)···Cl(3)^{iv}	0.85	3.379(5)	2.59	155
N(1a)–H(2a)···Cl(4)^{v}	0.86	3.260(6)	2.44	161
N(2a)–H(1n2)···O(1w)^{vi}	0.86	2.772(6)	1.91	175

For the sake of comparison, the contacts surrounding the cations A and B in the present compound,
$C_{13}H_{15}N_2Cl\cdot H_2O$ (GICMEK01)[24] and
$C_{13}H_{15}N_2[B(Ph)_4]\cdot CH_3CN$ (GOLFIW)[25]
are depicted in Figs. 3–6, respectively.

In two of the analyzed structures of protonated tacrine (cation B and GICMEK01), both hydrogen atoms from the amino group are involved in hydrogen bonding with chloride atoms. In the case of cation A, only one amine hydrogen is involved in NH···Cl hydrogen bonding. In the former cases, the intermolecular N–H···Cl bonds are more bent and weaker than in the latter one. In the crystal structure of $C_{13}H_{15}N_2[B(Ph)_4]\cdot CH_3CN$ (GOLFIW), one amine hydrogen is directional towards the phenyl group at the symmetry position $1-x, 1-y, 1-z$. This hydrogen is engaged in weak N–H···π (Ph) hydrogen bonding. The shortest N–H···C distance is 2.75 Å. In all the analyzed structures, the amino group is nearly coplanar with the aromatic ring system. The dihedral angle between the plane defined by the amino group and the plane defined by the aromatic ring system range from 1.6(6) to 8.6(3)°. The pyridinium nitrogen serves as a single hydrogen bond donor in the observed structures. The D–H···X angles of the two-centre hydrogen bonds involving pyridinium nitrogen are in the range 162–175°.

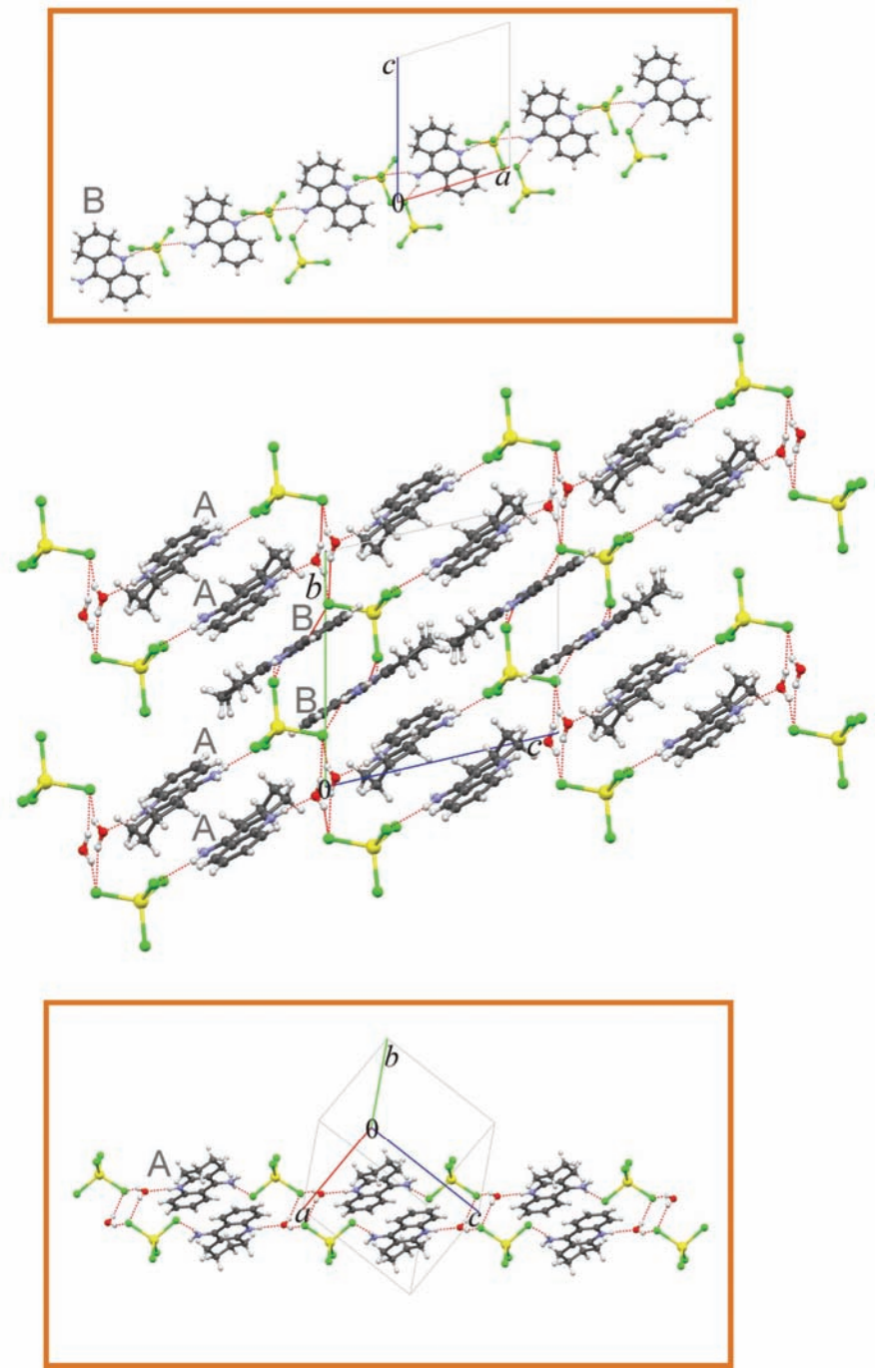

Fig. 2. The packing diagrams show intermolecular hydrogen bonding and π-stacking interactions in the crystal of (**1**).

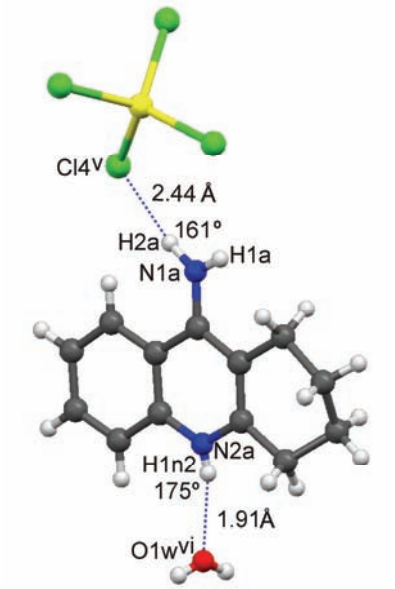

Fig. 3. The intermolecular contacts involving the functional groups of cation A. Symmetry codes: *v*) –*x*+1, –*y*+1, –*z*+1; *vi*) *x*, *y*–1, *z*.

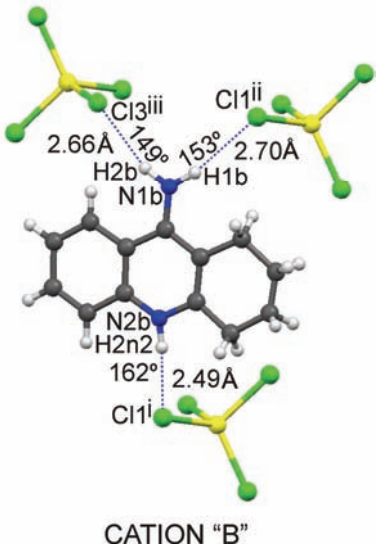

Fig. 4. The intermolecular contacts involving the functional groups of cation B. Symmetry codes: *i*) *x*, *y*, *z*; *ii*) *x*–1, *y*, *z*; *iii*) –*x*+1, –*y*+1, –*z*.

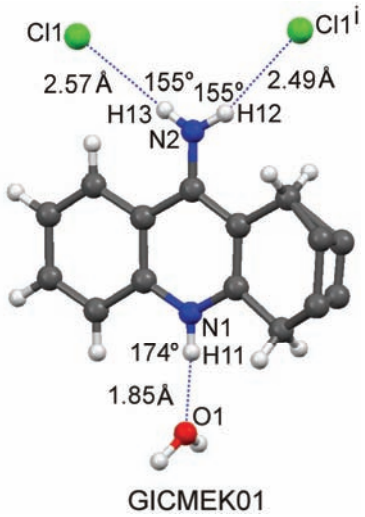

Fig. 5. The intermolecular contacts involving the functional groups of the cation in GICMEK01. Symmetry code: 3/2 – *x*; 1/2 + *y*; 1/2 – *z*.

The interesting characteristics of the structure are the differences in Zn–Cl bond lengths in the $[ZnCl_4]^{2-}$ anion: Zn–Cl(2), 2.232(2); Zn–Cl(4), 2.273(2); Zn–Cl(1) 2.282(2) and Zn–Cl(3) 2.293(2) Å. The difference between the longest [Zn-Cl(3)] and the shortest bond [Zn–Cl(2)] is 0.06 Å. The differences in bond

lengths are the result of various H-bonds in which the Cl atoms participate. The Cl(3), Cl(1) and Cl(4) atoms serve as triple, double and single hydrogen bond acceptor, respectively, while the Cl(2) atom does not form any H-bond. The Zn–Cl bond length increases with increasing the number of hydrogen bonds in which the Cl atom is involved. The tetrahedral coordination geometry around the Zn atom is distorted with Cl–Zn–Cl coordination angles in the range from 105.54(7) to 114.97(7)°. These structural differences could also be explained by intermolecular interactions with involvement of the Cl atoms.

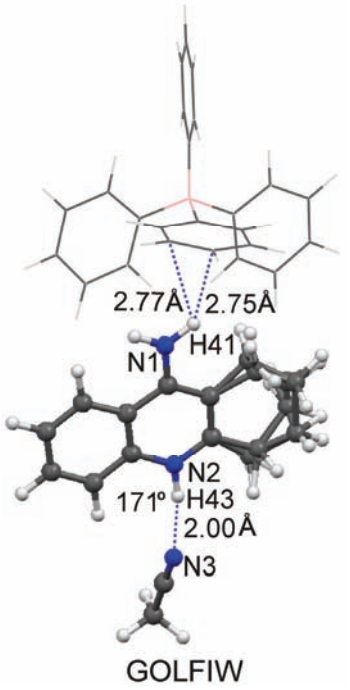

Fig. 6. The intermolecular contacts involving the functional groups of the cation in GOLFIW.

CONCLUSIONS

The $(C_{13}H_{15}N_2)_2[ZnCl_4]\cdot H_2O$ complex of distorted tetrahedral geometry was obtained in the reaction of $ZnCl_2$ with tacrine hydrochloride. The contacts surrounding the cations in the present structure and in the structures of $C_{13}H_{15}N_2Cl\cdot H_2O$[24] and $C_{13}H_{15}N_2[B(Ph)_4]\cdot CH_3CN$[25] reported elsewhere have been analyzed in detail. The prominent structural feature of $[ZnCl_4]^{2-}$ is the variation in the Zn–Cl bond lengths. The Zn–Cl bond length increases with increasing the number of intermolecular hydrogen bonds that involve the ligand atom.

Supplementary data. Cambridge Crystallographic Data Center, CCDC No. 695064, contains the supplementary crystallographic data for this paper. These data can be obtained free of charge *via* http://www.ccdc.cam.ac.uk/conts/retrieving.html (or from the CCDC, 12 Union Road, Cambridge CB2 1EZ, UK; fax: +44 1223 336033; e-mail: deposit@ccdc.cam.ac.uk).

Acknowledgements. This work was supported by the Ministry of Science and Technological Development of the Republic of Serbia (Grants Nos. 142010 and 142026).

ИЗВОД

СИНТЕЗА И КРИСТАЛНА СТРУКТУРА 1,2,3,4-ТЕТРАХИДРО-9-АМИНОАКРИДИН--ТЕТРАХЛОРОЦИНКАТА(II) МОНОХИДРАТА

ЂЕНАНА У. МИОДРАГОВИЋ[1], ДРАГОЉУБ ЈОВАНОВИЋ[2], ГОРАН А. БОГДАНОВИЋ[3], ДРАГАНА МИТИЋ[1] и КАТАРИНА АНДЈЕЛКОВИЋ[1]

[1]Хемијски факултет, Универзитет у Београду, п. пр. 158, 11001 Београд, [2]Катедра за исхрану и ботанику, Факултет ветеринарске медицине, Универзитет у Београду, Булевар ослобођења 18, Београд и [3]Институт Винча, Лабораторија за теоријску физику и физику кондензоване материје, п. пр. 522, 11001 Београд

У реакцији $ZnCl_2$ са такрин-хидрохлоридом у води, добијен је нови тетракоординовани $(C_{13}H_{15}N_2)_2[ZnCl_4]\cdot H_2O$ комплекс који је окарактерисан помоћу елементалне анализе, моларне проводљивости и рендгенске структурне анализе. Комплекс кристалише у просторној групи *P*–1 триклиничног кристалног система. Структура садржи два кристалографски различита молекула протонованог такрина који су присутни као контра-катјони, $[ZnCl_4]^{2-}$ комплексни анјон и молекул кристалне воде. Молекули катјона се незнатно разликују у степену набирања циклохексеновог прстена. Молекули протонованог такрина су укључени у различите интермолекулске водоничне везе. Интермолекулско водонично везивање у кристалу генерише 3Д молекулски скуп; π···π интеракције између прстенова протонованог такрина су примећене у кристалу. $[ZnCl_4]^{2-}$ има дисторговану тетраедарску геометрију. Три од четири Cl атома су укључена у интермолекулске водоничне везе. Интермолекулске водоничне интеракције које укључују Cl атоме утичу на дужину Zn–Cl веза.

(Примљено 2. марта, ревидирано 26. априла 2010)

REFERENCES

1. H. Kozłowski, D. R. Brown, G. Valensin, *Metallochemistry of Neurodegeneration, Biological, Chemical and Genetic Aspects*, The Royal Society of Chemistry, Cambridge, 2006
2. R. R. Crichton, R. J. Ward, *Metal-based Neurodegeneration: From Molecular Mechanisms to Therapeutic Strategies*, Wiley, Chichester, 2006
3. J. A. Hardz, G. A. Higgins, *Science* **256** (1992) 184
4. O. Wirths, G. Multhaup, T. A. Bayer, *J. Neurochem.* **91** (2004) 513
5. M. P. Cuajungco, K. Y. Fagét, *Brain Res. Rev*. **41** (2003) 44
6. C. S. Atwood , R. D. Moir, X. Huang, R. C. Scarpa, N. Michael, E. Bacarra, D. M. Romano, M. A. Hartshorn, R. E. Tanzi, A. I. Bush, *J. Biol. Chem.* **273** (1998) 12817
7. M. Stoltenberg, A. I. Bush, G. Bach, K. Smidt, A. Larsen, J. Rungby, S. Lund, P. Doering, G. Danscher, *Neuroscience* **150** (2007) 357
8. C. J. Frederickson, A. I. Bush, *BioMetals* **14** (2001) 353
9. S. Zirah, S. A. Kozin, A. K. Mazur, A. Blond, M. Cheminant, I. Ségalas-Milazzo, P. Debey, S. Rebuffat, *J. Biol. Chem*. **281** (2006) 2151
10. X. Huang, C. S. Atwood, M. A. Hartshorn, G. Multhaup, L. E. Goldstein, R. C. Scarpa, M. P. Cuajungco, D. N. Gray, J. Lim, R. D. Moir, R. E. Tanzi, A. I. Bush, *Biochemistry* **38** (1999) 7609
11. C. Opazo, X. Huang, R. A. Cherny, R. D. Moir, A. E. Roher, A. R. White, R. Cappai, C. L. Masters, R. E. Tanzi, N. C. Inestrosa, A. I. Bush, *J. Biol. Chem*. **227** (2002) 40302

12. X. Huang, C. S. Atwood, R. D. Moir, M. A. Hartshorn, J-P. Vonsattel, R. E. Tanzi, A. I. Bush, *J. Biol. Chem.* **272** (1997) 26464
13. *Enraf-Nonius CAD4 Software, version 5.0*, Enraf-Nonius, Delft, 1989
14. *CAD-4 Express Software*, Enraf-Nonius, Delft, 1994
15. G. M. Sheldrick, *SHELXS97. Program for the Solution of Crystal Structures*, University of Göttingen, Göttingen, 1997
16. G. M. Sheldrick, *SHELXL97. Program for the Refinement of Crystal Structures*, University of Göttingen, Göttingen, 1997
17. A. L. Spek, *Acta Crystallogr. D* **65** (2009) 148
18. A. L. Spek, *Platon, A Multipurpose Crystallographic Tool*, Utrecht University, Utrecht, 2010
19. L. J. Farrugia, *J. Appl. Crystallogr.* **32** (1999) 837
20. M. Nardelli, *J. Appl. Crystallogr.* **28** (1995) 659
21. L. J. Farrugia, *J. Appl. Crystallogr.* **30** (1997) 565
22. I. J. Bruno, J. C. Cole, P. R. Edgington, M. Kessler, C. F. Macrae, P. McCabe, J. Pearson, R. Taylor, *Acta Crystallogr. B* **58** (2002) 389
23. F. H. Allen, *Acta Crystallogr. B* **58** (2002) 380
24. G. Bandoli, A. Dolmella, S. Gatto, M. Nicolini, *J. Chem. Crystallogr.* **24** (1994) 301
25. K. N. Robertson, P. K. Bakshi, S. D. Lantos, T. S. Cameron, O. Knop, *Can. J. Chem.* **76** (1998) 583.

Journal of the Serbian Chemical Society
JSCS-info@shd.org.rs • www.shd.org.rs/JSCS
J. Serb. Chem. Soc. *75* (9) 1219–1230 (2010)
JSCS–4045
UDC 542.913:547.466+546.742:548.7:
541.121:536.7:535.33
Original scientific paper

Synthesis, crystal structure of and DFT calculations on bisglycinato-bis[*p*-(hydroxymethyl)pyridine]nickel(II)

PU SU ZHAO[1]*, JIE SONG[1], RONG CHANG SHANGGUAN[1] and FANG FANG JIAN[2]

[1]*Jiangsu Key Laboratory for Chemistry of Low-Dimensional Materials, Huaiyin Normal University, Huaian, Jiangsu, 223300 and* [2]*New Materials and Function Coordination Chemistry Laboratory, Qingdao University of Science and Technology, Qingdao Shandong, 266042, P. R. China*

(Received 28 October 2009, revised 12 January 2010)

Abstract: A new Ni(II) complex of bisglycinato-bis[*p*-(hydroxylmethyl)pyridine] was synthesized and characterized by elemental analysis, IR, UV–Vis spectroscopy and X-ray single crystal diffraction analysis. The thermal stability of the title complex was also determined. The complex adopts a distorted octahedral geometry and possesses inversion symmetry with the Ni(II) ion as the center of inversion. Density function theory (DFT) calculations of the structure, electronic absorption spectra, electron structure and natural population analysis (NPA) at the B3LYP/LANL2DZ level of theory were performed. The predicted geometric parameters and electronic spectra were compared with the experimental values and they supported each other. The NPA results indicate that the electronic transitions were mainly derived from the contribution of an intra-ligand (IL) transition, a ligand-to-metal charge transfer (LMCT) transition and a d-d transition. The electron structure calculations suggest that the central Ni(II) ion uses its 4s and 3d orbitals to form covalent bonds with coordinated N and O atoms. The calculated bond orders are also consistent with the thermal decomposition results. Based on vibrational analysis, the thermodynamic properties of the title complex were predicted and the correlative equations between these thermodynamic properties and temperature are also reported.

Keywords: amino acid complex; crystal structure; electronic spectra; DFT calculation; thermal stability.

INTRODUCTION

Recently, there is increasing interest in the realization of small and robust artificial DNA hydrolytic agents for their potential applications not only in molecular biology, but also in the development of new drugs.[1–3] Within these artificial nucleases, several examples of synthetic systems based on amino acid metal

* Corresponding author. E-mail: zhaopusu@163.com
doi: 10.2298/JSC091028101Z

complexes, which promote the hydrolysis of nucleic acids or of model phosphate esters, have been reported.[4–6] When the artificial nucleases establish interactions with DNA, metals are able to interact (covalently or not) with DNA through the electron-donating DNA bases and phosphate groups, thereby establishing either inter- or intra-strand interactions, while the coordinated groups in metal complexes contribute specific abilities, *i.e.*, intercalation, hydrogen bonding, electrostatic interaction, leading to a global effect.[1,7] On the other hand, nickel is an important trace element in organisms, which could promote the absorption of iron, the growth of erythrocyte and the synthesis of amino-enzyme in the body. It may also be a structural stabilizing agent of DNA and RNA.[8] Generally speaking, the Ni(II) ion frequently adopts coordination numbers of 4 or 6[9] and the coordination mode of Ni(II) depends on the structure of ligand, solvent and reaction conditions. Among these, the ligand plays a decisive role and determines not only the molecular structure of the complex, but also the aggregation fashion of the coordinated supermolecule.[10,11] Herein, a new Ni(II) complex with the amino acid bisglycinato-bis[*p*-(hydroxylmethyl)pyridine], in which the glycine exists as a bidentate chelating ligand and the complex adopts a distorted octahedral geometry, is reported. Density function theory (DFT) calculation results for the complex are also reported and compared with the experimental data. It is hoped that this report will provide useful structural information for the further study of the title compound with DNA.

EXPERIMENTAL

Physical measurements

Elemental analyses for carbon, hydrogen and nitrogen were performed by a Perkin-Elmer 240C elemental analyzer. The electronic absorption spectra were recorded on a Shimadzu UV3100 spectrophotometer in acetonitrile solution. Thermal gravimetric (TG) analysis was realized on an SDTA851e instrument (Mettler Toledo AG, Columbus, OH, USA) using samples of *ca* 10 mg under nitrogen (150 mL min^{-1}) at a heating rate of 20 °C min^{-1}.

Synthesis

All chemicals were obtained from a commercial source and used without further purification.

Freshly synthesized $Ni(OH)_2$ (0.93 g, 10 mmol), *p*-(hydroxymethyl)pyridine (2.18 g, 20.0 mmol) and glycine (1.5 g, 20 mmol) were mixed in water (50 mL) under stirring and the mixture was refluxed for 2 h. The resulting dark green solution was filtered and the filtrate was evaporated at room temperature. A dark green solid appeared which was separated by filtration. Yield: 68.2 % (2.9 g). Crystals suitable for X-ray structure determination were obtained by slowly evaporating an acetonitrile solution of the compound in air. Anal. Calcd. for $C_{16}H_{22}N_4NiO_6$: C, 45.20; H, 5.22; N, 13.18 %. Found: C, 45.14; H, 5.41; N, 13.01 %. IR (KBr, cm^{-1}): 3274(*s*), 2933 (*s*), 1586(*s*), 1499(*s*), 1393(*s*), 1350(*m*), 1302(*m*), 1225(*m*), 1130(*s*), 1057(*s*), 1017(*m*), 949(*m*), 898(*m*), 809(*m*), 722(*m*), 663(*m*), 590(*m*), 517(*m*).

Crystallographic data collection and solution of the structure

A summary of the key crystallographic information is given in Table I. The diffraction data were collected on an Enraf-Nonius CAD-4 diffractometer with graphite-monochromated Mo-Kα radiation (λ = 0.71073 Å, T = 293 K). The technique used was ω-scan with the limits 1.89 to 27.01°. The structure of the title compound was solved by direct methods and refined by least squares on F^2 using the SHELXTL[12] software package. All non-hydrogen atoms were anisotropically refined. The hydrogen atom positions were fixed geometrically at calculated distances and allowed to ride on the parent carbon atoms. The final conventional R = 0.0426 and Rw = 0.0906 for 1791 reflections with $I > 2\sigma(I)$ using the weighting scheme, w = = $1/(\sigma^2(F_0^2) + (0.0187P)^2 + 0.9868P$, where $P = (F_0^2 + 2F^{c2})/3$. The molecular graphics were plotted using SHELXTL software. Atomic scattering factors and anomalous dispersion corrections were taken from the International Tables for X-ray Crystallography.[13]

TABLE I. Summary of crystallographic results for the title compound

Empirical formula	$C_8H_{11}N_2Ni_{0.50}O_3$
Formula weight	212.54
Temperature, K	273(2)
Wavelength, Å	0.71073
Crystal system, space group	Monoclinic, *P*21/*c*
Unit cell dimensions, Å	a = 12.931(3)
	b = 5.6360(11), β = 123.35(2)°
	c = 14.476(6)
Volume, Å^3	881.3(5)
Z (calculated density, Mg/m^3)	4 (1.602)
Absorption coefficient, mm^{-1}	1.144
F(000)	444
θ range for data collection, °	1.89–27.01
Limiting indices	$-16 \le h \le 6$, $-7 \le k \le 7$, $-18 \le l \le 18$
Reflections collected/unique	3906/1837 (R_{int}= 0.0204)
Refinement method	Full-matrix least-squares on F^2
Data/restraints/parameters	1837/0/132
Goodness-of-fit on F^2	1.271
Final R indices ($I>2\sigma$ (I))	R_1 = 0.0426, wR_2 =0.0906
R indices (all data)	R_1 = 0.0439, wR_2 = 0.0912
Largest diffraction peak and hole, Å^{-3}	0.312 and –0.324

Computational methods

The initial molecular geometry was optimized using MM+ molecular modeling and semi-empirical AM1 methods (HYPERCHEM 6.0, Hypercube, Ont., Canada).[14] Then, DFT calculations with a hybrid functional B3LYP at the basis set LANL2DZ were performed by the Berny method[15] with the Gaussian 03 software package.[16] The calculated vibrational frequencies ascertained that the structure was stable (no imaginary frequencies). Based on the optimized geometry and using time-dependent density functional theory (TD-DFT)[17-19] methods, the electronic spectra of the title compound were predicted. Natural population analyses (NPA)[20] were also performed based on the optimized geometry.

All calculations were performed on a Dell PE 2850 server and a Pentium IV computer using the default convergence criteria.

RESULTS AND DISCUSSION

Crystal structure of the title compound

A displacement ellipsoid plot with the numbering scheme for the title compound is shown in Fig. 1. A perspective view of the crystal packing in the unit cell is shown in Fig. 2. Selected bond lengths and bond angles obtained by X-ray analysis are listed in Table II, together with the calculated bond parameters.

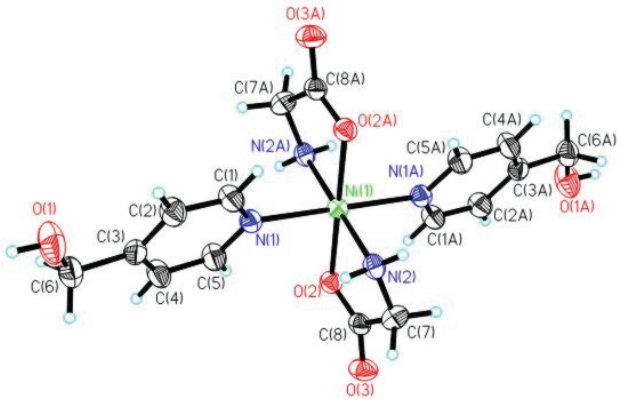

Fig. 1. Molecular structure of the title compound with atomic numbering.

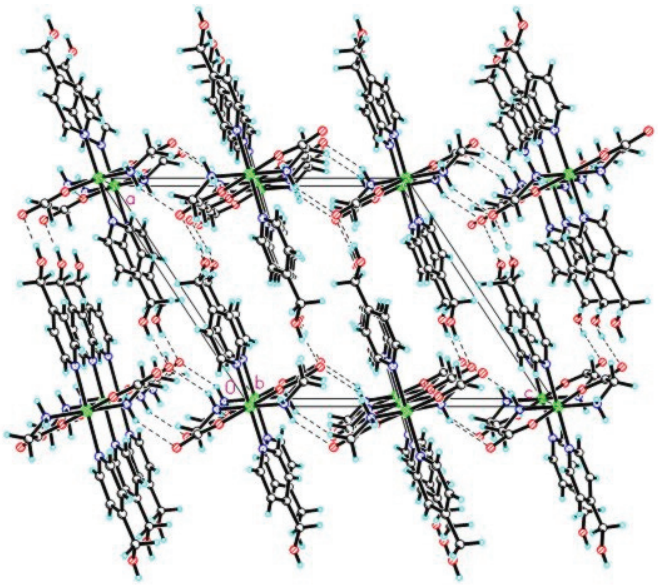

Fig. 2. Packing diagram of the unit cell along the *b*-axial direction for the title compound.

The crystal structure of the title complex is composed of two discrete monomeric molecules of $[(C_5H_4NCH_2OH)_2(CH_2NH_2COO)_2Ni(II)]$. The central nick-

el(II) ion is coordinated by two glycinato anions and two *p*-(hydroxymethyl)pyridine ligands with the Ni(II) ion as the center of inversion. The NiN_4O_2 core has a distorted octahedral geometry. The basal plane is formed by two oxygen atoms and two nitrogen atoms from the two glycinato anions and the chelating angle of N(1)–Ni(1)–O(2) is 81.08(9)°. The axial sites are occupied by two nitrogen atoms of the pyridyl rings from the two *p*-(hydroxymethyl)pyridine ligands. The bond length of Ni(1)–N(1) (2.162(2) Å) is slightly longer than that of Ni(1)–N(2) (2.075(2)Å), with both corresponding to those in other six-coordinated nickel(II) complexes.[21,22] The bond length of Ni(1)–O(2) is 2.063(19) Å, which is slightly longer than those in the above-cited structures (2.044(2) and 2.045(3) Å). All the bond lengths and bond angles in the *p*-(hydroxymethyl)pyridine ligand are within the normal range. The dihedral angle between the pyridine plane and the mean plane formed by atoms constituting the five-membered chelate ring is 86.72(1)°.

TABLE II. Selected geometric parameters from X-ray analysis and theoretical calculations at the B3LYP/LANL2DZ level of theory for the title compound

Bond length, Å					
Bond	Experimental	Calculated	Bond	Experimental	Calculated
Ni(1)–O(2)	2.063(19)	1.880	N(1)–C(1)	1.333(4)	1.356
Ni(1)–N(2)	2.075(2)	1.975	N(1)–C(5)	1.338(4)	1.356
Ni(1)–N(2A)	2.075(2)	1.975	N(2)–C(7)	1.471(4)	1.481
Ni(1)–N(1A)	2.162(2)	1.951	C(1)–C(2)	1.386(4)	1.398
Ni(1)–N(1)	2.162(2)	1.951	C(3)–C(4)	1.383(4)	1.408
O(1)–C(6)	1.402(4)	1.455	C(3)–C(6)	1.498(4)	1.514
O(2)–C(8)	1.263(3)	1.362	C(4)–C(5)	1.371(4)	1.401
O(3)–C(8)	1.249(3)	1.245	C(7)–C(8)	1.519(4)	1.539
Bond angle, °					
Bonds	Experimental	Calculated	Bonds	Experimental	Calculated
O(2)–Ni(1)–N(2)	81.08(9)	86.61	C(1)–N(1)–C(5)	116.4(2)	120.34
O(2A)–Ni(1)–N(2)	98.92(9)	93.39	N(1)–C(1)–C(2)	123.6(3)	120.95
O(2)–Ni(1)–N(2A)	98.92(9)	93.39	C(3)–C(2)–C(1)	119.5(3)	119.79
O(2A)–Ni(1)–N(2A)	81.08(9)	86.61	C(2)–C(3)–C(6)	122.9(3)	120.35
O(2)–Ni(1)–N(1)	90.96(8)	89.22	C(5)–C(4)–C(3)	119.9(3)	119.38
N(2)–Ni(1)–N(1)	89.73(9)	88.04	O(1)–C(6)–C(3)	110.6(3)	108.48
N(2A)–Ni(1)–N(1)	90.27(9)	91.96	N(2)–C(7)–C(8)	111.5(2)	110.00
C(8)–O(2)–Ni(1)	114.66(18)	115.68	O(2)–C(8)–C(7)	117.9(2)	113.79

In the crystal lattice, there are three types of hydrogen bonds and some weak intermolecular interactions (C–H···Y, Y = O)[23,24] (see Table III), which enable the molecules to form three-dimensional (3D) networks and stabilize the crystal structure.

TABLE III. Intermolecular hydrogen bonds and C–H···O supramolecular interactions

D–H···A	Symmetry on A	D···A Length, Å	∠D–H···A Angle, °
N(2)–H(1)···O(2)	*x*, 1+*y*, *z*	3.0633	167.42
O(1)–H(1A)···O(3)	1+*x*, 1/2–*y*, 1/2+*z*	2.7312	161.99
N(2)–H(2)···O(3)	–*x*, 1/2+*y*, 1/2–*z*	3.0631	151.30
C(1)–H(1B)···O(2)	–*x*, 1–*y*, *1–z*	3.0879	116.96
C(2)–H(2B)···O(1)	–	2.7468	100.53
C(5)–H(5A)···O(2)	–	3.0562	116.61

Optimized geometry

The optimized geometry possesses inversion symmetry and the Ni(II) is the center of inversion. A comparison of the theoretical and experimental values in Table III shows that most of the optimized bond lengths are slightly longer than those in the crystal structure and that larger differences mainly occur on the Ni(II) ion. The largest difference in bond length is 0.211 Å for Ni(1)–N(1) and the largest difference in bond angle is 5.53° for the angles around the Ni(II) ion, such as the bond angles O(2)–Ni(1)–N(2) and O(2A)–Ni(1)–N(2). The reason may be that the theoretical calculations consider isolated molecules in gaseous phase at 0 K while the experimental results belong to molecules in the solid phase. In the crystal state, the close packing of all the molecules and the existence of a crystal field result in the geometric parameters of the molecules differing from those found by calculations. On the other hand, those intermolecular hydrogen bonds and C-H···O supramolecular interactions in the crystal lattice may also lead to some differences in the bond lengths and bond angles between the experimental and predicted values. In spite of these differences, the Ni(II) ion in the optimized geometry still adopts a distorted octahedral coordination geometry and *p*-(hydroxymethyl)pyridine groups of the molecule represent a good approximation with the crystal structure. Based on the optimized geometry and natural population analysis (NPA), the electronic spectrum and thermodynamic properties of the title compound were calculated.

Electronic absorption spectra and electronic structure

The electronic absorption spectrum of the title compound in acetonitrile solution exhibits four bands. The two sharp peaks at 210 and 253 nm are ascribed to intra-ligand transitions between the glycinato anions and the *p*-(hydroxymethyl)pyridine groups, while the broad peak from 360 to 385 nm is assigned to charge transfer transitions from the low-energy π* orbital of the ligand to the d orbitals of the nickel (II) ion (LMCT).[25] The fourth broad band in the range of 540–556 nm arises from d–d transitions of Ni(II), which may be taken as evidence for octahedral Ni(II) complexes.[25] The DT-DFT electronic spectra calculations show that there are also four electronic transition bands which correspond to the experimental data. The two sharp predicted peaks are at 210 nm

(oscillator strength: 0.3454) and 238 nm (oscillator strength: 0.2610), respectively, and the band at 238 nm is blue shifted compared with the experimental value of 253 nm. The third broad band falls in the range of 300 to 370 nm with the biggest oscillator strength being 0.0401 at 342 nm, which has some blue shifts comparing with the experimental values of 360–385 nm. The fourth peak is from 470 to 520 nm with the largest oscillator strength of 0.0575 at 513 nm. This peak is located in the visible light range and is also blue shifted compared with the experimental data of 550–700 nm. The experimental and calculated electronic absorption spectra are shown in Fig. 3. Detailed experimental electronic absorption spectral values and the TD-DFT calculated ones, together with the detailed electronic transition modes, are given in Table IV. The reasons for the discrepancy between the experimental values and theoretical predictions may be as follows: TD-DFT approach is based on the random-phase approximation (RPA) method,[26,27] which provides an alternative to the computationally demanding multirefrence configuration interaction methods in the study of excited states. The TD-DFT calculations do not evaluate the spin-orbit splitting; the values are averaged. Here, in this paper, the objective was to evaluate the electronic structure by direct electronic excitations. Only singlet–singlet transitions are considered in these quasi-relativistic calculations. In addition, the role of the solvent effect of acetonitrile solution is not included in the theoretical calculations. Natural population analyses indicate that the frontier molecular orbitals are main-

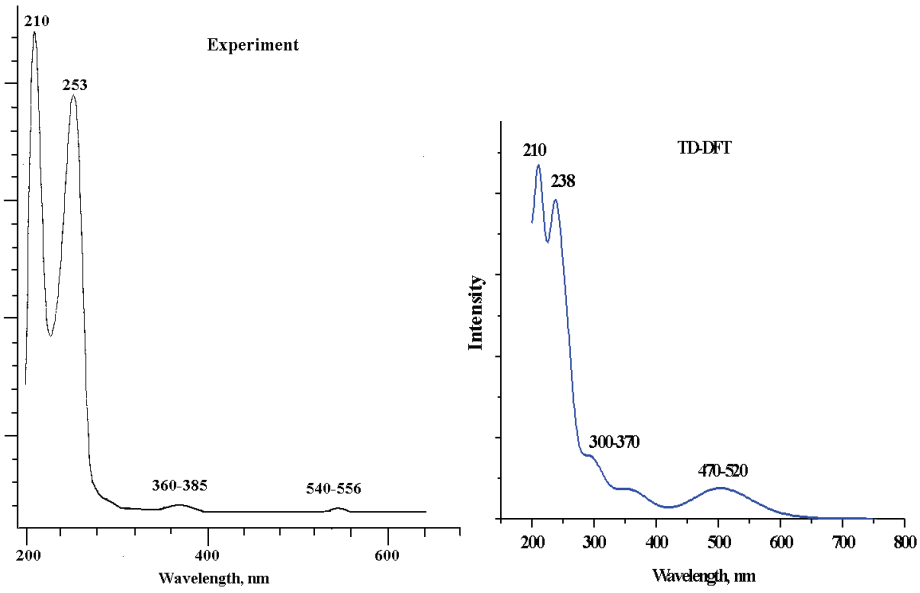

Fig. 3. Experimental (a) and calculated (b) electronic absorption spectra.

ly composed of d and p atomic orbitals, hence the above electronic transitions are mainly derived from the contribution of an intraligand (IL) transition, ligand-to-metal charge transfer (LMCT) transitions and d–d transitions. Some frontier molecular orbital stereographs for the title compound are shown in Fig. 4, from which it can be seen that the electron cloud distributions in the frontier molecular obitals support the above electronic transition models.

TABLE IV. Experimental and theoretical electronic absorption spectra values

Experimental		Calculated (TD-DFT)		
Wavelength, nm	Electronic transition modes	Wavelength, nm	Oscillator strength	Electronic transition modes
210	Intra-ligand	210	0.3454	104(HOMO-1) →108 (LUMO+2)
253	transition	238	0.2610	105(HOMO) →109 (LUMO+3)
360–385	LMCT	300–370	0.0401 at 342 nm	103 (HOMO-2) → →107 (LUMO+1)
540–556	d–d	470–520	0.0575at 513 nm	102 (HOMO-3) →106 (LUMO)

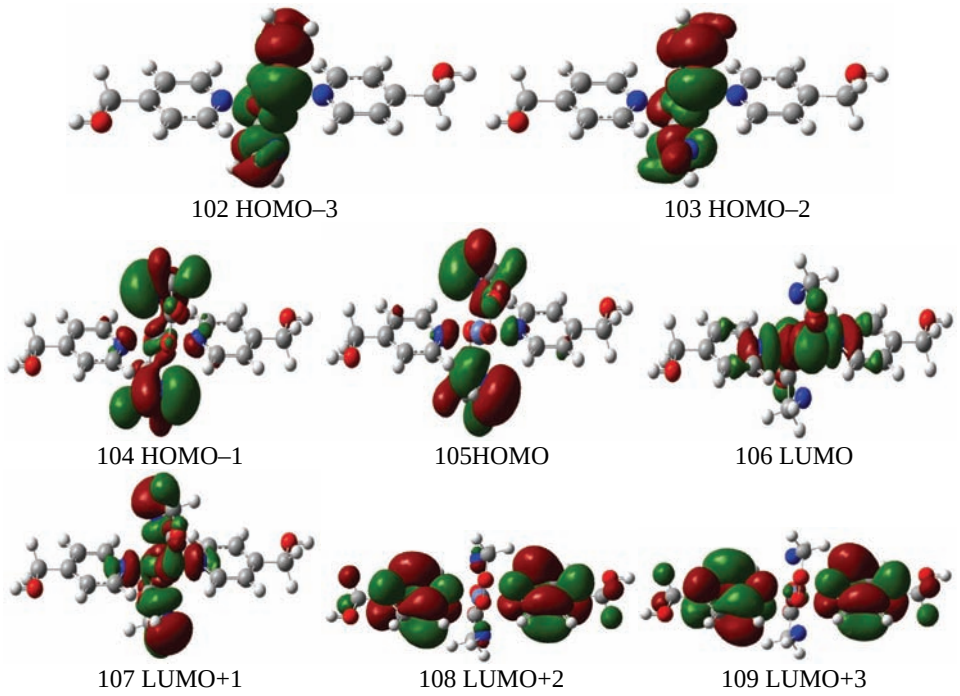

Fig. 4. Some frontier molecular orbital stereographs for the title compound.

The electronic structure of the title compound was calculated. The calculated natural population analysis charge and the natural electron configuration for the central Ni(1) ion and the coordinated N and O atoms are listed in Table V.

TABLE V. Natural population charge and natural electron configuration of the title compound

Atom	Net charge	Electron configuration
Ni(1)	1.22770	[core]4S(0.27)3d(8.46)4p(0.01)4d(0.01)5p(0.03)
N(1) and N(1A)	–0.48689	[core]2s(1.34)2p(4.12)3p(0.02)
N(2) and N(2A)	–0.87140	[core]2s(1.56)2p(4.29)3p(0.02)
O(2) and O(2A)	–0.73609	[core]2s(1.76)2p(4.96)3p(0.01)

From Table V, it can be seen that the net charge on the Ni(1) ion is +1.22770, deviating from +2. The net charges on the coordinated N atoms range from –0.48689 to –0.87140 and the net charges on the coordinated O atoms are both –0.73609, showing that these atoms transfer parts of their electrons to the central Ni(1) ion and then covalent bonds are formed. On the other hand, from the natural electron configuration, for the Ni(1) ion, the electron number of 4s (0.27) is larger than zero, the electron number of 3d (8.26) is larger than 8 and those of 4p, 4d and 5p are so small that can be neglected. These data suggest that the Ni(1) ion uses its 4s and 3d orbitals to form covalent bonds with the N and O atoms. While for the coordinated N and O atoms, the electron number of the 2s orbital ranges from 1.34 to 1.76 and can be ascribed to lone pair electrons.[28] The 2p orbital falls in the range of 4.12–4.96. Thus, it can be concluded that the coordinated N and O atoms form covalent bonds with the Ni(1) ion having 2p orbitals.

Thermal property analysis and the bond order

The thermal gravimetric curve of the title compound is given in Fig. 5, from which it can be seen that the decomposition of the title compound is accompanied by two mass-loss processes, the first one from 220 to 280 °C and the second one from 300 to 420 °C. During the first weight-loss process, the mass loss is 49.96 %, which can be assigned to the breakage of the Ni(1)–N(1) and Ni(1)–N(1A) bonds and the decomposition of the *p*-(hydroxymethyl)pyridine groups (Calcd. 51.35 %). After 300 °C, the second decomposition step accompanied by a weight loss of 34.62 % occurs, which is assigned to the scission of the Ni(1)–O(2), Ni(1)–N(2), Ni(1)–O(2A) and Ni(1)–N(2A) bonds and the loss of two glycinato anions (Calcd. 34.84 %). The residue of the decomposition (15.42 %) is Ni (Calcd. 13.81 %). These experimental facts reveal that the Ni(1)––N(1) and Ni(1)–N(1A) bonds are weaker than the Ni(1)–O(2), Ni(1)–O(2A), Ni(1)–N(2) and Ni(1)–N(2A) bonds. Theoretical calculations at the B3LYP/ /LANL2DZ level of theory show that the bond orders of the Ni(1)–N(1) and Ni(1)–N(1A) bonds are both 0.0973. The bond orders of the Ni(1)–O(2) and Ni(1)–O(2A) bonds are both 0.2770 and the bond orders of the Ni(1)–N(2) and Ni(1)–N(2A) bonds are both 0.3692. It is obvious that thermal analysis of the title compound proved the theoretical predictions to be correct. In other words, the theoretical calculations support the experimental facts.

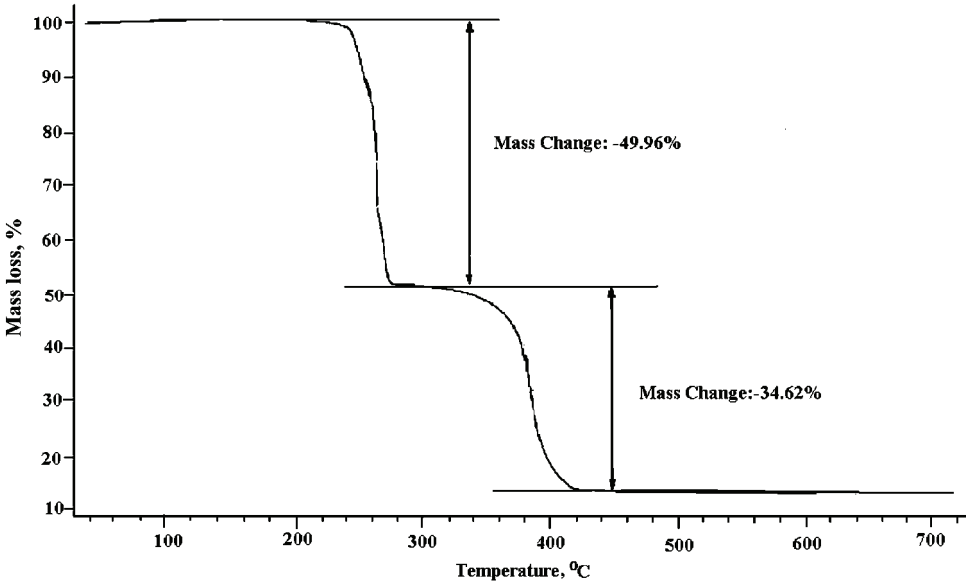

Fig. 5. Thermal gravimetric curve of the title compound.

Thermodynamic properties

Based on vibrational analysis at the B3LYP/LANL2DZ level and statistical thermodynamics, the standard thermodynamic functions: heat capacities ($C^0_{p,m}$), entropies (S^0_m) and enthalpies (H^0_m), were obtained and are listed in Table VI. The scale factor for frequencies is 0.96, which is a typical value for the B3LYP method.

TABLE VI. Thermodynamic properties of the title compound at different temperatures at the B3LYP/LANL2DZ level

T / K	$C^0_{p,m}$ / J·mol^{-1}·K^{-1}	S^0_m / J·mol^{-1}·K^{-1}	H^0_m / kJ·mol^{-1}
200.0	320.0	620.1	37.27
300.0	444.3	773.5	75.51
400.0	558.0	917.3	125.8
500.0	651.9	1052	186.4
600.0	726.6	1178	255.5
700.0	786.2	1295	331.3
800.0	834.6	1403	412.4

From Table VI, it can be observed that the standard heat capacities, entropies and enthalpies increase at any temperature ranging from 200.0 to 800.0 K because the intensities of molecular vibration increase with increasing temperature.

The correlative equations between these thermodynamic properties and temperatures are as follows:

$$C^0_{p,m} = 17.407 + 1.675T - 8.196\times10^{-4}T^2,\ R^2 = 0.9999$$
$$S^0_m = 287.124 + 1.756T - 4.521\times10^{-4}T^2,\ R^2 = 0.99999$$
$$H^0_m = -22.348 + 0.204T + 4.270\times10^{-4}T^2,\ R^2 = 0.9998$$

These equations will be helpful for the further studies of the title compound. For instance, when the interaction between the title compound and another compound is investigated, the thermodynamic properties $C^0_{p,m}$, H^0_m and S^0_m could be obtained from these equations and then used to calculate the change of Gibbs free energy of the reaction, which will assist in the judgement of the spontaneity of the reaction.

Supplementary material. CCDC – 649102 contains the supplementary crystallographic data for this paper. These data can be obtained free of charge at http://www.ccdc.cam.ac.uk/ /conts/retrieving.html or from the Cambridge Crystallographic Data Centre (CCDC), 12 Union Road, Cambridge CB2 1EZ, UK (fax: +44(0)1222-336033; e-mail: deposit@ccdc.cam.ac.uk).

Acknowledgement. This work was supported by Jiangsu Key Laboratory for Chemistry of Low-Dimensional Materials P. R. China (JSKC08047) and Fund of Huanyin Normal University (08HSJSK003).

И З В О Д

СИНТЕЗА, КРИСТАЛНА СТРУКТУРА И DFT ИЗРАЧУНАВАЊА ЗА БИСГЛИЦИНАТО--БИС[*p*-(ХИДРОКСИМЕТИЛ)ПИРИДИН]-НИКАЛ(II)

PU SU ZHAO[1], JIE SONG[1], RONG CHANG SHANGGUAN[1] и FANG FANG JIAN[2]

[1]*Jiangsu Key Laboratory for Chemistry of Low-Dimensional Materials, Huaiyin Normal University, Huaian, Jiangsu, 223300 и* [2]*New Materials and Function Coordination Chemistry Laboratory, Qingdao University of Science and Technology, Qingdao Shandong, 266042, P. R. China*

Синтетозован је нови бисглицинато-бис[*p*-(хидроксиметил)пиридин]-никал(II) комплекс. Поред елементарне микроанализе, за карактеризацију овог комплекса употребљени су IR и UV–Vis спектри, као и кристална дифракциона анализа помоћу X-зрака. Одређена је термичка стабилност добивеног комплекса. Нађено је да комплекс има дисторговану октаедраску геометрију и инверзиону осу симетрије са Ni(II) јоном у центру инверзије. Структура комплекса потврђена је на основу теоријских израчунавања применом методе функционалних густина (DFT израчунавања), електронских апсорпционих спектара, електронске структуре и NPA анализе за B3LYP/LANL2DZ теоријски степен. Предвиђени геометријски параметри и електронски спектри су у сагласности са одговарајућим експерименталним вредностима. Добијени NPA параметри указују да електронски прелази углавном деривирају од доприноса интралигандних (IL) прелаза, прелаза који потичу од лиганд-метал трансфера наелектрисања (LMCT) и d–d прелаза. Израчунавања електронске структуре указују да централни Ni(II) јон користи 4s и 3d орбитале за грађење ковалентних веза са донорским N и O атомиима. Израчунате вредности дужина веза су такође, у сагласности са резултатима добивеним на основу термичке декомпозиције комплекса. На основу вибрационих анализа предвиђене су термодинамичке особине добивеног Ni(II) комплекса и дате су корелативне једначине које повезују ове термодинамичке особине са температуром.

(Примљено 28. октобра 2009, ревидирано 12. јануара 2010)

REFERENCES

1. M. Livieri, F. Mancin, U. Tonellato, J. Chin, *Chem. Commun*. **24** (2004) 2862
2. L. Fernandes, F. L. Fischer, C. W. Ribeiro, G. P. Silveira, M. M. Sá, F. Nome, H. Terenzi, *Bioorg. Med. Chem. Lett.* **18** (2008) 4499
3. X. Q. Chen, J. Y. Wang, S. G. Sun, J. L. Fan, S. Wu, J. F. Liu, S. J. Ma, L. Z. Zhang, X. J. Peng, *Bioorg. Med. Chem. Lett.* **18** (2008) 109
4. P. U. Maheswari, S. Roy, H. den Dulk, S. Barends, G. van Wezel, B. Kozlevöar, P. Gamez, J. Reedijk, *J. Am. Chem. Soc*. **128** (2006) 710
5. S. Negi, Y. Umeda, S.Masuyama, K. Kano, Y. Sugiura, *Bioorg. Med. Chem. Lett.* **19** (2009) 2789
6. M. Dhanasekaran, S. Negi, Y. Sugiura, *Acc. Chem. Res*. **39** (2006) 45
7. L. Otero, P. Smircich, M. Vieites, M. Ciganda, P. C. Severino, H. Terenzi, H. Cerecetto, D. Gambino, B. Garat, *J. Inorg. Biochem.* **101** (2007) 74
8. J. G. Yang, F. Li, F. Y. Pan, W. P. Jia, *Chin. J. Struct. Chem.* **26** (2007) 1071
9. B. Gillon, C. Mathoniere, E. Ruiz, S. Alvarez, A. Cousson, T.M. Rajendiran, O. Kahn, *J. Am. Chem. Soc*. **124** (2002) 14433
10. S. Noro, R. Kitaura, M. Kondo, S. Kitagawa, T. Ishii, H. Matsuzaka, M. Yamashita, *J. Am. Chem. Soc*. **124** (2002) 2568
11. M. Devereux, M. McCann, D. O. Shea, R. Kelly, D. Egan, C. Deegan, K. Kavanagh, Y. McKee, G. Finn, *J. Inorg. Biochem.* **98** (2004) 1023
12. G. M. Sheldrick, *SHELXTL, v. 5 Reference Manual*, Siemens Analytical X-Ray Systems, Madison, WI, 1997
13. A. J. Wilson, *International Table for X-Ray Crystallography*, Vol. C, Kluwer Academic, Dordrecht, 1992, pp. 500–502, 219–222
14. M. J. S. Dewar, E. G. Zoebisch, E. F. Healy, J. J. P. Stewart, *J. Am. Chem. Soc.* **107** (1985) 3902
15. C. Peng, P. Y. Ayala, H. B. Schlegel, M. J. Frisch, *J. Comput. Chem.* **17** (1996) 49
16. *Gaussian 03 software package*, Gaussian Inc., Wallingford, CT, 2004
17. E. Runge, E. K. U. Gross. *Phys. Rev. Lett.* **52** (1984) 997
18. M. Petersilka, U. J. Gossmann, E. K. U. Gross, *Phys. Rev. Lett.* **76** (1966) 1212
19. R. Bauernschmitt, R. Ahlrichs, *Chem. Phys. Lett.* **256** (1996) 454
20. C. Jamorski, M. E. Casida, D. R. Salahub. *J. Chem. Phys.* **104** (1996) 5134
21. B. F. Abrahams, B. F. Hoskins, T. A. Hudson, R. Robson, *Acta Crystallogr., Sect. C* **56** (2000) e126
22. M. Du, X. H. Bu, M. Shionoya, M. Shiro, *J. Mol. Struct.* **607** (2002) 155
23. T. Steiner. *Crystallogr. Rev.* **6** (1996) 1
24. G. A. Jeffrey, H. Maluszynska, J. Mitra, *Int. J. Biol. Macromol.* **7** (1985) 336
25. F. F. Jian, L. Pang, H. L. Xiao, P. P. Sun, *Chin. J. Struct. Chem.* **23** (2004) 975
26. L. Olsenand, P. Jorgensen. in: *Modern Electronic Structure Theory*, Vol. 2, World Science, River Edge, NJ, 1995
27. M. Fernando, O. Claudio, *Int. J. Quantum Chem.* **103** (2005) 34
28. H. H. Li, Z. R. Chen, J. Q. Li, C. C. Huang, B. Zhao, Z. X. Ni, *Chin. J. Struct. Chem.* **24** (2005) 39.

Journal of the Serbian Chemical Society
JSCS-info@shd.org.rs • www.shd.org.rs/JSCS
J. Serb. Chem. Soc. 75 (9) 1231–1239 (2010)
JSCS–4046
UDC 547.235.2'211+547.288.4+546.3–386:542.913:615.281
Original scientific paper

Synthesis, complexation, spectral, antibacterial and antifungal activity of 2,4-dihydroxy-5-[(*E*)-phenyldiazenyl]benzaldehyde oxime

MÜKERREM KURTOGLU*

Department of Chemistry, Kahramanmaraş Sütçü İmam University, Kahramanmaraş, 46050, Turkey

(Received 18 November, revised 22 December 2009)

Abstract: A new substituted salicylaldoxime ligand containing an azo (–N=N–) group, 2,4-dihydroxy-5-[(*E*)-phenyldiazenyl]benzaldehyde oxime (H_3salox) (**2**), was synthesized by the reaction of 2,4-dihydroxy-5-[(*E*)-phenyldiazenyl]benzaldehyde (**1**) with hydroxylamine in ethanolic solution at room temperature. Mononuclear complexes of (H_3salox) (**2**), a bidentate hydroxyaldoxime ligand, were synthesized by reaction with nickel(II), cobalt(II) and copper(II) chloride salts. The complexes, [Ni(H_2salox)$_2$] (**3**), [Cu(H_2salox)$_2$] (**4**) and [Co(H_2salox)$_2$] (**5**) were characterized by elemental analyses (C, H, N), conductivity measurements and infrared and electronic spectral studies. The ^{1}H-NMR spectrum of the H_3salox (**2**) ligand was also recorded. The mononuclear Ni(II), Co(II) and Cu(II) complexes of the ligand, (H_3salox), have a metal:ligand ratio of 1:2 and the ligand coordinates through the N and O atoms, as is the case with most hydroxyaldoximes. The molar conductivities in DMF solution indicate the non-electrolytic nature of the metal chelates. The antimicrobial activities of the ligand and its metal complexes were estimated for eight bacteria, *i.e.*, *Escherichia coli*, *Staphylococcus aureus*, *Klebsiella pneumoniae*, *Mycobacterium smegmatis*, *Pseudomonas aeruginosa*, *Enterococcus cloacae*, *Bacillus megaterium* and *Micrococcus luteus* and three fungi, *i.e.*, *Kluyveromyces fragilis*, *Rhodotorula rubra* and *Saccharomyces cerevisiae.*

Keywords: azo; azomethine; oxime; metal complexes.

INTRODUCTION

In recent years, the chemistry of coordination compounds has shown a rapid development in diverse disciplines as a result of the possible use of these new compounds in biological applications. Transition metal complexes with potential biological activity are the focus of extensive investigations. Oximes and azo dyes have often been used as chelating ligands in the field of coordination chemistry

* mkurtoglu@ksu.edu.tr
doi: 10.2298/JSC091118102K

and their metal complexes have been of great interest for many years. The biological importance of oximes and their complexes is very well known.[1] Different oximes and their metal complexes have shown notable bioactivity as chelating therapeutics, as drugs, as inhibitors of enzymes and as intermediates in the biosynthesis of nitrogen oxides.[2,3] Transition metal complexes with *o*-hydroxy aromatic oximes have attracted much attention as they exist as *cis* and *trans* geometrical isomers. Copper complexes are known to assume *trans* structures while cobalt complexes have *cis* structures.[4]

The presence of mildly acidic hydroxyl groups and slightly basic nitrogen atoms makes *vic*-dioximes amphoteric ligands, which form square-planar, square-pyramidal or octahedral complexes with transition metal ions such as Ni(II), Co(II) and Cu(II) as the central atom.[5]

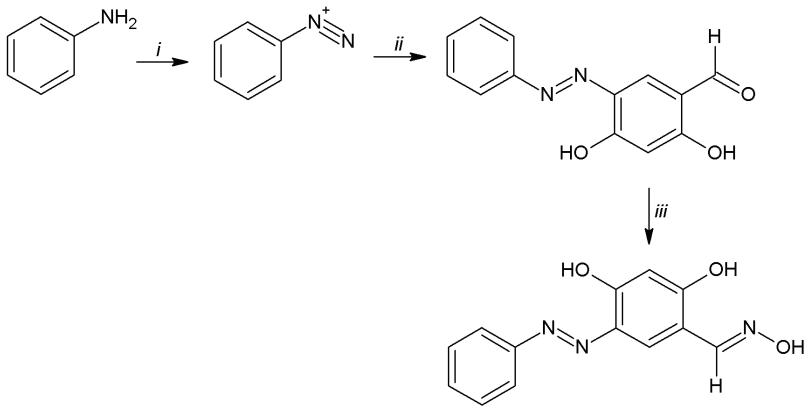

Fig. 1. The synthesis reaction of the substituted salicylaldoxime ligand; *i*) $NaNO_2$/HCl, *ii*) 2,4-dihydroxybenzaldehyde AND *iii*) hydroxylammoniumchloride.

In previous papers, the synthesis and characterization of new ligands and their various transition metal complexes were reported.[6–8] Due to the importance of azo-oxime compounds and in continuance of interest in the syntheses of azo and oxime compounds, the synthesis and spectral properties of a new azo-oxime compound and its metal complexes are reported herein. The proposed structure of the ligand is shown in Fig. 1. ^{1}H-NMR, IR and UV–Vis data and elemental analyses results of the azo-oxime compounds are presented.

EXPERIMENTAL

Materials and measurements

All chemicals used in the syntheses were of reagent grade and used without further purification. All solvents were of reagent grade and purified according to the standard procedure. Carbon, hydrogen and nitrogen elemental analyses were performed with a model Leco CHNS 932 elemental analyzer. The IR spectra were obtained as KBr discs (4000–400 cm^{-1}) using a Shimadzu 8300 FTIR spectrophotometer. The electronic spectra were obtained in

DMF on a Shimadzu UV-160 A spectrophotometer. The ^{1}H-NMR spectra were recorded on a Bruker Ultrashield 300 MHz FT-NMR spectrometer.

*2,4-Dihydroxy-5-[(E)-phenyldiazenyl]benzaldehyde, a-sal (**1**)*

Aniline (0.093 g, 1.0 mmol) was cooled to 0 °C and hydrochloric acid (35.5 %, 0.4 mL) was added. When the mixture had attained room temperature, it was stirred for complete solubilization. The solution was again cooled to 0 °C and $NaNO_2$ (crystals) (70 mg, 1.0 mmol) was added in 2 min. The suspension was stirred with a glass rod until a deep yellow precipitate was formed (10 min). To this suspension, ice (*ca*. 10 mg) was added in small pieces and the mixture was poured into a suspension of 2,4-dihydroxybenzaldehyde (128 mg, 1.0 mmol) and CH_3COONa (*ca*. 3 g) in EtOH (35 mL) at 0 °C. The color changed within a few minutes from blue to red. After 15 min stirring, aqueous sodium carbonate (20 %, 50 mL) was added at 0 °C and the solution was allowed to warm to room temperature and then extracted three times with EtOH (3×50 mL). The combined organic layers were washed with water, dried over Na_2SO_4 and the solvent was evaporated under vacuum. Anal. Calcd. for $C_{13}H_{10}N_2O_3$ (*FW* 242.23): C, 64.46, H, 4.16; N, 11.56 %. Found: C, 64.35; H, 4.24; N, 11.69 %. IR (KBr disc, cm^{-1}): 3422 (O–H), 3062 (Ar–C–H), 1700 (C=O), 1385 (–N=N–). ^{1}H-NMR (300 MHz, DMSO-d_6, δ / ppm): 10.20 (OH), 9.95 (CHO), 7.45–7.60 (Ar–H). Λ_M / Ω^{-1} cm^2 mol^{-1}: 11.

*Synthesis of 2,4-dihydroxy-5-[(E)-phenyldiazenyl]benzaldehyde oxime (H_3salox) (**2**)*

The oxime ligand was prepared by the reaction of hydroxylammonium chloride ($NH_2OH{\cdot}HCl$) with 2,4-dihydroxy-5-[(*E*)-phenyldiazenyl]benzaldehyde. $NH_2OH{\cdot}HCl$ (0.50 g, 7.2 mmol) and a-sal (1.215 g, 5.0 mmol) were taken in MeOH. The resulting mixture was neutralized with a few drops of 1 M NaOH solution and refluxed for 4–5 h. The precipitated compound was filtered, washed with cold MeOH and dried under vacuum.

*Synthesis of [Ni(H_2salox)$_2$] (**3**)*

A solution of H_3salox (0.257 mg, 1.0 mmol) in EtOH (25 mL) was added drop-wise to a solution of $NiCl_2{\cdot}6H_2O$ (0.12 g, 0.50 mmol) in EtOH (20 mL) at room temperature under air. The brown solution (pH 8) was stirred for 3 h, during which time it went darker and a dark green solid was formed. The solid was filtered and washed with cold EtOH and dried under vacuum.

*Synthesis of [Cu(H_2salox)$_2$] (**4**)*

This dark green complex was prepared by a procedure similar to that employed for the synthesis of [Ni(H_2salox)$_2$] but using $CuCl_2{\cdot}2H_2O$ (0.086 g, 0.50 mmol) instead of $NiCl_2{\cdot}6H_2O$.

*Synthesis of [Co(H_2salox)$_2$] (**5**)*

Cobalt(II) chloride hexahydrate (0.12 g, 0.50 mmol) in 10 mL of EtOH was added to a hot EtOH solution of H_3salox (1:2 molar ratio). The mixture was stirred for 5 h at room temperature with air bubbling, giving a reddish brown precipitate. The precipitate was collected by filtration, washed with cold EtOH, then Et_2O and dried in a desiccator.

Antibacterial and antifungal activities

The new salicylaldoxime derivative ligand and its metal complexes were evaluated for both their *in vitro* antibacterial activity against *Escherichia coli*, *Staphylococcus aureus*, *Klebsiella pneumoniae*, *Mycobacterium smegmatis*, *Pseudomonas aeruginosa*, *Enterococcus cloacae*, *Bacillus megaterium* and *Micrococcus luteus* and their *in vitro* antifungal activity against *Kluyveromyces fragilis*, *Rhodotorula rubra* and *Saccharomyces cerevisiae* by the disc diffusion method.[9]

RESULTS AND DISCUSSION

Synthesis

2,4-Dihydroxy-5-[(*E*)-phenyldiazenyl]benzaldehyde oxime (H_3salox) was prepared by the reaction of 2,4-dihydroxy-5-[(*E*)-phenyldiazenyl]benzaldehyde with hydroxylamine hydrochloride in EtOH at room temperature. The product of the condensation reaction of 2,4-dihydroxy-5-[(*E*)-phenyldiazenyl]benzaldehyde with hydroxylamine hydrochloride is depicted in Fig. 1. The new oxime ligand, 2,4-dihydroxy-5-[(*E*)-phenyldiazenyl]benzaldehyde oxime (H_3salox), gave mononuclear complexes (Fig. 2) with Ni(II), Co(II) and Cu(II) as follows:

$$2H_3\text{salox} + MX_2{\cdot}nH_2O \rightarrow M(H_2\text{salox})_2 + 2HX + nH_2O$$

where H_3salox: 2,4-dihydroxy-5-[(*E*)-phenyldiazenyl]benzaldehyde oxime; M: Ni(II), Co(II) or Cu(II); X: Cl; *n*: 6 or 2.

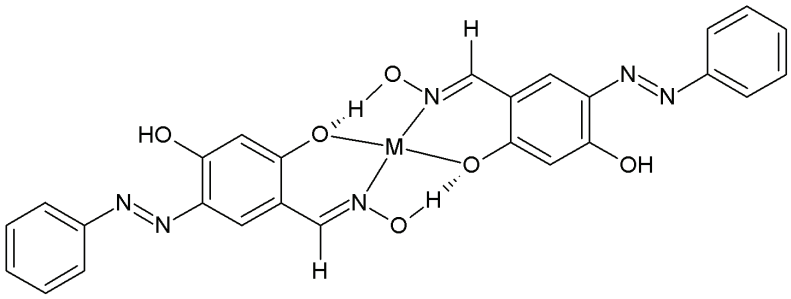

Fig. 2. The proposed structure of the metal complexes of the substituted salicylaldoxime ligand.

Analytic and spectral data of the ligand and its complexes

*2,4-Dihydroxy-5-[(*E*)-phenyldiazenyl]benzaldehyde oxime (H_3salox)* (***2***). Yield: 0.61 g (48 %); m.p.: 165 °C. Anal. Calcd. for $C_{13}H_{11}N_3O_3$ (*FW*: 257.25): C, 60.70, H, 4.31; N, 16.33 %. Found: C, 60.49; H, 4.11; N, 16.47 %. IR (KBr, cm^{-1}): 3434 (O–H), 3135 (N–H), 3037 (Ar–C–H), 1716 (O–H···O), 1639 (C=N), 1385 (–N=N–), 960 (N–O). ^{1}H-NMR (300 MHz, DMSO-d_6, δ / ppm): 14.15 (C=N–OH), 10.20 (OH), 8.55 (–CHO), 7.45–7.60 (Ar–H), 6.42 (N–H); UV–Vis (DMF) (λ_{max} / nm): 287, 348, 421. Λ_M / Ω^{-1} cm^2 mol^{-1}: 14.

[Ni(H_2salox)$_2$] (***3***). Yield: 0.25 g (89 %); m.p. > 250 °C; Anal. Calcd. for $C_{26}H_{20}N_6NiO_6$ (*FW*: 571.17): C, 54.67, H, 3.53; N, 14.71; Ni, 10.28 %. Found: C, 54.49; H, 3.61; N, 14.62; Ni, 10.36 %. IR (KBr, cm^{-1}): 3384 (O–H), 3049 (Ar–C–H), 1710 (O–H···O), 1629 (C=N), 1389 (–N=N–), 935 (N–O), 524 (Ni–O), 418 (Ni–N); UV–Vis (DMF) (λ_{max} / nm): 275, 340, 440, 647; Λ_M / Ω^{-1} cm^2 mol^{-1}: 21.

[Cu(H_2salox)$_2$] (***4***). Yield: 0.20 g (69 %); m.p.: > 250 °C; Anal. Calcd. for $C_{26}H_{20}N_6CuO_6$ (*FW*: 576.02): C, 54.21, H, 3.50; N, 14.59; Cu, 11.01 %. Found:

C, 54.34; H, 3.41; N, 14.63; Cu, 11.25 %. IR (KBr, cm^{-1}): 3448.5 (O–H), 3058 (Ar–C–H), 1716 (O–H···O), 1632 (C=N), 1385 (–N=N–), 939 (N–O), 511 (Cu–O), 424 (Cu–N). UV–Vis (DMF) (λ_{max} / nm): 276, 326, 430, 501, 514. Λ_M / Ω^{-1} cm^2 mol^{-1}: 19.

*[Co(H$_2$salox)$_2$] (**5**)*. Yield: 0.18 g (64 %); m.p.: >250 °C. Anal. Calcd. for $C_{26}H_{20}N_6CoO_6$ (*FW*: 571.41): C, 54.65, H, 3.53; N, 14.71; Co, 10.31 %. Found: C, 54.47; H, 3.63; N, 14.60; Co, 10,39 %. IR (KBr, cm^{-1}): 3383 (O–H), 3049 (Ar–C–H), 1720 (O–H···O), 1631 (C=N), 1386 (–N=N–), 941 (N–O), 526 (Co–O), 437 (Co–N). UV–Vis (DMF) (λ_{max} / nm): 279, 345, 436, 598, 661. Λ_M / Ω^{-1} cm^2 mol^{-1}: 23.

The experimental results of the elemental analyses of the synthesized ligand and its metal chelates are in good agreement with theoretical expectations. The elemental analyses of the complexes indicate that the metal–ligand ratios were 1:2 in the [M(H$_2$salox)$_2$] [M = Ni(II), Co(II), or Cu(II)], metal complexes. The level of impurity in the products was checked by TLC. The synthesized ligand and its mononuclear complexes were soluble in water giving stable solutions at room temperature. The low conductances of the chelates support the non-electrolytic nature of the metal complexes. Single crystals of the new oxime ligand and its transition metal chelates could not be isolated from any organic solution, thus, no definite structures could be described. However, the analytical and spectroscopic data enables possible structures, as shown in Figs. 1 and 2, to be predicted.

Spectral characterization

The ^{1}H-NMR data recorded in DMSO-d_6 provided further evidence for the structural characteristics of the oxime ligand. The ^{1}H-NMR spectrum of the a-sal compound displayed the presence of a broad sınglet signal due to the hydrogen of aldehyde group at 9.95 ppm, which is lower field shifted to 8.55 ppm in the spectrum of the aldoxime ligand through the oximation reaction.[10] The spectrum of the H$_3$salox ligand exhibited multiplet signals at 7.45–7.60 ppm due to aromatic protons.[11] The strong signals appearing in the chemical shift ranges 6.42––6.45 ppm can be attributed to the hydrogen of the –NH of the keto structure (Fig. 3). In addition, the spectrum of the ligand H$_3$salox showed a singlet signal at 10.20 ppm due to the hydrogen of the –OH group. The ^{1}H-NMR spectrum of the ligand exhibited a signal at 14.20 ppm, which can be attributed to the hydrogen bonded OH proton of the hydroxyimino group.

The electronic spectra of the complexes in 10^{-3} M DMF solutions at room temperature were recorded. The electronic spectra can often provide quick and reliable information about the ligand arrangement in transition metal complexes. The electronic spectra of the ligand and its metal complexes in DMF showed 3–5 absorption bands between 275 and 661 nm. The ligand showed absorption bands at 421, 348 and 287 nm. These bands are assigned to the n $\rightarrow$ π^* and $\pi \rightarrow \pi^*$ transitions, respectively.[12] The electronic absorption spectrum of the [Ni(H$_2$salox)$_2$]

complex showed weak bands at 647 and 440 nm, which are assigned to the $^1A_{1g} \rightarrow {}^1B_{1g}$ and $^1A_{1g} \rightarrow {}^1A_{2g}$ transitions, respectively. A d^8 metal ion, Ni(II) exhibits a preference for square planar geometry with oxime complexes. The decrease in the intensities of the transitions indicated coordination to the nitrogen atoms. The band at 340 nm is due to the charge-transfer transition and that at 275 nm is due to $\pi \rightarrow \pi^*$ transitions. The $[Cu(H_2salox)_2]$ complex exhibited bands at 514 and 501 nm, which can be assigned to d → d transitions, while absorption band at 430 nm is assignable to the charge-transfer transition. The bands at 326 and 276 nm are assigned to the $n \rightarrow \pi^*$ and $\pi \rightarrow \pi^*$ transitions, respectively. The electronic absorption spectrum of the Co(II) complex showed weak bands at 661 and 598 nm, which can be assigned to the d → d transitions $^2B_{2g} \rightarrow {}^2E_g$ and $^1A_{1g} \rightarrow {}^1B_{1g}$. This agrees with square-planar geometry.[13] The band at 436 nm is due to the charge-transfer transition, and the bands at 345 and 279 nm are assigned to the $n \rightarrow \pi^*$ and $\pi \rightarrow \pi^*$ transitions, respectively. The suggested structural formulae of the metal-oxime complexes under investigation are given in Fig. 2.

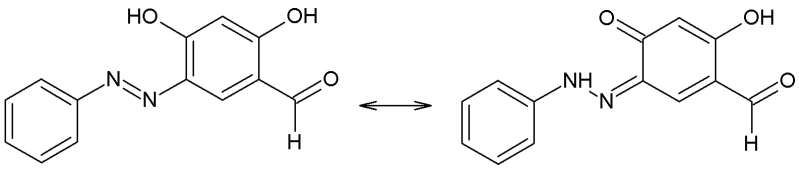

Fig. 3. Tautomerism in the a-sal compound.

The IR spectra of the free ligand and metal complexes were recorded in the range 4000–400 and 400–100 cm^{-1}. The infrared spectrum of the substituted salicylaldoxime ligand showed strong and broad bands due to the hydrogen-bonded phenolic OH at *o*-position in the region 3000–2800 cm^{-1}. It also exhibited two separate OH bands due to the oxime OH at 3237 and 3137 cm^{-1} and phenolic OH at 3400 cm^{-1}. The IR spectrum of the ligand showed a broad band between 3200 and 3450 cm^{-1}, which can be attributed to the phenolic OH group. The IR spectra provide valuable information regarding the nature of the functional group attached to the metal atom. The medium bands observed in the 1646–1620 cm^{-1} frequency ranges in the complexes were assigned to the ν(C=N) mode. The shift of the ν(C=N) vibration in all the complexes to a lower frequency suggests that the nitrogen atom of the ring contributes to the complexation. The lower ν(C=N) frequency also indicates stronger M–N bonding. In the IR spectra of the complexes, a band was observed between 430 and 460 cm^{-1}, which is attributed to ν(M–N) stretching vibrations.[14] Another band appeared between 660 and 672 cm^{-1}, which is assigned to the interaction of the phenolic oxygen to the metal atom, *i.e.*, the stretching vibrations *ν*(M–O).

Biological activity

The antibacterial and antifungal activity of the new compounds were tested using the disc diffusion method.[15] The antibacterial and antifungal activities of the compounds against eight bacteria, namely *E. coli*, *S. aureus*, *K. pneumoniae*, *M. smegmatis*, *P. aeruginosa*, *E. cloacae*, *B. megaterium* and *M. luteus*, and three fungi, namely *K. fragilis*, *R. rubra* and *S. cerevisiae*, are presented in Table I.

TABLE I. Antimicrobial effects of the synthesized compounds, a-sal (**1**), H_3salox (**2**), [Ni(H_2salox)$_2$] (**3**), [Cu(H_2salox)$_2$] (**4**) and [Co(H_2salox)$_2$] (**5**); concentration: 2000 ppm; 50 µl well^{-1}; 50 mL/disc (A – *E. coli*, B – *S. aureus*, C – *K. pneumoniae*, D – *M. smegmatis*, E – *P. aeruginosa*, F – *E. cloacae*, G – *B. megaterium*, H – *M. luteus*, I – *K. fragilis*, J – *R. rubra*, K – *S. cerevisiae*)

Compound	Diameter of inhibition zone, mm										
	Bacteria								Fungi		
	A	B	C	D	E	F	G	H	I	J	K
a-sal (**1**)	8	9	8	8	–	7	7	9	8	–	11
H_3salox (**2**)	–	–	–	–	–	–	–	–	–	–	16
[Ni(H_2salox)$_2$] (**3**)	–	–	–	–	–	–	–	–	–	–	8
[Cu(H_2salox)$_2$] (**4**)	–	7	–	8	–	–	–	–	–	–	12
[Co(H_2salox)$_2$] (**5**)	–	–	–	–	–	–	–	–	–	8	18

The results showed that the bidentate ligand exhibited activity against none of the tested species of bacteria, *E. coli*, *S. aureus*, *K. pneumoniae*, *M. smegmatis*, *P. aeruginosa*, *E. cloacae*, *B. megaterium* and *M. luteus*, nor against the fungi *K. fragilis* and *R. rubra*. The H_3salox ligand (**2**) had the highest effect against the fungus *S. cerevisiae*. The results indicate that the [Ni(H_2salox)$_2$] chelate (**3**) showed no activity except against *S. cerevisiae* under identical experimental conditions. However, the Cu(II) metal chelate of the ligand (**4**) showed low effects against *S. aureus* and *M. smegmatis* bacteria and *S. cerevisiae* fungus. The [Co(H_2salox)$_2$] chelate (**5**) had the highest activity against *S. cerevisiae* fungus, but it had low activity against *R. rubra* fungus. The complex has no activity against the other bacteria and fungi. The variation in the activity of the different metal complexes against the different microorganisms depends either on the impermeability of the cells of the microbes or differences in the ribosomes in the microbial cells.[10,16]

CONCLUSIONS

In this study, a phenolic oxime ligand, 2,4-dihydroxy-5-[(*E*)-phenyldiazenyl]benzaldehyde oxime (Fig. 1), derived from 2,4-dihydroxy-5-[(*E*)-phenyldiazenyl]benzaldehyde and hydroxylamine in EtOH, and some of its transition metal complexes were prepared. The analytical data and the spectroscopic studies suggested that the complexes had the general formula [M(H_2salox)$_2$], where M is nickel(II), cobalt(II) or copper(II). The molar conductance measurements of the

complexes showed their non-electrolytic nature. According to the UV–Vis and IR data of the phenylazo linked oxime ligand, H_3salox (**2**) was coordinated to the metal ion through the oxime nitrogen and oxygen atom of the hydroxyl group in salicylaldehyde.

Based on the obtained results, the structure of the coordination compounds under investigation can be formulated as in Fig. 2.

ИЗВОД

СИНТЕЗА, КОМПЛЕКСИРАЊЕ, СПЕКТРАЛНА, АНТИБАКТЕРИЈСКА И АНТИФУНГАЛНА АКТИВНОСТ ОКСИМА 2,4-ДИХИДРОКСИ-5-[(*E*)-ФЕНИЛДИАЗЕНИЛ]БЕНЗАЛДЕХИДА

M. KURTOGLU

Department of Chemistry, Kahramanmaraş Sütçü İmam University, Kahramanmaraş, 46050, Turkey

У реакцији између 2,4-дихидрокси-5-[(*E*)-фенилдиазенил]бензалдехида и хидроксиламина у етанолном раствору на собној температури синтетизован је оксим 2,4-дихидрокси-5-[(*E*)-фенилдиазенил]бензалдехида (H_3salox) (**2**). Овај лиганд је употребљен за синтезу мононуклеарних Ni(II), Co(II) и Cu(II) комплекса у којима је H_3salox лиганд бидентатно координован за испитиване јоне метала. За карактеризацију [Ni(H_2salox)$_2$] (**3**), [Cu(H_2salox)$_2$] (**4**) и [Co(H_2salox)$_2$] (**5**) комплекса употребљене су различите технике, као што су елементална (C, H и N) анализа, кондуктометријска мерења, инфра-црвена и електронска апсорпциона спектроскопија. Такође, у овом раду приказан је и ^{1}H-NMR спектар H_3salox (**2**) лиганда. У испитиваним Ni(II), Co(II) и Cu(II) комплексима H_3salox (**2**) лиганд је координован преко N и O донорских атома, при чему су за један јон метала координована два лиганда. Антибактеријска активност H_3salox лиганда и одговарајућих комплекса метала испитвана је на осам врста бактерија, као што су: *Escherichia coli*, *Staphylococcus aureus*, *Klebsiella pneumoniae*, *Mycobacterium smegmatis*, *Pseudomonas aeruginosa*, *Enterococcus cloacae*, *Bacillus megaterium* и *Micrococcus luteus*. Поред тога, испитивана је антифунгала активност на три врсте гљива и то: *Micrococcus luteus*, *Rhodotorula rubra* и *Saccharomyces cerevisiae*.

(Примљено 18. новембра, ревидирано 22. децембра 2009)

REFERENCES

1. a) H. A. Kists, E. F. Szymanski, D. E. Dorman, *J. Antibiot.* **28** (1975) 286; b) V. V. Ponomareva, N. K. Dalley, K. Xiaolan, N. N. Gerasimchuk, K. V. Domasevich, *J. Chem. Soc. Dalton Trans.* (1996) 2351; c) E. Abele, R. Abele, E. Lukevics, *Chem. Heterocycl. Compd.* **39** (2003) 825; d) C. J. Milios, T. C. Stamatatos, S. P. Perlepes, *Polyhedron* **25** (2006) 134
2. B. K. Singh, U. K Jetley, R. K. Sharma, B. S Garg, *Spectrochim. Acta A* **68** (2007) 63
3. I. Georgieva, N. Tredafilova, G. Bauer, *Spectrochim. Acta A* **63** (2006) 403
4. M. S. S. Babu, K. H. Reddy, P. G. Krishna, *Polyhedron* **26** (2007) 5721
5. Y. Gök, S. Karaböcek, H. Kantekin, *Transition Met. Chem.* **20** (1995) 234
6. a) S. Serin, M. Kurtoğlu, *Analyst* **119** (1994) 2213; b) M. Kurtoğlu, N. Birbiçer, Ü. Kimyonşen, S. Serin, *Dyes Pigm.* **41** (1999)141; c) N. Birbiçer, M. Kurtoğlu, S. Serin, *Synth. React. Inorg. Met.-Org. Chem.* **29** (1999) 1353; d) N. Kurtoğlu, M. Kurtoğlu, S. Serin. *Synth. React. Inorg. Met.-Org. Chem.* **29** (1999) 1779

7. a) M. Kurtoğlu, S. Serin, *Synth. React. Inorg. Met.-Org. Chem.* **31** (2001) 1129; b) M. Kurtoğlu, S. Serin, *Synth. React. Inorg. Met.-Org. Chem.* **31** (2001) 1229; c) M. Kurtoğlu, *Synth. React. Inorg. Met.-Org. Chem.* **34** (2004) 967
8. a) M. Kurtoğlu, S. Serin, *Synth. React. Inorg. Met.-Org. Chem.* **32** (2002) 629; b) M. Kurtoğlu, S. A. Baydemir, *J. Coord. Chem.* **60** (2007) 655
9. N. Kurtoğlu, *J. Serb. Chem. Soc.* **74** (2009) 917
10. M. Kurtoğlu, E. Ispir, N. Kurtoğlu, S. Serin, *Dyes Pigm.* **77** (2008) 75
11. R. M. Silverstein, G. C. Bassler, T. C. Morrill. *Spectrometric Identification of Organic Compounds*, 5th ed., Wiley, New York, 1991
12. K. Krishnankutty, M. B. Ummathur, P. Ummer, *J. Serb. Chem. Soc.* **74** (2009) 1273
13. L. Mitu, N. Raman, A. Kriza, N. Stănică, M. Dianu, *J. Serb. Chem. Soc.* **74** (2009) 1075
14. M. F. R. Fouda, M. M. Abd-Elzaher, M. M. E. Shakdofa, F. A. El Saied, M. I. Ayad, A. S. El-Tabl, *Transition Met. Chem.* **33** (2008) 219
15. C. H. Collins, P. M. Lyne, *Microbial Methods*, University Park Press, Baltimore, 1970
16. A. S. El-Tabl, F. A. El-Saied, W. Plass, A. N. Al-Hakimi, *Spectrochim. Acta A* **71** (2008) 90.

Journal of the Serbian Chemical Society
JSCS-info@shd.org.rs • www.shd.org.rs/JSCS
J. Serb. Chem. Soc. *75* (9) 1241–1249 (2010)
JSCS–4047
UDC 547.686.004.12:548.12:519.6
Original scientific paper

Diradical character of some fluoranthenes

SVETLANA MARKOVIĆ*, JELENA ĐURĐEVIĆ, SVETLANA JEREMIĆ and IVAN GUTMAN#

Faculty of Science, University of Kragujevac, 12 Radoja Domanovića, 34000 Kragujevac, Serbia

(Received 19 April, revised 18 May 2010)

Abstract: It is shown that some Kekuléan fluoranthenes are diradicals and that their ground state is a triplet. In the energetically less favorable singlet state, these hydrocarbons also exhibit pronounced diradical character. The diradical character *y* of the compounds under investigation was estimated using the unrestricted symmetry-broken (*y*PUHF) and complete active space (*y*NOON) methods. It was found that the *y*PUHF values better reproduce the diradical character of the investigated hydrocarbons. It was shown that singly occupied molecular orbital (SOMO) and SOMO-1 of a diradical structure occupy different parts of space with a small shared region, resulting in a spin density distribution over the entire molecule. The spatial diradical distribution in the singlet diradical structures was examined by inspecting the HOMOs and LUMOs for α and β spin electrons. It was shown that the α-HOMO and the β-LUMO (as well as the β-HOMO and the α-LUMO) occupy practically the same part of space. In this way, there are no unpaired electrons in a singlet diradical structure, yet two of them occupy different parts of space, thus allowing the π-electrons to delocalize.

Keywords: fluoranthenes; diradical; singlet diradical; triplet diradical; unrestricted symmetry-broken method; complete active space calculation.

INTRODUCTION

Density functional theory calculations of large systems sometimes produce energetically quasi-degenerate orbitals that cause a static correlation effect. Although computationally demanding, the complete active space (CAS) method is a straightforward way to include a correction of the static correlation. One of the alternatives to decrease the computational costs is the unrestricted symmetry-broken method, which allows a spin-symmetry breaking and approximates the static correlation correction by splitting α and β electrons into two different orbitals. In

* Corresponding author. E-mail: mark@kg.ac.rs
# Serbian Chemical Society member.
doi: 10.2298/JSC100419080M

the symmetry-broken method, a singlet spin state with strong static correlation is expressed as a singlet diradical.

A singlet diradical can be defined as a molecular species that has all electrons paired, but a pair of these electrons occupies different parts of space with a small shared region. The ground state of such species is a singlet, yet they exhibit diradical character. On the other hand, a pure diradical is a molecular species with two electrons occupying two degenerate, or nearly degenerate, molecular orbitals. We are interested in the usual case when this diradical is in a triplet ground state. In this paper, we are concerned with Kekuléan diradical hydrocarbons, *i.e.*, hydrocarbons for which at least one Kekulé structural formula can be written.

The electronic structure of singlet diradicals with Kekulé structures has attracted much attention.[1–14] Experimental and theoretical methods were used to investigate the diradical character of Chichibabin's hydrocarbon,[1] substituted fluoranthenes,[3] linear polyacenes,[4,7,9,14] phenalenyl-based hydrocarbons,[5,6,8,11–13] and zethrenes.[10] On the other hand, the question whether Kekuléan system can exist in a triplet ground state has been less thoroughly examined. An assumption that a sufficiently small HOMO–LUMO gap should allow the promotion of an electron to produce a diradical resulted in cyclohepta[*def*]fluorene[15] and nonacene and higher linear polyacenes[16–18] being proposed as possible representatives of triplet Kekuléan hydrocarbons. However, cyclohepta[*def*]fluorene has never been synthesized. In addition, Bendikov *et al*. showed that the RB3LYP wave function becomes unstable for polyacenes as small as hexacene, and all higher polyacenes,[4] implying that the calculated energies for singlet states are unrealistically high. They performed reoptimization applying the unrestricted symmetry-broken method and showed that higher polyacenes exist in a singlet state with a large amount of diradical character. In agreement with the findings of Bendikov *et al*., high level *ab initio* calculations showed that the ground state of linear polyacenes is a singlet for all chain lengths from naphthalene to dodecacene.[9] Furthermore, the assumptions that anthracene-2,3-dimethylene,[19] cyclopenta[*a*]cyclopenta[*i*]anthracene,[20] as well as pleiadene and benzopleiadene[21–24] are triplet Kekuléan hydrocarbons have never been confirmed.

The only Kekuléan hydrocarbon the triplet state of which has been confirmed experimentally is 2,2-dimethyl-2*H*-dibenzo[*cd*,*k*]fluoranthene (**6** in Fig. 1).[3,25] The compound was generated photochemically and examined spectroscopically in a cryogenic matrix and in solution using nanosecond laser flash photolysis. On the basis of spectroscopic measurements, trapping experiments and DFT calculations, the singlet–triplet gap of **6** was estimated to be 3.3–5.4 kJ/mol in favor of the triplet. It is worth mentioning that the DFT calculation was actually performed on a relative of **6** (the compound in which – for the sake of computational feasibility – the methyl groups of **6** were replaced with H atoms).

In a series of recent papers,[26–35] we studied various π-electron properties of fluoranthenes were studied including also their Kekulé structures.[33,34] Based on the observations made in,[33,34] some triplet-ground-state Kekuléan fluoranthenes were recognized.[35]

Fluoranthenes are polycyclic conjugated hydrocarbons consisting of two benzenoid units joined through a five-membered ring.[26] Interest in nonalternant polycyclic compounds of this kind has recently greatly increased, after the discovery that these compounds are formed from benzenoid hydrocarbons in flash vacuum pyrolysis experiments.[36,37] As fluoranthenes are Kekuléan hydrocarbons, one would expect a singlet ground state for them. Surprisingly, DFT calculations revealed that some fluoranthenes are diradicals, implying that their triplet ground state is energetically more favorable in comparison to the singlet state. In addition, their singlet ground state possesses a significant amount of diradical character. This phenomenon was explained by the tendency of the investigated molecules to delocalize their π-electrons. This leads to aromatic stabilization, which is stronger than the destabilization caused by the unpaired electrons.

In this work, some additional fluoranthene diradicals are reported. The triplet hydrocarbon **6** and the well-defined singlet fluorantheno[8,9-*b*]triphenylene (**7** in Fig. 1) were included in the investigation. The diradical character of the fluoranthenes under investigation is discussed in detail.

COMPUTATIONAL METHODS

All calculations were performed with the Gaussian 03W, version 6.1, program package,[38] at the B3LYP/6-311G(d,p) level of theory.[39,40] The frequency calculations showed that the examined structures have no imaginary vibrational frequencies. The hydrocarbons were calculated in their singlet and triplet states using the restricted and unrestricted schemes for closed-shell and open-shell calculations, respectively.

The singlet diradical character of the investigated hydrocarbons was estimated using two approaches. In the first approach, a CASSCF(6,6) method in the RB3LYP/6-311G(d,p) optimized geometry was used. The diradical index *y*NOON was determined according to the NOON (natural orbital occupation number) analysis,[41] *i.e.*, based on the occupation number (*n*) of the LUMO, resulting from the CAS calculation. In the second approach, a symmetry-broken UB3LYP/6-311G(d,p) method along with geometry optimization was applied. The diradical index *y*PUHF, related to the HOMO and LUMO for singlet states, is defined by the weight of the doubly-excited configuration in the multi-configurational MC-SCF theory, and is formally expressed in the case of the spin-projected UHF (PUHF) theory as:[10,42,43]

$$y_{\mathrm{PUHF}} = 1 - \frac{2T}{1+T^2} \tag{1}$$

where T is the orbital overlap between the corresponding orbital pairs, and can be calculated using the occupation numbers of UHF natural orbitals:

$$T = \frac{n_{\mathrm{HOMO}} - n_{\mathrm{LUMO}}}{2} \tag{2}$$

The applicability of both approaches was tested based on the results for singlet fluoranthene **7** and compound **6**, the triplet state of which has been confirmed experimentally.[3,25]

RESULTS AND DISCUSSION

The optimized geometries of the investigated fluoranthenes are presented in Fig. 1. The molecules **4** and **7** are planar, whereas in **6** only the two methyl groups deviate from planarity. The other investigated molecules afford non-planar geometries, due to the repulsion of the hydrogen atoms located on the opposite sides of the bays. The results of this research are summarized in Table I.

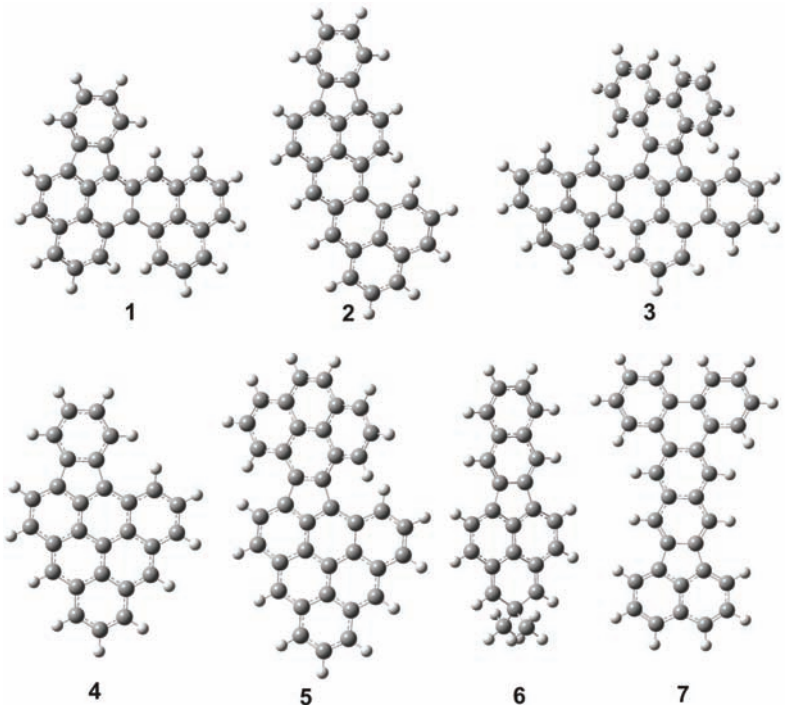

Fig. 1. Optimized geometries of triplet (**1**–**6**) and singlet (**7**) fluoranthenes.

As expected, the application of the symmetry-broken method to the triplet **6** led to a negative singlet–triplet gap, whereby the calculated value perfectly matched the experimental estimation. In the case of **7,** the singlet–triplet gap was positive. In addition, there was no energy lowering ($\Delta E_{OS–CS}$ = 0.0 kJ/mol) or invoked structural changes, in comparison to the closed-shell calculation. These findings are in harmony with the fact that **7** is a singlet Kekuléan hydrocarbon. All these facts confirm the applicability of the unrestricted symmetry-broken method to the hydrocarbons under investigation. According to the values for ΔET–OS and ΔEOS–CS in Table I, hydrocarbons **1**–**6** are pure diradicals, the less favorable

singlet states of which are best described by the unrestricted symmetry-broken method, and show pronounced diradical character.

TABLE I. Difference in the total energy (kJ mol^{-1}) between the open-shell symmetry-broken singlet and the closed-shell RB3LYP solution (ΔEOS-CS), singlet–triplet gap (ΔET-OS), *n*LUMO and diradical character *y* (%), calculated using the NOON and PUHF approaches, and the orbital overlap *T*

Compound	ΔE_{OS-CS}[a]	ΔE_{T-OS}[b]	*n*LUMO (NOON)	*y*NOON	*n*LUMO (PUHF)	*T*	*y*PUHF
1	–37.3[26]	–16.5[26]	0.431	43	0.979	0.021	96
2	–36.5[26]	–16.1[26]	0.495	50	0.955	0.045	91
3	–12.5	–10.9	0.175	18	0.943	0.057	89
4	–23.9	–17.7	0.085	8	0.890	0.110	78
5	–5.4[26]	–5.2[26]	0.128	13	0.785	0.215	59
6	–32.6[26]	–7.5[26]	0.412	41	0.925	0.075	85
7	0.0	192.4	0.083	8	0.293	0.707	6

[a]Open shell singlet energy minus RB3LYP singlet energy; [b]triplet energy minus open shell singlet energy

The diradical character of the investigated compounds is numerically expressed by means of the *y*NOON and *y*PUHF values (Table I). It is worth pointing out that both approaches assume that the diradical index ranges from 0 % for the closed-shell state to 100 % for the pure diradical state. Taking into account that **1**–**6** are pure diradicals, the *y*NOON values are relatively low. In addition, the value for the singlet hydrocarbon **7** (8 %) is identical to that for the triplet fluoranthene **4**. On the other hand, the *y*PUHF value for **7** (6 %) is negligible in comparison to the significantly higher *y*PUHF values for triplet hydrocarbons. In addition, the orbital overlap *T* decreases with increasing diradical character. It turns out that, in spite of the simplicity of the scheme using theunrestricted natural orbitals (UNOs), it successfully reproduces the diradical character of the investigated molecules.

The unpaired electrons reside in the delocalized singly occupied molecular orbitals (SOMOs) of each diradical. As an illustration, the SOMO, SOMO-1, and spin density map for triplet **1** (**1T**) are presented in Fig. 2. The SOMO and SOMO-1 are almost degenerate (–0.173 and –0.182 eV). Obviously, SOMO and SOMO-1 occupy different parts of space with a small shared region, resulting in a spin density distribution over the entire molecule.

The spatial diradical distribution in the singlet diradical structures was examined by inspecting the HOMOs and LUMOs for the α and β spin electrons. The frontier orbitals for the α and β spin electrons of triplet **1** and singlet **7**, calculated using the unrestricted symmetry-broken method (**1OS** and **7OS**), are depicted in Figs. 3 and 4, respectively. A remarkable feature of Fig. 3 is that the α-HOMO and β-LUMO of **1OS** occupy practically the same part of space, involving approximately 0.51+0.49 electrons. The same situation was found in the case of the β-

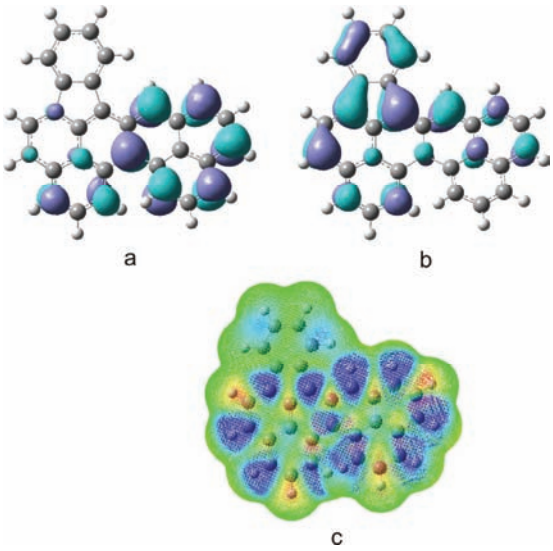

Fig. 2. SOMO (a), SOMO-1 (b), and spin density map (c) for **1T**. In the spin density map, the blue and red regions indicate the highest and lowest spin density values, respectively. In the grayscale presentation the dark regions indicate the highest spin density values.

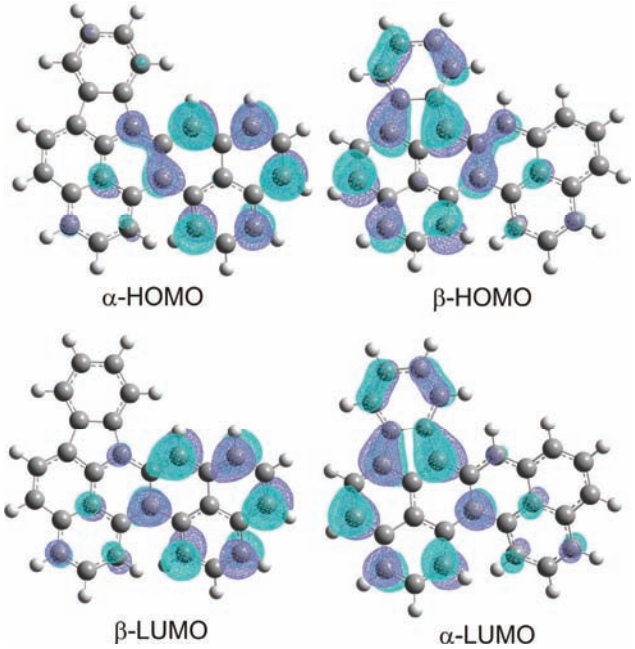

Fig. 3. Frontier orbitals for **1OS**.

-HOMO and α-LUMO. In this way, there are no unpaired electrons in **1OS**, yet two of them occupy different parts of space, thus allowing the π-electrons to delocalize. The situation is quite different in **7OS** (Fig. 4). Here, the α-HOMO and

β-HOMO, as well as the α-LUMO and β-LUMO, are of almost identical shapes. Thus, the HOMO and LUMO are occupied with 1.71 and 0.29 electrons, respectively. In addition, there is a noticeable shared region between the HOMO and LUMO, which is in agreement with the high *T* value for **7** (Table I). The frontier orbitals for the α and β spin electrons clearly reflect the triplet and singlet nature of the compounds **1** and **7**.

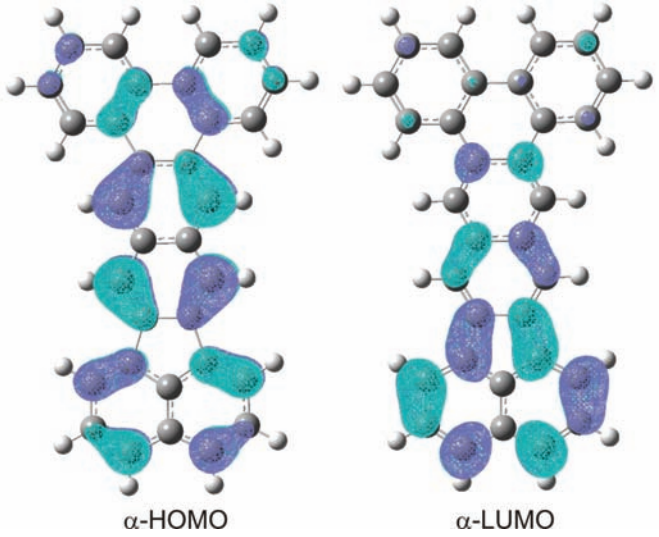

Fig. 4. Frontier orbitals for **7OS**. The shapes of the β-HOMO and β-LUMO are almost identical to those of the α-HOMO and α-LUMO.

CONCLUSIONS

The unrestricted symmetry-broken method was applied to the triplet 2,2-dimethyl-2*H*-dibenzo[*cd*,*k*]fluoranthene (**6**) and the singlet fluorantheno[8,9-*b*]triphenylene (**7**). The excellent agreement with the experimental results confirms the applicability of the symmetry-broken method to the Kekuléan fluoranthenes **1**–**5**. The triplet ground state of **1**–**6** was confirmed by the negative singlet–triplet gap values. These compounds tend to delocalize their π-electrons and thus they take up diradical structures. Even in the singlet state, these Kekuléan hydro-carbons show a pronounced diradical character, and their structures are best presented with those of singlet diradicals. Such structures provide a possibility for an electron pair to occupy different parts of space and allows for the achievement of aromatic stabilization. The diradical index y_{NOON} is not in good agreement with the diradical character of the investigated molecules. On the other hand, y_{PUHF} successfully reproduces the diradical character of the investigated molecules.

Acknowledgements. This work is supported by the Ministry of Science and Technological Development of the Republic of Serbia, Project Nos. 144015G and 142025.

ИЗВОД

ДИРАДИКАЛСКИ КАРАКТЕР НЕКИХ ФЛУОРАНТЕНА

СВЕТЛАНА МАРКОВИЋ, ЈЕЛЕНА ЂУРЂЕВИЋ, СВЕТЛАНА ЈЕРЕМИЋ и ИВАН ГУТМАН

Природно-математички факултет, Универзитет у Крагујевцу, Крагујевац

Показано је да су неки флуорантени дирадикали, тј. да је њихово основно стање триплетно. И у енергетски неповољнијем синглетном стању ови угљоводоници показују изразит дирадикалски карактер. Дирадикалски карактер испитиваних једињења процењен је помоћу unrestricted symmetry-broken (y_{PUHF}) и complete active space (y_{NOON}) метода. Нађено је да y_{PUHF} вредности успешније репродукују дирадикалски карактер испитиваних угљоводоника. Показано је да SOMO и SOMO-1 орбитале за дирадикалску структуру заузимају различите делове простора са малом заједничком регијом, што резултира расподелом спинске густине преко целог молекула. Просторна дирадикалска расподела у синглетно-дирадикалским структурама је испитана на основу облика HOMO и LUMO орбитала за електроне α и β спина. Показано је да α-HOMO и β-LUMO (као и β-HOMO и α-LUMO) заузимају практично исти део простора. На овај начин, у синглетном дирадикалу нема неспарених електрона, али два електрона ипак заузимају различите делове простора, што омогућава делокализацију π-електрона.

(Примљено 19. априла, ревидирано 18. маја 2010)

REFERENCES

1. L. K. Montgomery, J. C. Huffman, E. A. Jurczak, M. P. Grendze, *J. Am. Chem. Soc.* **108** (1986) 6004
2. K. Yamaguchi, F. Jensen, A. Dorigo, K. N. Houk, *Chem. Phys. Lett.* **149** (1988) 537
3. D. R. McMasters, J Wirz, *J. Am. Chem. Soc.* **123** (2001) 238
4. M. Bendikov, H. M. Duong, K. Starkey, K. N. Houk, E. A. Carter, F. Wudl, *J. Am. Chem. Soc.* **126** (2004) 7416
5. T. Kubo, A. Shimizu, M. Sakamoto, M. Uruichi, K. Yakushi, M. Nakano, D. Shiomi, K. Sato, T. Takui, Y. Morita, K. Nakasuji, *Angew. Chem.* **117** (2005) 6722
6. T. Kubo, M. Sakamoto, K. Nakasuji, *Polyhedron* **24** (2005) 2522
7. J. Poater, J. M. Bofill, P. Alemany, M. Solá, *J. Phys. Chem. A* **109** (2005) 10629
8. T. Kubo, A. Shimizu, M. Uruichi, K. Yakushi, M. Nakano, D. Shiomi, K. Sato, T. Takui, Y. Morita, K. Nakasuji, *Org. Lett.* **9** (2006) 81
9. J. Hachmann, J. J. Dorando, M. Avilés, G. K. L. Chan, *J. Chem. Phys.* **127** (2007) 134309
10. M. Nakano, R. Kishi, A. Takebe, M. Nate, H. Takahashi, T. Kubo, K. Kamada, K. Ohta, B. Champagne, E. Botek, *Co. Le.* **3** (2007) 333
11. J. Huang, M. Kertesz, *J. Am. Chem. Soc.* **129** (2007) 1634
12. M. Nakano, A. Takebe, R. Kishi, H. Fukui, T. Minami, K. Kubota, H. Takahashi, T. Kubo, K. Kamada, K. Ohta, B. Champagne, E. Botek, *Chem. Phys. Lett.* **454** (2008) 97
13. K. Iketaki, K. Kanai, A. Shimizu, T. Kubo, Z. H. Wang, Y. Ouchi, Y. Morita, K. Nakasuji, K. Seki, *J. Phys. Chem. C* **113** (2009) 1515
14. T. Ishida, J. Aihara, *Phys. Chem. Chem. Phys.* **11** (2009) 7197
15. P. Baumgartner, E. Weltin, G. Wagnière, E. Heilbronner, *Helv. Chim. Acta* **48** (1965) 751
16. H. Angliker, E. Rommel, J. Wirz, *Chem. Phys. Lett.* **87**(1982) 208
17. J. Roncali, *Chem. Rev.* **97** (1997) 173
18. K. N. Houk, P. S. Lee, M. Nendel, *J. Org. Chem.* **66** (2001) 5517
19. G. J. Gleicher, D. D. Newkirk, J. C. Arnold, *J. Am. Chem. Soc.* **95** (1973) 2526

20. J. Aihara, *Bull. Chem. Soc. Jpn.* **48** (1975) 3637
21. J. Kolc, J. Michl, *J. Am. Chem. Soc.* **92** (1970) 4147
22. J. Michl, J. Kolc, *J. Am. Chem. Soc.* **92** (1970) 4148
23. R. P. Steiner, J. Michl, *J. Am. Chem. Soc.* **100** (1978) 6413
24. A. Castellan, J. Kolc, J. Michl, *J. Am. Chem. Soc.* **100** (1978) 6687
25. D. R. McMasters, J. Wirz, *J. Am. Chem. Soc.* **119** (1997) 8568
26. I. Gutman, J. Đurđević, *MATCH Commun. Math. Comput. Chem*. **60** (2008) 659
27. I. Gutman, J. Đurđević, A. T. Balaban, *Polycyclic Aromat. Compd*. **29** (2009) 3
28. J. Đurđević, I. Gutman, J. Terzić, A. T. Balaban, *Polycyclic Aromat. Compd*. **29** (2009) 90
29. J. Đurđević, I. Gutman, R. Ponec, *J. Serb. Chem. Soc*. **74** (2009) 549
30. I. Gutman, J. Đurđević, *J. Serb. Chem. Soc*. **74** (2009) 765
31. S. Radenković, J. Đurđević, I. Gutman, *Chem. Phys. Lett.* **475** (2009) 289
32. J. Đurđević, S. Radenković, I. Gutman, S. Marković, *Monatsh. Chem*. **140** (2009) 1305
33. I. Gutman, *Z. Naturforsch*. **65a** (2010) 473
34. D. Vukičević, J. Đurđević, I. Gutman, *J. Serb. Chem. Soc*. 75 (2010) 1093
35. S. Marković, J. Đurđević, S. Jeremić, I. Gutman, *J. Mol. Mod.*, in press
36. A. Necula, L. T. Scott, *J. Anal. Appl. Pyrolysis* **54** (2000) 65 and references therein
37. A. Necula, L. T. Scott, *Polycyclic Aromat. Compd.* **30** (2010) and references therein, in press
38. *Gaussian 03, Revision E.01-SMP*, Gaussian Inc., Pittsburgh, PA, 2003
39. C. Lee, W. Yang, R. G. Parr, *Phys. Rev. B* **37** (1988) 785
40. A. D. Becke, *J. Chem. Phys.* **98** (1993) 5648
41. D. Dönhert, J. Koutecký, *J. Am. Chem. Soc.* **102** (1980) 1789
42. K. Yamaguchi, in: *Self-Consistent Field: Theory and Applications*, R. Carbo, M. Klobukowski, Eds., Elsevier, Amsterdam, 1990, p. 727
43. S. Yamanaka, M. Okumura, M. Nakano, K. Yamaguchi, *J. Mol. Struct. (Theochem)* **310** (1994) 205.

Journal of the Serbian Chemical Society
JSCS-info@shd.org.rs • www.shd.org.rs/JSCS
J. Serb. Chem. Soc. 75 (9) 1251–1257 (2010)
JSCS–4048
UDC 546.72'46–36:666.122.3+544.354–128.2:544.478:665.652.7
Original scientific paper

A study of thermally activated Mg–Fe layered double hydroxides as potential environmental catalysts

MILICA S. HADNAĐEV-KOSTIĆ*#, TATJANA J. VULIĆ# and RADMILA P. MARINKOVIĆ-NEDUČIN#

Faculty of Technology, University of Novi Sad, Bul. cara Lazara 1, Novi Sad, Serbia

(Received 15 January, revised 25 February 2010)

Abstract: Layered double hydroxides (LDHs) and mixed oxides derived after thermal decomposition of LDHs with different Mg–Fe contents were investigated. These materials were chosen because of the possibility to tailor their various properties, such as ion-exchange capability, redox and acid–base and surface area. Layered double hydroxides, $[Mg_{1-x}Fe_x(OH)_2](CO_3)_{x/2}\cdot mH_2O$ (where x presents the content of trivalent ions, x = M(III)/(M(II) + M(III)) were synthesized using the low supersaturation precipitation method. The influence of different Mg/Fe ratios on the structure and surface properties of the LDH and derived mixed oxides was investigated in correlation to their catalytic properties in the chosen test reaction (Fischer–Tropsch synthesis). It was determined that the presence of active sites in the mixed oxides is influenced by the structural properties of the initial LDH and by the presence of additional Fe phases. Furthermore, a synthesis outside the optimal range for the synthesis of single phase LDHs leads to the formation of metastable, multiphase systems with specific characteristics and active sites.

Keywords: Mg–Fe–LDHs; hydrotalcite; anionic clays; Mg–Fe mixed oxides; Fischer–Tropsch reaction.

INTRODUCTION

In recent years, many investigations have been focused on the development of low-cost heterogeneous materials with basic characteristics that could be used in reactions for industrial purposes. Layered double hydroxides, LDHs, are anionic clays that are also known as hydrotalcite-like materials $([M(II)_{1-x}M(III)_x(OH)_2]^{x+}(A_{x/n})^{n-}\cdot mH_2O)$, where x represents the content of trivalent ions, x = M(III)/[M(II) + M(III) and A^{n-} is the anion. LDHs are formed by isomorphic substitution of octahedrally

* Corresponding author. E-mail: hadnadjev@tf.uns.ac.rs
doi: 10.2298/JSC100115092H
Serbian Chemical Society member.

coordinated M(II) cations in brucite-like layers with trivalent cations. The positive charge is compensated by hydrated anions located in the interlayer space together with water forming the layered structure. The properties of LDHs and of thermally derived mixed oxides can be tailored by variation of the M(II), M(III) cations and interlayer ions and different M(II)/M(III) ratios, resulting in their wide application as acid-base and redox catalysts, catalyst supports, anion exchangers, adsorbents *etc*. The synthesis of single-phase LDHs is narrowed to the range $0.2 \leq x \leq 0.33$.[1,2] The influence of the extent of M(III) substitution (within and outside the optimal range), on surface properties of LDHs and derived mixed oxides and their efficiency as catalysts in the Fischer–Tropsch test reaction were investigated. The conversion of syngas ($CO + H_2$ mixtures) to a range of hydrocarbons using Fischer–Tropsch synthesis (FTS) is currently of increasing interest in the scientific field. The FTS products are complex mixtures of organic compounds that depend on the catalysts employed, as well as on the operating conditions. Therefore, selectivity of catalysts towards the desired products is of great importance. Magnesium was chosen as the M(II) ion, because of its basic properties, and iron as the active M(III) ion, because of its reductive characteristics and its ability to form specific active sites in the layered structure required for catalytic application.[3]

EXPERIMENTAL

Layered double hydroxides were synthesized using the low supersaturation co-precipitation method at constant pH with different Mg:Fe ratios and x in the range 0.15–0.7. Precursors with different Mg:Fe atomic ratios were prepared using aqueous solution of $Mg(NO_3)_2 \cdot 6H_2O$ and $Fe(NO_3)_3 \cdot 9H_2O$ continuously (4 cm^3 min^{-1}) added at constant pH (*ca*. 9.6–9.9) maintained by simultaneous addition of Na_2CO_3 and NaOH solution. The products of the precipitation were calcined for 5 h in air at 500 °C.

Structural analysis (XRD) of LDH and mixed oxide samples was investigated with a Siemens D500 X-ray diffractometer (Cu Kα radiation, λ = 0.154 nm, 45 kV, 25 mA) in the 2θ range from 3 to 63°. The texture of mixed oxides was evaluated by low temperature nitrogen sorption at –196 °C using a Micromeritics ASAP 2010 instrument.

The investigation was oriented to the selectivity of the synthesized samples because their selectivity towards particular hydrocarbons is of essential importance in evaluating their potential in the overall activity in FTS. Selectivity tests were performed in a tubular reactor. The catalysts were activated by reduction treatment with a pure hydrogen flow of 20 ml min^{-1} for 2 h at 350 °C. The gas flow was adjusted by mass flow controllers with the H_2:CO ratio of 2:1. The entire reactor system was placed inside a furnace at a temperature of 375 °C. Reaction products were analyzed using a gas chromatograph, HP 5890, Series II, equipped with TCD and FID detectors. The selectivity of the prepared catalysts was calculated using the following formula (S – selectivity, F – detector response factor, x – desired product, nC – number of C atoms in the product; A – value of the surface under the peak):

$$S = 100 \frac{(F_x nC_x A_x)}{\sum (F_{\text{product}} nC_{\text{product}} A_{\text{product}})} \quad (1)$$

RESULTS AND DISCUSSION

All the synthesized samples showed X-ray diffraction patterns that are typical for layered double hydroxides,[1,4] but a single LDH crystalline phase structure was observed only in the samples with x values of 0.15 and 0.3, Fig. 1. The sample with the lowest amount of Fe (x = 0.15) showed broad XRD lines, indicating a less ordered structure. Outside this composition range, x from 0.5 to 0.7, the XRD peaks typical for LDH decreased linearly with increasing amount of Fe in samples, corresponding to a lower crystallinity and a less ordered structure. Another crystalline Fe phase (goethite, FeO(OH)) was observed in the sample with an x value of 0.5. The typical XRD patterns for this additional Fe phase were not detected in the sample with the highest amount of Fe (x = 0.7), probably due to the low intensity of the peaks and the signal response noise, but its presence was also assumed in this sample.

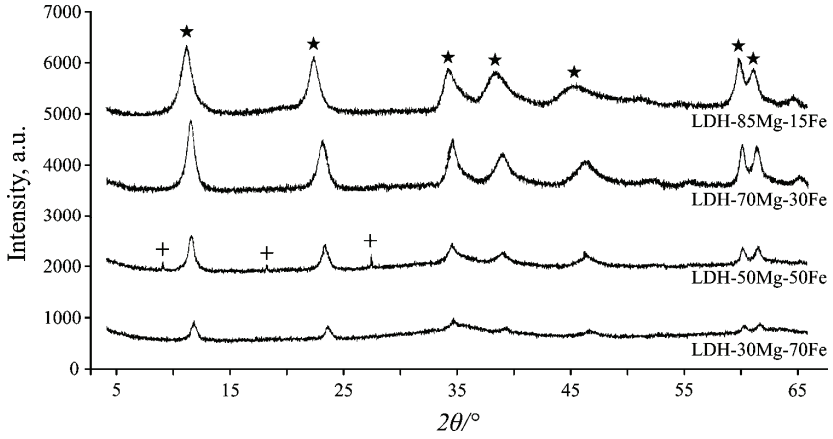

Fig. 1. XRD Patterns of all the synthesized LDH samples (★ – LDH; + – goethite).

The lattice parameters: basal spacing $d_0 = d(003)$, cation–cation distance $a_0 = 2d(110)$ and parameter $c_0 = 3d(003)$ are presented in Fig. 2. The $d(110)$ reflection is independent of the kind of layer stacking and can be utilized for the calculation of the parameter a, whereas the $d(003)$ reflection, the true c parameter, depends on the layer stacking sequence.[1] With increasing amount of Fe in the sample, a decrease in the lattice parameters, indicating a decrease in the interlayer distance and a higher attraction between the negatively charged hydroxide layers and the anions present in the interlayers, was also reported elsewhere.[5]

The XRD analysis of all the samples after thermal treatment showed diffraction peaks typical for mixed oxides with a regular, dense-packed, cubic, NaCl-type oxygen lattice, shown in Fig. 3. A collapse of the layered structure leading to the formation of mixed oxides after calcination was observed in all samples. The intensity of the XRD peaks decreased with increasing iron content in the

samples and with increasing deviation from the optimal range for the single-phase synthesis. The XRD analysis of the samples synthesized with a content of Fe higher than the mentioned optimal range revealed additional phases of hematite (Fe_2O_3) and spinel ($MgFe_2O_4$).[6] The intensity of the characteristic additional phase signals increased with increasing Fe content in the samples, indicating also higher amounts of these phases in the samples with $x = 0.7$. This also confirms the mentioned assumption about the presence of the additional Fe phase in the original LDH sample.

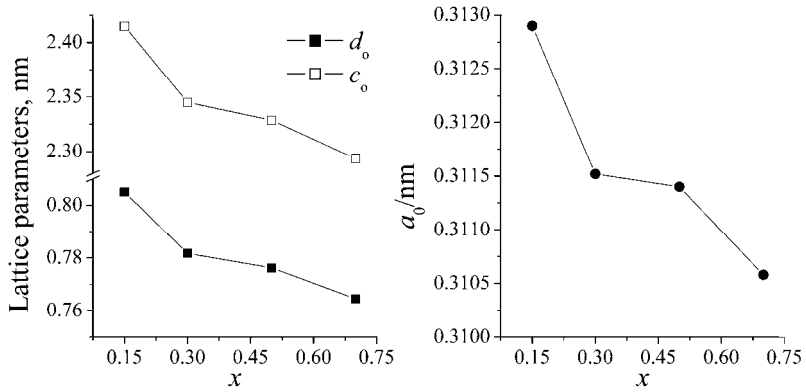

Fig. 2. The influence of the chemical composition of the LDH on the lattice parameters.

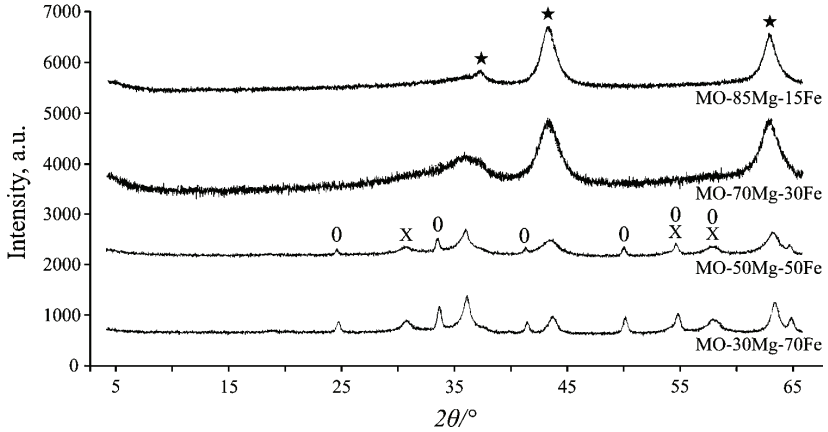

Fig. 3. XRD Patterns of the samples after thermal treatment (★ – mixed oxides; 0 – hematite, X – spinel).

The structural parameter a_0 as a function of the amount of Fe in the sample is presented in Fig. 4, from which it can be seen that the values for a_0 decreased with increasing amount of Fe in the samples.

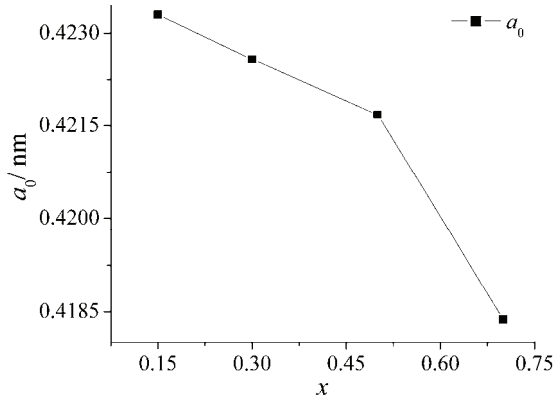

Fig. 4. Structural parameters of the mixed oxides.

The surface area of the as-synthesized LDH samples and after the thermal and reduction treatment, as well as the influence of the amount of iron in the samples is shown in Fig. 5. The increase of the surface area after thermal treatment for samples with $x = 0.15$ and 0.3 is due to the formation of smaller mesopores.[7] The presence of additional phases in samples with $x = 0.5$ and 0.7 negatively influences the development of surface area after calcination. A smaller decrease in the surface area was detected for the sample $x = 0.5$, which contained lower amounts of additional phases. The LDH sample with the highest iron content ($x = 0.7$) had the highest surface area that significantly decreased after calcination. This drastic fall was due to the lowest amount of carbonate in the LDH interlayers in this sample and the formation of additional crystalline phases identified by XRD analysis.

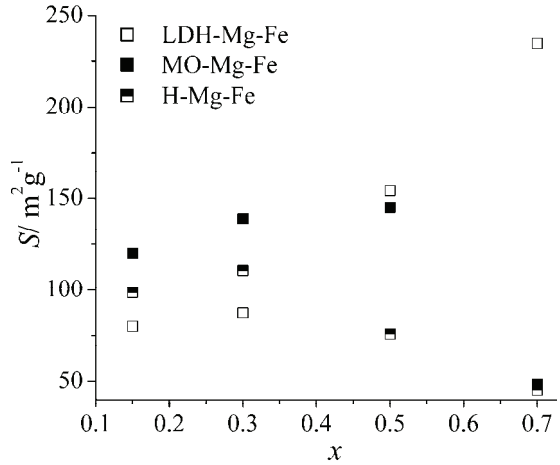

Fig. 5. Surface area of the LDH, derived mixed oxides and mixed oxides after reduction in dependence on the Fe content.

The surface area of the mixed oxides after reduction was lower than the surface area of the mixed oxides after calcination, Fig. 5, most likely due to the formation of new phases after the reduction.

The selectivity of all samples towards C_4 and C_5 products at 375 °C and a H_2:CO ratio of 2:1 is presented in Fig. 6. The sample with the lowest iron content, having the highest basicity compared to the other samples, exhibited the highest selectivity. These results are in agreement with literature data, where it was observed that with increasing MgO content in the sample, the selectivity of the Fe-catalysts in the FT reaction also increased.[8]

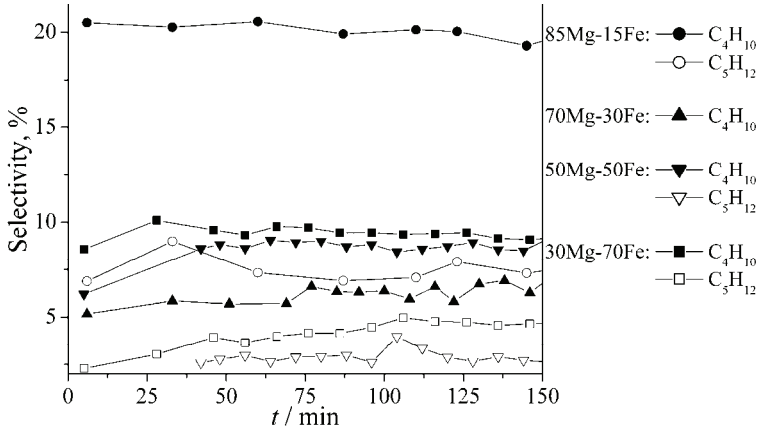

Fig. 6. Selectivity of all samples towards C_4 and C_5 products at 375 °C at an H_2:CO ratio of 2:1.

The sample synthesized in the optimal range for single-phase LDH synthesis (70 Mg–30 Fe) exhibited low selectivity towards C_4-compounds, while selectivity towards C_5-compounds was not detected. The very low selectivity of this sample is probably due to its stable structure, as observed by XRD analysis, which is not desirable for catalytic application. Both of the samples 50 Mg–50 Fe and 30 Mg––70 Fe exhibited selectivity towards C_4- and C_5-compounds. The sample with the highest Fe content showed selectivity towards C_5-compounds after 5 min of the reaction, whereas selectivity for the 50 Mg–50 Fe sample towards C_5-compounds was detected after 40 min.

CONCLUSIONS

The synthesis of Mg–Fe layered double hydroxides outside the optimal range for a single LDH phase resulted in the formation of complex, multiphase, layered double hydroxides, which gave metastable phases of oxides after thermal treatment. These mixed oxides enabled the development of active sites on the surface contributing to their catalytic performance. The reduction of mixed oxides before their application in the Fischer–Tropsch reaction decreased the surface

area, most likely due to the formation of new phases. All the samples synthesized outside the optimal range for a single LDH phase showed higher selectivity towards the chosen products compared to the samples synthesized within the optimal range. The sample with the lowest iron content having the highest basicity compared to other samples exhibited the highest selectivity in the FT reaction. The stable structure of the sample synthesized in the optimal range disenabled the formation of active sites and confirmed the positive effect of metastable structures on catalytic properties. Such results open up a new route for the synthesis of LDHs with desired properties for application in certain catalytic reactions.

Acknowledgements. The financial support from the Ministry of Science and Technical Development of the Republic of Serbia (Project No. OI 142024) is gratefully acknowledged.

ИЗВОД

ИСПИТИВАЊЕ ТЕРМИЧКИ АКТИВИРАНИХ Mg–Fe ДВОСТРУКИХ СЛОЈЕВИТИХ ХИДРОКСИДА КАО ПОТЕНЦИЈАЛНИХ КАТАЛИЗАТОРА У ЗАШТИТИ ЖИВОТНЕ ОКОЛИНЕ

МИЛИЦА С. ХАДНАЂЕВ-КОСТИЋ, ТАТЈАНА Ј. ВУЛИЋ и РАДМИЛА П. МАРИНКОВИЋ-НЕДУЧИН

Технолошки факултет, Универзитет у Новом Саду, Бул. цара Лазара 1, 21000 Нови Сад

Испитивани су двоструки слојевити хидроксиди (LDHs) са различитим садржајем Mg–Fe и мешовити оксиди који су настали њиховом термичком разградњом. Двоструки слојевити хидроксиди $[Mg_{1-x}Fe_x(OH)_2](CO_3)_{x/2}\cdot mH_2O$, где је x удео тровалентних анјона, x = = M(III)/(M(II) + M(III)) синтетисани су копреципитационом методом мале презасићености. Извршена је карактеризација мешовитих оксида насталих из LDHs, као и нетретираних LDHs, испитивањем кристалографске структуре, термичких карактеристика, текстуре, кисело–базних карактеристика и морфологије. Проучаван је утицај различитог односа Mg/Fe на структурне, површинске и кисело–базне карактеристике LDHs и њихових мешовитих оксида у корелацији са каталитичким карактеристикама у одабраној тест реакцији (Fischer–Tropsch синтеза). Утврђено је да структурне карактеристике полазног LDH, присуство додатних фаза Fe и кисело–базне карактеристике утичу на присуство активних центара код свих мешовитих оксида, као и да синтеза ван оптималног опсега за добијање једнофазних LDHs доводи до формирања метастабилних, вишефазних система са специфичним карактеристикама и активним центрима.

(Примљено 15. јануара, ревидирано 25. фебруара 2010)

REFERENCE

1. F. Cavani, F. Trifiro, A. Vaccari, *Catal. Today* **11** (1991) 173
2. A. Vaccari, *Catal. Today* **41** (1998) 53
3. M. Hadnadjev, T. Vulic, R. Marinkovic-Neducin, Y. Suchorski, H. Weiss, *Appl. Surf. Sci.* **254** (2008) 4297
4. W. Reichle, S. Fornasari, A. Vaccari, *Catal. Today* **77** (2003) 299
5. D. Tichit, M. Lhouty, A. Guida, B. Chiche, F. Figueras, A. Auroux, *J. Catal.* **151** (1995) 50
6. H. Hayakawa, H. Tanaka, K. Fujimoto, *Catal. Commun.* **8** (2007) 1820
7. T. Vulić, M. Hadnadjev, R. Marinković-Nedučin, *J. Microscopy* **232** (2008) 634
8. J. Yang, Y. Sun. Y. Tang. Y. Lui, *J. Mol Catal. A: Chem.* **245** (2006) 26.

Journal of the Serbian Chemical Society
JSCS-info@shd.org.rs • www.shd.org.rs/JSCS
J. Serb. Chem. Soc. *75* (9) 1259–1269 (2010)
JSCS–4049
UDC 621.352:546.34'72'185.001:544.6.004.12
Original scientific paper

Effects of the $LiFePO_4$ content and the preparation method on the properties of ($LiFePO_4$+AC)/$Li_4Ti_5O_{12}$ hybrid battery–capacitors

XUE BU HU[1]*, ZI JI LIN[2], LI LIU[2], YONG JIAN HUAI[2] and ZHENG HUA DENG[2]*

[1]*Department of Chemistry and Materials, Sichuan Normal University, Chengdu, Sichuan 610068 and* [2]*Chengdu Institute of Organic Chemistry, Chinese Academy of Sciences, Chengdu, Sichuan 610041, P. R. China*

(Received 28 December 2009, revised 17 March 2010)

Abstract: Two composite cathode materials containing $LiFePO_4$ and activated carbon (AC) were synthesized by an *in-situ* method and a direct mixing technique, which are abbreviated as LAC and DMLAC, respectively. Hybrid battery–capacitors LAC/$Li_4Ti_5O_{12}$ and DMLAC/$Li_4Ti_5O_{12}$ were then assembled. The effects of the content of $LiFePO_4$ and the preparation method on the cyclic voltammograms, the rate of charge–discharge and the cycle performance of the hybrid battery–capacitors were investigated. The results showed the overall electrochemical performance of the hybrid battery–capacitors was the best when the content of $LiFePO_4$ in the composite cathode materials was in the range from 11.8 to 28.5 wt. %, while the preparation method had almost no impact on the electrochemical performance of the composite cathodes and hybrid battery––capacitors. Moreover, the hybrid battery–capacitor devices had a good cycle life performance at high rates. After 1000 cycles, the capacity loss of the DMLAC/$Li_4Ti_5O_{12}$ hybrid battery–capacitor device at 4*C* was no more than 4.8 %. Moreover, the capacity loss would be no more than 9.6 % after 2000 cycles at 8*C*.

Keywords: hybrid battery–capacitor; $LiFePO_4$ content; preparation method; long cycle life; high rate; electrochemical performance.

INTRODUCTION

The emergence of hybrid electric vehicles (HEVs) requires the development of power sources that can provide high power as well as high energy.[1–4] However, neither secondary batteries (low power density) nor capacitors (low energy density) as a single power source for HEVs can meet the needs of practical application.[5–7] A hybrid battery–capacitor is a new energy storage system in which

* Corresponding authors. E-mail: xuebu@sicnu.edu.cn
doi: 10.2298/JSC091028101Z

the secondary battery and capacitor coexist. It consists of an oxidation–reduction anode and a composite cathode composed of an oxidation-reduction battery electrode and an electric double-layer capacitor carbon electrode. During the charge––discharge process, the two oxidation–reduction electrodes form a battery system of oxidation–reduction cathode/oxidation–reduction anode, while at the same time, the electric double-layer carbon electrode and the oxidation–reduction anode form a hybrid capacitor system; hence the energy storage of the electrodes have not only Faradic energy but also electric double-layer energy. Therefore, a battery system and a capacitor system coexist in such an energy storage device, each of which brings its own good electrochemical performance into the whole system. The hybrid battery–capacitor has an energy density as high as the secondary battery and a power density as high as the capacitor.[8–11] This makes it one of the most promising auxiliary power supplies for HEVs. Previously, a composite cathode material containing $LiFePO_4$ and activated carbon (AC), abbreviated as LAC, was synthesized by an *in-situ* method. Although the assembled hybrid battery––capacitor LAC/$Li_4Ti_5O_{12}$ showed the advantages of a high rate capability and high capacity,[8] the *in-situ* synthesis required high system stability. It is hard to control product performance, stability and consistency, particularly an accurate content of $LiFePO_4$ in composite materials. The shortage of *in-situ* methods of synthesis increased the difficulty of industrial production. One possible solution to this problem is to synthesize the products by a direct mixing technique. In a direct mixing technique, the composite materials are synthesized *via* high-speed mechanical mixing, which is simple and the content of each component in composite materials can be easily controlled.

In this study, through the direct mixing technique, a series of composite materials containing commercial $LiFePO_4$ and AC, abbreviated as DMLAC, with different $LiFePO_4$ contents was synthesized. The effects of the $LiFePO_4$ content and preparation method on the electrochemical performance of the hybrid battery–capacitors were systematically studied.

EXPERIMENTAL

The LAC composite material was prepared *via* the *in-situ* method described in the literature.[8] $Li_4Ti_5O_{12}$ powder was prepared *via* a solid-state reaction.[8] The DMLAC composite material was prepared *via* the direct mixing technique. A stoichiometric mixture of $LiFePO_4$ and AC was dispersed in distilled water (the solid content was about 30 or 35 mass %) and then stirred at 2000 rpm for 6 h to give the final $LiFePO_4$+AC (DMLAC) composite material.

X-Ray diffraction (XRD) analysis of the electrode materials was realized a Philips X'Pert automated X-ray diffraction machine with CoKα1 radiation of λ = 0.178897 nm, 50 kV, 35 mA, in the range of $15° < 2\theta < 85°$. Scanning electron microscopy (SEM) was conducted on a JEOL JSM-6700F scanning electron microscopy at 5 kV. The tap-density of the powders was tested by adding a weighed amount powder into a dry measuring cylinder and then the measuring cylinder was tapped until the volume of the powders no longer changed. The ratio of the mass and the volume of the powder gave the tap-density.[12]

A well mixed slurry of the active material LAC powder (or DMLAC, $Li_4Ti_5O_{12}$, $LiFePO_4$, AC), the electric conducting agent acetylene black and an aqueous binder LA132 (from Indigo, China) in a weight ratio of 85:10.5:4.5 was pasted onto aluminum foil and dried at 120 °C to give the electrodes. All electrodes were cut into discs with a diameter of 1.0 cm (*i.e.*, an area of 0.785 cm^2), pressed, dried at 90 °C under vacuum for 4 h, and then stored in an argon-filled dry box. The hybrid battery–capacitor LAC/$Li_4Ti_5O_{12}$ (or DMLAC/$Li_4Ti_5O_{12}$) was assembled in an argon-filled dry box by pressing an LAC (or DMLAC) disc, a Celgard 2400 polypropylene membrane and a $Li_4Ti_5O_{12}$ disc. The electrolyte was a 1.0 M $LiPF_6$ solution in the mixture of ethylene carbonate (EC), dimethyl carbonate (DMC) and ethylene methyl carbonate (EMC) at a weight ratio of 1:1:1. For comparison, the capacitors of AC/ /$Li_4Ti_5O_{12}$ and AC/AC and the battery $LiFePO_4$/$Li_4Ti_5O_{12}$ were assembled in the same way. The constant current charge–discharge, rate capability and cycle performance of the hybrid battery–capacitors, capacitors and battery were tested on a Qing-tian battery tester (BS9300, China) and cyclic voltammograms were recorded on an Arbin instrument (USA).

In order to show the cycle life at a high rate, two kinds of DMLAC/$Li_4Ti_5O_{12}$ hybrid battery–capacitor devices were assembled. The cathodes were prepared with $LiFePO_4$ (STL, China) and AC (GH-6, China). The conductive additives used were colloidal graphite (F-0, China) and conductive carbon black (SuperP, TIMCAL) termed SP hereinafter. The binder used was LA132 (Indigo, China). Anodes were prepared in the same way using $Li_4Ti_5O_{12}$ as the active material. The formulations of the prepared electrodes are summarized in Table I. The cells were assembled in an argon-filled dry box by pressing a DMLAC cathode, a Celgard 2400 polypropylene membrane, and a $Li_4Ti_5O_{12}$ anode. The electrolyte was a 1.0 M $LiPF_6$ solution in a mixture of EC, DMC and EMC (1:1:1 by weight). The cells were packaged with an aluminum–plastic membrane and shaped. The final size of hybrid battery–capacitor was 4.5 mm×30 mm×48 mm (thickness×width×length). The cycle life performance of the hybrid battery–capacitors were tested on a Repower Battery Tester (China). All the tests were performed at 20 °C.

TABLE I. Formulations of the tested electrodes

Electrode	Active material	Conductive additives	Binder
15 % LFP + AC	$LiFePO_4$ 15 % + AC 60 %	F-0 12 % + SP 6 %	LA132 7 %
22.5 % LFP + AC	$LiFePO_4$ 22.5 % + AC 52.5 %	F-0 12 % + SP 6 %	LA132 7 %
LTO	$Li_4Ti_5O_{12}$ 86 %	F-0 6 % + SP 4 %	LA132 4 %

RESULTS AND DISCUSSION

Analyses of XRD data

The XRD patterns of the LAC composites with different $LiFePO_4$ contents from 5.1 to 34.2 wt. % are shown in Fig. 1. Except for characteristic patterns of a small amount of Graphite-2H and $Li_4P_2O_7$, all the peaks are in accordance with the reference $LiFePO_4$ pattern (PDF No. 40-1499). Graphite-2H is formed because AC can transform to graphite at high temperatures.[13,14] $Li_4P_2O_7$ is derived from the decomposition of $LiFePO_4$ at high temperatures.[15] The decomposition process may be represented by the following reaction:

$$4\ LiFePO_4 \rightarrow Li_4P_2O_7 + Fe_2P + 9/2O_7$$

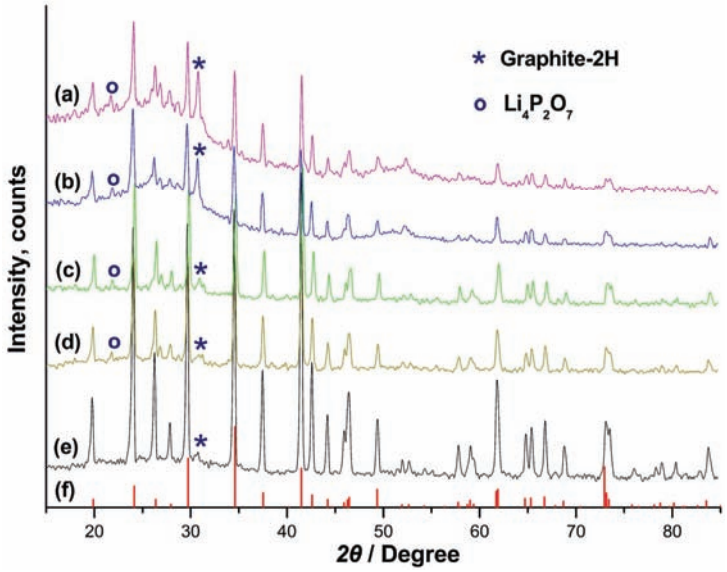

Fig. 1. XRD Patterns of the LAC composites with different $LiFePO_4$ contents: a) 5.1, b) 11.8, c) 21.1, d) 28.5, e) 34.2 and f) 100 wt. % (*i.e.*, the reference, $LiFePO_4$).

With increasing $LiFePO_4$ content, the XRD patterns became more similar to the reference pattern and the peak intensities of the impurities were correspondingly decreased.[16] Moreover, the tap-density of the LAC composite increased with increasing $LiFePO_4$ content, which would improve the volume density of the composite cathode and the volume energy density of the hybrid battery–capacitor. The tap-densities of the LAC composites with different $LiFePO_4$ contents are listed in Table II.

TABLE II. The tap-density of the LAC composites with different $LiFePO_4$ contents

Content of $LiFePO_4$, wt. %	0	5.1	11.8	21.1	28.5	34.2
Tap-density, g cm^{-3}	0.547	0.667	0.691	0.732	0.751	0.786

Morphologies of the samples

The SEM images of LAC composites with different $LiFePO_4$ contents are shown in Fig. 2. The images provide clear evidence that small crystal particles of $LiFePO_4$ either coat the surface of the AC particles or lie among them. These $LiFePO_4$ particles have a small particle size (100–500 nm) and a regular quadrate form. With the increasing of $LiFePO_4$ content, these small crystal particles at the surface or among the AC particles are increased.

Cyclic voltammetric behavior

The cyclic voltammograms (CVs) of the hybrid battery–capacitors LAC/ /$Li_4Ti_5O_{12}$ and DMLAC/$Li_4Ti_5O_{12}$ are shown in Fig. 3. The CVs were all recorded

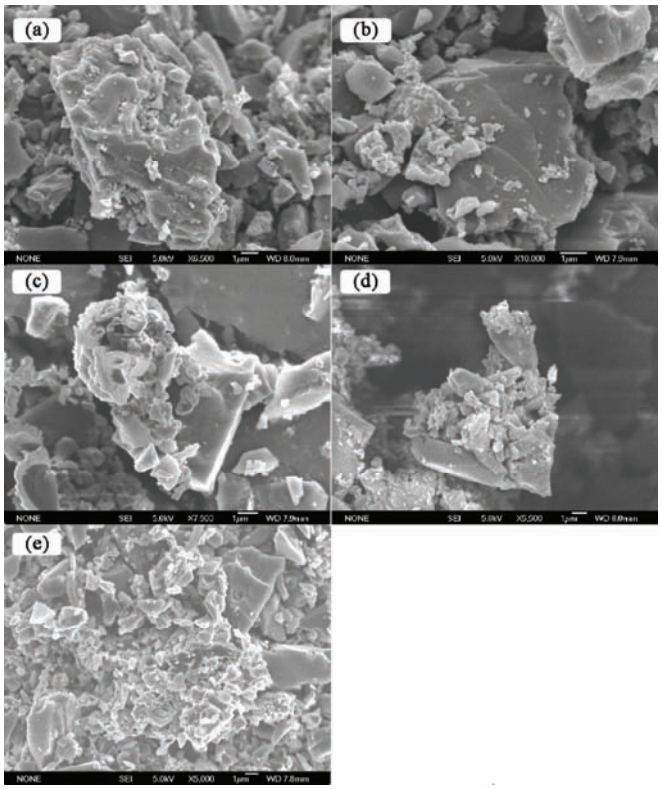

Fig. 2. SEM Microphotographs of the LAC composites with different $LiFePO_4$ contents: a) 5.1, b) 11.8, c) 21.1, d) 28.5 and e) 34.2 wt. %.

in the voltage range 1.0–2.6 V at a scan rate of 0.2 mV s^{-1}. As can be seen from Figs. 3a and 3b, the two hybrid battery–capacitors using the composite cathode prepared by the two methods exhibited the same electrochemical behavior. The hybrid battery–capacitor system retained the oxidation–reduction behavior of a $LiFePO_4/Li_4Ti_5O_{12}$ battery system. Furthermore, there was a larger response current when the hybrid battery–capacitor system was in the high voltage range. As shown in Figs. 3c and 3d, with a $LiFePO_4$ content of 11.8 wt. %, a pair of redox peaks of the LAC and DMLAC composites were both located at 1.74 and 2.00 V. With a $LiFePO_4$ content of 21.1 wt. %, the pair of redox peaks of the LAC composite was still located at 1.74 and 2.00 V. However, the pair of redox peaks of the DMLAC composite was located at 1.69 and 2.05 V. This result indicates that the preparation method of composite materials have a certain impact on the peak potentials of the CVs. The composite obtained by *in-situ* synthesis has small particles, a uniform distribution and no reunion phenomena. Therefore, the $LiFePO_4$ had a good interface combination with AC, a high degree of dispersion and weak electrode polarization, which is due to the good dispersion of $LiFePO_4$ in the LAC

composite. Moreover, the increase of the $LiFePO_4$ content did not affect their degree of dispersion in the LAC composite; hence the pair of redox peak was still located at 1.74 and 2.00 V. Compared with the direct mixing technique, $LiFePO_4$ in the DMLAC composite was not well-dispersed in the AC, had a weak interface combination with AC and a large electrode polarization. The increase in the $LiFePO_4$ content lowered the dispersion degree of $LiFePO_4$ in the DMLAC composite. Therefore, the pair of redox peak changes from 1.74 and 2.00 V (11.8 wt. % $LiFePO_4$) to 1.69 and 2.05 V (21.1 wt. % $LiFePO_4$). The above results of the CVs illustrate that the hybrid battery–capacitors LAC/$Li_4Ti_5O_{12}$ and DMLAC/ /$Li_4Ti_5O_{12}$ exhibited the same CVs behavior, but there was a difference in the redox peak potentials due to the different preparation methods.

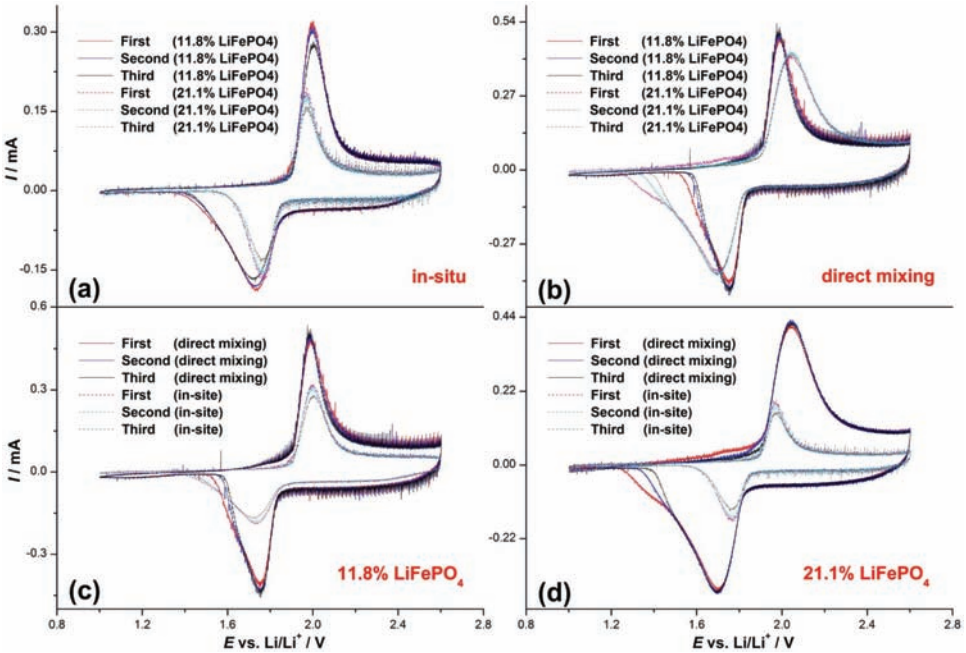

Fig. 3. CVs of the hybrid battery–capacitors with different $LiFePO_4$ contents: a) *in-situ* synthesis, b) direct mixing technique, c) 11.8 and d) 21.1 wt. %.

Rate capability of the hybrid battery–capacitor

The discharge curves of the hybrid battery–capacitors LAC/$Li_4Ti_5O_{12}$ and DMLAC/$Li_4Ti_5O_{12}$ at different discharge current densities (the charge–discharge rates were the same for each case) are shown in Fig. 4. The specific capacities decreased slightly after 20 cycles when the hybrid battery–capacitors were discharged at several rates ranging from 2*C* to 10*C*. At the same rate, the capacity of the hybrid battery–capacitors increased when the content of $LiFePO_4$ in the com-

posite materials was increased. At 4*C*, with the *in-situ* synthesis, when the content of $LiFePO_4$ in LAC was 5.2, 11.8, 21.1, 28.5 and 34.2 wt. %, after 20 cycles, the capacity losses of the LAC/$Li_4Ti_5O_{12}$ hybrid battery–capacitor were 1.2, 1.0, 2.6, 4.4 and 4.8 %, respectively. Clearly, all the values were less than 4.8 %. However, when the direct mixing technique was used, after 20 cycles, the capacity loss were 2.0, 2.3, 1.9, 2.6 and 2.9 %, respectively, and noticeably, all the value were less than 2.9 %. These results demonstrate the hybrid battery–capacitors LAC/$Li_4Ti_5O_{12}$ and DMLAC/$Li_4Ti_5O_{12}$ with different $LiFePO_4$ content exhibited good performances at high charge–discharge rates, indicating that the preparation method of the composite cathode materials have almost no impact on the high rate charge–discharge performance of the hybrid battery–capacitors.

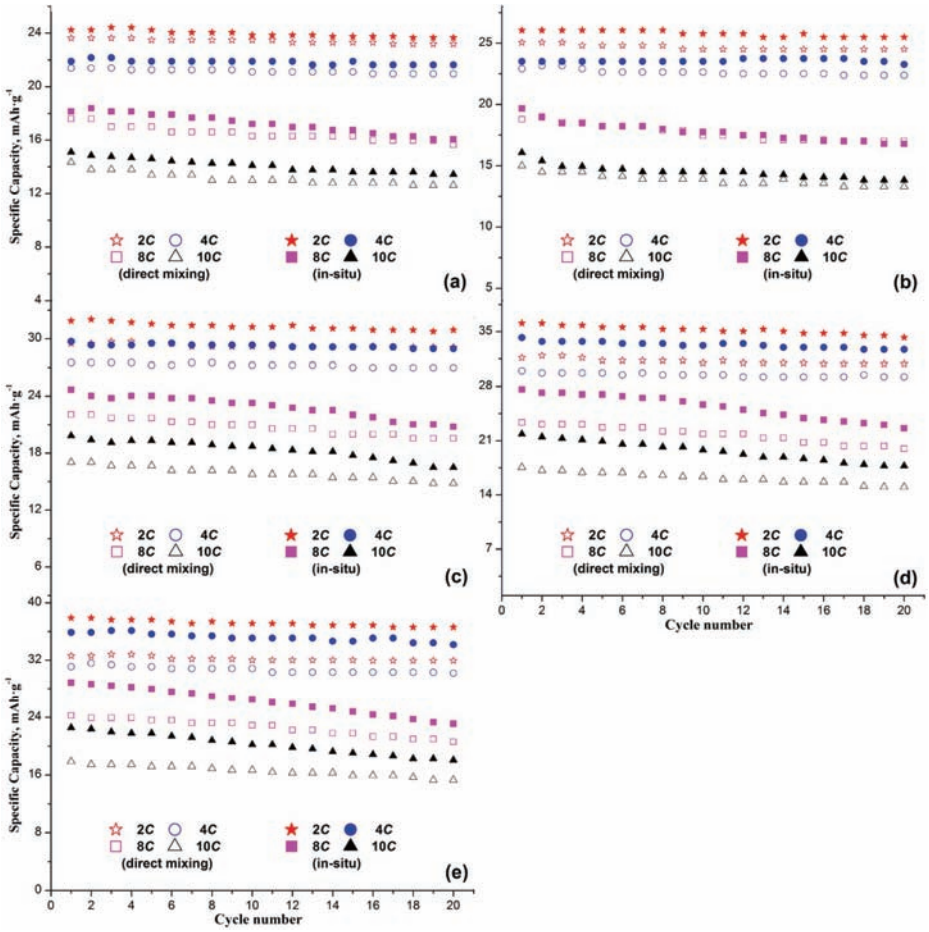

Fig. 4. Specific capacity of the hybrid battery–capacitors with different $LiFePO_4$ contents at different rates, where the specific capacity was calculated by the total mass of the active material in the hybrid battery–capacitors: a) 5.1, b) 11.8, c) 21.1, d) 28.5 and e) 34.2 wt. %.

Cycle performance of the hybrid battery–capacitor

A comparison of the discharge capacity between LAC/$Li_4Ti_5O_{12}$ and DMLAC/$Li_4Ti_5O_{12}$ hybrid battery–capacitors, an AC/$Li_4Ti_5O_{12}$ capacitor and a $LiFePO_4$/$Li_4Ti_5O_{12}$ battery during long-term cycling is shown in Fig. 5, for the same mass of cathode active material in each cell. In the *in-situ* synthesis, when the content of $LiFePO_4$ in the LAC was 5.2, 11.8, 21.1, 28.5 and 34.2 wt. %, the capacity loss of the LAC/$Li_4Ti_5O_{12}$ hybrid battery–capacitors was 8.6, 9.2, 10.1, 12.0 and 15.8 %, respectively, after 100 cycles. However, in direct mixing technique, the capacity loss was 8.5, 8.7, 9.6, 11.4 and 12.4 %, respectively, after 100 cycles. This indicates that the cycle performances of LAC/$Li_4Ti_5O_{12}$ and DMLAC/ /$Li_4Ti_5O_{12}$ were better than those of AC/$Li_4Ti_5O_{12}$ and $LiFePO_4$/$Li_4Ti_5O_{12}$ when the same cathode or anode was used in these cells. However, with increasing $LiFePO_4$ content, the cycle performances of the hybrid battery–capacitors LAC/$Li_4Ti_5O_{12}$ and DMLAC/$Li_4Ti_5O_{12}$ slightly decreased. At the same $LiFePO_4$ content, the capacity loss of DMLAC/$Li_4Ti_5O_{12}$ was less than that of LAC/$Li_4Ti_5O_{12}$, which was due to the better cycle performance of the commercial $LiFePO_4$-coated carbon or doped-carbon. These facts illustrate that the hybrid battery–capacitors LAC/$Li_4Ti_5O_{12}$ and DMLAC/$Li_4Ti_5O_{12}$ had good cycle performances. This also means that the preparation methods of the composite cathode materials had almost no impact on the high rate cycle performances of the hybrid battery–capacitors.

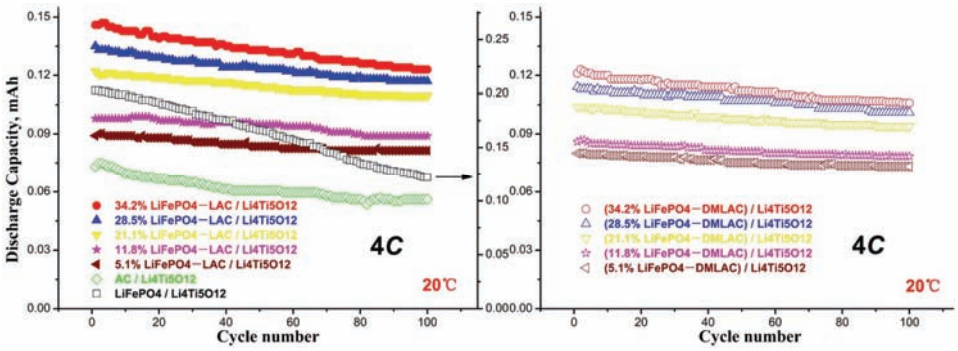

Fig. 5. Comparison of cycle performance of the LAC/$Li_4Ti_5O_{12}$ and DMLAC/$Li_4Ti_5O_{12}$ hybrid battery–capacitors, the AC/$Li_4Ti_5O_{12}$ capacitor and the $LiFePO_4$/$Li_4Ti_5O_{12}$ battery at a rate of 4*C*.

Comparison of the cathode materials performance

The results of the performances of the cathode materials (LAC, DMLAC composite electrodes and AC electrode) in different cell systems are given in Table III. Using the same electrolyte, when the content of $LiFePO_4$ in cathode composite was 5.2, 11.8, 21.1, 28.5 and 34.2 wt. %, the specific capacity of an LAC

single electrode in a LAC/$Li_4Ti_5O_{12}$ hybrid battery–capacitor was 11.6, 23.2, 44.6, 60.6 and 70.4 % higher than of that of an AC single electrode in an AC/ /$Li_4Ti_5O_{12}$ hybrid capacitor and an AC/AC electric double-layer capacitor, which was also about 87.8, 76.3, 69.2, 65.0 and 61.7 % of the maximum theoretical capacity. However, with a DMLAC single electrode, the specific capacity was 3.6, 8.4, 23.4, 35.4 and 41.6 % higher than that of that of an AC single electrode, which is also about 81.5, 67.1, 59.0, 54.8 and 51.3 % of the maximum theoretical capacity. These results indicate that the LAC and DMLAC composite cathode materials with different $LiFePO_4$ contents had high capacity characteristic. However, with increasing $LiFePO_4$ content, the capacity utilizetion of the hybrid battery–capacitors LAC/$Li_4Ti_5O_{12}$ and DMLAC/$Li_4Ti_5O_{12}$ slightly decreased. The above results illustrate that the preparation method of the composite cathode materials had almost no impact on the capacity performance of the composite cathodes.

TABLE III. Cathode performances of the different capacitors

Content of $LiFePO_4$ wt. %	LAC (calculated)	LAC (LAC/$Li_4Ti_5O_{12}$)		DMLAC (DMLAC/$Li_4Ti_5O_{12}$)		AC (AC/$Li_4Ti_5O_{12}$)	AC (AC/AC)
	C_g mA h g^{-1}		Utilization rate, %	C_g mA h g^{-1}	Utilization rate, %		
34.2	76.56	47.25	61.7	39.26	51.3	27.72	28.00
28.5	68.47	44.51	65.0	37.52	54.8		
21.1	57.96	40.08	69.2	34.22	59.0		
11.8	44.76	34.14	76.3	30.04	67.1		
5.1	35.24	30.95	87.8	28.71	81.5		

Cycle life performance of the hybrid battery–capacitor device

The results for the cycle life of the DMLAC/$Li_4Ti_5O_{12}$ hybrid battery–capacitor devices at a high rate are shown in Fig. 6. The hybrid battery–capacitor devices at a high rate provide high coulombic efficiencies close to 100 %. At 4*C*, when the contents of $LiFePO_4$ in the composite cathode were 15 and 22.5 wt. %, the capacity losses of the DMLAC/$Li_4Ti_5O_{12}$ hybrid battery–capacitor devices were 3.4 and 4.8 %, respectively, after 1000 cycles. Clearly, neither of the values was more than 4.8 %. However, at 8*C*, after 2000 cycles, the capacity losses were 8.1 and 9.6 %, respectively, but noticeably, neither of the values was more than 9.6 %. The results show that the DMLAC/$Li_4Ti_5O_{12}$ hybrid battery–capacitor devices had a good cycle life performance at a high rate.

All the above electrochemical testing data demonstrate that the preparation method of the composite cathode materials had almost no impact on rate capability, cycle performance or capacity performance of the composite cathodes. At 4*C*, when the content of $LiFePO_4$ in the cathode composite was 11.8, 21.1 and 28.5 wt. %, after 100 cycles the capacity losses of the LAC/$Li_4Ti_5O_{12}$ and DMLAC/

/$Li_4Ti_5O_{12}$ hybrid battery–capacitors were less than 12.0 and 11.4 %, respectively. Moreover, the capacity and capacity utilization of the composite cathodes achieved better results. These facts illustrate that the overall electrochemical performance of the composite cathodes and the hybrid battery–capacitors was the best when the content of $LiFePO_4$ in the composite cathode materials ranged from 11.8 to 28.5 wt. %, while the preparation method of the composite cathode materials had almost no impact on the electrochemical performances of the composite cathodes and the hybrid battery–capacitors.

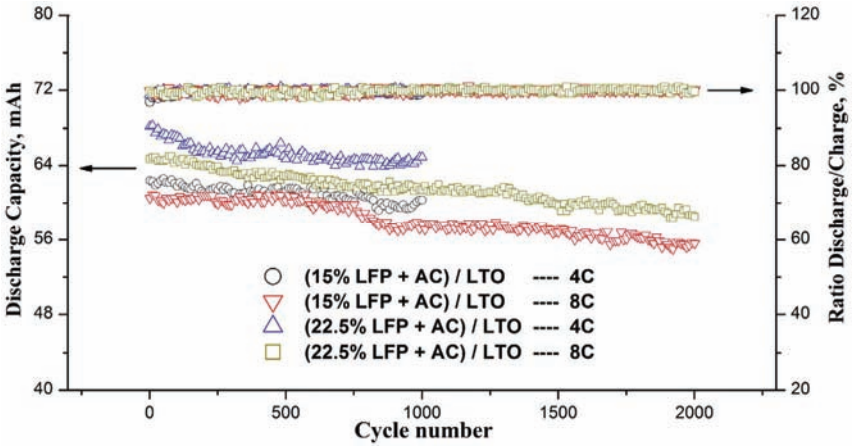

Fig. 6. Discharge capacity and discharge–charge ratio *vs.* number of cycle for the hybrid battery–capacitor devices at a high rate.

CONCLUSIONS

In this work, LAC and DMLAC composite cathode materials with different $LiFePO_4$ contents were synthesized by the *in-situ* synthesis method and the direct mixing technique, respectively, and then the hybrid battery–capacitors LAC/ /$Li_4Ti_5O_{12}$ and DMLAC/$Li_4Ti_5O_{12}$ with a $Li_4Ti_5O_{12}$ anode were assembled. The results showed that the hybrid battery–capacitors LAC/$Li_4Ti_5O_{12}$ and DMLAC/ /$Li_4Ti_5O_{12}$ had advantages of both a high rate capability and a high capacity, while the method of preparation of the composite cathode materials had almost no impact on the electrochemical performance of the hybrid battery–capacitors. Moreover, taking into account the capacity and capacity utilization, the overall electrochemical performance of the composite cathodes and the hybrid battery–capacitors was the best when the content of $LiFePO_4$ in the composite cathode materials ranges from 11.8 to 28.5 wt. %. More importantly, the hybrid battery–capacitor devices had a good cycle life performance at a high rate. When the content of $LiFePO_4$ in composite cathode was 15 and 22.5 wt. %, after 1000 cycles, the capacity losses of the DMLAC/$Li_4Ti_5O_{12}$ hybrid battery–capacitor device at

4*C* were less than 4.8 %. However, at 8*C*, after 2000 cycles, the capacity losses were less than 9.6 %.

И З В О Д

УТИЦАЈ САДРЖАЈА $LiFePO_4$ И НАЧИНА ДОБИЈАЊА НА СВОЈСТВА ($LiFePO_4$ + AC)/$Li_4Ti_5O_{12}$ ХИБРИДА БАТЕРИЈА–КОНДЕНЗАТОР

XUE BU HU[1], ZI JI LIN[2], LI LIU[2], YONG JIAN HUAI[2] и ZHENG HUA DENG[2]

[1]*Department of Chemistry and Materials, Sichuan Normal University, Chengdu, Sichuan 610068 и* [2]*Chengdu Institute of Organic Chemistry, Chinese Academy of Sciences, Chengdu, Sichuan 610041, P. R. China*

In-situ техником и техником директног мешања синтетисана су два катодна композитна материјала, означена као LAC, односно DMLAC, који садрже $LiFePO_4$ и активирани угљеник (AC). Од њих су формирани LAC/$Li_4Ti_5O_{12}$ и DMLAC/$Li_4Ti_5O_{12}$ хибриди батерија–кондензатор. Испитиван је утицај садржаја $LiFePO_4$ и технике припремања на цикличне волтамограме, брзину процеса и број циклуса пуњење/пражњење хибридних извора. Резултати су показали да су најбоље електрохемијске карактеристике хибридног извора постигнуте са садржајем $LiFePO_4$ у катодном композитном материјалу у опсегу 11,8–28,5 mas. %, док начин припреме није имао утицаја. Хибридни уређај батерија–кондензатор имао је задовољавајући број циклуса пуњење/пражњење при великим брзинама овог процеса. Након 1000 циклуса, губитак капацитивности уређаја DMLAC/$Li_4Ti_5O_{12}$ при 4*C* брзини није био већи од 4,8 %, а након 2000 циклуса при 8*C* брзини не већи од 9,6 %.

(Примљено 28. децембра 2009, ревидирано 17. марта 2010)

REFERENCES

1. J. R. Miller, The Electrochemical Society, Proceedings, 1995, Chicago, IL, USA, 1995, p. 246
2. G. Sikha, R. E. White, B. N. Popov, *J. Electrochem. Soc*. **152** (2005) A1682
3. S. Pay, Y. Baghzouz, *in Proceedings* of IEEE Bologna PowerTech Conference, 2003, Bologna, Italy, 2003, p. 6
4. A. F. Burke, *in Proceedings of the Second International Advanced Battery Conference*, 2002, Las Vegas, NV, USA, 2002, p. 37
5. S. Y. Kan, M. Verwaal, H. Broekhuizen, *J. Power Sources* **162** (2006) 971
6. C. E. Holland, J. W. Weidner, R. A. Dougal, R. E. White, *J. Power Sources* **109** (2002) 32
7. A. C. Baisden, A. Emadi, *IEEE Transactions On Vehicular Technology* **53** (2004) 199
8. X. B. Hu, Y. J. Huai, Z. J. Lin, J. S. Suo, Z. H. Deng, *J. Electrochem. Soc*. **154** (2007) A1026
9. A. D. Pasquier, I. Plitz, J. Gural, F. Badway, G. G. Amatucci, *J. Power Sources* **136** (2004) 160
10. L. T. Lam, R. Louey, *J. Power Sources* **158** (2006) 1140
11. G. Amatucci, (G. Amatucci), U.S. Pat. 6,517,972B1 (2003)
12. J. Gao, J. Ying, C. Jiang, C. Wan, *J. Power Sources* **166** (2007) 255
13. Y. Hishiyama, M. Inagaki, S. Kimura, S. Yamada, *Carbon* **12** (1974) 249
14. R. E. Franklin, *Proc. Roy. Soc. London Ser. A* **209** (1951) 196
15. Y. Z. Dong, Y. M. Zhao, H. Duan, L. Chen, Z. F. He, Y. H. Chen, *J. Solid State Electrochem.* **14** (2010) 131
16. K. Konstantinov, S. Bewlay, G. X. Wang, M. Lindsay, J. Z. Wang, H. K. Liu, S. X. Dou, J.-H. Ahn, *Electrochim. Acta* **50** (2004) 421.

Journal of the Serbian Chemical Society
JSCS-info@shd.org.rs • www.shd.org.rs/JSCS
J. Serb. Chem. Soc. 75 (9) 1271–1277 (2010)
JSCS–4050
UDC 546.657'72'27:66.017+
537.622:621.318.12
Original scientific paper

An overstoichiometric Nd–Fe–B hard magnetic material

TOMÁŠ ŽÁK[1]*, NADEŽDA M. TALIJAN[2#], VLADAN R. ĆOSOVIĆ[2#], JASNA T. STAJIĆ-TROŠIĆ[2#] and ALEKSANDAR S. GRUJIĆ[2#]

[1]Institute of Physics of Materials, Academy of Sciences of the Czech Republic, v.v.i., Žižkova 22, 616 62 Brno, Czech Republic and [2]Institute of Chemistry, Technology and Metallurgy, Department of Materials and Metallurgy, University of Belgrade, Njegoševa 12, 11000 Belgrade, Serbia

(Received 17 February, revised 16 April 2010)

Abstract: A commercial Nd-rich Nd–Fe–B-based hard magnetic material was studied. The obtained results were compared before and after recording of the thermomagnetic curve up to 800 °C. The curve itself showed clearly besides Curie points of the $Nd_2Fe_{14}B$ phase and α-Fe also another critical temperature. Mössbauer spectroscopic (MS) phase analysis and X-ray diffraction analysis (XRD) showed in addition to the commonly known phases $Nd_2Fe_{14}B$ and $NdFe_4B_4$ also some paramagnetic and ferromagnetic iron atoms (MS) and $Fe_{17}Nd_2$ intermetallics (XRD). During the exerted thermal treatment, the content of the $Nd_2Fe_{14}B$ and $NdFe_4B_4$ phases remained almost unchanged, while iron atoms from remnant minor phases built a separate α-Fe phase. The XRD pattern also showed the presence of some minor Nd phase. The results of Squid magnetic measurements suggest a nanocrystalline decoupled structure of the Nd-rich alloy in the optimized magnetic state. Measurement of the magnetization loop showed, in spite of small changes in the phase composition, that magnetic properties of the quality material deteriorated during the thermal treatment.

Keywords: rapid quenched Nd–Fe–B; overstoichiometric Nd content; Mössbauer phase analysis; XRD; magnetic properties.

INTRODUCTION

Permanent magnetic materials are key components of numerous electronic, data processing and medical devices, and recently, significant amounts are also required in the automotive.[1] Rapid quenched Nd–Fe–B alloys are an important class of permanent magnets because of their excellent magnetic properties originating from the ferromagnetic $Nd_2Fe_{14}B$ compound, which has a large saturation

* Corresponding author. E-mail: zak@ipm.cz
# Serbian Chemical Society member.
doi:10.2298/JSC100217058Z

magnetization and high anisotropy field, as the principal phase.[2,3] Hence, studies of Nd–Fe–B hard magnetic materials have become very significant over the last few decades.[4] Besides alloys with lowered neodymium contents exhibiting nanocomposite character, Nd–Fe–B alloys with enhanced qualities arising through the use of overstoichiometric Nd atoms are employed. Overstoichiometric (Nd-rich) Nd–Fe–B alloys have an almost monophase composition with the $Nd_2Fe_{14}B$ phase being dominant. Grains of this phase are magnetically isolated (decoupled) by intergranular layers of Nd-rich phases.[5–7] This structure leads essentially to a magnetic decoupling and each hard magnetic grain behaves like a small permanent magnet, which results in high coercivities.[1,8] The superior magnetic performance of this type of Nd–Fe–B alloy arises from the higher values of coercivity compared to nanocomposite Nd–Fe–B alloys[9,10] and ferrite-based magnetic materials.[11,12] In addition, their resistivity to higher temperatures is better than that of nanocomposite Nd–Fe–B alloys with a low Nd content.[13]

EXPERIMENTAL

The influence of the content of overstoichiometric Nd on the microstructure of commercial Nd–Fe–B alloy (Xiamen Yuxiang Magnetic Materials Ind. Co. Ltd, China) was analyzed by comparing the phase composition in the optimized magnetic state and after thermomagnetic measurement. The nominal composition of the material was >26 wt. % of Nd and < 1.3 wt. % of B, with the balance being Fe; the particle size was between 74 and 177 μm, the induction B_T = 0.603 T, the coercivities H_c(B) = 0.374 MA m^{-1} and H_c(J) = 0.974 MA m^{-1} and the energy product $(BH)_{max}$ = 57.1 kJ m^{-3}. The thermomagnetic curve was measured on an EG & G vibrating sample magnetometer in the field of 4 kA m^{-1} in vacuum. The heating and cooling rate was 4 °C min^{-1} with 30 min. hold at the maximum of 800 °C. Interpretation of comparable thermomagnetic measurements can be found in a previous investigations.[14] Mössbauer spectra were taken at room temperature in the standard transmission geometry using a ^{57}Co(Rh) source. The calibration was realized against an α-iron foil. The "Confit" program package[15] was used for spectra fitting and deconvolution,. Omitting the possible influence of the Lamb–Mössbauer factor, the relative content of the iron containing phases was derived from the intensities of the corresponding spectral components. The phase analysis was realized in manner similar to that described in Hinomura *et al.*[16] The X-ray diffraction (XRD) patterns were recorded on an X'Pert Pro MRD diffractometer from PANanalytical with Co Kα radiation operated at 40 kV and 30 mA. For routine characterization, diffraction data was collected in the range of 2θ Bragg angles (20 to 110°, step 0.08°). All XRD measurements were performed with powder samples at ambient temperature. For a quantitative analysis and determination of the crystallite size, HighScore plus with Rietweld structural models based on the ICSD database was used. The magnetic properties of the alloy *i.e.*, the corresponding hysteresis loops, were obtained at ambient temperature using Quantum Design MPMS 5XL superconducting quantum interference device (SQUID) magnetometer with magnetic field strength in range −4 to 4 MA m^{-1}.

RESULTS AND DISCUSSION

The curve of the thermomagnetic measurement, coming out from the optimized state, is presented in Fig. 1. It was completed taking into account the Curie

temperature of phases. Questionable is the FeB phase with a Curie temperature at about 325 °C, as it was detected neither in the optimized state nor in the final one. However, its intermediate presence during the heating process cannot be excluded. The rapid increase of the magnetic moment during cooling can be assigned, in addition to the structural changes, to the field cooling process. From the magnetically disordered state, during cooling the moments tend to minimize energy against the external magnetic field and the final state results in an anisotropic moments distribution, appearing externally as an enlargement of the bulk magnetic moment.

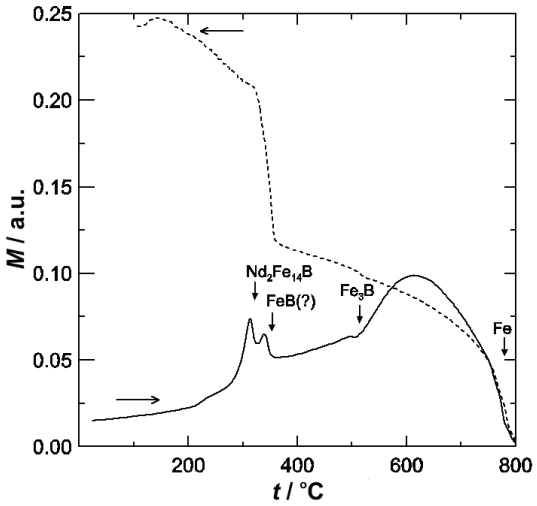

Fig. 1. The thermomagnetic curve measured on the Nd-rich Nd–Fe–B material in vacuum at a field of 4 kA m^{-1}. Heating: solid line, cooling: dotted line. The heating and cooling rates were both 4 °C min^{-1}.

The results of the Mössbauer phase analysis are presented in Figs. 2 and 3, and quantitatively in Table I. The original material was of high quality with a high content of the hard magnetic $Nd_2Fe_{14}B$ phase and a small amount of the $NdFe_4B_4$ phase. The presence of these crucial phases was confirmed by XRD analysis.

The kind and amount of other the phases correspond to the fraction of overstoichiometric Nd atoms. The Fe(Nd) solid solution component in the Mössbauer spectrum, with a spectral contribution looking like a "slightly broadened α-Fe phase", consists of a few sextets originating from iron atoms with 0, 1, 2, *etc.* neodymium atoms as nearest neighbors. Assuming an absence of atomic order, it is possible to plot theoretical relative intensities of such components depending on the concentration of Nd atoms as derived from the binomial distribution. The content of Nd atoms was then estimated by comparing these plots with the measured intensities to roughly 10 at.%. The $Fe_{17}Nd_2$ intermetallics structure found in XRD pattern (Fig. 4) is of a very similar composition. we cannot It is impossible to determine which atoms brought the iron of the phase labeled as Fe-para

into the paramagnetic region, especially as it has no evident match in the XRD pattern.

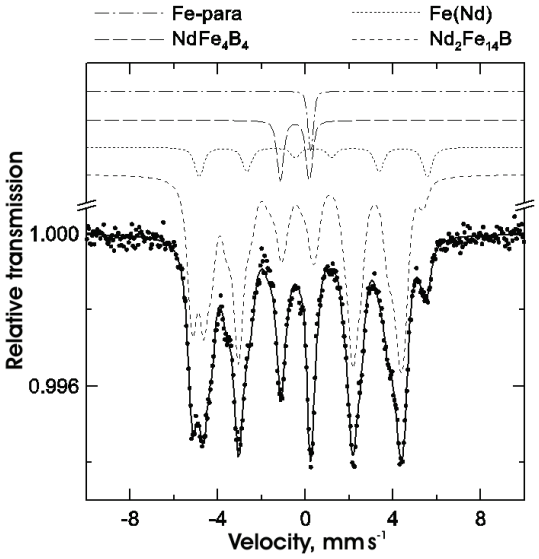

Fig. 2. Mössbauer phase analysis of the sample in the optimized state.

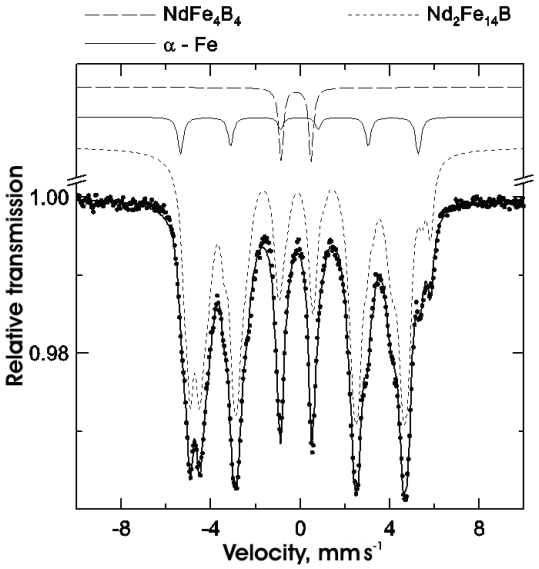

Fig. 3. Mössbauer phase analysis of the sample after thermomagnetic measurement.

Contrary to the data obtained by S. C. Wang and Y. Li,[6] no Nd oxide phases were distinguished using the XRD method. The thermal treatment during the thermomagnetic measurement brought an insignificant change in content of the dominating $Nd_2Fe_{14}B$ phase and of the $NdFe_4B_4$ phase. As the main decompo-

sition product, a weak component of the magnetically soft α-Fe phase was found, simultaneously giving rise of a separate Nd phase, as obvious from the XRD results only (Fig. 5).

TABLE I. The relative amount of iron-containing phases as determined from the Mössbauer spectra in the optimized state and after thermomagnetic measurement

Phase	Optimized state	After annealing
$Nd_2Fe_{14}B$	0.87	0.92
$NdFe_4B_4$	0.05	0.03
Fe(Nd)	0.08	–
α-Fe	–	0.05

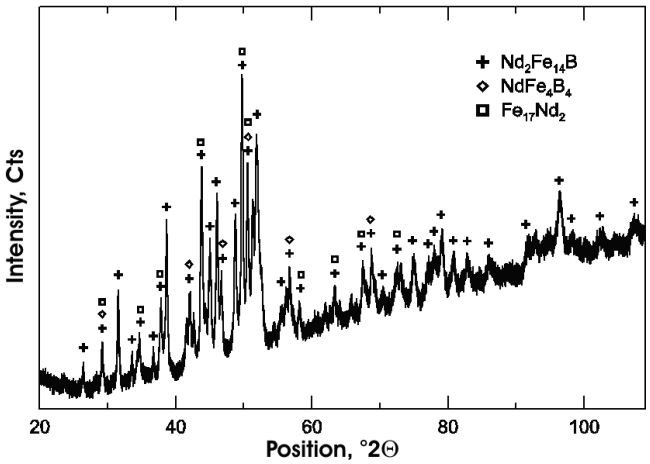

Fig. 4. The XRD pattern of the sample in the optimized state.

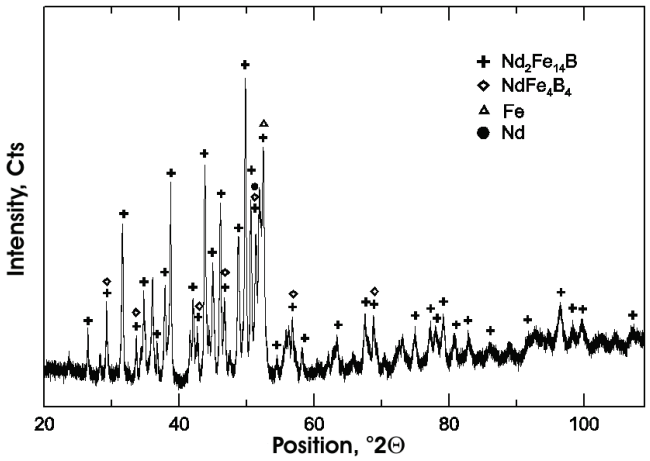

Fig. 5. XRD Pattern of the sample after thermomagnetic measurement.

The shape of the Squid hysteresis loop of the Nd-rich Nd–Fe–B alloy (Fig. 6) in the optimized magnetic state implies the presence of a magnetically decoupled nanocrystalline structure. The obtained high value of coercivity supports this and indicates a nearly monophase structure of the alloy with a dominant content of the main hard magnetic phase $Nd_2Fe_{14}B$. From the magnetization loop measurement (Fig. 6), it follows that, in spite of small changes in phase constitution, the thermal treatment during thermomagnetic measurement deteriorated the magnetic properties of the quality hard magnetic material.

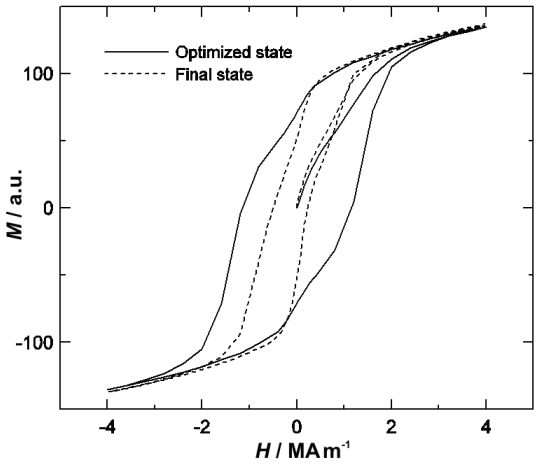

Fig. 6. Hysteresis loops of the samples in the optimized state and after thermomagnetic measurement.

CONCLUSIONS

In agreement with the thermomagnetic curve analysis, the process of thermal degradation of the material mainly occurred in the intergranular layer, leaving the dominant $Nd_2Fe_{14}B$ phase and the minor $NdFe_4B_4$ phase almost unchanged. The iron–neodymium phase underwent decomposition and both elements moved to separate phases, whereby the neodymium was not detectable by the Mössbauer effect but could be distinguished in XRD pattern. Thus, from a magnetic point of view, the main thermal decomposition product was the soft magnetic α-Fe phase. In spite of the conservation of the volume of the $Nd_2Fe_{14}B$ phase, the final state of the material was different from the optimal and deterioration of the magnetic properties (of magnetic hardness) was evident. It is obvious that the magnetic properties of the investigated alloy are in strong relationship to its structure and phase composition.

Acknowledgments. This work was supported by the Czech Ministry of Education, Youth and Sports, Project 1M0512, and by the Ministry of Science and Technological Development of the Republic of Serbia under Project OI 142035B.

И З В О Д

НАДСТЕХИОМЕТРИЈСКИ Nd–Fe–B ТВРДИ МАГНЕТНИ МАТЕРИЈАЛИ

ТОМÁШ ŽÁК[1], НАДЕЖДА М. ТАЛИЈАН[2], ВЛАДАН Р. ЋОСОВИЋ[2], ЈАСНА Т. СТАЈИЋ-ТРОШИЋ[2] и АЛЕКСАНДАР С. ГРУЈИЋ[2]

[1]*Institute of Physics of Materials, Academy of Sciences of the Czech Republic, v.v.i., Žižkova 22, 616 62 Brno, Czech Republic и* [2]*Институт за хемију, технологију и металургију, Центар за материјале и металургију, Универзитет у Београду, Његошева 12, 11000 Београд*

Испитиван је комерцијални магнетно-тврди материјал на бази Nd–Fe–B легуре обогаћене неодијумом. Добијени резултати испитивања материјала у оптималном стању и после термомагнетних (ТМ) мерења до 800 °C поређени су и дискутовани. На добијеној термомагнетној кривој се, поред јасно видљивих Кири температура фаза $Nd_2Fe_{14}B$ и α-Fe, може уочити и још једна критична температура. Применом Mössbauer-ове спектроскопске (МС) фазне анализе и методе дифракције X-зрака (XRD) утврђено је, поред присуства очекиваних $Nd_2Fe_{14}B$ и $NdFe_4B_4$ фаза, и присуство парамагнетних и феромагнетних јона Fe (МС), као и $Fe_{17}Nd_2$ интерметалних једињења (XRD). У току примењеног термичког третмана удео $Nd_2Fe_{14}B$ и $NdFe_4B_4$ фаза је остао скоро непромењен, док су атоми Fe из осталих фаза са мањим уделом формирали засебну α-Fe фазу. Резултати магнетних мерења на Squid магнетометру указују на нанокристалну декупловану структуру легуре обогаћене на неодијуму у оптималном магнетном стању. Из добијених хистерезисних петљи се може видети да је и поред малих промена у фазном саставу термички третман довео до делимичног губитка магнетних својстава испитваног материјала.

(Примљено 17. фебруара, ревидирано 16. априла 2010)

REFERENCES

1. O. Gutfleisch, *J. Phys. D: Appl. Phys.* **33** (2000) R157
2. N. C. Koon, B. N. Das, M. Rubinstein, J. Tyson, *J. Appl. Phys.* **57** (1985) 4091
3. C. Abache, H. Oesterreicher, *J. Appl. Phys.* **57** (1985) 4112
4. J. J. Croat, J. F. Herbst, R. W. Lee, F. E. Pinkerton, *J. Appl. Phys.* **55 (**1984) 2078
5. I. Ahmad, H. A. Davies, R. A. Buckley, *J. Magn. Magn. Mater.* **157**–**158** (1996) 31
6. S. C. Wang, Y. Li, *J. Magn. Magn. Mater.* **285** (2005) 177
7. A. Grujić, N. Talijan, A. Maričić, J. Stajić-Trošić, V. Ćosović, V. Radojević, *Sci. Sinter.* **37** (2005) 139
8. D. Goll, H. Kronmüller, *Naturwissenschaften* **87** (2000) 423
9. N. Talijan, V. Ćosović, J. Stajić-Trošić, A. Grujić, T. Žák, Z. Lee, V. Radmilović, *Mater. Trans. JIM* **50** (2009) 2302
10. V. Ćosović, N. Talijan, A. Grujić, J. Stajić-Trošić, T. Žák, Z. Lee, V. Radmilović, *Sci. Sinter.* **41** (2009) 209
11. D. Gingasu, I. Mindru, L. Patroni, S. Stoleriu, *J. Serb. Chem. Soc.* **73** (2008) 979
12. J. Ding, W. F. Miao, P. G. McCormick, R. Street, *J. Alloys Compd.* **281** (1998) 32
13. N. Talijan, T. Žák, J. Stajić-Trošić, V. Menushenkov, *Metalurgija – J. of Metall.* **8** (2002) 201
14. N. Talijan, V. Ćosović, J. Stajić-Trošić, T. Žák, *J. Magn. Magn. Mater.* **272**–**276** (2004) e1911
15. T. Žák, Y. Jirásková, *Surf. Interface Anal.* **38 (**2006) 710
16. T. Hinomura, S. Nasu, H. Kanekio, M. Uehara, S. Hirosawa, *Mater. Trans. JIM* **12 (**1997) 1106.

Journal of the Serbian Chemical Society
JSCS-info@shd.org.rs • www.shd.org.rs/JSCS
J. Serb. Chem. Soc. 75 (9) 1279–1289 (2010)
JSCS–4051
UDC 544.142+633.844:546.56:
66.061:504.53.054
Original scientific paper

Chelate-assisted phytoextraction: effect of EDTA and EDDS on copper uptake by *Brassica napus* L.

TIJANA M. ZEREMSKI-ŠKORIĆ[1*#], PETAR Đ. SEKULIĆ[1], IVANA V. MAKSIMOVIĆ[2], SRĐAN I. ŠEREMEŠIĆ[2], JORDANA M. NINKOV[1#], STANKO B. MILIĆ[1] and JOVICA R. VASIN[1]

[1]*Institute of Field and Vegetable Crops, Maksima Gorkog 30, Novi Sad and* [2]*Faculty of Agriculture, University of Novi Sad, Trg Dositeja Obradovića 8, Novi Sad*

(Received 7 December 2009, revised 12 January 2010)

Abstract: Chelate-assisted phytoextraction is proposed as an effective approach for the removal of heavy metals from contaminated soil through the use of high biomass plants. The aim of the present study was to compare the efficiency of the two chelators: EDTA and biodegradable EDDS in enhancing Cu uptake and translocation by *Brassica napus* L. grown on moderately contaminated soil and treated with increasing concentrations of EDTA or EDDS. Increasing amounts of EDDS caused serious growth suppression of *B. napus* and an increase in shoot metal concentrations. Growth suppression limited the actual amount of phytoextracted Cu at high concentrations of EDDS. The maximum amount of extracted Cu was achieved by the application of 8.0 and 4.0+4.0 mmol kg^{-1} EDDS. The shoot Cu concentrations after EDTA application were much lower than with EDDS at the same doses. According to these experiments, EDTA does not appear to be an efficient amendment if Cu phytoextraction with *B. napus* is considered but EDDS is.

Keywords: phytoextraction; copper; EDTA; EDDS; *Brassica napus* L.

INTRODUCTION

Soil pollution by heavy metals is a widespread problem posing considerable threats to the environment. Copper (Cu) enters the soil by deposition from local foundries and smelters, through manuring with contaminated sludges and from application of fungicides. With its known antifungal and algaecidal properties, elevated levels of Cu in soil adversely affect microbially mediated soil processes.[1]

* Corresponding author. E-mail: tijana@ifvcns.ns.ac.rs
# Serbian Chemical Society member.
doi: 10.2298/JSC091207086Z

Although clean-up of contaminated sites is necessary, often the application of environmental remediation strategies is very expensive and intrusive.[2] Thus, the development of a low-cost and environmentally friendly strategy is needed.

Phytoremediation is a method for *in situ* clean-up of contaminated soils. This technique uses the ability of certain plants to accumulate heavy metals in high concentrations in their above-ground parts.[3] The development of large-scale phytoextraction techniques could consider crop species as bioaccumulators of heavy metals; in fact, some of them can accumulate heavy metals while producing high biomass in response to established agricultural management.[4,5]

The major problem hindering plant remediation efficiency is that some of the metals are immobile in soils and their availability and phytoextraction rates are limited by solubility and diffusion to the root surface.[6,7] Synthetic chelators, *e.g.*, ethylenediamine tetraacetic acid (EDTA), have been used to artificially enhance heavy metals solubility in soil solution from the soil solid phase and thus to increase phytoavailability of heavy metals. The addition of chelators into the soil induces phytoextraction and translocation of heavy metals from the roots to harvestable, above-ground parts of plants.[8] The use of chelators is especially important for induced phytoextraction of Cu, since in general, the Cu concentration of plants tends to be internally rather than externally regulated. Plants use an exclusion strategy, comprising the avoidance of metal uptake and restriction of metal translocation from roots to the shoots, to adapt to toxic Cu concentrations in soil. Only high concentrations of phytoavailable Cu, *e.g.*, achieved by chelator addition, result in a breakdown of the exclusion mechanism and enhanced Cu uptake.[6]

One of the main drawbacks of chelator-induced phytoextraction is that most synthetic chelators, such as EDTA, form chemically and microbiologically stable complexes with heavy metals that pose a threat of groundwater contamination.[9,10] Ethylenediamine disuccinic acid (EDDS) is a structural isomer of EDTA and has two chiral carbon atoms and three stereoisomenrs.[11] Among them, only the (*S*,*S*) isomer is readily biodegradable. It is a low-toxic chelator with strong chemical affinity for heavy metals that produces benign degradation products,[12] which makes it a potentially suitable replacement of EDTA in chelate-assisted phytoextraction. Meers *et al.*[13] describe a high degree of biodegradability for EDDS with observed half lives ranging from 3.8 to 7.5 days, depending on the application rates.

Phytoextraction with *Brassica napus* L. has the potential to become a profitable enterprise when combined with biofuel production, especially in view of the expected increasing oil prices over the coming years. The aim of the present study was to compare the efficiency of the two chelators: EDTA and biodegradable EDDS in enhancing Cu-uptake and translocation by *B. napus* L. grown on moderately contaminated soil.

EXPERIMENTAL

The contaminated soil used in these experiments was collected from a former vineyard in a vine growing area near Novi Sad, Serbia with an over five-decade history of soil contamination with Cu-containing pesticides. The soil was air-dried, homogenized and sieved through a 2-mm stainless sieve before analysis.

The water and potential soil pH, organic matter content, free $CaCO_3$ content, specific electrical conductivity (*EC*), cation exchange capacity (*CEC*) and the content of exchangeable cations (Ca, Mg, K and Na) in the soil were determined in accordance with ISO methods for soil quality.[14-18] The particle size distribution was determined in the < 2 mm fraction by the internationally recognized pipette method.

Total soil Cu concentration was determined by microwave assisted digestion using the Usepa method 3051A[19] employing a Milestone Ethos 1 microwave sample preparation system. Analysis was subsequently performed using inductively coupled plasma-optical emission spectrometer, ICP-OES, (Varian Vista Pro-axial).

To assess the distribution of Cu among various components of the soil, a fractionation analysis was performed according to the sequential procedure of Tessier *et al.*[20] The exchangeable fraction was released with 1 M $MgCl_2$ at pH 7, the carbonate fraction with 1 mol dm^{-3} CH_3COONa (pH 5), the reducible fraction with 40 mol m^{-3} $NH_2OH{\cdot}HCl$ in 25 % CH_3COOH (95 °C) and the oxidizable fraction with 30 % H_2O_2 in 20 mol m^{-3} HNO_3 (pH ~2 and 85 °C).

Pot experiments were performed during April–June in an outdoor vegetation hall. The pots were filled with 5 kg of air dried soil and brought to 2/3 of field capacity with deionized water. Subsequently, ten seeds of a spring variety of *B. napus* were sown in the pots and after germination, thinned to two plants per pot. Considering the duration of the pot experiments (11 weeks), all pots were fertilized with a mineral fertilizer solution to avoid limiting nutritional conditions. The nutrient solution contained 1.00 g of N (2.86 g of NH_4NO_3) per pot. The soil moisture content was maintained constant at 2/3 of field capacity. After 7 weeks of growth, the pots were treated with the soil amendments outlined in Table I.

TABLE I. Chelator concentrations used for the treatments in the plant experiments (applied 4 weeks before harvest). Ctrl presents the untreated control, treatments A4 and A5 received a second application 7 days after the initial treatment

Treatment	Concentration, mmol kg^{-1}	Chelator
Control	0.0	–
A1	2.0	EDDS
A2	4.0	EDDS
A3	8.0	EDDS
A4	2.0 + 2.0	EDDS
A5	4.0 + 4.0	EDDS
B1	2.0	EDTA
B2	4.0	EDTA
B3	8.0	EDTA

The second application of EDDS was performed 7 days after the first based on EDDS data on half lives ranging from 3.8 to 7.5 days.[13] EDTA and EDDS, in the form of Na-salts, were dissolved in deionized water and applied to the top of the pot. Chelate treatment closer to the harvest was preferred as opposed to pre-sow or post-germination treatment to avoid pos-

sible growth suppressions. As observed by Meers *et al.*[21] and Lesage *et al.*,[22] phytotoxic effects by metal mobilization in a pre-sow or post-germination treatment considerably limited the success of metal extraction due to severely reduced biomass production. The harvest time was selected to be 4 weeks after chelate addition based on results given in literature,[13,23] in which a surge in metal accumulation by plants was observed 3 weeks after chelate addition.

The plants were harvested 11 weeks after sowing, oven dried at 60 °C to constant mass and weighed to determine the dry weight biomass production. The plant roots were separated from the soil, washed three times with deionized water, oven dried at 60 °C to constant mass and weighed. The total concentrations of Cu in the plant tissues were determined by ICP-OES (Varian, Vista-Pro) after digestion in a mixture of 10 ml of HNO_3 (65 %) and 2 ml of H_2O_2 (30 %) using the microwave technique.

To study the effects of the various amendments on the translocation of Cu, the translocation efficiency (τ), defined as the fraction that after root absorption was successfully translocated to the above-ground plant parts was used, *i.e.*,:

$$\tau\,(\%) = 100 \times Cu\text{shoot} \times DW\text{shoot} / (Cu\text{shoot} \times Da_{\text{shpot}} + Cu\text{root} \times DW\text{root})$$

where *Cu*shoot and *Cu*root are the heavy metal concentration in the shoot and root (μg g^{-1}), respectively, and *DW*shoot and *DW*root are the dry weight production in the shoot and root (g), respectively.[21]

Statistical analysis was performed using Statistica 7 (StatSoft, Inc. Corporation, Tulsa, OK, USA) and Excel (Microsoft Inc., Seattle, NY, USA) software packages. Means of replicates and evaluation of significance of differences between the various treatments were determined by descriptive statistics and one-way Anova analysis, followed by the Tukey *post hoc* test (α = 0.05). Correlations between amendment concentration, dry weight production and shoot heavy metal concentrations were evaluated using Pearson's correlation coefficient.

TABLE II. Basic physical and chemical properties of the soil under study

pH-H_2O	–	8.22
pH-KCl	–	7.15
EC	μS cm^{-1}	107.3
Clay (< 2 μm)	%	17.2
Silt (< 20 μm)	%	32.1
Fine sand (20–200 μm)	%	47.2
Sand (200–2000 μm)	%	2.90
$CaCO_3$	%	3.82
OM	%	2.44
CEC	$cmol_{(+)}$ kg^{-1}	23.7
Exchangeable Ca	$cmol_{(+)}$ kg^{-1}	14.8
Exchangeable Mg	$cmol_{(+)}$ kg^{-1}	2.28
Exchangeable Na	$cmol_{(+)}$ kg^{-1}	0.10
Exchangeable K	$cmol_{(+)}$ kg^{-1}	1.45
Total Cu	mg kg^{-1}	256.4
Cu in soil fractions		
Exchangeable	mg kg^{-1}	1.2
Precipitated with carbonates	mg kg^{-1}	23.3
Bound to Fe + Mn oxides	mg kg^{-1}	124.0
Bound to organic matter	mg kg^{-1}	39.3

RESULTS AND DISCUSSION

According to the basic physical and chemical characteristics summarized in Table II, the soil used in the pot experiments can be classified as alkaline with a medium content of organic matter. The soil texture was clay loam. The total Cu content was 2.5 times higher than the maximum allowable concentration (*MAC*) of 100 mg kg^{-1} for agricultural soils, as prescribed by the laws of the Republic of Serbia.[24] The chemical fractionation of Cu in the soil enabled the determination of Cu concentrations in the exchangeable, carbonate, Fe + Mn oxides and organic matter fractions of the soil. As shown in Table II, Cu was predominantly bound to Fe and Mn oxides. The very low concentrations of Cu in bioavailable forms (exchangeable and precipitated with carbonates) limit its phytoavailability.

The dry matter yields of *B. napus* are shown in Fig. 1. When no chelates were added to the soil, all of the plants showed normal development without visual symptoms of metal toxicity. The treatments with 2.0 mmol kg^{-1} soil EDTA, 2.0 and 2.0 + 2.0 mmol kg^{-1} soil EDDS had no significant effect on the shoot biomass. However, the treatments with 4.0, 8.0 and 4.0 + 4.0 mmol kg^{-1} soil EDDS significantly affected plant growth and the shoot dry matter yields decreased to 63, 35 and 41 % of the control plants, respectively. Serious growth suppression upon EDDS addition at higher doses indicates that the plants were

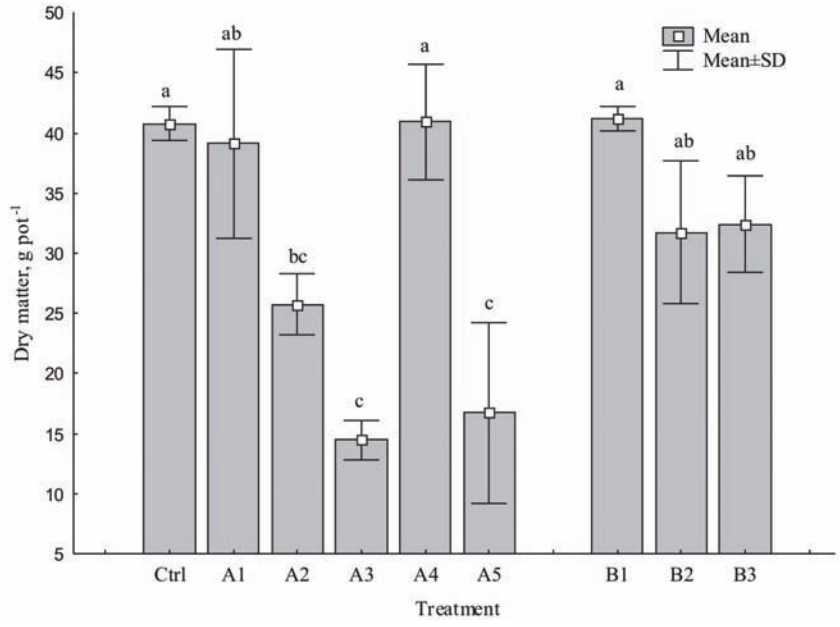

Fig 1. Effects of the application of chelates on the dry matter yields of shoots in *B. napus*. The values are means ±*SD* (*n* = 3); the superscript letters (a, b, ab, c) denote statistically different treatments according to the Tukey test (*P* = 0.05). (For detailed description of the treatments, *cf*. Table I).

subjected to heavy metal stress. This is supported by the significant negative correlation between dry-weight production of *B. napus* and the shoot Cu concentration (Table III).

The treatments with 4.0 and 8.0 mmol kg^{-1} soil EDTA appeared to be less toxic to *B. napus* compared to EDDS, decreasing the shoot dry matter yields to 78 and 79 % of the values for the control plants, respectively, which is similar to the results reported by Luo *et al.*[25] for the effect of 5.0 mmol kg^{-1} EDTA on the shoot dry matter of *Zea mays* L. and *Phaseolus vulgaris* L. The smaller effect of EDTA on plant growth is also visible through the lower coefficient of correlation between the EDTA dose and the dry weight production of *B. napus* compared with the same coefficient for EDDS (Table III).

TABLE III. Pearson's correlation coefficients between amendment concentrations, dry weight production of *B. napus* (DW), Cu concentrations in shoot and root and the phytoextracted amount of Cu

	EDDS	DW	Cu_{shoot}	Cu_{root}	$Cu_{phytoextracted}$
EDDS	–	–0.812[a]	0.811[a]	–0.626[a]	0.754[a]
DW		–	–0.790[a]	0.681[a]	–0.635[a]
Cu_{shoot}			–	–0.657[a]	0.898[a]
Cu_{root}				–	–0.662[a]
$Cu_{phytoextracted}$					–
	EDTA	DW	Cu_{shoot}	Cu_{root}	$Cu_{phytoextracted}$
EDTA	–	–0.672[b]	0.735[b]	0.558	0.678[b]
DW		–	–0.648[b]	–0.274	–0.342
Cu_{shoot}			–	0.254	0.925[a]
Cu_{root}				–	0.272
$Cu_{phytoextracted}$					–

[a]Correlation is significant at the 0.01 level; [b]correlation is significant at the 0.05 level

At harvest, the concentration of Cu in the control plants was 16.5 mg kg^{-1} dry weight in the shoots and 220.6 mg kg^{-1} dry weight in the roots, which is in good agreement with the results of experiments on copper uptake by *B. napus* when no amendments were applied.[26,27] These results indicate that Cu uptake and translocation from roots to shoots was limited in the absence of amendments.

In the present study, the most significant increase in Cu concentration in the plant shoots occurred at the doses of 4.0+4.0 and 8.0 mmol kg^{-1} EDDS, when the Cu shoot concentration was approximately 18 times higher than in the control plants and the application of 4.0 mmol kg^{-1} EDDS increased Cu uptake by approximately 8 times (Table IV). In the present experiments, the treatment with 4.0 mmol kg^{-1} EDDS resulted in a much greater Cu uptake than was the case in experiments by other authors who studied Cu uptake by other species of the family *Brassicaceae* at 3.0 and 5.0 mmol kg^{-1} EDDS and found that Cu shoot uptake increased three to four times.[13,28,29] It is possible that the increased uptake

of Cu shown here was a result of the fact that the present experiments were set up in a way that simulated field conditions to a great extent (growing season, outdoors, natural light, a small number of plants per pot).

TABLE IV. Shoot and root Cu concentration (mg kg^{-1} dry weight) and translocation efficiency (%) with application of EDTA and EDDS. Values are means ±*SD* (*n* = 3); the superscript letters (a, b, ab, c) denote statistically different treatments according to the Tukey test (*P* = 0.05)

Treatment	Cu_{shoot}	Cu_{root}	Translocation efficiency
Untreated control	16.6±2.3[a]	220.6±18.1[ab]	33.6±8.9[a]
EDDS, mmol kg^{-1} soil:			
2.0	38.6±16.8[a]	244.4±30.3[ab]	52.2±6.3[ab]
4.0	131.5±6.3[ab]	91.2±13.0[a]	92.7±4.4[c]
8.0	316.4±208.2[b]	78.1±32.1[a]	93.1±8.3[c]
2.0 + 2.0	40.0±10.7[a]	236.6±78.4[ab]	55.7±12.8[b]
4 + 4	295.6±43.9[b]	143.7±6.9[ab]	89.1±0.8[c]
EDTA, mmol kg^{-1} soil:			
2.0	34.2±2.8[a]	202.1±111.5[ab]	53.4±15.7[a]
4.0	51.5±19.3[a]	287.8±117.9[ab]	52.5±20.1[a]
8.0	52.0±11.6[a]	390.6±186.2[b]	41.6±10.6[a]

There was no statistically significant increase in shoot Cu concentration compared to the control at the doses of 2.0 and 2.0+2.0 mmol kg^{-1} EDDS and it may be speculated that these treatments were insufficient to break down the uptake barriers of the plant under the conditions of the present experiments. The significant difference in metal uptake when 4.0 mmol kg^{-1} EDDS was applied in a single and split dose can be explained in light of ligand half lives;[13] the half lives in soil were estimated to be 4.7 days for 2.4 mmol kg^{-1} and 7.5 days for 4.0 mmol kg^{-1} EDDS. According to these findings, when EDDS was applied at a dose of 2.0 mmol kg^{-1}, the concentration of metal-chelate complex would be significantly decreased before the second application, performed 7 days after the first, keeping the metal–chelate concentration too low to break down the plant uptake barriers. On the other hand, there was no statistically significant difference in metal uptake between single and split applications of 8.0 mmol kg^{-1} EDTA, which was probably due to the prolonged ligand half life at the higher concentration.

The addition of EDTA to the soil at doses of 4.0 and 8.0 mmol kg^{-1} increased the Cu uptake by approximately 3 times, which is in good agreement with results of other studies in which application of EDTA at 3.0 to 5.0 mmol kg^{-1} increased the Cu uptake by *Brassicaceae* by 2 to 3.5 times.[10,28,30] However, the shoot Cu concentration was 2.5 and 6 times lower than with EDDS at the same doses. This observation was consistent with the observation that EDTA was less toxic to *B. napus* than EDDS (Fig. 1), which is also supported by the less significant correlations between EDTA dose and shoot Cu concentrations.

The results of the present experiments suggest that EDDS can be regarded as a better candidate chelate for the phytoextraction of Cu in soils. The effectiveness of chelate-enhanced metal accumulation by *B. napus* was consistent with the greater ability of EDDS than EDTA to solubilize soil metals.[13,25] The higher observed mobilization of Cu by EDDS could not be explained by its respective stability constants with the two chelators: log K = 18.7 for Cu–EDTA and log K = 18.4 for Cu–EDDS. These stability constants would suggest equal or better mobilezation of Cu by EDTA. The higher mobilization of Cu by EDDS in the current experiments can be explained by lower affinity (based on stability constants) of EDDS for competitor ions, such as: Ca^{2+} (log $K_{Ca–EDDS}$ = 4.2; log $K_{Ca–EDTA}$ = = 10.6), Mg^{2+} (log $K_{Mg–EDDS}$ = 5.8; log $K_{Mg–EDTA}$ = 8.8), Fe^{3+} (log $K_{Fe–EDDS}$ = = 22.0; log $K_{Fe–EDTA}$ = 25.0) and Mn^{2+} (log $K_{Mn–EDDS}$ = 9.0; log $K_{Mn–EDTA}$ = = 13.8).[31]

The limited translocation of heavy metals following absorption by the roots is one of the bottlenecks limiting the overall efficiency of phytoextraction. In their patent on the induced hyper accumulation of metals in plant shoots, Ensley *et al*.[32] described chemically enhanced phytoextraction as a two-step process. The plants first accumulate metals in their roots. Induction is then applied, which enhances the transfer of the metals to the shoots. This transfer is attributed to a disruption of the plant's metabolism, which regulates the transport of metal to shoots. The respective translocation efficiency values are presented in Table IV. The translocation efficiency for Cu in the untreated control was 33 %, which was lower than that reported by Marschiol *et al*.[26] when *B. napus* grown on soil polluted with 280 mg kg^{-1} Cu with no amendments achieved an efficiency of 57 %. The results of the present experiments indicate that the application of EDDS can dramatically increase the translocation of Cu from the roots to the shoots of *B. napus*. No statistically significant improvement was observed only at the dose of 2.0 mmol kg^{-1}, medium translocation efficiency was observed after the treatment with 2.0+2.0 mmol kg^{-1} EDDS, and when 4.0, 8.0, and 4.0+4.0 mmol kg^{-1} EDDS was applied, the translocation efficiency increased from 33 to 93 %. Similar efficiency in Cu translocation after the application of 5.0 mmol kg^{-1} EDDS was reported in the literature for corn (from 8.5 to 83 %) and beans (from 10.2 to 93 %).[25] It appears that only at very high phytoavailable Cu concentrations can the breakdown of the exclusion mechanisms result in a greatly enhanced Cu uptake. The increases of the translocation efficiency after the application of 2.0, 4.0 and 8.0 mmol kg^{-1} EDTA were very small and statistically insignificant compared to the control. Moreover, this is in good agreement with efficiencies that Luo *et al*.[25] obtained for corn (39 %) and bean (50 %) after the application of 5.0 mmol kg^{-1} EDTA.

The phytoextracted amount of Cu is the product of the metal concentration in the shoots and the dry-weight yield of the plant (Fig. 2). Although increasing

doses of EDDS resulted in increased shoot Cu concentrations, up to 18 times, compared to the control, the phytoextracted amount of Cu did not follow the same order of magnitude due to growth suppression at high EDDS concentrations. The only statistically significant increase in phytoextracted Cu compared to the control was achieved after the application of 8.0 and 4.0+4.0 mmol kg^{-1} EDDS, when totals of 4.6 and 4.5 mg Cu per pot were phytoextracted, respectively.

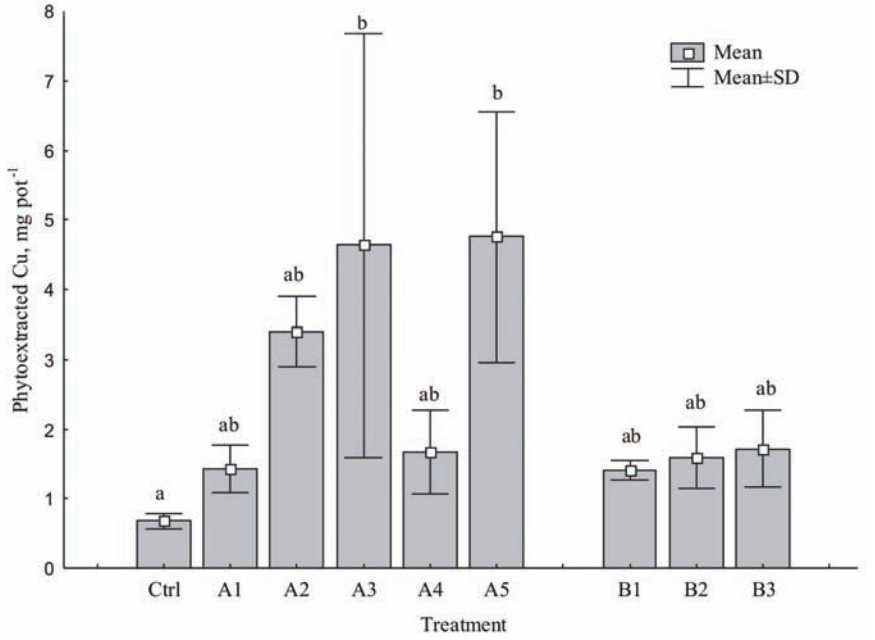

Fig. 2. Phytoextracted amount of copper (mg pot^{-1}) at different amendment concentrations The values are means ±*SD* (*n* = 3); the superscript letters (a, b, ab) denote statistically different treatments according to the Tukey test (*P* = 0.05). (For detailed descriptionof the treatments, *cf.* Table I.).

The amount of phytoextracted Cu after EDTA application did not differ statistically from the control even at the highest dose, although growth suppression was smaller than in the treatment with EDDS, as the Cu concentrations in the above-ground plant parts were only 2 to 3.5 higher than in the control.

Considerably smaller metal extraction rates were also found in other studies and they may be related to toxicity problems leading to yield reduction.[10,13,26] It could be, therefore, realistically hypothesized that they could perform better in the case of light soil pollution.

CONCLUSIONS

The two main important bottlenecks in the phytoextraction process are the limited bioavailability of heavy metals in soils and the limited translocation to the

shoots. The presented experiments tried to overcome these bottlenecks by adding EDDS or EDTA to Cu-polluted soil. The soil originated from a former vineyard and contained low concentrations of Cu in an exchangeable form. Increasing amounts of EDDS caused serious growth suppression of *B. napus* and an increase in shoot metal concentrations, leading to the assumption that plants suffered heavy metal stress. Growth suppression limited the actual amount of phytoextracted Cu at high concentrations of EDDS. The maximum amount of extracted Cu was achieved by the application of 8.0 and 4.0+4.0 mmol kg^{-1} EDDS. The shoot Cu concentrations after EDTA application were much lower than with EDDS at the same doses and there was no statistical difference in phytoextracted amount of Cu between the control and EDTA treatments.

According to the performed experiments, EDTA does not appear to be an efficient amendment if Cu phytoextraction with *B. napus* is considered but EDDS does.

Acknowledgements. These experiments were performed as part of the project TR 20086, financed by the Ministry of Science and Technological Development of the Republic of Serbia.

ИЗВОД

ФИТОЕКСТРАКЦИЈА ПОТПОМОГНУТА ХЕЛАТОРИМА: ЕФЕКАТ EDTA И EDDS НА ВЕЗИВАЊЕ БАКРА КОД *Brassica napus* L.

ТИЈАНА М. ЗЕРЕМСКИ-ШКОРИЋ[1], ПЕТАР Ђ. СЕКУЛИЋ[1], ИВАНА В. МАКСИМОВИЋ[2], СРЂАН И. ШЕРЕМЕШИЋ[2], ЈОРДАНА М. НИНКОВ[1], СТАНКО Б. МИЛИЋ[1] и ЈОВИЦА Р. ВАСИН[1]

[1]Институт за ратарство и повртарство,Максима Горког 30, Нови Сад и [2]Пољопривредни факултет, Универзитет у Новом Саду,Трг Доситеја Обрадовића 8, Нови Сад

Сматра се да употреба биљака са високом биомасом за фитоекстракцију потпомогнуту хелаторима може представљати ефикасан начин за уклањање тешких метала из контаминираног земљишта. Циљ овог истраживања је био да се упореди ефикасност два хелатора: EDTA и биодеградабилног EDDS у повећању везивања и транслокације бакра код врсте *Brassica napus* L. гајене на умерено загађеном земљишту. Растуће концентрације EDDS су изазвале и повећано везивања бакра и изражен застој у порасту надземног дела биљке *B. napus* L. Количина фитоекстрахованог бакра при високим концентрацијама EDDS је била ограничена застојем у порасту надземног дела биљке. Највећа количина фитоекстрахованог бакра је постигнута са применом 8,0 и 4,0+4,0 mmol kg^{-1} EDDS. Концентрација бакра у надземном делу након примене EDTA је била много нижа него приликом примене EDDS у истим концетрацијама. На основу резултата добијених у овом експерименту, утврђено је да, за разлику од EDDS, EDTA није довољно ефикасан хелатор за фитоекстракцију бакра помоћу *B. napus* L.

(Примљено 7. децембра 2009, ревидирано 12. јануара 2010)

REFERENCES

1. D. A. Wright, P. Welbourn, *Environmental Toxicology*, Cambridge University Press, Cambridge, 2002, p. 301
2. S. P. McGrath, A. M. Chaudri, K. E. Giller, *J. Ind. Microbiol.* **14** (1995) 94
3. *USEPA*, United States Environmental Protection Agency, 1998, EPA-542-F-98-011

4. Y. M. Li, R. Chaney, E. Brewer, R. Roseberg, J. S. Angle, A. J. M. Baker, R. Reeves, J. Nelkin, *Plant Soil* **249** (2003) 107
5. B. Žarković, S. Blagojević, *J. Serb. Chem. Soc.* **74** (2009) 1009
6. H. Dahmani-Muller, F. van Oort, B. Gelie, M. Balabane, *Environ. Pollut.* **109** (2000) 231
7. L. A. Brun, J. Maillet, P. Hinisinger, M. Pepin, *Environ. Pollut.* **111** (2001) 293
8. E. Meers, F. M. G. Tack, S. Van Slycken, A. Ruttens, J. Vangronsveld, M. G. Verloo, *Int. J. Phytoremediat.* **10** (2008) 390
9. H. Grčman, Š. Velikonja-Bolta, D. Vodnik, B. Kos, D. Leštan, *Plant Soil* **235** (2001) 105
10. W. W. Wenzel, R. Unterbrunner, P. Sommer, P. Sacco, *Plant Soil* **249** (2003) 83
11. P. Vandevivere, H. Saveyn, W. Verstraete, T. C. J. Feijtel, D. Schowanek, *Environ. Sci. Technol*. **35** (2001) 1765
12. J. S. Jaworska, D. Schowanek, T. C. J. Feijtel, *Chemosphere* **38** (1999) 3597
13. E. Meers, A. Ruttens, D. Samson, M. Hopgood, F. M. G. Tack, *Chemosphere* **58** (2005) 1011
14. *ISO 10390, Soil quality – Determination of pH*, 1994
15. *ISO 14235, Soil quality – Determination of organic carbon by sulfochromic oxidation*, 1998
16. *ISO 10693, Soil quality – Determination of carbonate content - Volumetric method*, 1995
17. *ISO 11265, Soil quality – Determination of the specific electrical conductivity*, 1994
18. *ISO 11260, Soil quality – Determination of effective cation exchange capacity and base saturation level using barium chloride solution*, 1994
19. *US EPA 3051A, Microwave assisted acid digestion of sediments, sludges, soils, and oils*, 2007
20. A. Tessier, P. G. C. Campbell, M. Bisson, *Anal. Chem.* **51** (1979) 844
21. E. Meers, M. Hopgood, E. Lesage, P. Vervaeke, F. M. G. Tack, M. G. Verloo, *Int. J. Phytoremediat.* **6** (2004) 95
22. E. Lesage, E. Meers, P. Vervaeke, S. Lamsal, M. Hopgood, F. M. G. Tack, M. G. Verloo, *Int. J. Phytoremediat.* **7** (2005) 143
23. K. K. Chiu, Z. H. Ye, M. H. Wong, *Chemosphere* **60** (2006) 1365
24. *Regulations concerning the allowed quantities of dangerous and harmful matters in soil and irrigation waters, and methods for their analysis, Official Gazette of the Republic of Serbia*, No. 23/94 (in Serbian)
25. C. Luo, Z. Shen, X. Li, *Chemosphere* **59** (2005) 1
26. L. Marchiol, S. Assolari, P. Sacco, G. Zerbi, *Environ. Pollut.* **132** (2004) 21
27. T. J. Purakayastha, T. Viswanth, S. Bhadraray, P. K. Chhonkar, P. P Adhikari, K. Suribabu, *Int. J. Phytoremediat.* **10** (2008) 61
28. B. Kos, D. Leštan, *Environ. Pollut.* **132** (2004) 333
29. M. F. Quartacci, B. Irtelli, A. J. M. Baker, F. Navari-Izzo, *Chemosphere* **68** (2007) 1920
30. C. Luo, Z. Shen, L. Lou, X. Li, *Environ. Pollut.* **144** (2006) 862
31. A. E. Martell, R. M. Smith, *NIST Critically Selected Stability Constants of Metal Complexes*, Version 7.0. NIST, Gaithersburg, MD, 2003
32. B. D. Ensley, M. J. Blaylock, S. Dushenkov, N. P. B. A. Kumar, Y. Kapulnik, C. S. Orser, U.S. Patent 5 917 117 (1999).

Journal of the Serbian Chemical Society
JSCS-info@shd.org.rs • www.shd.org.rs/JSCS
J. Serb. Chem. Soc. 75 (9) 1291–1302 (2010)
JSCS–4052
UDC 547.551.1:615.9:626.812:579.81/.85
Original scientific paper

Toxicity of five anilines to crustaceans, protozoa and bacteria•

MARILIIS SIHTMÄE, MONIKA MORTIMER, ANNE KAHRU and IRINA BLINOVA*

Laboratory of Molecular Genetics, National Institute of Chemical Physics and Biophysics, Akadeemia tee 23, Tallinn 12618, Estonia

(Received 19 December 2009, revised 18 February 2010)

Abstract: Aromatic amines (anilines and related derivates) are an important class of environmental pollutants that can be released to the aquatic environment as industrial effluents or as breakdown products of pesticides and dyes. The toxicity of aniline, 2-chloroaniline, 3-chloroaniline, 4-chloroaniline and 3,5-dichloroaniline towards a multitrophic test battery comprised of bacteria *Aliivibrio fischeri* (formerly *Vibrio fischeri*), a ciliated protozoan *Tetrahymena thermophila* and two crustaceans (*Daphnia magna* and *Thamnocephalus platyurus*) were investigated. Under the applied test conditions, the toxicity of the anilines notably varied among the test species. The bacteria and protozoa were much less sensitive towards the anilines than the crustaceans: EC_{50} values 13–403 mg L^{-1} *versus* 0.13–15.2 mg L^{-1}. No general tendency between toxicity and the chemical structure of the anilines (the degree of chloro-substitution and the position of the chloro-substituents) was found in the case of all the tested aquatic species. The replacement of the artificial test medium (ATM) by the river water remarkably decreased the toxicity of anilines to crustaceans but not to protozoa. This research is part of the EU 6th Framework Integrated Project OSIRIS, in which ecotoxicogenomic studies of anilines (*e.g.*, for *Daphnia magna*) will also be performed that may help to clarify the mechanisms of toxicity of different anilines.

Keywords: ecotoxicity; anilines; test battery; river water; ECOSAR.

INTRODUCTION

Aromatic amines (anilines and related derivates) are widely used industrial chemicals and are therefore an important class of environmental pollutants. Aniline is the parent molecule of a vast family of aromatic amines. Since its discovery in 1826, it has become one of the hundred most important building blocks in

* Corresponding author. E-mail: irina.blinova@kbfi.ee
• The paper was partially presented at the 2nd REP LECOTOX Workshop "Trends in Ecological Risk Assessment", 21–23 September, 2009, Novi Sad, Serbia (EC FP 6 funded project INCO-CT-2006-043559-REP-LECOTOX).
doi: 10.2298/JSC091219103S

chemistry. Aniline and its derivatives containing chloro-substituents are used as intermediates in many different fields of applications, such as the production of isocyanates, rubber processing chemicals, dyes and pigments, agricultural chemicals and pharmaceuticals.[1] These compounds can be released into the surface water as industrial effluents or as break-down products of pesticides and dyes.

According to Registration, Evaluation, Authorization and Restriction of Chemicals (REACH) regulation,[2] all substances on the European Market, which are manufactured or imported in a quantity of 1 tonne or more per year will have to be registered by June 1, 2018. The latest evaluation made by Rovida and Hartung[3] in 2009 suggests that around 68,000 to 101,000 chemicals will have to be registered in the EU under the REACH regulation. This is a huge task and responsibility for industry, regulators and scientists to manage the risks that chemicals may pose to health and the environment.

This article focuses on the ecotoxicity of aniline and four of its derivatives: aniline, 2-chloroaniline (2-CA), 3-chloroaniline (3-CA), 4-chloroaniline (4-CA) and 3,5-dichloroaniline (3,5-DCA). According to European Chemical Substances Information System (ESIS) and data on chemical production from 1990–1994, aniline and 2-CA are high production volume (HPV) chemicals (placed on the EU market in volumes exceeding 1000 tonnes per year per producer or importer) and 3-CA, 4-CA and 3,5-DCA are LPV (low production volume) chemicals, *i.e.*, volumes of 10–1000 tonnes per year.[4] Aniline and 4-CA are classified as hazardous substances in Annex I of Directive 67/548/EEC,[5] whereas 2-CA, 3-CA and 3,5-DCA were not evaluated at the EU-level under previous legislation, suggesting the need to collect information on their environmental and health properties and to classify them under REACH-legislation. The (eco)toxicity data available for aniline and its derivates show that 2-CA, 3-CA and 3,5-DCA could also be dangerous to humans and the environment. For example, according to International Agency for Research on Cancer (IARC), 4-CA is classified as possibly carcinogenic to humans. Chen *et al.*[6] showed that 2-CA is also potentially carcinogenic to humans. Aniline and 4-CA are also classified as dangerous for the environment according to European Chemical Substances Information System (ESIS).

The main aim of REACH is not only to provide a high level of protection of human health and the environment, but also to reduce animal testing to a minimum, to promote the use of alternative methods and to combine all sources of data[7] (available existing data, *in silico*, *in vitro* and *in vivo* approaches) for the assessment of the hazardous properties of substances. Thus, expectations towards *in vitro* studies and QSARs (quantitative structure-activity relationship) are very high.

In the field of aquatic toxicology, QSARs have been developed as alternative tools for predicting the toxicity of chemicals, when little or even no empirical data are available. Elaboration of SARs (structure-activity relationships) or some other computational toxicity prediction models is primarily based on experiment-

ally measured toxic effects of chemicals. Therefore, there is a direct relationship between the amount and quality of available information on toxicity of different chemicals towards different test species and adequacy of the models.

The fate and biological effects of chemicals in aquatic ecosystems depend, above all, on the chemical composition of natural water.[8] However, the majority of toxicity data for chemicals available for standard freshwater test organisms has been generated using standard test media, and, as a result, the available information concerning toxicity of chemicals, including anilines, in natural waters is limited. Environmentally irrelevant conditions in standard toxicity tests reduce their predictive power for environmental risk assessment.

The objectives of this study were: 1) to establish the relationship between chemical structure and the toxicity of five anilines (aniline, 2-CA, 3-CA, 4-CA and 3,5-DCA) toward different aquatic test species belonging to different trophic levels and 2) to evaluate the effect of replacement of the artificial test medium by the natural water on the toxicity test results.

EXPERIMENTAL

Chemicals

Aniline, 2-chloroaniline, 3-chloroaniline and 4-chloroaniline were purchased from Sigma-Aldrich and 3,5-dichloroaniline from Acros-Organics. Stock solutions (aniline – 8000 mg L^{-1}, 2-CA – 500 mg L^{-1}, 3-CA – 1100 mg L^{-1}, 4-CA – 550 mg L^{-1} and 2,3-DCA – 200 mg L^{-1}) were prepared in MilliQ water, taking into account their solubility (Table I), and stored in the dark.

TABLE I. Selected characteristics of the five tested anilines

Chemical	CAS No.	Purity %	Measured water solubility mg L^{-1}	Estimated water solubility[a] mg L^{-1}	Measured log K_{ow}[b]	Estimated log K_{ow}[c]
Aniline	62-53-3	≥ 99.5	36000 (25 °C)[b] 34000[d]	20820	0.90	1.08
2-Chloroaniline (2-CA)	95-51-2	≥ 99.5	8160 (25 °C)[b]	2241	1.90	1.72
3-Chloroaniline (3-CA)	108-42-9	99	5400 (20 °C)[b]	2331	1.88	1.72
4-Chloroaniline (4-CA)	106-47-8	98	3900 (25 °C)[b] 2000[e]	2572	1.83	1.72
3,5-Dichloroaniline (3,5-DCA)	626-43-7	98	784 (25 °C)[b] 600 (26 °C)[f]	223	2.90	2.37

[a]EPI Suite™ program WSKOWWIN, v. 1.41; [b]U.S. EPA ECOSAR;[9] [c]EPI Suite™ program KOWWIN™, v. 1.67; [d]Ref. 10; [e]Provider's Material Safety Data Sheet (MSDS) (Sigma-Aldrich); [f]Provider's MSDS (Acros-Organics)

Bioassays

The toxicity of five anilines was studied toward four aquatic organisms: bacteria, protozoa and two crustaceans, using the following bioassays:

The kinetic luminescent bacteria test (modified Flash assay) with *Aliivibrio fischeri* (formerly *Vibrio fischeri*) is based on the inhibition of the light output of naturally bioluminescent bacteria by toxic compounds. The acute test (exposure time 15 min) was performed at room temperature (≈ 20 °C) in 96-well microplates using a modified Flash test protocol described in Mortimer *et al.*[11] Reconstituted *Aliivibrio fischeri* Reagent (Aboatox, Turku, Finland) was used as the test bacteria suspension and all chemicals and their dilutions were tested in 2 % NaCl. Inhibition of bacterial bioluminescence by the tested compounds was calculated as a percentage of the unaffected control (2 % NaCl).

Daphtoxkit F™, Thamnotoxkit F™ and Protoxkit F™ were purchased from MicroBio-Tests, Inc. (Mariakerke-Gent, Belgium) and tests were performed according to the procedures described in the instruction supplied with the corresponding Toxkits.

The 48-h acute immobilization test with the crustacean *Daphnia magna* (Daphtoxkit F™) adhered to OECD 202 guideline. The tests with neonates less than 24 h old, obtained by the hatching of ephippia, were performed at 20 °C.

The 24-h mortality test with the crustacean *Thamnocephalus platyurus* (Thamnotoxkit FTM) was performed at 25 °C with larvae of shrimp *T. platyurus* (< 24 h old) obtained by the hatching of cysts.

The growth inhibition test (24-h) with the ciliated protozoan *Tetrahymena thermophila* (Protoxkit FTM) is based on the measurement of the population density of protozoa. Briefly, the investigated chemical and *T. thermophila* culture (strain BIII) were added to the food substrate suspension in MilliQ water. While normal proliferating protozoan culture clears the substrate suspension in the test vessels during exposure, inhibition of the growth of protozoa is reflected by the residual turbidity of the food substrate, measured as the optical density (*OD*) of the test samples at 440 nm. The incubation was performed at 30 °C.

The acute inhibition test (24-h) of the viability of *Tetrahymena thermophila* was conducted essentially as described in Mortimer *et al.*[12] Briefly, *T. thermophila* (strain BIII, the growth inhibition test) was grown axenically in nutrient medium. During the exponential growth phase (5×10^5 cells mL^{-1}), the cells were harvested by centrifugation and washed with Osterhout's medium, which was also used as the test medium. The test plates with protozoa were incubated for 24 h at 25 °C without shaking. Cell viability was tested using the fluorescent dye propidium iodide (PI, Fluka) and by measuring the ATP content of the cellular suspensions using the luciferin–luciferase method.

To prevent potential photolytic breakdown of anilines the exposure of protozoan and crustacean tests were conducted in the dark.[13]

The EC_{50} values were determined using Regtox software for Microsoft Excel.[14] The average EC_{50} values and standard deviations (*SD*) were calculated from 3–5 independent experiments, each in several replicates (four for *D. magna*, three for *T. platyurus*, and two for *T. thermophila* and *A. fischeri*).

Test media

The artificial test medium – ATM (test medium used in the standard test procedure) in the crustacean assays had the following composition (mg L^{-1}): for *D. magna* - $CaCl_2{\cdot}2H_2O$, 294; $MgSO_4{\cdot}7H_2O$, 123.25; $NaHCO_3$, 64.75; KCl, 5.75; pH 7.8 ± 0.2 and for *T. platyurus* - $CaSO_4{\cdot}2H_2O$, 60; $MgSO_4{\cdot}7H_2O$, 123; $NaHCO_3$, 96; KCl, 4; pH 7.8±0.2, dissolved in MilliQ water. MilliQ water or Osterhout's medium (NaCl, 104; $MgCl_2$, 8.5; $MgSO_4$, 4; KCl, 2.3; $CaCl_2$, 1 mg L^{-1}; pH 6.6, dissolved in MilliQ water) were used as the standard test medium for *T. thermophila*, and a 2 % solution of NaCl for *A. fischeri*. Thus, the ATM used in the assays did not contain any organic compounds.

Natural waters were sampled from a well (subsurface water) in a small village in northern Estonia and from the River Jägala (Estonia). Chemical analyses of the natural water samples (Table II) were performed using standard analytical methods in an accredited laboratory.

TABLE II. Characterization of the natural waters used as test media

Parameter	Unit	Water from the well	Water from the River Jägala
pH	–	7.5	8
Conductivity	µS	156	282
DOC[a]	mg C L^{-1}	9.6	16.1
BOD_7[b]	mg O_2 L^{-1}	1.4	1.6
Nitrate	mg N L^{-1}	0.27	2.3
Phosphate	mg P L^{-1}	0.195	0.018
Ca^{2+}	mg L^{-1}	33	68
HCO_3^-	mg L^{-1}	96.4	192.2
SO_4^{2-}	mg L^{-1}	4	25
Fe_{tot}	mg L^{-1}	0.21	0.76

Before the biotesting, suspended solids and plankton were separated from the water samples by filtration through a 0.45 µm pore size standard filter (Millipore).

Use of ECOSAR for predicting the aquatic toxicity of anilines

The toxicity of the anilines (EC_{50}) to *D. magna* were calculated using the ECOSAR model – a computerized predictive system used by the United States Environmental Protection Agency (US EPA) to estimate the aquatic toxicity of industrial chemicals. The ECOSAR model uses Structure Activity Relationships (SARs) for the prediction of the aquatic toxicity of untested chemicals based on their structural similarity to chemicals for which aquatic toxicity data are available. The SARs in the ECOSAR model express correlations between the physico–chemical properties and aquatic toxicity of a compound within specific chemical classes. ECOSAR version 1.00a (February 2009), downloadable from the US EPA website,[9] was used in the current study.

RESULTS AND DISCUSSION

The results of the toxicity testing of the five anilines using the above-listed bioassays in ATM (the respective artificial test medium) are presented in Table III. The experimental data on the toxicity of the investigated anilines are comparable with the data published by other authors (Table IV).

It should be mentioned that the 48-h EC_{50} values for *D. magna* available in the literature vary considerably. However, when averaged (Table IV), these data are in agreement with the present results (Table III). Unfortunately, no information on the toxicity of the anilines to *T. platyurus* and *T. thermophila* could be found, but the toxicity of investigated anilines to close protozoan species *T. pyriformis* (Table IV) were comparable to the present data (Table III). In the current study, much higher EC_{50} values were obtained in the acute inhibition test (exposure of protozoa during 24 h with no food added, see Experimental) than in the growth inhibition test with *T. thermophila* (Table III). Exposure of *T. thermophila* to aniline in the acute inhibition test yielded the following EC_{50} values:

2007 mg L^{-1}, measured with propidium iodide, and 2140 mg L^{-1}, according to the measurement of the ATP level. Considering that the EC_{50} value from the acute inhibition test is over 5 times higher than the EC_{50} value of the growth inhibition test (2007 *vs*. 358 mg L^{-1}), it can be assumed that in case of toxicity testing of aniline, the growth inhibition test of *T. thermophila* is more relevant than the acute inhibition test. The difference in the EC_{50} values of the two test formats could be attributed to the mode of action of aniline, which has been classified as a polar narcotic which exerts non-covalent bioreactivity by disturbing the structure and functioning of biomembranes.[19] As a result of the slow narcotic mechanism of action, aniline probably inhibits the normal functioning of the cell, including cell proliferation, but does not kill the cells during that time, rendering the mortality endpoint (propidium iodide assay) less sensitive. However, this supposition has to be verified.

TABLE III. Toxicity of anilines (EC_{50} ,mg L^{-1}, mean±*SD*) towards four aquatic species tested in ATM

Compound	Exposure time			
	24 h	15 min	48 h	24 h
	Protozoa *Tetrahymena thermophila*[a]	Bacteria *Aliivibrio fischeri*	Crustacean *Daphnia magna*	Crustacean *Thamnocephalus platyurus*
Aniline	358±180	403±101	0.13±0.04	2.8±0.6
2-Chloroaniline	252±16	43±19	1.2±0.4	15.2±4.5
3-Chloroaniline	135±9.0	59±14	0.24±0.07	2.0±0.6
4-Chloroaniline	36±3.5	13±0.5	0.19±0.04	4.4±1.1
3,5-Dichloroaniline	29±2.4	36±3.8	0.48±0.24	3.9±0.8

[a]Growth inhibition test (Protoxkit F™)

TABLE IV. EC_{50} values (mg L^{-1}) for the five anilines published by other authors

Chemical	*Tetrahymena pyriformis*	*Aliivibrio fischeri* (*V. fischeri, P. phosphoreum*)[a]	*Daphnia magna*[b]
Aniline	158.1[c]	69 (15 °C)	0.39±0.23
	190[d]	488 (15 °C)	
2-Chloroaniline	188.7[c]	15 (15 °C	0.94±0.68
	200[d]	36.5 (20 °C)	
3-Chloroaniline	76.9[c]	13.4 (15 °C)	0.23±0.13
	100[d]	39.5 (20 °C)	
4-Chloroaniline	113.7[c]	3.77 (15 °C)	0.24±0.13
	10[d]	21 (20 °C)	
3,5-Dichloroaniline	31.6[c]	10.7 (15 °C)	1.16±0.06

[a]Ref.15, exposure time 15 min; testing temperature indicated in the brackets; [b]mean±*STD* from U.S. EPA ECOSAR and Ref.16, exposure time 48 h; [c]Ref.17, exposure time 40 h; [d]Ref.18, exposure time 24 h

The toxicity of investigated anilines varied notably among the test species (Table III). All tested compounds were remarkably more toxic (10–100 times) to

crustaceans than to bacteria and protozoa (both unicellular organisms). *D. magna* was the most sensitive species. Other authors[20,21] also showed that *D. magna* was more sensitive than other aquatic species, *i.e.*, algae and fish, to anilines. Although it was previously demonstrated that *T. platyurus* can be more sensitive than *D. magna*, *e.g.*, to pyrene[22] and insecticides,[23] in case of anilines, *D. magna* was about an order of magnitude more sensitive than *T. platyurus*. It should be emphasized, however, that the acute assays with the two crustacean test species used different exposure times (24-h for *T. platyurus vs.* 48-h for *D. magna*) which could explain the different results obtained. The high sensitivity of *D. magna* to aromatic amines, compared to other crustaceans, was also shown by Ramos *et al.*[24]

Thus, the present study confirms that extrapolation of toxicity data from one species to another (even if the species are taxonomically similar) could lead to incorrect deductions.

Relationship between toxicity and the chemical structure of the anilines

There was no common relationship between the toxicity and chemical structure of the anilines (the degree of chlorosubstitution and the position of chloro-substituents) for all the tested aquatic species (Table III). In case of protozoa, the toxicity of anilines depended on the position of chloro-substituents and increased in accordance with the degree of chlorosubstitution, with aniline (EC_{50} = 358 mg L^{-1}) being about 12-fold less toxic than 3,5-DCA (EC_{50} = 29 mg L^{-1}). Aniline was also approximately 10-fold less toxic than the substituted anilines to the bacteria *A. fischeri* (403 mg L^{-1} *vs.* 13–59 mg L^{-1}; Table III). As mentioned above, both crustaceans and especially *Daphnia magna* were remarkably (up to 3 orders of magnitude) more sensitive towards anilines than protozoa and bacteria. For both crustaceans, it was difficult to recognize a clear relationship between toxicity and the chemical structure of the tested compounds. Interestingly, for both crustaceans, 2-CA was noticeably more toxic than the other four tested anilines. This indicates that, regardless of the different sensitivity of two species, the mechanism of action of anilines is probably the same for both crustaceans.

A comparison of the present results with the predicted toxicity values for *D. magna* obtained with the ECOSAR model (experimentally obtained octanol-water partitioning coefficient, K_{ow}, values were used for the calculations, Table I) shows that the predictive power of the ECOSAR model, at least in case of anilines, is limited. Moreover, the ECOSAR model under predicted the toxicity of four anilines by almost one order of magnitude (Fig. 1).

As a rule, there is a correlation between the toxicity of an organic chemical and its K_{ow} value: the higher the log K_{ow}, the lower the $L(E)C_{50}$ value, *i.e.*, the higher the toxicity. For example, in previous studies on MEIC chemicals, a good correlation was shown between the toxicity of 24 MEIC chemicals to photobacteria and their K_{OW} value; the correlation coefficient of the linear regression

(log–log) was –0.84).[25] Lee *et al.*[26] showed that the toxicity of 16 phenols toward *Selenastrum capricornutum* and *D. magna* was closely related to the log K_{ow} values. In the current study, this trend was observed for 5 tested anilines in the case of protozoa and bacteria. However, the most toxic compound to crustaceans was aniline, which is the least hydrophobic of the five tested compounds (Fig. 2).

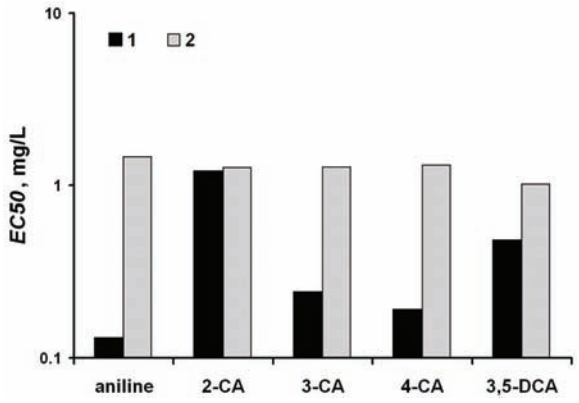

Fig. 1. Toxicity of anilines to crustacean *Daphnia magna:* measured (1) and predicted by ECOSAR (2). Note the logarithmic *y*-scale.

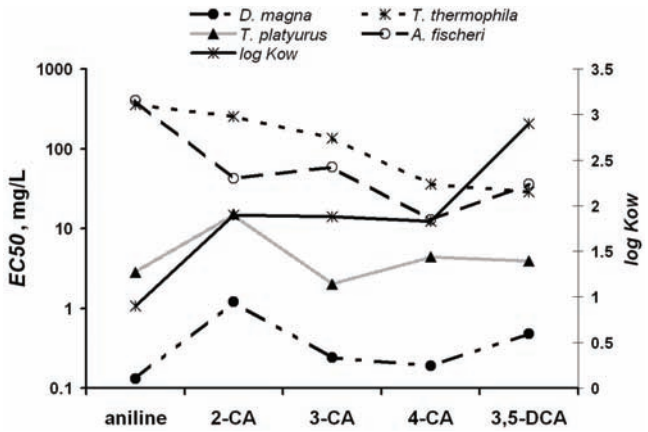

Fig. 2. Toxicity of anilines to the four test species (EC_{50} values obtained in the current study) *vs.* log K_{ow}.

As was shown above, the existing tools for the prediction of the toxicity of aniline (ECOSAR) to aquatic species yields inaccurate toxicity data. There are many reasons why the predictive power of QSAR models is not reliable. Firstly and most importantly, experimentally determined physic–chemical properties should be used to develop QSARs. Secondly, the descriptors should be selected very carefully and the toxicity of chemicals should be predicted by more than one descriptor. Certainly, QSAR models are rapid and cost-effective methods, which can

be used as important alternative screening tools for prioritising and predicting the toxicity of untested chemicals, but it must be born in mind that the calculated values may differ considerably from the experimental ones.

Modulation of the toxicity of anilines in natural water

There are an increasing number of studies showing the modulating effect of the composition of natural water on the toxicity of different chemicals, mostly heavy metals but also metal oxide nanoparticles.[27] The presence of humic compounds in natural water may also modulate the toxicity of organic chemicals. For example, it was shown that dissolved humic materials (DHM) significantly reduced the toxicity of 4-CA to *D. magna*, but the effect of DHM on the toxicity of 4-CA to zebrafish (*Brachydanio rerio*) was not observed.[28] In the present study, the effect of natural water on toxicity of anilines to bacteria, protozoa and crustaceans was evaluated.

It is known that photolysis and microbial degradation are the most important degradative processes affecting anilines in aquatic environments.[29] To prevent breakdown of the chemical structures by photolysis, the exposure of protozoa and crustaceans to the anilines was realised in the dark (see Experimental).[13] In addition, it was previously shown[29,30] that during short incubation periods (up to 3 days in the dark), there was no measurable microbial degradation of aniline and the chloroanilines in natural water. Therefore, it could be presumed that in the short-term tests performed in the current study, the tested compounds remained stable and that the differences between the results obtained with ATM and natural water indicate the impact of water composition on the bioavailability of anilines to different aquatic species.

The mitigation effect of natural water on the toxicity of anilines to four test species is presented in Table V. The tests organisms were exposed to the anilines at concentrations that were close to the EC_{50} values obtained in the respective standard test media (Table II). The results are presented as a ratio of the toxic effect (%) in natural waters and in ATM (Table V). Thus, values lower than one indicate a decrease of toxicity in natural water and values exceeding one, accordingly, indicate an increase in toxicity. For example, when the immobilization of *D. magna* exposed to 2-CA at a concentration 0.2 mg L^{-1} in ATM was 80 % and in natural water only 40 %, the toxicity in natural water decreased 2 times (40/80 = 0.5).

In general, the effect of natural water on the toxicity of anilines was minimal. However, some tendencies were observed: *i*) different to particle-feeding organisms (protozoa and crustaceans), the toxicity of anilines to bacteria was practically the same in natural water and ATM and *ii*) toxicity of anilines for protozoa *T. thermophila* and crustacean *T. platyurus* seemed to be slightly increased when exposed in natural water, and for *D. magna*, natural water slightly decreased the toxic effect of chloroanilines (but not of aniline). These data are in accordance with the data of Lee *et al.*[28] (see above). However, the data on the other crus-

tacean *T. platyurus* did not confirm this tendency (Table V). This discrepancy may be explained by the different sensitivity of the test species to background pollution. It seems that in case of anilines, the mitigation effect of natural water on toxicity to crustaceans depended mainly on the integrated effect of the water composition (including background pollution) and tested chemical, but not on the dissolved organic matter (DOC) content. Thus, the current data on anilines are different from the data of a previous study on the effect of natural waters on the toxicity of CuO nanoparticles to *D. magna* and *T. platyurus*, in which it was shown that natural waters remarkably (up to 100-fold) decreased the toxicity of nano-CuO to both crustaceans and this effect depended mainly on the DOC concentration.[27]

TABLE V. The ratio between the toxicity of anilines in natural water (NW) and artificial test medium (ATM) tested at the same concentrations (effect in NW / effect in ATM)

Compound	*Tetrahymena thermophila*[a]		*Aliivibrio fischeri*		*Daphnia magna*		*Thamnocephalus platyurus*	
	Well	River	Well	River	Well	River	Well	River
Aniline	2.4	2.2	1.1	1	2.1	1.9	1.8	1.5
2-Chloroaniline	1.3	1.5	1.2	1.1	0.6	0.5	0.8	1
3-Chloroaniline	0.95	1.2	0.9	0.85	0.7	0.5	2.2	1.9
4-Chloroaniline	1.2	1.6	0.8	0.9	0.7	0.7	0.8	0.9
3,5-Dichloroaniline	1.8	2.4	1.1	1.1	0.3	0.5	1.1	1.3

[a]Growth inhibition test (Protoxkit F™)

CONCLUSIONS

It may be concluded that the opinion stated 15 years ago: "…at present no prediction about the behaviour of a previously untested chemical can be made, which is based on the physico-chemical or structural properties of the organic chemical."[28] – is still valid, at least in the case of anilines.

QSARs can be used as an initial evaluation of the toxicity of a chemical, however, tests with bioassays must be performed for confirmation.

Acknowledgements. This work was supported by the Estonian targeted funding project SF0690063s08, the Estonian Science Foundation Project 8066 and the EU 6th Framework Integrated Project OSIRIS (Contract No. GOCE-CT-2007-037017).

И З В О Д

ТОКСИЧНОСТ ПЕТ АНИЛИНСКИХ ЈЕДИЊЕЊА ПРЕМА ЉУСКАРИМА, ПРОТОЗОАМА И БАКТЕРИЈАМА

MARILIIS SIHTMÄE, MONIKA MORTIMER, ANNE KAHRU и IRINA BLINOVA

Laboratory of Molecular Genetics, National Institute of Chemical Physics and Biophysics, Akadeemia tee 23, Tallinn 12618, Estonia

Ароматични амини (анилини и деривати) су важна класа загађујућих супстанци које могу бити испуштене у животну средину као индустријски ефлуенти или као производи раз-

градње пестицида и боја. Испитали смо токсичност анилина, 2-хлоранилина, 3-хлоранилина, 4-хлоранилина, и 3,5-дихлоранилина за мултитрофичну тест батерију која се састоји од бактерија *Aliivibrio fischeri* (раније *Vibrio fischeri*), протозоа бичара *Tetrahymena thermophila* и два љускара (*Daphnia magna* и *Thamnocephalus platyurus yypyc*). У примењеним условима токсичност анилина је приметно варирала међу тестираним врстама. Бактерије и протозое су биле много мање осетљиве према анилинима него љускари: вредности EC_{50} су биле 13–403 mg L^{-1} према 0,13–15,2 mg L^{-1}. Није откривен никакав општи тренд између токсичности и хемијске структуре анилина (степен супституције хлора и позиција хлорних супституената) ни у једном случају тестираних водених врста. Замена вештачког тест медијума (ATM) речном водом уочљиво је смањила токсичност анилина за љускаре, али не и за протозое. Ово истраживање је део интегрисаног пројекта OSIRIS у оквиру европског FP6 програма, у коме ће се спровести и екотоксикогеномске студије анилина (нпр. за *D. magna*), које могу помоћи у разјашњавању механизама токсичности различитих анилина.

(Примљено 19. децембра 2009, ревидирано 8. фебруара 2010)

REFERENCES

1. Z. Rappoport, *Patai series, The Chemistry of Anilines*, Wiley, 2007, p. 1180
2. *EC No. 1907/2006: Regulation of the European Parliament and of the Council concerning the Registration, Evaluation, Authorisation and Restriction of Chemicals (REACH), Official J. of the European Union* L 396/1-849 (2006)
3. C. Rovida, T. Hartung, *ALTEX* **26** (2009) 1
4. R. Allanou, B. G. Hansen, Y. van der Bilt, *Public Availability of Data on EU High Production Volume Chemicals*, European Chemicals Bureau, Ispra, Italy, 1999, p. 21
5. *EC Directive 67/548/EEC*: *Dangerous Substances Directive*, 1967
6. H.-I. Chen, S.-H. Liou, C.-H. Loh, S.-N. Uang, Y.-C. Yu, T.-S. Shih, *Urology* **66** (2005) 305
7. T. Hartung, *Nature* **460** (2009) 208
8. H. E. Witters, *Ecotox. Environ. Safe*. **41** (1998) 90
9. ECOSAR, http://www.epa.gov/opptintr/newchems/tools/21ecosar.htm (8.12.2009)
10. K. Verschueren, *Handbook of Environmental Data on Organic Chemicals*, Van Nostrand, New York, 1996
11. M. Mortimer, K. Kasemets, M. Heinlaan, I. Kurvet, A. Kahru, *Toxicol. in Vitro* **22** (2008) 1412
12. M. Mortimer, K. Kasemets, A. Kahru, *Toxicology* **269** (2010) 182
13. *OECD No. 23: Guidance Document on Aquatic Toxicity Testing of Difficult substances and mixtures*, 2000
14. E. Vindimian, MSExcel macro REGTOX_EV7.0.5.xls, http://eric.vindimian.9online.fr/ (8.12.2009)
15. C. K. L. E. Kaiser, J. Devillers, *Ecotoxicity of Chemicals to Photobacterium Phosphoreum (Handbooks of Ecotoxicological Data)*, Gordon and Breach Sciences Publishers, Amsterdam, 1994, p. 879
16. T. Abe, M. Saito, Y. Niikura, T. Shigeoka, Y. Nakano, *Chemosphere* **45** (2001) 487
17. T. W. Schultz, *Chem. Res. Toxicol*. **12** (1999) 1262
18. Y. Yoshioka, Y. Ose, T. Sato, *Sci. Total Environ.* **43** (1985) 149
19. H. J. M. Verhaar, C. J. van Leeuwen, J. L. M. Hermens, *Chemosphere* **25** (1992) 471
20. A. Kahru, H.-C. Dubourguier, *Toxicology* **269** (2010) 105

21. J. Martins, L. O. Teles, V. Vasconcelos, *Environ. Int.* **33** (2007) 414
22. I. Blinova, *Environ. Toxicol*. **4** (2004) 425
23. P. Palma, V. L. Palma, R. M. Fernandes, A. M. V. M. Soares, I. R. Barbosa, *Bull. Environ. Contam. Toxicol.* **81** (2008) 485
24. E. U. Ramos, M. A. Vaal, J. L. M. Hermens, *Environ. Toxicol. Pharmacol.* **11** (2002) 149
25. A. Kahru, B. Borchardt, *ATLA* **22** (1994) 147
26. Y. G. Lee, S. H. Hwang, S. D. Kim, *Arch. Environ. Contam. Toxicol*. **50** (2006) 213
27. I. Blinova, A. Ivask, M. Heinlaan, M. Mortimer, A. Kahru, *Environ. Pollut.* **158** (2010) 41
28. S. K. Lee, D. Freitag, C. Steinberg, A. Kettrup, Y. H. Kim, *Water Res.* **27** (1993) 199
29. H.-M. Hwang, R. E. Hodson, R. F. Lee, *Water Res*. **21** (1987) 309
30. F. Gosetti, M. Bottaro, V. Gianotti, E. Mazzucco, P. Frascarolo, D. Zampieri, C. Oliveri, A. Viarengo, M. C. Gennaro, *Environ. Pollut.* **158** (2010) 592.

Journal of the Serbian Chemical Society
JSCS-info@shd.org.rs • www.shd.org.rs/JSCS
J. Serb. Chem. Soc. *75* (9) 1303–1312 (2010) UDC 628.132:582.26/.27:615.9:577.112.386
JSCS–4053 *Original scientific paper*

Temporal and spatial variability of cyanobacterial toxins microcystins in three interconnected freshwater reservoirs

LUDĚK BLÁHA*, LUCIE BLÁHOVÁ, JIŘÍ KOHOUTEK, ONDŘEJ ADAMOVSKÝ, PAVEL BABICA and BLAHOSLAV MARŠÁLEK

Masaryk University, Faculty of Science, Research Centre for Toxic Compounds in the Environment – RECETOX, Kamenice 3, CZ62500 Brno and Institute of Botany, Academy of Sciences of the Czech Republic, Lidická 25/27, 657 20 Brno, Czech Republic

(Received 13 January, revised 18 February 2010)

Abstract: In spite of substantial research on health and the ecological risks associated with cyanobacterial toxins in the past decades, the understanding of the natural dynamics and variability of toxic cyanobacterial blooms is still limited. Herein, the results of long term monitoring 1998–1999/2001–2008 of three reservoirs (Vír, Brno and Nové Mlýny, Chech Republic), where toxic blooms develop annually, are reported. These three reservoirs provide a unique model because they are interconnected by the Svratka River, which allows possible transfer of phytoplankton as well as toxins from one reservoir to another. The frequency of the occurrence and dominance of the major cyanobacterial taxa *Microcystis aeruginosa* did not change during the investigated period but substantial variability was observed in the composition of other phytoplankton. Although absolute concentrations of the studied toxins (microcystins) differed among the reservoirs, there were apparent parallel trends. For example, during certain years, the microcystin concentrations were systematically elevated in all three studied reservoirs. Furthermore, the concentration profiles in the three sites were also correlated (parallel trends) within individual seasons based on monthly sampling. Microcystin-LR, a variant for which the World Health Organization has recommended a guideline value, formed only about 30–50 % of the total microcystins. This is of importance, especially in the Vír reservoir that serves as a drinking water supply. The maxima in the cell-bound microcystins (intracellular; expressed per dry weight biomass) generally preceded the maxima of total microcystins (expressed per volume of water sample). Overall, the maximum concentration in the biomass (all three reservoirs, period 1993–2005) was 6.1 mg g^{-1} dry weight and the median values were in the range 0.065–2.3 mg g^{-1} dry weight. These are generally high concentrations in comparison with both Czech Republic and worldwide reported data. The present data revealed substantial variability of both toxic cyanobacteria and their peptide toxins that should be reflected by detailed monitoring programs.

* Corresponding author. E-mail: blaha@recetox.muni.cz
doi: 10.2298/JSC100113106B

Keywords: microcystin; monitoring; trends; HPLC; ELISA.

INTRODUCTION

Anthropogenic contamination of surface waters with non-toxic nutrients (phosphorus and nitrogen) has resulted in massive cyanobacterial water blooms worldwide. Especially the production of cyanobacterial secondary metabolites (cyanotoxins) has attracted the attention of both scientists and public health authorities, since serious adverse health effects in both domestic animals and humans have been reported.[1]

Microcystins (MCs), unusual cyclic heptapeptides produced by several planktonic species of cyanobacteria, are the most frequently studied cyanotoxins. Based on toxicological data, the World Health Organization (WHO) recommended a provisional guideline value for MC-LR in drinking water of 1 μg L^{-1} (WHO, 1998). Preliminary surveys conducted in Europe (including the Czech Republic) showed that cyanobacterial blooms occur in about 80 % of large reservoirs.[2] About 90 % of the water blooms in the Czech Republic contained MCs (MC-LR, the toxin considered by the WHO, was present in 98 % of the positive samples) with median and maximum concentrations in the biomass of 0.7 and 5.8 mg g^{-1} dry weight (dw), respectively.[3] There are also some preliminary indications on the occurrence of toxic cyanobacteria in less explored areas of South and East Europe, *e.g.*, Serbia.[4,5] However, to the best of our knowledge, the highly important issue of cyanobacterial toxins in surface waters and their impacts on ecosystem quality and the health of the population in this region have not yet attracted sufficient scientific attention and remain to be explored in more detail.

In this paper, analyses of long-term data (1998–2008) on toxic cyanobacteria and their toxins in three large reservoirs, which are connected by a river in the region of South Moravia, the Czech Republic, are presented The Reservoir Vír (the most upstream) serves as an important supply of drinking water for the city of Brno (population 400,000), while other two reservoirs (Brno and Nové Mlýny) were built to help regulate water regimes, and were supposed to be also used for recreational purposes. The unique long-term data enabled the natural variability in the occurrence of dominant toxic cyanobacteria and the levels of cyanotoxins microcystins in these reservoirs to be studied, as there is a possible transfer of toxic blooms among reservoirs *via* the Svratka River (Fig. 1).

In spite of extensive research on the health and ecological risks associated with cyanobacterial toxins, a general understanding of the natural dynamics and variability of toxic cyanobacterial blooms is still limited. The presented analytical data provide some new insights into the relationships between the concentrations of MCs and the dominant cyanobacteria in water blooms.

Fig. 1. Map of the studied reservoirs in the Czech Republic (Vír, Brno and Nové Mlýny) interconnected by the River Svratka.

EXPERIMENTAL

Samples

Samples were collected annually from the Reservoirs Vír, Brno and Nové Mlýny (Fig. 1) during the vegetation seasons (during several seasons, repeated samplings were performed to obtained a more detailed picture about the intra-seasonal variation). The covered period includes the years 1998–2008; the results from the year 2000 are not presented as no monitoring of the Brno Reservoir was performed this year. Water bloom samples were collected using a plankton net (20 μm diameter); they were stored frozen at –20 °C, freeze-dried and stored for extraction and analyses by HPLC (described below). Samples of raw waters (for analyses of total microcystins, μg L^{-1}) were collected from the upper water layers (≈0.5 m depth) at each locality and stored at –20 °C until analysed by Elisa. Detailed observations at the studied reservoirs were compared with the results of the National Monitoring Program in the Czech Republic, which was organized by the authors of this paper. The same methods of sampling and microcystin analyses were employed for all samples.

Taxonomical determination

A portion of the cyanobacterial biomass collected in the plankton net was fixed with 4 % (v/v) formaldehyde for taxonomical identification, and the dominant phytoplankton species were identified and quantified according to current literature.[6] For evaluation purposes, the occurrence of each group of organisms was categorized according to their dominance.

Elisa analyses (total microcystin content)

Prior to MCs determination, the samples were thawed, sonicated, centrifuged (10,000 g, 5 min) and the supernatant analysed for MCs by direct competitive Elisa according to Zeck *et al.*[7] and as described in detail in a recent survey.[8] Briefly, high protein binding microplates (NUNC, Roskilde, Denmark) were pre-incubated with anti-mouse anti-Fc-IgG (ICN) following incubation with monoclonal antibodies developed against microcystin-LR (ALEXIS, Lausen, Switzerland). To visualize the reaction, MC-LR conjugated with horseradish peroxidase (HRP), prepared according to Zeck *et al.*[7] and TMB substrate (Sigma, Prague, Czech Republic), was used. The absorbance (420 nm with reference 660 nm) was determined using a GENios microplate reader (Tecan, Mannerdorf, Switzerland). The samples were analyzed in three replicates and compared with a 0.125–2 mg L^{-1} calibration curve constructed using a MC-LR standard (Alexis).

HPLC Analyses

Cyanobacterial blooms were extracted with 50 % methanol (100 mg dw mL^{-1}), and analysed as described previously[9] using an HPLC Agilent 1100 Series instrument (Agilent Technologies, Waldbronn, Germany) on Supelcosil ABZ+ Plus, 150×4.6 mm, 5 µm column (Supelco, Bellefonte, USA) at a temperature of 30 °C. The binary gradient mobile phase consisted of (A) H_2O + 0.1 % trifluoroacetic acid (TFA) and (B) acetonitrile + 0.1% TFA (linear increase from 20 % B at 0 min to 59 % B at 30 min); the flow rate was 1 mL min^{-1}. The chromatograms at 238 nm were recorded with an Agilent 1100 Series PDA detector (Agilent Technologies) and the MCs were identified by the retention time and characteristic UV-absorption spectra (200–300 nm) of individual peaks. Quantification was based on external calibrations of MC-RR, -YR and -LR.

Statistics

Relationships between the occurrence of phytoplankton and the concentrations of MCs were evaluated by χ^2 in Statistica for Windows 8.0 (StatSoft, Tulsa, OK, USA); *P*-values less than 0.05 were considered statistically significant.

RESULTS AND DISCUSSION

The concentrations of the cyanobacterial toxins microcystins in the three studied reservoirs together with the summary statistics from the Czech National Monitoring Program are presented in Table I. As calculations of the arithmetic mean are affected by the log-normal distribution (a few extreme concentrations), the median values, as another statistical parameter, are also presented (Table I). The concentrations of MCs in the dry biomass (expressed in µg g^{-1} dry wt), which reflects the actual toxic potential of the respective water bloom (sum of the dominant variants MC-LR, -RR, -YR is presented in Table I) were also investigated. Furthermore, the MC concentrations were also analysed directly in the raw water samples (µg L^{-1}), which corresponds to the total microcystin content. These values might be translated to the actual health risks resulting, for example, from consumption of contaminated drinking water, *etc.*[10,11]

Regarding the water bloom biomass, detectable concentrations of microcystins were found in all the collected biomass samples at the studied localities (no values the detection limit). The median values ranged from 25 µg g^{-1} dry weight

(2006 – Nové Mlýny) up to more than 6000 μg g^{-1} (1999 – Brno). The latter value from Brno Reservoir was the highest concentration determined in 1999 in the all Czech National Monitoring Program (Table I). In general, very high microcystin concentrations in the biomass were observed in the Vír Reservoir (see for example the years 2003–2005), which is the drinking water supply for the city of Brno with a population of about 400,000.

Table I. Summary statistics of microcystins concentrations in the reservoirs Vír, Brno and Nové Mlýny in 1998–2008 (*N*-number of samples, mean, median, maximum) in comparison with the overall data from the Czech National Monitoring Program. Concentrations in biomass (mg g^{-1} d.w.) and total water concentrations (μg L^{-1})

Year	Czech Republic (total)				Vír Reservoir				Brno Reservoir				Nové Mlýny Reservoir			
	Concentrations in biomass, μg g^{-1} d.w.															
	N	Mean	Med	Max	*N*	Mean	Med	Max	*N*	Mean	Med	Max	*N*	Mean	Med	Max
1998	21	452	98	3793	1	91	91	91	4	473	333	1130	2	157	157	289
1999	83	1049	588	6171	3	1914	2608	3134	14	1655	846	6171	9	1328	1315	2931
2001	43	979	830	3027	1	81.5	81.5	81.5	15	937	1090	1638	10	2087	2185	3027
2002	52	790	760	2438	2	1212	1212	1529	25	911	936	1371	2	818	818	1138
2003	84	505	318	3335	5	2075	2231	3335	41	236	154	1109	11	807	716	1489
2004	210	534	348	3945	2	1528	1528	2760	24	627	597	1303	13	820	850	1797
2005	198	467	183	3673	2	2929	2929	3213	30	434	343	1291	5	751	616	2082
2006	151	395	153	3954	3	238	112	542	2	1129	1129	1354	1	24.9	24.9	24.9
2007	161	347	81	2759	3	318	250	955	3	324	341	632	7	872	176	2609
2008	98	422	51	3312	2	2566	2566	3312	3	202	77	528	6	1588	1496	2665
	Concentrations in water, μg L^{-1}															
2004	285	0.99	0.22	36.9	2	5.26	5.26	9.18	56	0.81	0.15	4	12	1.21	1.03	2.63
2005	229	0.74	0.2	18.7	1	0.62	0.62	0.62	13	0.49	0.21	1.3	8	0.37	0.18	1.14
2006	208	1.29	0.5	24.8	3	0.86	1.27	1.32	2	0	0	0	3	0.5	0.19	1.17
2007	322	1.23	0.57	29.7	4	0.68	0.59	1.30	4	1.79	1.08	4.5	14	5.22	2.19	29.7
2008	197	1.05	0.3	20.1	3	0.40	0	1.2	2	0.38	0.38	0.49	5	2.85	1.49	9.4

The measured concentrations from the Czech Republic are comparable (and in many cases higher) in comparison with literature data from Europe. For example, the maximum reported from Poland was 1687 μg g^{-1}.[12] In Germany, the maxima ranged from 1100μg g^{-1} d.w. [13] to 5595μg g^{-1}.[14] The highest value of 2565 μg g^{-1} was detected during 1994–2000 in Greece.[15] In Portugal, very high concentration of microcystin, 7100 μg g^{-1}, was detected.[16]

The concentrations of microcystins in water samples (μg L^{-1}, analysed by Elisa) were analysed in the years 2004–2008. When considering the national statistics, the mean values were in general about two-times higher than the median. A similar trend was also observed at the three localities studied in detail. However, the differences were not highly pronounced with respect to the lower number of values. In some cases, concentrations above the WHO guideline value of 1 μg L^{-1} were observed (including the Vír Reservoir) but most of the values were

lower even in the studied raw (untreated) water as also discussed elsewhere.[10] On the other hand, extreme concentrations (> 10 μg L^{-1}) were observed in several cases and the maximum value 29.7 μg L^{-1}, observed in Nové Mlýny during 2007, was the highest within the whole country.

The observed extreme concentrations (9–36 μg L^{-1}) are comparable with those given in the literature. For example, Zhang *et al.*[17] reported a maximum of 8 μg L^{-1} in China during the 2002 season. Very high concentrations were found in surface cyanobacterial scum in Germany[18] (up to 120 μg L^{-1}) and Algeria[19] (711.8 μg L^{-1}) but these represent a different type of sample and also a different analytical method (protein-phosphatase assay inhibition) was employed[19] than that used in the present study. Lower maximum concentrations were reported from Finland 0.21 μg L^{-1},[20] where water blooms are often dominated by different cyanobacterial species than *Microcystis* sp., which is the most common in the Czech Republic and Central Europe.[10,8,21]

As is apparent from Table I, there was no clear temporal trend in the microcystin concentrations in the biomass (decrease or increase) during the studied years in the studied localities, which might be attributed to specific environmental or meteorological factors.[22,23] During the present study, the summers of the years 1998, 2006–2007 were unusually cold, which might explain the lower incidence of toxic cyanobacterial blooms as well as the decrease in the microcystin concentrations in the biomass.[24,25]

Detailed seasonal variations in both biomass-bound MCs (Fig. 2A) and MCs in water (Fig. 2B) are shown in Fig. 2. As is apparent, there was no uniform trend within each of the investigated seasons. For the biomass concentrations (Fig. 2A), there seemed to be an increase in the Vír and Nové Mlýny Reservoirs, but a slight decrease during all the studied seasons was observed in Brno. On the other hand, these trends were not in all cases confirmed by the MC concentrations in water (Fig. 2B), where a slight increases could be observed also in the Brno reservoir (for example during 2004–2005). The observations at Vir and Nove Mlyny, in general, correspond to some previously published studies that demonstrated an increase in the production of MCs in the biomass during the vegetation season.[26] On the other hand, some studies reported two peaks in the concentrations of MCs (early summer *vs.* end of the season).[27,28]

The observed differences might be related to the biochemistry of microcystin production and its excretion, which are known to be influenced by a number of environmental factors. For example, different seasonal profile of temperature and other parameters can be expected in the Vír Reservoir, which is situated upstream of the Svratka River in an area of highlands, while the other two reservoirs (Brno and Nové Mlýny) are lowland reservoirs. MCs are mostly accumulated inside the cyanobacterial cells, while extracellular (dissolved) toxins form usually up to 10 % of the total MCs in water.[18] However, at the end of the season – following the

collapse of the water bloom – the ratio of the extracellular MCs significantly increases up to 96 % of the total content, as documented by Nasri *et al.*[19] During the short periods, dissolved MCs concentrations can rise to 100 μg L^{-1} and these concentrations might remain in the water for several days to weeks.[18] On the other hand, MC bound to particulate matter is known to be more rapidly degraded.[20]

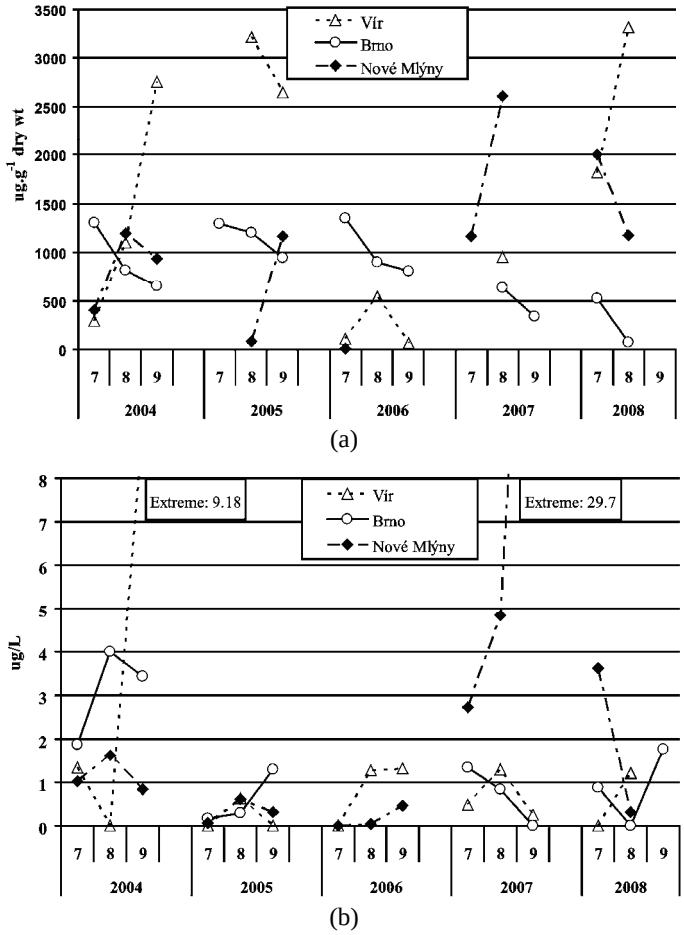

Fig. 2. Detailed seasonal variations in the concentrations of microcystin (MCs) in the biomass (upper panel, concentrations in microgram per gram biomass dry weight) and water (bottom panel, microgram per litre) in three reservoirs (Vír, Brno, Nové Mlýny) during July, August and September (7, 8, 9) of the years 2004–2008.

The present study, as well as literature data, indicates that under certain environmental situation, high concentrations of MCs may be observed during all vegetation seasons, and this should be carefully considered during monitoring studies.

In addition to the MCs concentrations, the composition of the water blooms in the studied reservoirs was also studied. In all three studied reservoirs, *Microcystis aeruginosa* was the most dominant species, which also correspond to the general situation in Central Europe.[8,12,13,21] However, during the studied period (1998–2008), an increase in the occurrence of other species, such as *Anabaena* sp., *Aphanizomenon* sp. or *Planktothrix* sp, were also observed. However, the issue of the occurrence and toxicity of less-studied species, including the tropical *Cylindrospermopsis raciborskii* , in Europe will require further research attention.[29]

CONCLUSIONS

The present report provides further insight into the occurrence and dynamics of toxic cyanobacterial metabolites – microcystins. The analyses showed that the appearance of dominant cyanobacterial taxa (*M. aeruginosa*) did not significantly change during the investigated period but there was an increase in the occurrence of other species belonging to genus Aphanizomenon, Anabaena and Planktothrix. Although absolute concentrations of the studied toxins microcystins differed between the reservoirs, there were apparent parallel trends. For example, during certain years, the microcystin concentrations were systematically elevated in all the studied reservoirs. Furthermore, based on monthly sampling, the concentration profiles in the three sites were also correlated (parallel trends) within individual seasons. Microcystin-LR, a variant for which the WHO has recommended a guideline value, formed only about 30–50 % of the total microcystins. In addition, a shift between the peaks of the cell-bound microcystins (expressed per biomass dry weight) was determined that seemed to precede the maxima of microcystins in water. The overall maximum toxin concentration in the biomass (all three reservoirs, period 1998–2008) was about 6000 microgram per gram dry weight with median values ranging from 65 to 2300. The concentrations of MCs in the raw waters only occasionally exceed the WHO limit of 1 microgram per litre but they occurred throughout the season and cannot be easily predicted. In summary, the obtained data revealed substantial variability of both toxic cyanobacteria and their peptide toxins that should be reflected in detailed monitoring programs.

Acknowledgements. This research was supported by grants from the Czech Ministries of Agriculture (NAZV QH71015) and Education (1M0571 and MSM0021622412), and by the project CETOCOEN (No. CZ.1.05/2.1.00/01.0001).

ИЗВОД

ПРОСТОРНО–ВРЕМЕНСКА ВАРИЈАБИЛНОСТ ЦИЈАНОБАКТЕРИЈСКИХ ОТРОВА МИКРОЦИСТИНА У ТРИ ПОВЕЗАНА РЕЗЕРВОАРА СВЕЖЕ ВОДЕ

LUDĚK BLÁHA, LUCIE BLÁHOVÁ, JIŘÍ KOHOUTEK, ONDŘEJ ADAMOVSKÝ, PAVEL BABICA and BLAHOSLAV MARŠÁLEK

Masaryk University, Faculty of Science, Research Centre for Toxic Compounds in the Environment – RECETOX, Kamenice 3, CZ62500 Brno u Institute of Botany, Academy of Sciences of the Czech Republic, Lidická 25/27, 657 20 Brno, Czech Republic

Упркос значајном обиму истраживања ризика по здравље и животну средину који су повезани са цијанобактеријским токсинима последњих деценија, схватање природне динамике и варијабилности токсичних цијанобактеријских цветања још увек је ограничено. Овде су приказани резултати дугорочног мониторинга 1998–1999/2001–2008. три резервоара (Vír, Brno и Nové Mlýny, Република Чешка) где се токсична цветања јављају сваке године. Ови резервоари представљају јединствен модел, зато што су повезани реком Svratka, што омогућава трансфер фитопланктона, као и токсина, између резервоара. Фреквенција појављивања и доминације већинских таксона *Microcystis aeruginosa* није се мењала током испитиваног периода, али значајна варијабилност је уочена у саставу осталог фитопланктона. Иако су се апсолутне концентрације проучаваних токсина (микроцистина) разликовале између резервоара, паралелни трендови су били очигледни. На пример, током неких година, концентрације микроцистина су систематски расле у сва три резервоара. Осим тога, концентрациони профили на све три локације су такође били корелисани (паралелни трендови) у оквиру појединачних сезона, на основу месечних узорковања. Микроцистин-ЛР, варијанта за коју је Светска здравствена организација препоручила оквирну референтну вредност, чинила је само 30–50 % укупних микроцистина. Ово је важно нарочито за резервоар Vír, који служи за снабдевање питком водом. Максимуми микроцистина везаних за ћелије (интрацелуларни, изражени по тежини суве биомасе) генерално се јављају пре максимума укупних микроцистина (изражених по запремини узорка воде). Општи максимум концентрације у биомаси (сва три резервоара, период 1993–2005.) био је 6,1 mg g^{-1} тежине суве материје; вредности медијане су биле у распону 0,065–2,3 mg g^{-1} тежине суве материје. Опште узевши, ово су високе концентрације у поређењу са подацима објављеним за Републику Чешку и свет. Подаци указују на значајну варијабилност како токсичних цијанобактерија тако и њихових пептидних токсина, што би требало да има одраза на детаљне програме мониторинга.

(Примљено 13. јануара, ревидирано 18. фебруара 2010)

REFERENCES

1. I. Chorus, J. Bartram, *Toxic Cyanobacteria in Water: A guide to their public health consequences, monitoring and management*, E & FN Spon, London, 1999, p. 432
2. L. Blaha, B. Marsalek, *Arch Hydrobiol.* **158** (2003) 421
3. B. Marsalek, L. Blaha, in *Current approaches to cyanotoxin risk assessment, risk management and regulations in different countries*, Federal Environmental Agency (Umweltbundesamt), Dessau, Germany, 2005, p. 37
4. Z. Svircev, S. Krstic, *J. Environ. Sci. Health C* **27** (2009) 36
5. M. F. Jukovic, Z. B. Svircev, *Arch Oncol.* **16** (2008) 55
6. J. Komarek, B. Marsalek, in *Cyanobacterial water blooms*, Nadatio Flos Aquae, Brno, p. 34 (in Czech)
7. A. Zeck, A. Eikenberg, *Anal. Chim. Acta* **441** (2001) 1

8. L. Bláhová, P. Babica, *CLEAN – Soil, Air, Water* **35** (2007) 348
9. P. Babica, J. Kohoutek, *Anal. Bioanal. Chem.* **385** (2006) 1545
10. L. Blahova, P. Babica, *Environ. Chem. Lett.* **6** (2008) 223
11. *WHO, Guidelines for drinking water quality*, World Health Organisation, Geneva, 1998, p. 95
12. T. Jurczak, M. Tarczynska, *Chromatographia* **59** (2004) 571
13. C. A. Frank, *Environ. Toxicol.* **17** (2002) 361
14. J. Fastner, U. Neumann, *Environ. Toxicol.* **14** (1999) 13
15. S. Gkelis, V. Harjunpaa, *Environ. Toxicol.* **20** (2005) 249
16. V. M. Vasconcelos, K. Sivonen, *Water Res.* **30** (1996) 2377
17. L. Zhang, X. Ping, *Talanta* **62** (2004) 191
18. M. Welker, C. Steinberg, *Release and persistence of microcystins in natural waters, in Cyanotoxins – Occurrence, Causes, Consequences*, Springer-Verlag, Berlin, 2001, p. 83
19. A. B. Nasri, N. Bouaicha, *Arch. Environ. Contam. Toxicol.* **46** (2004) 197
20. K. Lahti, J. Rapala, *Water Res.* **31** (1997) 1005
21. J. Mankiewicz-Boczek, K. Izyorezyk, *Environ. Toxicol.* **10** (2006) 49
22. P. Znachor, T. Jurczak, *Environ. Toxicol.* **21** (2006) 236
23. H. Yang, P. Xie, *Bull. Environ. Contam. Toxicol.* **77** (2006) 367
24. C. B. Halstvedt, T. Rohrlack, *J. Plankton Res.* **30** (2008) 607
25. M. V. Ame, D. A. Wunderlin, *Water Air Soil Pollut.* **168** (2005) 235
26. Q. Xu, W. Chen, *Environ. Monit. Assess.* **145** (2008) 75
27. B. Pawlik-Skowronska, T. Skowronski, *Pol. J. Chem. Ecol.* **52** (2004) 479
28. J. F. Briand, C. Robillot, *Arch. Hydrobiol.* **153** (2002) 605
29. L. Bláhová, M. Oravec, *Toxicon* **53** (2009) 519.

Journal of the Serbian Chemical Society
JSCS-info@shd.org.rs • www.shd.org.rs/JSCS
J. Serb. Chem. Soc. 75 (9) 1313 (2010)

Errata (printed version only)

Issue No. 8 (2010), Vol. 75:

– Page 1053 (paper JSCS-4030). One of the authors, Milena R. Spasić, is the member of the Serbian Chemical Society.

– Page 1060 (paper JSCS-4030). Acknowledgements should read: The authors wish to thank Filip Stojanović and Gordana Kukić for their excellent technical assistance. This research was supported by Ministry of Science and Technological Development of the Republic of Serbia, Grant No. 145035.

– Page 1161 (paper JSCS-4039). Paper should be denoted as Extended Abstract of the Section Lecture at the Meeting of the Chemical Engineering Section of the Serbian Chemical Society, held 5 February, 2010.